

MODELING AND DESIGN METHODOLOGIES FOR SOUND ABSORBING
POROUS MATERIALS WHEN USED AS LAYERED VIBRATION DAMPERS

A Dissertation

Submitted to the Faculty

of

Purdue University

by

Yutong Xue

In Partial Fulfillment of the

Requirements for the Degree

of

Doctor of Philosophy

December 2019

Purdue University

West Lafayette, Indiana

THE PURDUE UNIVERSITY GRADUATE SCHOOL
STATEMENT OF DISSERTATION APPROVAL

Dr. J. Stuart Bolton, Chair

School of Mechanical Engineering

Dr. Patricia Davies

School of Mechanical Engineering

Dr. Jeffrey F. Rhoads

School of Mechanical Engineering

Dr. Vikas Tomar

School of Aeronautics and Astronautics

Approved by:

Dr. Jay Gore

Head of the Graduate Program

To my Grandpa and the seed of curiosity he planted in my heart

ACKNOWLEDGMENTS

I cannot thank Professor J. Stuart Bolton enough for his guidance, patience and encouragement, without which I would never have such huge motivation and confidence to finish my work during the past four years. I would also like to thank Professor Patricia Davies for encouraging me and teaching me how to structure my time when things became really overwhelming in my last semester. Thanks to Professor Jeff Rhoads and Professor Vikas Tomar for being my committee members and for their valuable advice during my preliminary exam. Thanks a lot to Professor Yangfan Liu for his brilliant idea, which makes the classic transfer matrix method now a more comprehensive and efficient modeling tool. And thanks to all of my kind and helpful colleagues in Herrick Labs.

We would like to deliver a sincere appreciation to our colleagues at the 3M Company, who provided both financial and technical support of this work.

I would like to express my deepest love and gratefulness to my parents, who always encourage me to chase my goals, and always remind me of the importance of education. As I grow older, I understand them better and better.

I would like to say “I love you” to my wife, April, who is always there for me with her best love and support.

TABLE OF CONTENTS

	Page
LIST OF TABLES	ix
LIST OF FIGURES	x
ABSTRACT	xix
1. INTRODUCTION	1
1.1 Motivations and Objectives	1
1.2 Modeling Outline and Approach	3
2. ACOUSTICAL PROPERTIES EVALUATION BASED ON BULK PROP- ERTIES OF POROUS MEDIA	12
2.1 Introduction	12
2.2 The JCA Model for Evaluating the Effective Density and Bulk Modulus of Porous Media	12
2.3 The Biot Theory for Rigid, Limp, Elastic Porous Media	14
2.4 The TMM and the ACM for Multilayered Acoustical System Boundary Condition Implementation	17
2.4.1 The TMM Model Used for Rigid and Limp Porous Medium	17
2.4.2 The ACM Model Used for Poro-Elastic Medium	22
2.5 A Case Study of the JCA-Biot-TMM Model for Modeling a Limp- Framed Double-Component Fiber-Particle Porous Medium	22
2.6 Conclusions	24
3. ACOUSTICAL MODELING OF A MULTILAYERED SYSTEM	28
3.1 Introduction	28
3.2 A Review of Multilayered Acoustical System Modeling Methodologies	29
3.3 The Modified TMM Model to Couple Higher-Order Elements in a Lay- ered System	32
3.4 Transfer Matrix Dimension Reduction for a Poro-Elastic Layer	34
3.4.1 Introduction of Matrices	35
3.4.2 Singular Value Decomposition (SVD)	40
3.4.3 QR Decomposition (QRD)	44
3.4.4 An Alternative Matrix Dimension Reduction Method and a Comparison to the SVD+QRD Method	46
3.4.5 Calculation of Acoustical Properties	48
3.5 Transfer Matrix Dimension Reduction for an Elastic Solid Layer	48
3.6 Poro-Elastic Layer Surface Treatments Coupling Methodologies	54

	Page
3.6.1 Impermeable Thin Treatments Coupling Methodologies	54
3.6.2 Rigid/Flexible/Stiff Micro-Perforated Panels Coupling Methodologies	56
3.7 Transversely Isotropic Poro-Elastic Layers Coupling Methodology . . .	61
3.8 The Modified TMM Model Validation	62
3.9 Conclusions	63
4. THE NEAR-FIELD DAMPING (NFD) MODEL	78
4.1 Introduction	78
4.2 A Layered Structure with a Harmonic Line Force-Driven, Infinitely-Extended Panel: the Incorporation of Acoustical Models	78
4.3 A More Realistic Structure with a Harmonic Line Force-Driven, Partially-Constrained Panel	83
4.4 A Fuselage-Like Structure with a Convective Pressure-Driven, Periodically-Constrained Panel	87
4.5 Wavenumber Response Inverse Discrete Fourier Transform (IDFT) for the Spatial Response of the Panel	91
4.5.1 Choices of Sampling Rates	92
4.5.2 Identification of Conventional Panel Critical Frequencies	94
4.6 Power Analysis	95
4.6.1 Power Distribution in a Layered Structure	95
4.6.2 System Equivalent Damping Loss Factor	97
4.7 Model Validations	98
4.7.1 Model Validation for a Partially-Constrained Structure by Using a Finite Element Model	98
4.7.2 Model Validation for a Periodically-Constrained Structure by Using a Finite Element Model	99
4.7.3 Model Validation for a Periodically-Constrained Structure by Using an Analytical Model	99
4.8 Conclusions	100
5. PREDICTIONS OF DAMPING PERFORMANCE FOR POROUS DAMPING TREATMENTS BASED ON THE NFD MODEL	117
5.1 Introduction	117
5.2 Limp Porous Damping Treatments Applied to an Infinitely-Extended Vibrating Panel	117
5.2.1 Spatial Response: Treated <i>vs.</i> Untreated Panels	118
5.2.2 Power Distribution: Treated <i>vs.</i> Untreated Panels	119
5.2.3 Damping Loss Factor: Parametric Studies on Limp Fibrous Treatments	120
5.3 The Effects of Adding Bulk Elasticity to the Porous Media	121
5.3.1 Power Dissipation: Limp Layer <i>vs.</i> Elastic Layer	122
5.3.2 Bonding Effect for Poro-Elastic Damping Media	122

	Page
5.3.3 Damping Loss Factor: Limp Layer <i>vs.</i> Elastic Layer	123
5.4 Limp Porous Damping Treatments Applied to a Fuselage-Like Structure	123
5.4.1 Wavenumber Response and the Identification of Convective Ex- citation Critical Frequencies	124
5.4.2 Velocity Response Spectrum: Treated <i>vs.</i> Untreated Panels . .	124
5.4.3 Spatial Response: Treated <i>vs.</i> Untreated Panels	125
5.4.4 Damping Loss Factor: Parametric Studies on Limp Fibrous Treatments	125
5.5 Conclusions	125
6. THE AIRFLOW RESISTIVITY (AFR) MODEL TO BUILD THE MICRO- BULK RELATIONS FOR FIBROUS MEDIA	141
6.1 Introduction	141
6.2 Single-Component Fibrous Media with Uniform Fiber Radius (SCUR)	142
6.2.1 AFR-SCUR Models Review and General Comparison	142
6.2.2 AFR-SCUR Models Prediction Accuracy Evaluated by Com- parison to Measurements	145
6.3 Two-Component Fibrous Media with Various Fiber Radii (TCVR) . .	146
6.3.1 AFR-TCVR Model Development	146
6.3.2 AFR-TCVR Model Validation by Measurements	149
6.4 Conclusions	150
7. MICROSTRUCTURAL OPTIMIZATIONS FOR FIBROUS DAMPING TREAT- MENTS BASED ON THE AFR MODEL	157
7.1 Introduction	157
7.2 Finding Optimal Fiber Radii of Fibrous Damping Treatments	157
7.3 Optimized Limp Fibrous Damping Treatments for an Infinitely-Extended Vibrating Panel	160
7.4 Optimized Limp <i>vs.</i> Elastic Fibrous Damping Treatments for a Partially- Constrained Vibrating Panel	161
7.5 Optimized Glass <i>vs.</i> Polymeric Fibrous Damping Treatments for a Fuselage-Like Structure	162
7.6 Practical Case Study: A Vehicle Floor Pan-Like Structure with a Har- monic Line Force-Driven, Arbitrarily-Shaped Panel	163
7.6.1 General Approach	164
7.6.2 Identification of the Strong Vibration Region for a Floor Pan- like Structure	165
7.6.3 Evaluation of the Damping Performance for a Limp Fibrous Layer	166
7.7 Optimization of the Limp Fibrous Damping Treatment for a Vehicle Floor Pan-Like Structure	168
7.8 Conclusions	168
8. CONCLUSIONS AND NEXT STEPS	183
8.1 Summary of Conclusions	183

	Page
8.2 Recommendation of Next Steps	186
REFERENCES	188
A. THE GRANULAR ACTIVATED CARBON (GAC) MODEL USED TO COUPLE BULK MODULI FROM DIFFERENT SCALES OF PORES OF THE DOUBLE-COMPONENT FIBER-PARTICLE POROUS MEDIUM .	195
B. THE TRANSFER MATRIX METHOD (TMM) USED TO PREDICT ACOUS- TICAL PROPERTIES FOR LIMP POROUS MEDIA	198
C. THE ARBITRARY COEFFICIENT METHOD (ACM) USED TO PRE- DICT ACOUSTICAL PROPERTIES FOR PORO-ELASTIC MEDIA . . .	200
D. SPACE-HARMONIC ANALYSIS TO PREDICT THE RESPONSES OF PERIODICALLY-SUPPORTED BEAMS	208
E. SUMMARY OF THE FORMULAE FROM THE AFR-SCUR CLASSIC MODELS	210
VITA	213

LIST OF TABLES

Table	Page
3.1 Parameters for the poro-elastic layer.	66
3.2 Parameters for the elastic solid layer.	66
3.3 Parameters for the aluminum panel.	66
3.4 Parameters for the air ambient environment when the temperature is 25 °C. 66	
4.1 Parameters for the air ambient environment when the temperature is 25 °C.102	
4.2 Parameters for the aluminum panel.	102
4.3 Parameters of the discontinuity (constraint) having a dimension of 20 cm × 5 cm and a density of 20000 kg/m ³ to create a partially-clamped condition.102	
4.4 Parameters of the discontinuity (constraint)the discontinuity (constraint) having a dimension of 20 cm × 5 cm and a density of 20000 kg/m ³ to create a periodically-clamped condition.	102
4.5 Parameters for the limp porous layer.	102
4.6 Parameters for the poro-elastic layer.	103
5.1 Parameters of discontinuity (constraint) to create a partially-constrained condition.	127
5.2 Parameters of discontinuity (constraint) to create a periodically-clamped condition.	127
6.1 Inputs for regenerating the measured TCVR fiber radii distributions. . .	152
7.1 Parameters for the limp TCVR fibrous layer applied to the unconstrained structure.	170
7.2 Parameters for the limp SCUR fibrous layer applied to the fuselage-like structure.	170

LIST OF FIGURES

Figure	Page
1.1 The reduction of both airborne noise and structural vibration after the substrate is treated with a multi-functional porous layer.	10
1.2 The near-field damping depth of a 3 mm thick, harmonic line force-driven, aluminum panel.	10
1.3 A typical acoustical model that connects porous media's bulk properties and their acoustical properties.	10
1.4 General modeling process consisting of the NFD model with the TMM or the ACM acoustical model and the AFR micro-bulk model for either damping prediction or optimization.	11
1.5 A harmonic line force-driven, infinitely-extended panel treated with a porous damping layer.	11
1.6 A harmonic line force-driven, partially-constrained panel treated with a porous damping layer.	11
1.7 A convective pressure-driven, periodically-constrained panel treated with a porous damping layer.	11
1.8 A harmonic line force-driven, arbitrarily-shaped panel.	11
2.1 The Transfer Matrix Method (TMM) for a rigid or limp porous layer. . . .	26
2.2 (a) Front and (b) back views of a double-component limp porous layer. . .	26
2.3 (a) An intergranular-scale SEM of a single particle of the double-component limp porous medium, (b) pore structures of the particle to show micro-scale and nano-scale pores.	27
2.4 Absorption coefficient prediction for a 1.2 cm thick double-component limp porous medium that consists of fibers and activated carbon particles. . . .	27
3.1 The general idea of the matrix dimension reduction process for a poro-elastic layer-involved case by using the modified Transfer Matrix Method (TMM).	67
3.2 The general idea of the matrix dimension reduction process for an elastic solid layer-involved case by using the modified Transfer Matrix Method (TMM).	67

Figure	Page
3.3 The predictions of the acoustical properties for a front-open, rigid-backed poro-elastic layer: the modified TMM <i>vs.</i> the classical ACM.	68
3.4 The predictions of the acoustical properties for a poro-elastic layer having open surfaces on both sides: the modified TMM <i>vs.</i> the classical ACM. . .	69
3.5 The predictions of the acoustical properties for a poro-elastic layer having bonded stiff panels on both sides: the modified TMM <i>vs.</i> the classical ACM.	70
3.6 The predictions of the acoustical properties for a poro-elastic layer having a bonded stiff panel at its front surface, and an unbonded stiff panel with 1 cm air gap from its back surface: the modified TMM <i>vs.</i> the classical ACM.	71
3.7 The predictions of the acoustical properties for a poro-elastic layer having an unbonded stiff panel with 1 cm air gap from its front surface, and a bonded stiff panel at its back surface: the modified TMM <i>vs.</i> the classical ACM.	72
3.8 The predictions of the acoustical properties for an elastic solid layer having open surfaces on both sides: the modified TMM <i>vs.</i> the classical ACM. . .	73
3.9 The predictions of the acoustical properties for an elastic solid layer having bonded stiff panels on both sides: the modified TMM <i>vs.</i> the classical ACM.	74
3.10 Normal incidence absorption coefficient for four cases with a limp membrane bonded/unbonded with the poro-elastic foam, and/or with the foam bonded/unbonded to the rigid backing.	75
3.11 Regeneration of the normal incidence absorption coefficient for the four cases with a limp membrane bonded/unbonded with the poro-elastic foam, and/or with the foam bonded/unbonded to the rigid backing.	76
3.12 Structural resonances between Rayleigh waves below the Rayleigh angle (blue line) of an aluminum layer modeled as an elastic solid by the modified TMM model.	77
4.1 A harmonic line force-driven, infinitely-extended aluminum panel treated with a limp porous damping layer.	103
4.2 A harmonic line force-driven, infinitely-extended panel treated with a bonded poro-elastic damping layer.	103
4.3 A harmonic line force-driven, infinitely-extended panel treated with an unbonded poro-elastic damping layer.	104
4.4 A harmonic line force-driven, partially-constrained panel treated with a limp porous damping layer.	104

Figure	Page
4.5 A harmonic line force-driven, partially-constrained panel treated with a bonded poro-elastic damping layer.	104
4.6 Aircraft fuselage-like structure modeled for the current study.	105
4.7 A typical aircraft fuselage structure as shown in Nadeau <i>et al.</i> 's study [5] and a fuselage acoustical treatment as shown in Klos <i>et al.</i> 's study [65]. .	105
4.8 A harmonic line force-driven, unconstrained aluminum panel directly loaded by an air half-space.	105
4.9 Evaluation of the wavenumber/frequency domain response for a 3 mm thick aluminum panel driven by a harmonic line force and loaded by an air half-space as shown in Figure 4.8.	106
4.10 Selection of the cutoff level of -130 dB based on the evaluation as shown in Figure 4.9.	107
4.11 Choice of the sampling rate for a certain frequency based on the cutoff level of -130 dB as marked in Figure 4.10.	107
4.12 A 1 mm thick, harmonic line force-driven, partially-clamped aluminum panel directly loaded by an air half-space in the NFD model.	108
4.13 Choices of the sampling rates (marked as the magenta line) based on the wavenumber/frequency response for the panel shown in Figure 4.12 at a cutoff level of -200 dB.	108
4.14 A 1 mm thick, harmonic line force-driven, periodically-clamped aluminum panel directly loaded by an air half-space in the NFD model.	109
4.15 Choices of the original sampling rates (marked as the black line) based on the wavenumber/frequency response for the panel shown in Figure 4.14 at a cutoff level of -300 dB, and further adjusted sampling rates (marked as the magenta line) to ensure a complete periodic structure.	109
4.16 Identification of the critical frequency of a 3 mm aluminum panel in the NFD model.	110
4.17 A 1 mm thick, harmonic line force-driven, partially-clamped aluminum panel loaded by a limp porous layer plus an air half-space in the NFD model.	110
4.18 A 1 mm thick, harmonic line force-driven, partially-clamped aluminum panel loaded by a poro-elastic layer plus an air half-space in the NFD model.	111
4.19 A 1 mm thick, 1 m long, harmonic line force-driven, aluminum panel directly loaded by an air half-space, and fixed at the ends in COMSOL model.	111

Figure	Page
4.20 A 1 mm thick, 1 m long, harmonic line force-driven, aluminum panel loaded by a limp porous layer plus an air half-space, and fixed at the ends in COMSOL model.	111
4.21 A 1 mm thick, 1 m long, harmonic line force-driven, aluminum panel loaded by a poro-elastic layer plus an air half-space, and fixed at the ends in COMSOL model.	112
4.22 NFD <i>vs.</i> COMSOL of the velocity response spectrum at the driving point ($x = 0$ m) for configuration (1): a bare clamped panel.	112
4.23 NFD <i>vs.</i> COMSOL of the velocity response spectrum at the driving point ($x = 0$ m) for configuration (2): a clamped panel treated by a limp porous layer.	113
4.24 NFD <i>vs.</i> COMSOL of the velocity response spectrum at the driving point ($x = 0$ m) for configuration (3): a clamped panel treated by a poro-elastic layer.	114
4.25 A 1 mm thick, convective pressure-driven, periodically-clamped aluminum panel loaded by a limp porous layer plus an air half-space in the NFD model.	114
4.26 A 1 mm thick, 1 m long, convective pressure-driven, aluminum panel loaded by a limp porous layer plus an air half-space, and fixed at the ends in COMSOL model.	115
4.27 NFD <i>vs.</i> COMSOL of the velocity response spectrum at $x = 0$ m for the convective pressure-driven, periodically-clamped structure.	115
4.28 NFD <i>vs.</i> Mead's space harmonic model of the velocity response spectrum at $x = 0.11$ m for the convective pressure-driven, periodically-clamped structure in a vacuum.	116
5.1 Spatial velocity level comparison between case (1): a bare 3 mm thick, unconstrained aluminum panel (solid lines) and case (2): a 3 mm thick, unconstrained aluminum panel with a 3 cm layer of limp porous media (dashed lines), both driven by the harmonic force under different frequencies: 10 Hz, 56 Hz, 316 Hz, 1778 Hz and 10000 Hz.	127
5.2 Spatial velocity level for case (1): a bare 3 mm thick, unconstrained aluminum panel, driven by a harmonic force under 100 different frequencies: log-spaced within 10–10000 Hz.	128
5.3 Spatial velocity level for case (2): a 3 mm thick, unconstrained aluminum panel with a 3 cm layer of limp porous media, driven by a harmonic force under 100 different frequencies: log-spaced within 10–10000 Hz.	129

Figure	Page
5.4 A side view of the spatial velocity level differences at $x = 10$ m between case (1): an unconstrained aluminum panel driven by a harmonic force under 100 different frequencies (log-spaced within 10–10000 Hz), and case (2): the panel treated with a 3 cm layer of limp porous medium with (a) 3 mm, (b) 1.5 mm and (c) 6 mm as panel thicknesses.	130
5.5 Power distribution for case (1): a bare 3 mm thick, unconstrained aluminum panel, driven by a harmonic force under 100 different frequencies: log-spaced within 10–10000 Hz.	131
5.6 Power distribution for case (2): a 3 mm thick, unconstrained aluminum panel with a 3 cm layer of limp porous medium, driven by a harmonic force under 100 different frequencies: log-spaced within 10–10000 Hz. . .	132
5.7 System equivalent damping loss factor of a 1 mm thick, unconstrained aluminum panel treated with limp fibrous layers with the same thickness and airflow resistivity but different bulk densities, driven by a harmonic force under 100 different frequencies: log-spaced within 10–10000 Hz. . .	133
5.8 System equivalent damping loss factor of a 1 mm thick, unconstrained aluminum panel treated with limp fibrous layers with the same airflow resistivity but different combinations of thicknesses and bulk densities, driven by a harmonic force under 100 different frequencies: log-spaced within 10–10000 Hz.	134
5.9 System equivalent damping loss factor of a 1 mm thick, unconstrained aluminum panel treated with limp fibrous layers with the same thickness and bulk density but different airflow resistivities, driven by a harmonic force under 100 different frequencies: log-spaced within 10–10000 Hz. . .	135
5.10 Normalized power dissipations within either a bonded poro-elastic layer (red solid lines) or a limp porous layer (green dashed lines) acting on a 1 mm (circled lines) or a 3 mm (starred lines) thick, unconstrained aluminum panel, driven by a harmonic force under 50 different frequencies: log-spaced within 10–10000 Hz.	136
5.11 Adding normalized power dissipations within an unbonded poro-elastic layer acting on a 1 mm (blue dotted-circled line) or a 3 mm (blue dotted-starred line) thick, unconstrained aluminum panel, driven by a harmonic force under 50 different frequencies: log-spaced within 10–10000 Hz. . . .	136
5.12 System equivalent damping loss factor for a 1 mm thick, partially-constrained aluminum panel treated either by a bonded poro-elastic layer (red solid line) or a limp porous layer (green dashed line), driven by a harmonic force under 500 different frequencies: log-spaced within 1–1000 Hz.	137

Figure	Page
5.13 Wavenumber domain velocity level for a 3 mm thick, fuselage-like structure treated by a 3 cm thick, limp porous layer, driven by (a) subsonic convective pressure ($M = 0.8$), (b) sonic convective pressure ($M = 1.0$), (c) supersonic convective pressure ($M = 1.2$), with the convective excitations marked as black dashed lines.	138
5.14 Velocity response spectrum from 10 Hz to 10000 Hz of the velocity at $x = 0.11$ for the 3 mm thick, bare fuselage-like structure (blue line) or the limp porous layer-treated, fuselage-like structure (orange line) both driven by (a) subsonic ($M = 0.8$), (b) supersonic ($M = 1.2$) convective pressure, both with conventional and convective critical frequencies marked by red arrows.	139
5.15 Velocity response spectrum from 100 Hz to 1200 Hz of the velocity at $x = 0.11$ for the 3 mm thick, bare fuselage-like structure (blue line) or the limp porous layer-treated, fuselage-like structure (orange line) both driven by (a) subsonic ($M = 0.8$, with 420 Hz selected as a spatial response observation frequency), (b) supersonic convective pressure ($M = 1.2$, with 521 Hz selected as a spatial response observation frequency).	139
5.16 Spatial responses between the constraints at $x = \pm 0.5$ m for the 3 mm thick, bare fuselage-like structure (blue line) or the limp porous layer-treated fuselage-like structure (orange line) both driven by (a) subsonic convective pressure ($M = 0.8$) at 420 Hz, (b) supersonic convective pressure ($M = 1.2$) at 521 Hz.	140
5.17 System equivalent damping loss factor for the 3 mm thick, fibrous layer-treated fuselage-like structure driven by (a) subsonic convective pressure ($M = 0.8$), (b) supersonic convective pressure ($M = 1.2$), with input fibrous layer's airflow resistivity as 10000 Rayls/m (orange line), 20000 Rayls/m (magenta line), 50000 Rayls/m (blue line).	140
6.1 Target fibrous material of the current study with two fiber components and varying fiber radii.	152
6.2 (a) Fibrous material microstructure [89], (b) partially-reticulated foam microstructure [90], (c) Voronoi cells [91].	152
6.3 General comparison among AFR-SCUR models.	153
6.4 (a) Gas Permeameter GP-05A-C-522 for ASTM-C522-03 AFR measurements, (b) SEM view of fiber component 2.	153
6.5 AFR-SCUR models predictions compared to measurements.	154
6.6 (a) Micro-CT scanned TCVR fiber radii distributions, (b) regenerated TCVR fiber radii distributions as inputs.	155

Figure	Page
6.7 AFR-TCVR model predictions (marked as the blue dots) based on 500 normally-distributed (with mean value of $5.5 \mu\text{m}$ and standard deviation of $0.2 \mu\text{m}$) inputs of r_1 's corresponding to 500 uniformly-distributed (within $0.3\text{--}0.38 \text{ kg/m}^2$) inputs of basis weights, or (marked as the green line) based on a constant input of r_1 as $5.5 \mu\text{m}$ corresponding to 500 line-spaced (within $0.3\text{--}0.38 \text{ kg/m}^2$) inputs of basis weights, compared to the repeated measurements (marked as the red crosses) for six samples with verified microstructure details, and the 1 st -degree polynomial fitting of the measured results (marked as the black line).	156
7.1 Fibrous material acoustical and damping properties prediction by an analytical approach.	170
7.2 Fibrous material microstructure design by an analytical approach.	170
7.3 Optimal airflow resistivity, σ_o 's (blue stars) selected from 200 log-spaced σ candidates ranging from 500 to 500000 Rayls/m, and the AFR-TCVR model-fitted airflow resistivity, σ_{fit} 's (orange stars) corresponding to the optimal r_1 shown in Figure 7.4 for a 3 mm thick, unconstrained aluminum panel with a 3 cm layer of limp fibers, driven by a harmonic force under 10 different frequencies: line-spaced within 100–1000 Hz.	171
7.4 σ_{fit} -corresponded optimal r_1 (orange stars) identified from 100 line-spaced r_1 candidates ranging from $0.01 \mu\text{m}$ (blue dashed line) to $11 \mu\text{m}$ (red dashed line) for a 3 mm thick, unconstrained aluminum panel with a 3 cm layer of limp fibers, driven by a harmonic force under 10 different frequencies: line-spaced within 100–1000 Hz, with the optimal r_1 at four different frequencies: 100 Hz (in blue circle), 300 Hz (in red circle), 500 Hz (in green line) and 700 Hz (in purple line) being selected for radii distribution observation.	171
7.5 Regenerated fiber radii distributions corresponding to the optimal r_1 's designed for TCVR fibers for a 3 mm thick, unconstrained aluminum panel with a 3 cm layer of limp fibers (σ ranging from 500 to 500000 Rayls/m), driven by a harmonic force under four different frequencies: 100 Hz (blue line), 300 Hz (red line), 500 Hz (green line) and 700 Hz (purple line). . .	172
7.6 Optimal σ 's for either a 3 cm thick bonded poro-elastic layer (red solid line) or a limp porous layer (green solid line) to achieve the largest η_e 's when acting on a 1 mm thick, partially-constrained aluminum panel, driven by a line force at ten equally-spaced frequencies ranging from 100 to 1000 Hz.	172

Figure	Page
7.7 The largest η_e 's achieved by either a 3 cm thick bonded poro-elastic layer (red solid line) or a limp porous layer (green solid line) applied to a 1 mm thick, partially-constrained aluminum panel, driven by a line force at ten equally-spaced frequencies ranging from 100 to 1000 Hz.	173
7.8 Optimal r_1 's for either a 3 cm thick bonded poro-elastic layer (red solid line) or a limp porous layer (green solid line) to achieve the largest η_e 's when acting on a 1 mm thick, partially-constrained aluminum panel, driven by a line force at ten equally-spaced frequencies ranging from 100 to 1000 Hz.	173
7.9 Optimal damping in terms of η_e achieved by a 3 cm thick layer of microstructural-optimized polymeric fibers (blue solid line) or glass fibers (red dashed line) for a 3 mm thick fuselage-like structure driven by (a) subsonic convective pressure ($M = 0.8$), (b) supersonic convective pressure ($M = 1.2$) at ten equally-spaced frequencies ranging from 100 to 1000 Hz.	174
7.10 Optimal fiber radii, r_1 , designed for a 3 cm thick layer of polymeric fibers (orange line) or glass fibers (green line) to achieve the optimal damping for a fuselage-like structure driven by (a) subsonic convective pressure ($M = 0.8$), (b) supersonic convective pressure ($M = 1.2$) at ten equally-spaced frequencies ranging from 100 to 1000 Hz.	174
7.11 A 1 mm thick, harmonic line force-driven, arbitrarily-shaped aluminum panel to model a vehicle floor pan-like structure.	175
7.12 Transverse velocity response spectra at $x = 0.382$ m (blue line) and $x = 0.8$ m (green line) returned by the COMSOL finite element model.	175
7.13 Transverse velocity (real part) spatial response at $f = 100$ Hz (blue line), $f = 1000$ Hz (green line) and $f = 10000$ Hz (red line).	176
7.14 Wavenumber/frequency domain transverse velocity level (dB) of the bare (untreated) floor pan-like structure, with the strong vibration region marked in blue rectangle, and speed of sound (sonic) lines mark in magenta. . . .	177
7.15 A line-driven, infinitely-extended bare limp fibrous layer for damping evaluation based on the NFD analytical model.	177
7.16 Power dissipation [W/m^2] within a line-driven, infinitely-extended limp fibrous layer.	178
7.17 Parametric study of the effect of airflow resistivity on the fibrous layer's damping performance in terms of the power dissipation [W/m^2].	179

Figure	Page
7.18 Energy dissipation per cycle per unit length of y -direction [J/m] within the strong vibration region under different airflow resistivities to identify the optimal airflow resistivity for the limp fibrous damping treatment. . .	180
7.19 Wavenumber/frequency velocity level (dB) spectrum within the strong vibration region of (a) the untreated floor pan-like structure, (b) the floor pan-like structure treated by the optimized fibrous damping layer, (c) the difference between (a) and (b) to show the vibration reduction.	181
7.20 Spatial responses at peak frequencies within the target region of (a) the untreated floor pan-like structure, and (b) the floor pan-structure treated by the optimized fibrous damping layer.	182

ABSTRACT

Xue, Yutong. Ph.D., Purdue University, December 2019. Modeling and Design Methodologies for Sound Absorbing Porous Materials when Used as Layered Vibration Dampers. Major Professor: J. Stuart Bolton, School of Mechanical Engineering.

Modeling methodologies based on state-of-the-art and classic theories of acoustics have been developed to provide a comprehensive toolbox, which can be used to model multilayer systems that involve acoustical and/or damping treatments, and to optimize these treatments' performance by designing their geometrical structures. The objective of this work was to understand, predict and optimize conventional sound absorbing porous media's near-field damping performance, so that automotive and aerospace industries can take full advantage of layered porous treatments' lightness and multi-functionality: *i.e.*, absorption of airborne sound and reduction of structure-borne vibration, for noise control applications. First, acoustical models that include the Transfer Matrix Method and the Arbitrary Coefficient Method were developed to build connections between the bulk properties and acoustical properties of porous media when coupled into layered systems. Given a specified layered system consisting of a vibrating panel and a porous damping treatment, the acoustics models were then incorporated into the Near-Field Damping model to predict the acoustical near-field and spatial response of the panel, based on which the near-field damping performance can be evaluated for a limp or an elastic porous layer when applied on different structures including an infinitely-extended panel, a partially-constrained panel, an aircraft fuselage-like structure and a vehicle floor pan-like structure. Furthermore, the relations between the material's microstructural details and bulk properties were established *via* an Air-Flow Resistivity model for porous media that are made of fibers, and the optimal fiber size that provides the largest damping for certain vibrating structures was identified. Relatively large fibers were found to be better at reducing

lower frequency vibrations; fibers made of polymer were found to have manufacturing benefits over fibers made of glass to achieve equivalent optimal damping performance; and elastic fibers were found to have both manufacturing and damping advantages over limp fibers.

1. INTRODUCTION

1.1 Motivations and Objectives

Subject to considerations of cost-effectiveness and fuel-economy, the automotive and aerospace industries are actively seeking acoustical solutions that do not require the addition of substantial weight. Conventionally, there are two separate solutions that are applied to reduce vehicle or aircraft interior noise. First, porous media including various types of fibers and foams are used for absorbing cabin noise since they effectively dissipate the acoustic energy of propagating sound waves. Second, damping treatments like constrained viscoelastic solid layers are applied to panel structures (*e.g.*, vehicle roof/door panel, floor pan, aircraft fuselage, *etc.*) to control structure-borne noise by attenuating the structural vibrations. However, several previous studies [1–10] have shown that porous “acoustical” materials can also provide levels of structural damping comparable to conventional dampers while holding a prominent advantage of lightness over the latter. For example, Lai *et al.* [2] demonstrated that layers of fibrous material placed on panels could effectively reduce the panel motion by removing energy from the near-field acoustical motion generated by the panel vibration. That idea was verified by Gerdes *et al.*’s [3] numerical models. Afterwards, Gerdes *et al.* [4] showed that fibrous dampers could provide damping performance equivalent to three other traditional viscoelastic dampers. Furthermore, the effectiveness of fibrous layered damping treatments was also verified by Nadeau *et al.* [5] through aircraft fuselage tests. Cummings *et al.* [6] and Tomlinson *et al.* [7] studied the damping effect of plastic foams placed close to vibrating plates by experimental measurements and analytical models. Fricke [8] also experimentally verified the damping performance of low-density granular materials. And recently, Kim *et al.* [10] proposed and experimentally verified a numerical method to design the thick-

nesses of different lightweight fibrous sound absorbers for them to be used as structural dampers for automotive applications. A review of the literature shows that the structural damping by porous media is primarily effective in the sub-critical frequency range of the vibrating panel. In that frequency range, the acoustical near-field of a panel consists of oscillatory flow oriented primarily parallel with the panel surface. When a porous layer occupies that region, energy is dissipated by the viscous interaction of the evanescent (*i.e.*, non-propagating) near-field and the porous medium, and the result is a damping of the panel motion. Due to this specific damping mechanism, the structural damping by porous media is referred to as “near-field damping” in the current study. Note that the near-field damping described in this article is achieved by the action of porous media removing energy from the near-field acoustical motion (*i.e.*, mostly from the in-plane direction motion), and relies on a distinctly different mechanism than that resulting from the application of viscoelastic damping layers, as described in Refs. [11–13], for example, where the damping is due to viscoelastic energy dissipation. The acoustical performance of conventional sound absorbing porous materials has, of course, been studied for many years, in contrast, the focus here is specifically on the examination of these materials’ near-field damping performance, so that when a properly-designed porous layer is placed adjacent to a vibrating structure as shown in Figure 1.1, it will serve multi-functional roles by attenuating both airborne noise and panel structural vibration, and the near-field damping performance of the porous layer makes the addition of a separate damping treatment unnecessary, thus reducing the number of elements required to achieve a specified level of noise and vibration reduction, with the result that the cost and total weight of the sound package in a vehicle or an aircraft can be reduced.

Based on the definition of the near-field damping, an obvious question here is: How thick is the acoustical near-field, *i.e.*, what is the near-field damping effective depth perpendicular to the panel toward the adjacent medium. As an example, parameters listed in Tables 4.1 and 4.2 were input into the models to be introduced in Chapters 2 to 4 for a 3 mm thick aluminum panel driven by a harmonic line force at

different frequencies, and loaded by an air half-space above it, and the solution of the equation $e^{-ik_z d_{\text{nf}}} = 0.1$ quantified the near-field depths, d_{nf} , as the z -location of 90% decay of the evanescent wave having wavenumber, $k = 2\pi f/c$, and trace wavenumber, k_x , where $k_z = \sqrt{k^2 - k_x^2}$ is the normal direction evanescent wavenumber on the transmission side of the panel when $k^2 < k_x^2$. Details about these wavenumbers will be further introduced in Chapter 2. The near-field depths, d_{nf} , for the panel configuration mentioned above were evaluated in terms of k_x and f , and are plotted in Figure 1.2, and the results provide a general impression on damping effective depth of such a panel structure: *i.e.*, near-field depths are becoming larger for the evanescent wavenumber components that are closer to but outside of the speed of sound lines ($k^2 = k_x^2$), and there are no evanescent near-field existing between the speed of sound lines, because when $k^2 > k_x^2$, all the wave components are propagating in that region.

The main objective of the current study was thus to build connections between porous materials' parameters (microstructure details or macroscopic properties) and their performances (acoustical properties, damping properties), so that damping performance of certain porous treatment could be predicted based on the specification of a layered structure, and so that parametric studies can be conducted to help understand the connection between the materials' structures and their performances. Further, the objective here also relates to designing the microstructure for certain types of porous dampers, for example, a porous damping layer that is made of fibers. In particular, the intention here is to develop an approach to relate fibers' microscopic properties with the damping properties of the fibrous layer, so that the fibrous material's microstructure can be designed to achieve optimal damping performance in a particular circumstance.

1.2 Modeling Outline and Approach

Based on the objectives mentioned in the last section, it was decided to build the various connections mentioned above mainly by analytical models. There were

three reasons for this choice. First, analytical models have relatively high calculation efficiency compared to numerical simulations using finite element methods, for example, which is convenient for the relatively large load of calculations involved when performing parametric studies. Secondly, an analytical approach can accurately capture specific acoustical and damping characteristics (*e.g.*, the spatial resonance at a panel's critical frequency), which is useful when studying the connections between the material structure and its performance. Thirdly, there are well-developed analytical models related to porous media that allow their macroscopic properties (alternatively referred to as bulk properties), acoustical properties and damping properties to be evaluated.

As shown on the right-hand side of Figure 1.1, a typical configuration to describe a near-field damping problem consists of two parts: the substrate (*i.e.*, the panel structure) and the treatment (*i.e.*, the porous layer). To simulate a near-field damping problem, the substrate with a certain type of excitation should first be modeled to represent the target vibrating panel structure being studied. Also, the general type of porous layer: *i.e.*, rigid, limp or elastic [14], should first be chosen according to the nature of the target material's solid phase. Cummings *et al.* [6] and Tomlinson *et al.* [7], for example, modeled a damping treatment consisting of plastic foam as a rigid-framed porous layer. Due to the low stiffness and density of the lightweight porous materials typically used in the automobile and aerospace industries, the porous layer in this study was first modeled as being limp, which means that the influence of the elasticity of the bulk solid phase of the material is assumed to be negligible. However, earlier Bruer and Bolton [1] indicated that compared to just one type of wave that propagates within a rigid or limp porous layer, multiple types of waves could propagate within a poro-elastic layer [15] with non-negligible bulk elasticity of the frame, and that together they acted to create additional means of energy dissipation. Further, Varanasi and Nayfeh [9] applied modal expansion to compute the damping effect of low-density, low-wave-speed media, which verified the damping advantage of poro-elastic materials. Therefore, here, a near-field damping (NFD)

model was developed that incorporated both limp porous and poro-elastic media in order to examine a poro-elastic medium's potential damping advantages over the limp porous media considered previously.

Furthermore, proper acoustical models should be developed to couple the treatment and the substrate into a layered system, as well as to accurately evaluate the acoustical near-field of the panel, which directly relates to the damping of the panel motion. A typical acoustical model that relates porous media's bulk properties and their acoustical properties can be summarized in Figure 1.3. First, the fundamental acoustical properties including effective density and bulk modulus of a porous medium can be predicted based on classic acoustical theories such as the Johnson-Champoux-Allard (JCA) model [16] model given the porous medium's bulk properties. Then complex wavenumber(s) within the porous medium can be solved for based on the Biot theory [15, 17–20]. Finally, the acoustical properties of a layered system that involves the porous medium can be predicted based on the implementation of the boundary conditions (B.C.s) of the system, and the B.C.s implementation can be achieved by using either the Transfer Matrix Method (TMM) [21] or the Arbitrary Coefficient Method (ACM) [18] given the complex wavenumber(s) of the porous medium. In Chapter 2, all of these classic acoustical theories are reviewed, and as an extension of the study, these theories were also modified to be capable of predicting acoustical properties for a specific type of porous medium consisting of two components: *i.e.*, fibers and particles. In Chapter 3, the TMM was further modified to be capable of coupling a poro-elastic layer or an elastic solid layer into a layered system, which made it an alternative method of the ACM for multilayered acoustical system modeling, and the prediction accuracy of the modified TMM was validated by the ACM [18]. The modification of the TMM was meant to increase the modeling efficiency when predicting either acoustical properties or damping properties of porous media in a layered system that involves layered acoustical elements having different matrix dimensions. Therefore, as an extension of this coupling methodologies study, different layered acoustical elements, including the micro-perforated panel (MPP) and

transversely isotropic poro-elastic (TIP) materials, were also built into the modified TMM to improve its modeling capability.

The development and evaluation of the acoustical models including the TMM model and the ACM model provide a reliable connection between porous media's bulk properties and acoustical properties, which served as fundamental prerequisites for the near-field damping modeling. Based on the validated acoustical models, the general methodology that incorporates the TMM and the ACM models into the NFD model is shown in Figure 1.4 and is introduced in Chapter 4, which helped to further transfer porous media's acoustical properties to the layered system's damping properties. Based on a certain near-field damping configuration with a vibrating panel treated with a layer of porous medium, first, the bulk properties of the porous medium (*i.e.*, airflow resistivity, σ , porosity, ϕ , bulk density, ρ_b , layer thickness, d , and tortuosity, α_∞ , for the limp porous medium, plus Young's modulus, E_1 , Poisson's ratio, ν , and mechanical loss factor, η_m , for the poro-elastic medium) were given to calculate the layer's acoustical properties by using either the TMM [21] or the ACM [18], which are both based on the JCA model [16], Biot theory [15,17–20] and the implementation of boundary conditions of the layered system [18,21]. Note that when incorporated with the NFD model, the TMM was used to calculate the acoustical properties for limp porous media, and the ACM was used to calculate the acoustical properties for poro-elastic media, since the ACM was proven to perform equivalently as the TMM model for coupling a poro-elastic layer, but it holds an advantage over the modified TMM model on numerical stability, which is especially important for the NFD modeling. At the same time, the governing equation of the panel motion was generated in the time and space domain based on the Euler-Bernoulli beam theory, and it was then Fourier transformed to the frequency and wavenumber domain, so that the wavenumber domain response of the panel was obtained given the previously-specified acoustical properties and the panel structure-related properties. The wavenumber domain response was then inverse discrete Fourier transformed (IDFT) [22] to the spatial domain, from which the power dissipation within the porous layer could be

calculated based on a power analysis, and the system equivalent damping loss factor (also abbreviated as “damping loss factor” or “loss factor” in this thesis), η_e , could be evaluated by using the power injection method (PIM) [23]. Note that η_m mentioned above represents the loss factor that accounts for the mechanical energy dissipation associated with the motion of the solid phase of the poro-elastic medium, and it is distinct from the η_e introduced here. The process connected by the purple arrows in Figure 1.4 describes the NFD analytical model, which is elaborated here in Section 4.2 to describe how it was incorporated with the TMM or ACM models, and in Sections 4.5 and 4.6 to illustrate how to evaluate the panel’s spatial response and the porous layer’s damping performance. Finally in Section 4.7, the spatial responses are compared to results based on finite element models to validate the near-field damping prediction accuracy.

The TMM or the ACM model combined with the NFD model provides an analytical toolbox for connecting a porous medium’s bulk properties with its damping performance: following the black blocks in Figure 1.4 leads to a prediction of the damping properties of the porous medium given its bulk properties (by following the calculation routine of TMM/ACM–NFD). The damping predictions and parametric studies of porous media based on their bulk properties are introduced in Chapter 5. The prediction model developed here was first used to show the damping effectiveness of a limp porous layer based on the observation of the spatial response of a harmonically line-driven, infinitely-extended (unconstrained) panel treated by the layer as shown in Figure 1.5. Parametric studies on a limp porous layer’s bulk properties were also conducted based on this configuration. The same configuration was then used to compare the power dissipated by either a poro-elastic or a limp porous treatment when resting on an unconstrained panel, in which case, the cause of the improved damping performance of the poro-elastic layer compared with the limp layer was established through a power distribution analysis. Also, two types of boundary conditions (*i.e.*, bonded and unbonded) between the poro-elastic layer and the unconstrained panel were compared to highlight the importance of bonding the poro-elastic

layer to the panel to achieve better damping performance. The NFD modeling based on the unconstrained panel structure is introduced in Section 4.2, and the NFD performance predictions on limp and elastic porous damping media are introduced in Sections 5.2 and 5.3.

Though it is convenient to model an unconstrained panel structure to observe general damping characteristics, that type of structure does not closely represent practical industrial applications. Thus, the panel was then given two identical discontinuities (also referred to as constraints in this thesis) with finite translational and rotational inertias to create a partially-constrained panel structure as shown in Figure 1.6. The velocity response spectrum of the partially-constrained panel model was validated by comparison with a closely-related finite element model. The NFD modeling based on the partially-constrained panel structure is introduced in Section 4.3, and the NFD performance predictions based on limp and elastic porous damping media are introduced in Section 5.3.

Furthermore, identical discontinuities with finite translational and rotational inertias and stiffnesses were uniformly distributed along the panel to create a periodically-constrained structure, as shown in Figure 1.7, which was driven by a distributed convective pressure. The intention was to create a fuselage-like structure driven by a boundary layer excitation, and to examine the damping effectiveness of different types of limp porous treatments under this condition. The velocity response spectrum of the periodically-constrained panel model was validated by comparison with a closely-related finite element model. The NFD modeling based on the periodically-constrained panel structure is introduced in Sections 4.4, and the NFD performance predictions on limp porous damping media are introduced in Section 5.4.

On the other hand, there are multiple existing models, such as the airflow resistivity (AFR) model (a specific model introduced in Chapter 6 that was used for fibrous media), that relate a porous medium's microstructure with its bulk properties. Therefore, the micro-bulk relations shown as the red block and arrows in Figure 1.4 can be added into the analytical toolbox, so that the damping properties can be pre-

dicted given either the porous medium's microstructure (by following the calculation routine of AFR–TMM/ACM–NFD). Furthermore, optimizations can be conducted (by following the calculation routine of TMM/ACM–NFD–AFR) to find the optimal bulk properties and corresponding optimal microstructures of the porous layer that would create the largest damping at certain frequencies for certain panel structures. This optimization process was described here in Section 7.2, to specifically design porous damping media that are made of fibers.

Finally, a damping-oriented microstructural design process for fibrous damping media based on this micro-bulk relations model is introduced in Chapter 7, and this process was applied to design the microstructures for fibrous media to achieve the largest η_e 's given different frequencies and panel structures of interest: the NFD performance optimizations on fibrous damping media applied to an unconstrained, a partially-constrained, a periodically-constrained and an arbitrarily-shaped panels are introduced in Sections 7.3, 7.4, 7.5 and 7.7, respectively.

To realize a more practical application of the NFD model, a case study of an arbitrarily-shaped panel driven by a harmonic line force, as shown in Figure 1.8, is introduced in Section 7.6 in order to create a very simple representation of a vehicle floor pan-like structure. The spatial/frequency response of this structure was calculated based on a finite element model, and then was transformed to the wavenumber/frequency domain, based on which a strong vibration region can be identified. At the same time, the damping performance of a limp fibrous layer was evaluated in terms of power dissipation in the wavenumber/frequency domain (shown in Section 7.6.3), and parametric studies were then conducted for the limp layer of fibers to maximize its damping performance based on the identified strong vibration region.

To conclude, fibrous damper design concepts and recommendations for future work are summarized in Chapter 8.

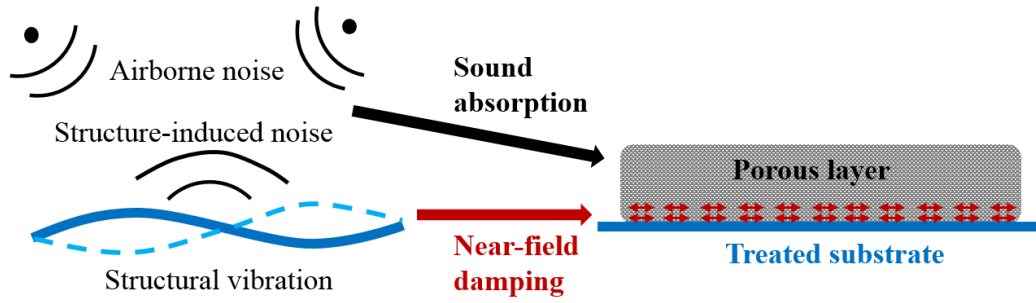


Figure 1.1. The reduction of both airborne noise and structural vibration after the substrate is treated with a multi-functional porous layer.

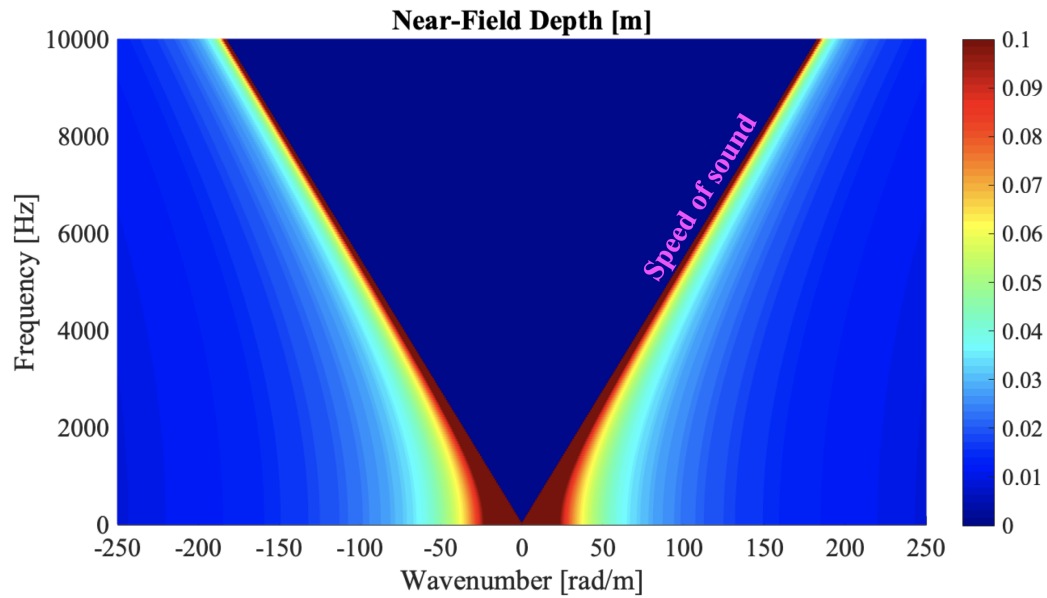


Figure 1.2. The near-field damping depth of a 3 mm thick, harmonic line force-driven, aluminum panel.

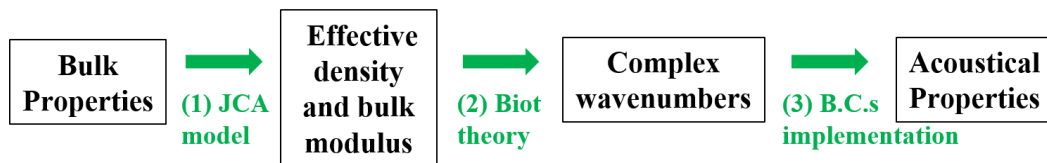


Figure 1.3. A typical acoustical model that connects porous media's bulk properties and their acoustical properties.

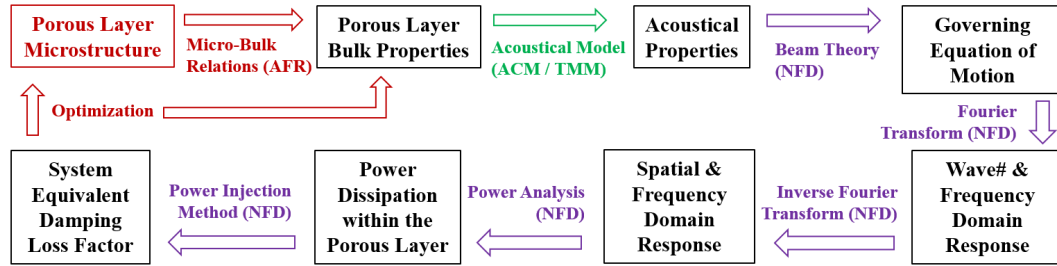


Figure 1.4. General modeling process consisting of the NFD model with the TMM or the ACM acoustical model and the AFR micro-bulk model for either damping prediction or optimization.

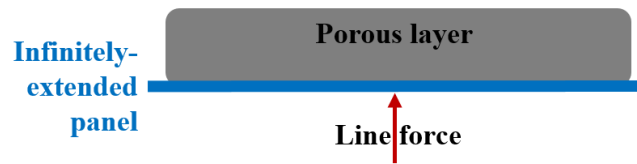


Figure 1.5. A harmonic line force-driven, infinitely-extended panel treated with a porous damping layer.

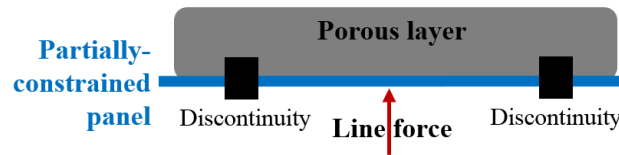


Figure 1.6. A harmonic line force-driven, partially-constrained panel treated with a porous damping layer.

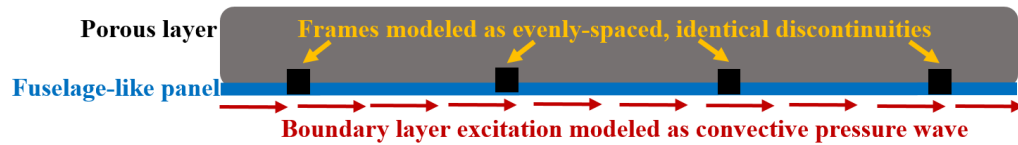


Figure 1.7. A convective pressure-driven, periodically-constrained panel treated with a porous damping layer.

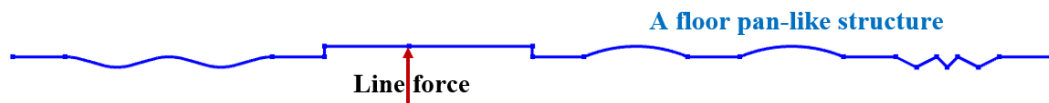


Figure 1.8. A harmonic line force-driven, arbitrarily-shaped panel.

2. ACOUSTICAL PROPERTIES EVALUATION BASED ON BULK PROPERTIES OF POROUS MEDIA

2.1 Introduction

Due to the mechanism of near-field damping mentioned in Chapter 1, the acoustical properties of the porous media need to be accurately captured as a prerequisite for the prediction of their damping performance. In this chapter, classic acoustical theories that include the Johnson-Champoux-Allard (JCA) model [16, 24, 25], the Biot theory [15, 17–20] and boundary condition (B.C.s) implementation methods (the Transfer Matrix Method (TMM) [21] and the Arbitrary Coefficient Method (ACM) [18]) are introduced respectively in Sections 2.2, 2.3 and 2.4. These various parameters help to build the connection between a porous medium’s bulk properties and its acoustical properties. These theories will further be used in the study of layered system coupling methodologies introduced in Chapter 3, and were also applied in combination with the NFD model for simulating near-field damping problems as described in Chapter 4. As an extension of the study, these acoustical theories were also modified and evaluated in Section 2.5 for modeling a double-component porous material that consists of polymeric fibers and activated carbon particles.

2.2 The JCA Model for Evaluating the Effective Density and Bulk Modulus of Porous Media

With characterized bulk properties of a porous medium, the first step of the acoustical property evaluation is usually to calculate the effective density, and bulk modulus of the fluid phase (*i.e.*, air) of the material by quantifying the viscous and thermal effects in the pores, based on the assumption that the bulk frame of the material does not move (*i.e.*, that the material is rigid-framed). The history of how to quan-

tify viscous and thermal effects of porous media was comprehensively summarized in Chapters 4 and 5 of Refs. [16, 17] and in Section 2.2 of Ref. [19]. The theory used in the current study is the Johnson-Champoux-Allard (JCA) model described on pages 92–93 of Ref. [16] plus the content described on page 89 of Ref. [17], in which the viscous characteristic length, Λ , and thermal characteristic length, Λ' , can be evaluated given porous media's airflow resistivity, σ , porosity, ϕ , and tortuosity, α_∞ , as

$$\Lambda = \frac{1}{c} \left(\frac{8\alpha_\infty\eta}{\phi\sigma} \right), \quad (2.1)$$

and

$$\Lambda' = \frac{1}{c'} \left(\frac{8\alpha_\infty\eta}{\phi\sigma} \right), \quad (2.2)$$

respectively, where shape factors, $c = 1$ and $c' = 0.5$, and the dynamic viscosity of air, $\eta = 1.846 \times 10^{-5}$ kg/(s · m), are commonly used for the fibrous type of porous media involved in this study. Then the effective density, ρ_{eff} , and bulk modulus, K_f , of the fluid phase within the pores can be evaluated as

$$\rho_{\text{eff}} = \alpha_\infty \rho_0 \left[1 + \frac{\sigma\phi}{i\omega\rho_0\alpha_\infty} G_J(\omega) \right], \quad (2.3)$$

and

$$K_f = \gamma P_0 \left/ \left[\gamma - (\gamma - 1) \left[1 + \frac{\sigma'\phi}{iB^2\omega\rho_0\alpha_\infty} G'_J(\omega) \right]^{-1} \right] \right., \quad (2.4)$$

respectively, where

$$G_J(\omega) = \left(1 + \frac{4i\alpha_\infty^2\eta\rho_0\omega}{\sigma^2\Lambda^2\phi^2} \right)^{1/2}, \quad (2.5)$$

and

$$G'_J(B^2\omega) = \left(1 + \frac{4i\alpha_\infty^2\eta\rho_0B^2\omega}{\sigma'^2\Lambda'^2\phi^2} \right)^{1/2}, \quad (2.6)$$

and where the Prandtl number, $B^2 = 0.71$, the specific heat ratio, $\gamma = 1.402$, and the ambient pressure, $P_0 = 1.015 \times 10^5$ Pa, are commonly used in this study. Note that $\gamma P_0 = \rho_0 c_0^2$ per the definition of the speed of sound, so the speed of sound in the

air, $c_0 = 343$ m/s, and the density of air, $\rho_0 = 1.21$ kg/m³, are also commonly used in this study. Also note that $\sigma' = c'^2\sigma$, and that $\omega = 2\pi f$ is the angular frequency. Furthermore, the effective density, ρ'_{eff} , and bulk modulus, K'_f , of the porous medium can be calculated, per Ref. [17], as

$$\rho'_{\text{eff}} = \rho_{\text{eff}}/\phi, \quad (2.7)$$

and

$$K'_f = K_f/\phi, \quad (2.8)$$

respectively. Note that there were many follow-up parametric studies such as the one in Ref. [26] that have tested the fundamental acoustical properties' sensitivities due to the change of each JCA input parameter (Λ , Λ' , σ , ϕ and α_∞), which will not be discussed here, but can be a potential future study.

2.3 The Biot Theory for Rigid, Limp, Elastic Porous Media

The JCA model helped to calculate the fundamental acoustical properties related to the fluid phase of the porous medium assuming that the solid phase does not move, and the Biot theory originally developed by Maurice Anthony Biot [15] extended the fluid-solid interaction in porous media to a more general situation, where motions are allowed for the solid phase (frame) of the material, and where the elasticity of the frame is non-negligible. Therefore, for acoustical purpose, all porous media can be divided into three general types: *i.e.*, rigid-framed, limp-framed and elastic-framed [14], or referred to as a rigid porous, limp porous or elastic porous (poro-elastic) medium, where rigid or limp should be understood as extreme cases of an elastic porous medium when the bulk elasticity of the frame is extremely large or small, respectively. As was mentioned in Chapter 1, to model a porous layer, the general type of the porous medium should first be chosen according to the nature of the target material's solid phase. Based on that choice, the wavenumber of the

propagating wave within the porous medium should then be solved for given the fundamental acoustical properties described in the last section.

If the solid phase of the target material is very hard and heavy, such as a layer of hard plastic foam, metal foam, or packed granules, it can be modeled as rigid-framed, and there will be one longitudinal wave propagating within the rigid porous medium with a complex wavenumber calculated as

$$k_c = \omega (\rho_{\text{eff}}/K_f)^{1/2} = \omega (\rho'_{\text{eff}}/K'_f)^{1/2}, \quad (2.9)$$

and the complex density of the rigid porous medium can be expressed as

$$\rho_c = \rho'_{\text{eff}} = \rho_{\text{eff}}/\phi. \quad (2.10)$$

If the solid phase of the target material is soft and light such as a lightweight polymeric fibrous layer, it can be modeled as limp-framed, and there will also just be one longitudinal wave propagating within the limp porous medium with complex wavenumber calculated as

$$k_c = \left[\frac{\omega^2 (\rho_{11}^* \rho_{22}^* - \rho_{12}^{*2})}{\rho_{11}^* R - 2\rho_{12}^* Q + \rho_{22}^* P} \right]^{1/2}, \quad (2.11)$$

and the complex density of the limp porous medium can be expressed in terms of the limp porous medium complex wavenumber as

$$\rho_c = \frac{k_c^2 (P + Qa + Q + Ra)}{\omega^2 (1 - \phi + \phi a)}, \quad (2.12)$$

with

$$a = \frac{\rho_{12}^* Q - \rho_{11}^* R}{\rho_{12}^* R - \rho_{22}^* Q}, \quad (2.13)$$

where the elasticity coefficients P , Q and R of the limp porous medium can be expressed as

$$P = \frac{K_f(1 - \phi)^2}{\phi} = K'_f(1 - \phi)^2, \quad (2.14a)$$

$$Q = K_f(1 - \phi) = K'_f\phi(1 - \phi), \quad (2.14b)$$

$$R = K_f \phi = K'_f \phi^2, \quad (2.14c)$$

and Biot's modified mass densities coefficients, ρ_{11}^* , ρ_{12}^* and ρ_{22}^* , can be expressed, per Refs. [17, 27], as

$$\rho_{22}^* = \phi \rho_0 \alpha_\infty - i \sigma \phi^2 \frac{G_J(\omega)}{\omega} = \phi \rho_{\text{eff}} = \phi^2 \rho'_{\text{eff}}, \quad (2.15a)$$

$$\rho_{12}^* = -\phi \rho_0 (\alpha_\infty - 1) + -i \sigma \phi^2 \frac{G_J(\omega)}{\omega} = \rho_0 \phi - \rho_{22}^*, \quad (2.15b)$$

$$\rho_{11}^* = \rho_b + \phi \rho_0 (\alpha_\infty - 1) - i \sigma \phi^2 \frac{G_J(\omega)}{\omega} = \rho_b - \rho_{12}^*, \quad (2.15c)$$

where ρ_b is the bulk density of the porous medium, which can be calculated given the density of the solid material used for making the porous medium, ρ_s , and porosity, ϕ , by $\rho_b = \rho_s(1 - \phi)$. Note that the detailed derivation of the Biot limp porous theory can be found in Refs. [19, 20].

If the solid phase of the target material has a finite elasticity like a layer of polyurethane foam, it can be modeled as elastic-framed, and there will be three types of waves (two longitudinal and one transverse) that can propagate through a poro-elastic medium. The complex wavenumbers of the two longitudinal (compressional) waves, k_1 and k_2 , and of the transverse (shear) wave, k_3 , can be calculated as

$$k_1 = \left[\frac{\omega^2 \left(P \rho_{22}^* + R \rho_{11}^* - 2Q \rho_{12}^* - \sqrt{\Delta} \right)}{2(PR - Q^2)} \right]^{1/2}, \quad (2.16a)$$

$$k_2 = \left[\frac{\omega^2 \left(P \rho_{22}^* + R \rho_{11}^* - 2Q \rho_{12}^* + \sqrt{\Delta} \right)}{2(PR - Q^2)} \right]^{1/2}, \quad (2.16b)$$

$$k_3 = \left[\frac{\omega^2 (\rho_{11}^* \rho_{22}^* - \rho_{12}^{*2})}{N \rho_{22}^*} \right]^{1/2}, \quad (2.16c)$$

where Δ is given by

$$\Delta = (P \rho_{22}^* + R \rho_{11}^* - 2Q \rho_{12}^*)^2 - 4(PR - Q^2)(\rho_{11}^* \rho_{22}^* - \rho_{12}^{*2}), \quad (2.17)$$

and the shear modulus of the poro-elastic medium, N , can be expressed in terms of the Young's modulus, E_1 , Poisson's ratio, ν , and mechanical loss factor, η_m , for an isotropic poro-elastic medium, as

$$N = \frac{E_1(1 + i\eta_m)}{2(1 + \nu)}. \quad (2.18)$$

At the same time, the elasticity coefficient, P , of the poro-elastic medium can be expressed as

$$P = \frac{4}{3}N + K_b + \frac{K_f(1 - \phi)^2}{\phi} = \frac{4}{3}N + K_b + K'_f(1 - \phi)^2, \quad (2.19)$$

where K_b is the bulk modulus of the poro-elastic medium given by

$$K_b = \frac{2N(1 + \nu)}{3(1 - 2\nu)}. \quad (2.20)$$

Note that the expressions of Q , R , ρ_{11}^* , ρ_{12}^* and ρ_{22}^* for poro-elastic medium are the same as those for limp porous medium, and that the complete derivation of Biot poro-elastic medium theory can be found in Refs. [15, 17, 18].

2.4 The TMM and the ACM for Multilayered Acoustical System Boundary Condition Implementation

2.4.1 The TMM Model Used for Rigid and Limp Porous Medium

When modeling a rigid or limp porous medium, as shown in Figure 2.1, if the layer is open to the fluid (air) medium on both sides: *i.e.*, the B.C.s comprise motion continuity and stress-pressure continuity, then the acoustical properties: *i.e.*, acoustic pressures, p , and particle velocities, v_z , on both sides of the layer can be connected by the two-by-two transfer matrix of the porous layer: *i.e.*,

$$\begin{bmatrix} p \\ v_z \end{bmatrix}_{z=0} = [\mathbf{T}]_{2 \times 2} \begin{bmatrix} p \\ v_z \end{bmatrix}_{z=d}, \quad (2.21)$$

where

$$[\mathbf{T}] = \begin{bmatrix} T_{11} & T_{12} \\ T_{21} & T_{22} \end{bmatrix} = \begin{bmatrix} \cos \sqrt{k_c^2 - k_x^2} d & i \frac{\rho_c \omega}{\sqrt{k_c^2 - k_x^2}} \sin \sqrt{k_c^2 - k_x^2} d \\ i \frac{\sqrt{k_c^2 - k_x^2}}{\rho_c \omega} \sin \sqrt{k_c^2 - k_x^2} d & \cos \sqrt{k_c^2 - k_x^2} d \end{bmatrix}. \quad (2.22)$$

Here, k_c and ρ_c are the complex wavenumber and complex density of the rigid or limp layer with the expressions shown in the last section, $k_x = k \sin \theta$ is the in-plane (x) direction wavenumber component of $k = \omega/c_0$, which is the wavenumber of the wave propagating within the fluid (air), θ is the incident angle shown in Figure 2.1, and d is the thickness (depth) of the layer. Note that k_x is also referred to as the trace wavenumber.

On the other hand, if there is a thin surface treatment (*e.g.*, resistive screens, limp impermeable membranes, stiff panels, micro-perforated panels, *etc.*) applied to either side of the rigid or limp porous layer, the B.C.s comprise motion continuity and the equation of motion of the treatment. In that case, the treatment is conventionally modeled as a separate two-by-two matrix, $[\mathbf{S}]$: *i.e.*,

$$[\mathbf{S}] = \begin{bmatrix} 1 & z_m \\ 0 & 1 \end{bmatrix}, \quad (2.23)$$

where z_m is the transfer impedance of the treatment, and in this case, $[\mathbf{S}]$ can be multiplied by the porous layer transfer matrix depending on which side the treatment is applied to. For example, if the surface treatment is applied to the incident side (*i.e.*, a front treatment applied at $z = 0$), then the transfer matrix of the layered system combining the porous layer and the surface treatment can be expressed, in this case, as

$$[\mathbf{T}] = \begin{bmatrix} 1 & z_m \\ 0 & 1 \end{bmatrix} \begin{bmatrix} \cos \sqrt{k_c^2 - k_x^2} d & i \frac{\rho_c \omega}{\sqrt{k_c^2 - k_x^2}} \sin \sqrt{k_c^2 - k_x^2} d \\ i \frac{\sqrt{k_c^2 - k_x^2}}{\rho_c \omega} \sin \sqrt{k_c^2 - k_x^2} d & \cos \sqrt{k_c^2 - k_x^2} d \end{bmatrix}. \quad (2.24)$$

For a rigid resistive screen that allows no motion of the treatment, but having flow resistance, R_f ,

$$z_m = R_f. \quad (2.25)$$

For a limp impermeable membrane that has negligible flow resistance, but allows motion and having mass per unit area (surface density), m_s ,

$$z_m = i\omega m_s. \quad (2.26)$$

And a flexible resistive screen with flow resistance, R_f , and mass per unit area (surface density), m_s , is a parallel combination of the two treatments mentioned above, where

$$z_m = 1 / \left(\frac{1}{i\omega m_s} + \frac{1}{R_f} \right) = \frac{i\omega m_s R_f}{i\omega m_s + R_f}. \quad (2.27)$$

For a stiff panel that allows for the motion of the panel, and has non-negligible flexural stiffness,

$$z_m = i \left(\omega m_s - D k_x^4 / \omega \right), \quad (2.28)$$

where $m_s = \rho_p h_p$ is the mass per unit area of the panel based on its density, ρ_p , and thickness, h_p , and $D = [h_p^3 E_0 (1 + i\eta_p)] / [12(1 - \nu_p^2)]$ is the flexural stiffness of the panel per unit width in the y -direction, respectively, based on h_p , the Young's modulus, E_0 , the loss factor, η_p , and the Poisson's ratio, ν_p . For a rigid micro-perforated panel (MPP) per Ref. [28],

$$z_m = z_{mr} = \rho_0 c_0 (r_{mpp} + i\omega m_{mpp}), \quad (2.29)$$

where r_{mpp} is the relative resistance of the MPP expressed in terms of the perforate constant, k_{mpp} , perforation ratio (porosity of the MPP), ϕ_{mpp} , the diameter of the perforation (hole) of the MPP, d_{mpp} , and the thickness of the hole of the MPP (here equal to the thickness of the MPP), t_{mpp} , as

$$r_{mpp} = \left[\frac{32\eta t_{mpp}}{\phi_{mpp} \rho_0 c_0 d_{mpp}^2} \right] \left[\left(1 + \frac{k_{mpp}^2}{32} \right)^{1/2} + \frac{\sqrt{2} k_{mpp} d_{mpp}}{32 t_{mpp}} \right], \quad (2.30)$$

where

$$k_{mpp} = d_{mpp} \sqrt{\omega \rho_0 / 4\eta}, \quad (2.31)$$

and m_{mpp} is the normalized mass per unit area of the MPP expressed as

$$m_{mpp} = \left[\frac{t_{mpp}}{\phi_{mpp} c_0} \right] \left[1 + \left(9 + \frac{k_{mpp}^2}{2} \right)^{-1/2} + \frac{0.85 d_{mpp}}{t_{mpp}} \right]. \quad (2.32)$$

For a flexible (limp) MPP that allows for the motion of the panel,

$$z_m = 1 / \left(\frac{1}{i\omega m_s} + \frac{1}{z_{mr}} \right) = \frac{i\omega m_s z_{mr}}{i\omega m_s + z_{mr}}. \quad (2.33)$$

And for a stiff MPP that allows for the motion of the panel, and has non-negligible flexural stiffness,

$$z_m = 1 / \left(\frac{1}{i(\omega m_{\text{mpp}} - D_{\text{mpp}} k_x^4 / \omega)} + \frac{1}{z_{\text{mr}}} \right) = \frac{i(\omega m_{\text{mpp}} - D_{\text{mpp}} k_x^4 / \omega) z_{\text{mr}}}{i(\omega m_{\text{mpp}} - D_{\text{mpp}} k_x^4 / \omega) + z_{\text{mr}}}, \quad (2.34)$$

where $m_{\text{mpp}} = \rho_{\text{mpp}} t_{\text{mpp}}$ is the mass per unit area of the panel based on its density, ρ_{mpp} , and thickness, t_{mpp} , and $D_{\text{mpp}} = [t_{\text{mpp}}^3 E_{0\text{mpp}}(1 + i\eta_{\text{mpp}})] / [12(1 - \nu_{\text{mpp}}^2)]$ is the flexural stiffness of the panel per unit width in the y -direction, based on t_{mpp} , the Young's modulus, $E_{0\text{mpp}}$, the loss factor, η_{mpp} , and the Poisson's ratio, ν_{mpp} , of the MPP. Note that the flexible and stiff MPPs' transfer impedance expressions were inspired by the development presented in Ref. [29], and that more detailed theories and coupling methodologies related to the MPP are introduced in Section 3.6.2 of this thesis.

Further, if there is a fluid (air) gap with depth, d_a , between a thin surface treatment and a rigid or limp porous layer, another two-by-two transfer matrix, $[\mathbf{A}]$, that represents the fluid (air) layer can be expressed as

$$[\mathbf{A}] = \begin{bmatrix} \cos k_z d_a & i \frac{\rho_0 c_0}{\cos \theta} \sin k_z d_a \\ i \frac{\cos \theta}{\rho_0 c_0} \sin k_z d_a & \cos k_z d_a \end{bmatrix}, \quad (2.35)$$

where $k_z = k \cos \theta = \sqrt{k^2 - k_x^2}$ is the normal (z) direction wavenumber component of k , and θ is the angle between the propagating directions of k and k_z . Note that θ is also used in Figure 2.1 to represent the incident angle. In this case, $[\mathbf{A}]$ can be placed in between $[\mathbf{S}]$ and the transfer matrix of the porous layer. For example, if the air gap is between the front surface treatment and the porous layer, then the transfer matrix of the layered system combining the porous layer, the air gap and the surface treatment can be expressed, in this case, as

$$[\mathbf{T}] = \begin{bmatrix} 1 & z_m \\ 0 & 1 \end{bmatrix} [\mathbf{A}] \begin{bmatrix} \cos \sqrt{k_c^2 - k_x^2} d & i \frac{\rho_c \omega}{\sqrt{k_c^2 - k_x^2}} \sin \sqrt{k_c^2 - k_x^2} d \\ i \frac{\sqrt{k_c^2 - k_x^2}}{\rho_c \omega} \sin \sqrt{k_c^2 - k_x^2} d & \cos \sqrt{k_c^2 - k_x^2} d \end{bmatrix}. \quad (2.36)$$

Finally, Eq. (2.21) can be rewritten in terms of the transmission coefficient, TC, and reflection coefficient, RC, as

$$\begin{bmatrix} 1 + \text{RC} \\ (1 - \text{RC}) \cos \theta / (\rho_0 c_0) \end{bmatrix}_{z=0} = [\mathbf{T}]_{2 \times 2} \begin{bmatrix} \text{TC} e^{-ik_z d_s} \\ \text{TC} e^{-ik_z d_s} \cos \theta / (\rho_0 c_0) \end{bmatrix}_{z=d}, \quad (2.37)$$

where d_s is the depth of the whole layered system. For example, $d_s = d$ for the bare porous layer, or for a front and/or back surface(s)-treated porous layer, and $d_s = d_a + d$ for a layered system where there is an air gap having depth d_a between the front or back surface treatment and the porous layer. Based on the elements in the layered system transfer matrix, $\mathbf{T} = [T_{11}, T_{12}; T_{21}, T_{22}]$, TC and RC of an anechoically-backed layered system can be calculated, based on Ref. [30], as

$$\text{TC} = \frac{2e^{ik_z d_s}}{T_{11} + T_{12} \cos \theta / (\rho_0 c_0) + T_{21} \rho_0 c_0 / \cos \theta + T_{22}}, \quad (2.38)$$

and

$$\text{RC} = \frac{T_{11} + T_{12} \cos \theta / (\rho_0 c_0) - T_{21} \rho_0 c_0 / \cos \theta - T_{22}}{T_{11} + T_{12} \cos \theta / (\rho_0 c_0) + T_{21} \rho_0 c_0 / \cos \theta + T_{22}}. \quad (2.39)$$

Also, the reflection coefficient of a rigid-backed layered system can be calculated as

$$\text{RC} = \frac{T_{11} \cos \theta / (T_{21} \rho_0 c_0) - 1}{T_{11} \cos \theta / (T_{21} \rho_0 c_0) + 1}. \quad (2.40)$$

Further, the absorption coefficient, AC, and transmission loss, TL, can be calculated as

$$\text{AC} = 1 - |\text{RC}|^2, \quad (2.41)$$

and

$$\text{TL} = 10 \log_{10} (1/|\text{TC}|^2). \quad (2.42)$$

The TMM of a limp porous layer is further used in Section 2.5 to model a double-component porous medium, and the incorporation of the TMM with the NFD for limp porous layer near-field damping modeling is introduced in Chapter 4 (with details of the incorporated TMM given in Appendix B).

2.4.2 The ACM Model Used for Poro-Elastic Medium

As shown above, the TMM model is convenient when modeling multilayered acoustical systems including elements that can all be modeled as two-by-two transfer matrices. However, when a layered system involves higher-order elements such as poro-elastic or elastic solid layers, the B.C.s need to be implemented differently to realize the coupling. The ACM developed by Bolton *et al.* in Ref. [18] is a classical method that can be used to couple poro-elastic layers, and it is further used in Chapter 3 as a comparison to validate the modified TMM model for coupling higher-order elements. The incorporation of the ACM with the NFD model for poro-elastic layer near-field damping modeling is introduced in Chapter 4 (with details of the incorporated ACM in Appendix C).

2.5 A Case Study of the JCA-Biot-TMM Model for Modeling a Limp-Framed Double-Component Fiber-Particle Porous Medium

To evaluate the models mentioned above, and as an extended case study, the JCA model combined with the Biot limp porous theory and the TMM model are used to predict the acoustical performance of a double-component limp porous medium that consists of polymeric fibers and activated carbon particles. A sample layer of this material is shown in Figure 2.2, and fibers can be seen embedded between the carbon particles, and the pore structures of the particle can be divided into three scales: intergranular-scale, micro-scale and nano-scale. An intergranular-scale SEM of a single particle and its pore structures can be seen in Figure 2.3

First, the viscous and thermal effects due to the intergranular-scale pores of the particles were accounted for in combination with the polymeric fibers by using the JCA model. To be more specific, given the material's characterized airflow resistivity, $\sigma = 1.44 \times 10^5$ Rayls/m, porosity, $\phi = 0.48$, and $\alpha_\infty = 1.55$, together with shape factors $c = 1$ and $c' = 0.5$, and the ambient parameters, $\rho_0 = 1.21$ kg/m³, $c_0 = 343$ m/s, $B^2 = 0.71$, $\gamma = 1.402$, $P_0 = 1.015 \times 10^5$ Pa and $\eta = 1.846 \times 10^{-5}$ kg/(s ·

m), the viscous and thermal characteristic lengths, $\Lambda = 57 \text{ } \mu\text{m}$ and $\Lambda' = 114 \text{ } \mu\text{m}$ were calculated by using Eqs. (2.1) and (2.2), and the effective density, ρ'_{eff} , and intergranular bulk modulus, E_p , were predicted by using Eqs. (2.7) and (2.8). Then E_p was coupled with the micro-scale and nano-scale bulk moduli, E_m and E_n , by using the Granular Activated Carbon (GAC) bulk modulus model described in Eq. (42) of Ref. [31] (also introduced here in Appendix A) to return the overall bulk modulus, K'_f , of the material. Further, the complex wavenumber, k_c , and complex density, ρ_c , were predicted by using Eqs. (2.11) and (2.12) given ρ'_{eff} , K'_f and the characterized bulk density, $\rho_b = 275 \text{ kg/m}^3$, of the material. Finally, k_c and ρ_c together with the depth of the material, $d = d_s = 1.2 \text{ cm}$, and the incident angle, $\theta = 0^\circ$ (normal incidence), were input into Eqs. (2.22), (2.40) and (2.41) for the prediction of the absorption coefficient of the double-component material when applied to a rigid backing, and the predicted results are shown as the blue line in Figure 2.4. Further, if the micro-scale and nano-scale pores are closed by making $E_m = E_n = 0$ (*i.e.*, $K'_f = E_p$) from the GAC model, then an obvious drop of the absorption coefficient can be observed by comparing the green to the blue dashed lines. Also, the drop occurred mainly in the low frequency region. This result was as expected, since the high frequency region acoustical performance results mainly from the intergranular-scale viscous and thermal effects resulting from E_p and ρ'_{eff} , which were both modeled by the JCA model. In contrast, the low frequency region acoustical performance of this material results from the absorptive effect due to both the micro- and nano-scales pores modeled in the GAC model. Therefore, a larger absorption reduction will occur in lower frequency regions when closing smaller-scales pores from the GAC model, while maintaining the intergranular-scale viscous and thermal effects from the JCA model: see the green line in Figure 2.4.

On the other hand, a 10-layer stack of this material with total a thickness of 1.2 cm was tested by using the two-microphone impedance tube method based on standard E1050-12 [32]. The comparison of the prediction and the measurement is shown in Figure 2.4. A good agreement can be observed between the prediction (blue dashed

lines) and the repeated measurements (red line and error bounds) especially in the high frequency region, which validated the prediction accuracy of the JCA model, the Biot limp porous theory and the TMM model used for limp porous layers. Note that the difference between the prediction and measured results in the low frequency region was mainly due to the fact that the particle parameter inputs used in the GAC model were only based on empirical approximations (*i.e.*, input the micro- and nano-geometries by using the data characterized in Ref. [31] rather than an accurate characterization of the target material shown here). A more accurate characterization of the micro- and nano-geometries will result in a better low frequency fit between the predictions and measurements. The main point here is that the small-scale geometries and porosities of the particles have a significant impact on low frequency absorption. In contrast, the material's high frequency absorption performance is mainly controlled by the inter-granular scale porosity and geometries of the particles and fibers, which were already accurately-captured by using experimental and analytical methods during and after the material manufacturing process. As potential studies in the future, the GAC model can be modified as to the characterization of the boundary layer depth and radius of the particles' micro- and nano-pores, and the inter-granular JCA parameters can be further optimized to enhance the high frequency performance.

2.6 Conclusions

Classic acoustical theories were introduced in this chapter; the theories include the JCA model to predict a porous medium's effective density and bulk modulus based on their bulk properties, the Biot theory to solve for the wavenumber(s) of the wave(s) propagating within the porous medium based on the assumption of the nature of the solid phase of the material (rigid, limp or elastic), and the B.C.s implementation methods including the TMM and the ACM.

The JCA-Biot-TMM model was then used to predict the absorption coefficient of a limp-framed double-component porous medium that consists of polymeric fibers

and activated carbon particles. The JCA model was first used to predict the effective density, ρ'_{eff} , and bulk modulus, E_p , of the material based on the characterized intergranular-scale bulk properties of the material that include $\sigma = 1.44 \times 10^5$ Rayls/m, $\phi = 0.48$, $\alpha_\infty = 1.55$, $\Lambda = 57 \mu\text{m}$ and $\Lambda' = 114 \mu\text{m}$, plus shape factors $c = 1$ and $c' = 0.5$, and ambient parameters $\rho_0 = 1.21 \text{ kg/m}^3$, $c_0 = 343 \text{ m/s}$, $B^2 = 0.71$, $\gamma = 1.402$, $P_0 = 1.015 \times 10^5 \text{ Pa}$ and $\eta = 1.846 \times 10^{-5} \text{ kg/(s} \cdot \text{m)}$. Given additional particle structural-related parameters that include $\phi_p = 0.55$, $\phi_m = 0.71$, $\phi_n = 0.26$, $r_p = 0.74 \text{ mm}$, $r_m = 0.41 \mu\text{m}$, $r_n = 0.33 \text{ nm}$, and $L_b = 3.47 \times 10^{-6} \text{ Pa}^{-1}$, and ambient parameters that include $R_g = 287.05 \text{ J/(kg} \cdot \text{K)}$, $T_g = 293.15 \text{ K}$ (20°C), $D_c = 1.35 \times 10^{-10} \text{ m}^2/\text{s}$, $C_p = 1006.1 \text{ J/K}$, $\kappa = 0.02587 \text{ W/(m} \cdot \text{K)}$, $m_m = 4.8 \times 10^{-26} \text{ kg}$ and $S_m = 4.3 \times 10^{-19} \text{ m}^2$, the intergranular bulk modulus, E_p , was then coupled with the micro-scale bulk modulus, E_m , and nano-scale bulk modulus, E_n , by using the GAC model described in Ref. [31] and summarized in Appendix A, which returned the overall bulk modulus, K'_f , of the material. Then, based on the Biot limp porous theory, the complex wavenumber, k_c , and complex density, ρ_c , of the material were solved given ρ'_{eff} , K'_f , and $\rho_b = 275 \text{ kg/m}^3$. Finally, given d_s and θ , the TMM model helped to predict the absorption coefficient of the target material in a wide frequency range, based on which, the low frequency sound absorption mainly due to the absorptive effects resulting from micro-scale and nano-scale pores was successfully captured by the GAC model, and the high frequency sound absorption mainly due to the intergranular viscous and thermal effects was successfully modeled by the JCA model. A good agreement between the repeated E-1050-12 normal incidence sound absorption test and the predicted absorption coefficient helped to verify the model prediction accuracy, which also proves that these acoustical models are reliable enough to be used in the following multilayered acoustical system model to be described in Chapter 3 and the near-field damping model to be described in Chapter 4.

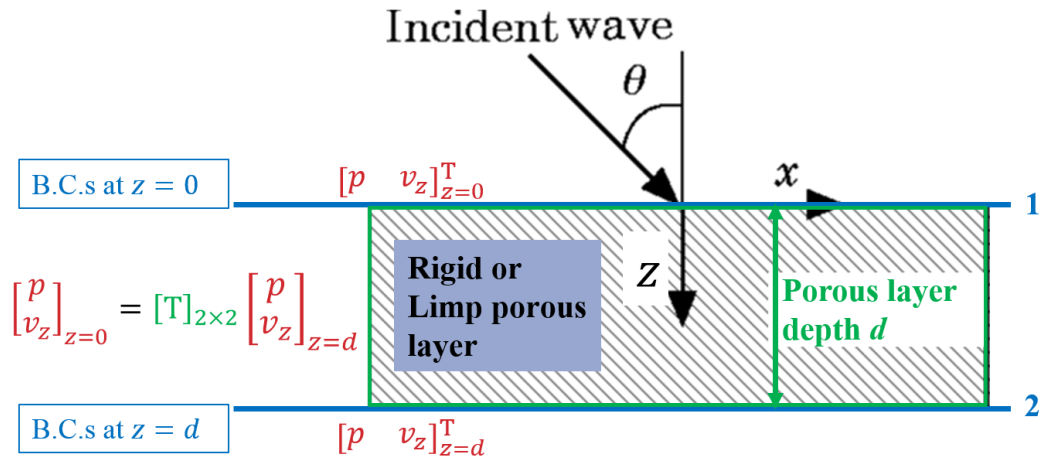


Figure 2.1. The Transfer Matrix Method (TMM) for a rigid or limp porous layer.

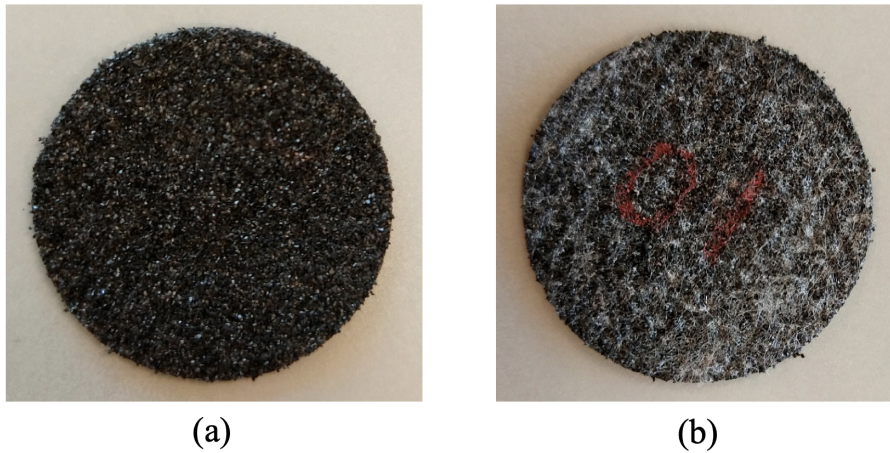


Figure 2.2. (a) Front and (b) back views of a double-component limp porous layer.

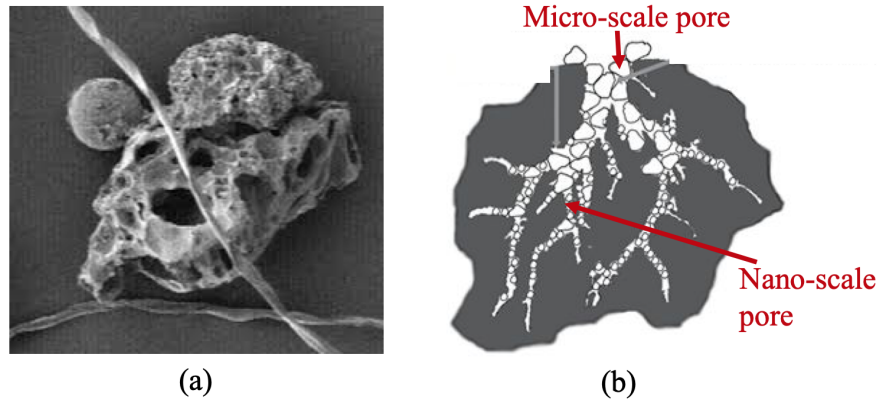


Figure 2.3. (a) An intergranular-scale SEM of a single particle of the double-component limp porous medium, (b) pore structures of the particle to show micro-scale and nano-scale pores.

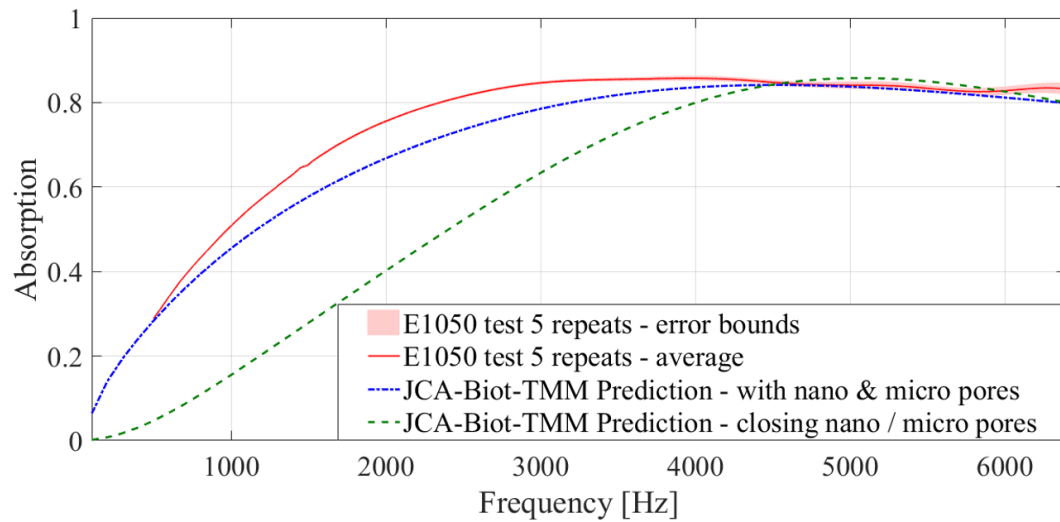


Figure 2.4. Absorption coefficient prediction for a 1.2 cm thick double-component limp porous medium that consists of fibers and activated carbon particles.

3. ACOUSTICAL MODELING OF A MULTILAYERED SYSTEM

3.1 Introduction

Based on the Introduction, there are two prerequisites for modeling a near-field damping problem: (1) acoustical modeling of the damping treatment (porous layer), and (2) a modeling methodology to couple the porous layer and the substrate (vibrating panel structure) so that the damping performance due to the interaction at the acoustical near-field of the panel can be accurately predicted. The acoustical theories that were reviewed and evaluated in Chapter 2 provide reliable tools for the acoustical modeling of a porous layer. The necessary coupling methodologies were studied and are introduced in this chapter to allow convenient modeling of multilayered acoustical structures, and to ensure a proper coupling between the porous treatment and the vibrating panel.

When a limp or rigid porous damping treatment is placed adjacent to a vibrating panel, both limp and rigid layers can be modeled as two-by-two transfer matrices, which share the same dimension as the transfer matrix of the panel. This is due to the fact that both limp and rigid porous layers are “fluid-equivalent”, which behave as an acoustically-effective fluid that contains one longitudinal wave propagating through the medium. Therefore, the TMM model introduced in Section 2.4.1 is efficient to couple any “effective fluid” treatments with the panel, and the coupling is straightforward through motion and stress-pressure continuities.

On the contrary, the ACM model is normally preferred when a poro-elastic layer or any damping treatment that has more than one wave (*e.g.*, an elastic solid layer) is applied to a vibrating structure, or when the whole multilayered system is complex. Although the ACM approach has many advantages, such as being numerically stable when modeling most layered structures, one disadvantage of the ACM model is lower

modeling efficiency, because the equation sets that implement the B.C.s need to be reconstructed every time when there is a change made to the system, such as swapping one layered element in the system to another type, or adding a layer to or eliminating a layer from the system. Therefore, to take advantage of the modeling efficiency of the TMM, the focus of this chapter is to modify the TMM model by using matrix dimension reduction procedures for it to be capable of coupling higher-order layered element such as the poro-elastic layer (introduced in Section 3.4) or an elastic solid layer (introduced in Section 3.5) into multilayered acoustical systems. In that case, the TMM can serve as an alternative method to the ACM when a complex multilayered acoustical or damping system needs to be modeled. Further, to make the TMM model even more comprehensive, methodologies are also introduced in Sections 3.6.1, 3.6.2 and 3.7 to couple a poro-elastic layer with impermeable surface treatments, with rigid/flexible/stiff micro-perforated panels (MPP), and to couple transversely isotropic poro-elastic layers (*e.g.*, a layer of honeycomb structure) with stiff panels, respectively.

3.2 A Review of Multilayered Acoustical System Modeling Methodologies

The modeling of multilayered acoustical systems is a classical topic in noise and vibration control engineering. Despite the fact that numerical analyses based on the finite element or boundary element methods are becoming more and more popular, especially for modeling artificial, complex structures such as acoustic metamaterials and/or metasurfaces, analytical methods remain popular for modeling systems that consist of sequential layers of conventional acoustical treatments (*e.g.*, fibers, foams, scrims, panels, *etc.*) since the analytical models are based on well-developed and reliable theories, and allow a straightforward modeling process and relatively high calculation efficiency. When modeling different layered acoustical treatments, a layer of limp or rigid porous media (*e.g.*, fibers with either negligible or extremely high bulk

frame elasticity) [14] can usually be treated as an equivalent fluid medium like air, in which only one longitudinal wave propagates [33]. In contrast, two types of waves (one longitudinal and one transverse) propagate through an elastic solid layer, while three types of waves (two longitudinal and one transverse) can propagate through a poro-elastic layer (*e.g.*, foams with non-negligible bulk frame elasticity) [15]. As a result, one of the challenges during the modeling process is to couple two contacting layers that possess an inconsistent number of propagating waves.

Previously, two major coupling solutions have been used. One solution that was proposed by Bolton *et al.* [18,34], for example, consists of representing the multilayered system by field variables expressed in terms of the propagating waves' amplitude coefficients, and then constructing the equation system that results from the application of the boundary conditions (B.C.s) at the interfaces of the layered structure. This method has been referred to as the "Arbitrary Coefficient Method" (ACM) in recent publications [35–38]. The alternative solution proposed by Brouard *et al.* [39] was based on modeling each layer by using a transfer matrix. The matrix representation methodology was first described in the 1920's by Mason [40] in the form of an acoustical-electrical analogy that allows two-by-two transfer matrices to be used to model acoustical lumped elements that are combined in series to form acoustic filters or horns, for example. This procedure was later described in Pierce's book [41] as the concept of "Acoustical Two-Ports", and it has been used by various researchers for modeling layered acoustical elements. For example, Lai *et al.* [21] modeled resistive scrims, limp impermeable membranes, flexurally-stiff panels, air spaces and limp fibrous layers as two-by-two transfer matrices; Thompson [33], Brekhovskikh [42], Folds and Loggins [43] and Scharnhorst [44] modeled elastic solid layers by using four-by-four transfer matrices; and Allard *et al.* [45] modeled poro-elastic layers as six-by-six transfer matrices owing to the three types of Biot waves [15] that propagate within such a layer.

Thus, from a mathematical point-of-view, the challenge then becomes coupling multilayered acoustical elements that are described by transfer matrices having dif-

ferent dimensions. Brouard *et al.* [39] solved this problem by assembling the inter-layer B.C.s into a “global transfer matrix” (GTM). The GTM approach was later summarized in Allard and Atalla’s book. [17] The ACM and GTM differ from each other only in the form of their expressions, since the principles behind the calculation routines are the same, which is to connect the propagating waves in different layers by assembling the B.C.s into a global system.

Recall that, in contrast, when several two-port acoustical lumped elements are combined in series, they are coupled simply by multiplying all the transfer matrices together, which is possible since they share the same two-by-two dimension. Inspired by this idea, presented in this chapter is a modified transfer matrix method (TMM) based on the use of matrix operations, including singular value decomposition (SVD) and QR decomposition (QRD) that make it possible to reduce the higher-dimension transfer matrices of an elastic solid or poro-elastic layer (*i.e.*, higher-order elements) to two-by-two, so that they can then be easily coupled with other two-by-two elements in series simply by multiplication. Note that other multilayer modeling methods that involve transfer matrix representations are also introduced below, for the purpose of comparing different methodologies, but in this thesis, the abbreviation “TMM” refers *only* to the coupling approach proposed here.

Both similarities and differences can be recognized when comparing the TMM proposed here with previous multilayer models. For example, a similar method of matrix dimension reduction was introduced by Lauriks *et al.* [46] to explicitly derive a two-by-two matrix from a six-by-six matrix of a double-panel plus poro-elastic layer sandwich structure, but the TMM proposed here is different in that the dimension reduction is achieved through implicit matrix operations (SVD and QRD), so that the process used to derive the two-by-two matrix can be simplified. Also, the TMM is similar to the GTM since they are both based on a matrix representation of each layered element, but compared to either the ACM or the GTM, the TMM handles the B.C.s in a different way: *i.e.*, it represents the B.C.s in the form of matrices (so called boundary condition matrices), and the boundary condition matrices are manipulated

separately for each layer to realize the dimension reduction of the higher-order matrices. Most recently, Dazel *et al.* [47] proposed a method that makes it possible to couple different order transfer matrices in series based on an implicit and recursive process applied to the whole layered system, while the current study was focused on the manipulation of individual element matrices to facilitate the coupling process. The further advantages, applications and development in terms of the transfer matrix dimension reduction process of the modified TMM are illustrated in Sections 3.3 to 3.7. Finally, the proposed TMM is verified through a comparison with predictions made using the ACM, and the results are shown in Section 3.8, and model comparisons are drawn in Section 3.9 among the TMM proposed here, the recursive transfer matrix method [47] and the ACM.

3.3 The Modified TMM Model to Couple Higher-Order Elements in a Layered System

To further illustrate the advantages and application of the TMM, the general approach to the prediction and optimization of a porous medium's acoustical and/or damping performance when applied to a vibrating, stiff panel can be recalled and is illustrated in Figure 1.4. In this approach, multiple models are combined to connect the porous medium's parameters (micro-geometry and/or bulk properties) with its performance (acoustical attenuation and/or damping). First, for different types of porous media, certain relations can be established between their microstructural details and bulk properties. For example, an airflow resistivity (AFR) model [35, 48] was previously developed to connect a fibrous material's fiber size distribution with its airflow resistivity. Secondly, bulk properties, including airflow resistivity, can be connected with a porous medium's acoustical properties by using acoustical models, such as the ACM and the TMM. In a third stage, the acoustical properties can be connected to the damping properties by using the near-field damping (NFD) model [36–38, 49–52], for example. Therefore, the acoustical model (*i.e.*, the ACM

or TMM) plays an intermediate role in connecting the material’s parameters and its performance.

Typically, in the acoustical model, the TMM model has only been used for cases that involve a limp porous layer [38, 49–52] (or as described in Sections 2.4.1, 4.2 and Appendix B in this thesis), and the ACM model has been used for modeling cases that involve a poro-elastic layer [36, 37] (or as described in Sections 2.4.2, 4.2 and Appendix C in this thesis). However, when changing configurations, the ACM model requires a redevelopment of the global system of B.C. equations, which is potentially time-consuming and awkward to automate. That observation motivated the current focus on modifying the TMM model to be capable of coupling higher-order layered elements, so that instead of reassembling the B.C.s, the modeling of different configurations only requires the individual transfer matrix elements to be changed, which is a more straightforward approach that allows greater modeling efficiency especially when the layered system is complex.

A more specific modified TMM modeling process for a layered system involving a higher-order element (*e.g.*, a poro-elastic layers) can be recalled in Figure 1.3, in which bulk properties can be input to predict the layered system’s acoustical properties. The modeling comprises three steps. For a poro-elastic layer, the first step is based on the Johnson-Champoux-Allard (JCA) model [16, 24, 25], and involves the calculation of the viscous and thermal characteristic lengths, effective density, and bulk modulus of the fluid phase and/or of the material given the bulk properties of the material and the ambient properties (as described in Section 2.2). Note that the JCA model was originally developed for fully-isotropic porous media with arbitrary pore shapes, and was then extended by Lafarge [53] to a more comprehensive form by allowing for anisotropic situations and by modifying the JCA model to account for low frequency thermal effects; the result became known as the JCAL model. [17] The JCA model was also refined by both Pride *et al.* [54] and Lafarge *et al.* [53] to account for situations when there are constrictions between the pores, thus creating the JCAPL model.

Given the properties predicted in the first step, the second step is based on the Biot theory, in which stress-strain relations and dynamic equations are applied to calculate the complex wavenumbers in the poro-elastic material (as described in Section 2.3). Note that for an elastic solid layer, the bulk moduli and complex wavenumbers can be easily found based on the elasticity and wave theory of elastic solid media. [17]

In the third step, satisfactory solutions for the stress and displacement waves propagating within the medium can be constructed in terms of wavenumbers and arbitrary amplitude coefficients; the details of that construction process for poro-elastic media were introduced in Refs. [18,34]. Based on those satisfactory solutions, B.C.s can finally be applied in different ways to solve for acoustical properties such as the absorption coefficient or transmission loss. Recall that both the ACM and GTM implement B.C.s by assembling them into a global equation or matrix system, followed by a solution of the global system for the acoustical properties of interest. In contrast, the implementation of B.C.s based on the TMM described here principally consists of two parts: *i.e.*, constructing the transfer matrix of the higher-order layer, and then reducing the order of that transfer matrix. The construction of the transfer matrices for an elastic solid and a poro-elastic layer, four-by-four and six-by-six, respectively, were previously introduced in Refs. [43,45]. From those starting points, the dimension reduction process for higher-order transfer matrices is introduced next, in Sections 3.4 and 3.5.

3.4 Transfer Matrix Dimension Reduction for a Poro-Elastic Layer

A poro-elastic layer being driven by an oblique incidence plane wave is shown in Figure 3.1 to help frame the general approach to the matrix dimension reduction process.

3.4.1 Introduction of Matrices

First, the state vectors of propagating waves (also referred to as “field variables”) at the two surfaces of the poro-elastic layer can be connected by a six-by-six transfer matrix, $[\mathbf{T}]$: *i.e.*,

$$\begin{bmatrix} \sigma_z & u_z & s & U_z & \tau_{xz} & u_x \end{bmatrix}_{z=0}^T = [\mathbf{T}]_{6 \times 6} \begin{bmatrix} \sigma_z & u_z & s & U_z & \tau_{xz} & u_x \end{bmatrix}_{z=d}^T, \quad (3.1)$$

where σ_z is the force per unit material area acting on the solid phase of the poro-elastic medium in the z -direction, s is the force per unit material area acting on the fluid phase of the poro-elastic medium (opposite in sign to a pressure), u_z and U_z are the z -direction displacements of the solid and fluid phases of the poro-elastic medium, respectively, τ_{xz} is the shear force per unit material area acting on the solid phase in the x - z plane, and u_x is the x -direction displacement of the solid phase. The detailed form of $[\mathbf{T}]$ for a poro-elastic layer can be found in previous literature, for example, Refs. [17, 45].

Further, by applying the appropriate B.C.s, the field variable vectors can be connected with the acoustic pressures, p , and particle velocities, v_z , on both sides of the layer. That process can be implemented by using boundary condition matrices: *i.e.*, $[\mathbf{M}_1]$ and $[\mathbf{N}_1]$

$$[\mathbf{M}_1]_{4 \times 6} \begin{bmatrix} \sigma_z & u_z & s & U_z & \tau_{xz} & u_x \end{bmatrix}_{z=0}^T = [\mathbf{N}_1]_{4 \times 2} \begin{bmatrix} p & v_z \end{bmatrix}_{z=0}^T, \quad (3.2)$$

and $[\mathbf{M}_2]$ and $[\mathbf{N}_2]$

$$[\mathbf{M}_2]_{4 \times 6} \begin{bmatrix} \sigma_z & u_z & s & U_z & \tau_{xz} & u_x \end{bmatrix}_{z=d}^T = [\mathbf{N}_2]_{4 \times 2} \begin{bmatrix} p & v_z \end{bmatrix}_{z=d}^T. \quad (3.3)$$

To be more specific, when the layer has fluid on both sides (*e.g.*, open to air or adjacent to limp or rigid porous layers), the B.C.s to be satisfied are two normal stress conditions, one normal volume velocity condition and one shear stress condition as described in Ref. [18]: *i.e.*,

$$s = -\phi p, \quad (3.4a)$$

$$\sigma_z = -(1 - \phi)p, \quad (3.4b)$$

$$i\omega(1 - \phi)u_z + i\omega\phi U_z = v_z, \quad (3.4c)$$

$$\tau_{xz} = 0, \quad (3.4d)$$

where ϕ is the porosity of the layer, and ω is the angular frequency. Therefore,

$$\begin{bmatrix} \mathbf{M}_1 \end{bmatrix} = \begin{bmatrix} \mathbf{M}_2 \end{bmatrix} = \begin{bmatrix} 1 & 0 & 0 & 0 & 0 & 0 \\ 0 & 0 & 1 & 0 & 0 & 0 \\ 0 & i\omega(1 - \phi) & 0 & i\omega\phi & 0 & 0 \\ 0 & 0 & 0 & 0 & 1 & 0 \end{bmatrix}, \quad (3.5)$$

and

$$\begin{bmatrix} \mathbf{N}_1 \end{bmatrix} = \begin{bmatrix} \mathbf{N}_2 \end{bmatrix} = \begin{bmatrix} -(1 - \phi) & 0 \\ -\phi & 0 \\ 0 & 1 \\ 0 & 0 \end{bmatrix}. \quad (3.6)$$

On the other hand, when the layer is bonded to a stiff panel, the B.C.s to be satisfied include four motion continuity conditions, one shear stress condition and one panel equation of motion, as per Ref. [18]: *i.e.*,

$$v_z = i\omega w_t, \quad (3.7a)$$

$$u_z = w_t, \quad (3.7b)$$

$$U_z = w_t, \quad (3.7c)$$

$$u_x = w_p(-/+)ik_x \frac{h_p}{2} w_t, \quad (3.7d)$$

$$(+/-)\tau_{xz} = (D_p k_x^2 - m_s \omega^2) w_p, \quad (3.7e)$$

$$(+/-)p(+/-)s(+/-)\sigma_z - ik_x \frac{h_p}{2} \tau_{xz} = (Dk_x^4 - m_s \omega^2) w_t, \quad (3.7f)$$

where recall $k_x = \omega \sin \theta / c_0$ is the trace wavenumber in terms of incidence angle, θ , and the speed of sound in the air, c_0 . Further, w_t and w_p are the transverse and in-plane displacements of the panel, respectively, $m_s = \rho_p h_p$ is the mass per unit area of the panel based on its density, ρ_p , and thickness, h_p , and $D = [h_p^3 E_0 (1 + i\eta_p)] / [12(1 - \nu_p^2)]$ and $D_p = E_0 h_p$ are the flexural and longitudinal stiffnesses of the panel per unit width in the y -direction, respectively, based on h_p , the Young's modulus, E_0 , the loss factor, η_p , and the Poisson's ratio, ν_p . Note that this set of boundary conditions appears in slightly different forms in the literature (*e.g.*, Lauriks *et al.* [46]) depending on whether or not the shear stress coupling is fully accounted for. Also note that in B.C.s (3.7d) to (3.7f), and for the coordinate system shown in Figure 3.1, the first signs are used when the panel is bonded to the incident side of the layer, and the second signs are used when the panel is bonded to the transmission side of the layer. Therefore, in this case, w_t and w_p can be eliminated by algebra, and

$$[\mathbf{M}_1] = \begin{bmatrix} -1 & Dk_x^4 - m_s \omega^2 & -1 & 0 & ik_x h_p / 2 & 0 \\ 0 & -ik_x h_p / 2 & 0 & 0 & -1 / (D_p k_x^2 - m_s \omega^2) & 1 \\ 0 & i\omega & 0 & 0 & 0 & 0 \\ 0 & 0 & 0 & i\omega & 0 & 0 \end{bmatrix}, \quad (3.8a)$$

$$[\mathbf{M}_2] = \begin{bmatrix} 1 & Dk_x^4 - m_s \omega^2 & 1 & 0 & ik_x h_p / 2 & 0 \\ 0 & ik_x h_p / 2 & 0 & 0 & 1 / (D_p k_x^2 - m_s \omega^2) & 1 \\ 0 & i\omega & 0 & 0 & 0 & 0 \\ 0 & 0 & 0 & i\omega & 0 & 0 \end{bmatrix}, \quad (3.8b)$$

and

$$[\mathbf{N}_1] = \begin{bmatrix} 1 & 0 \\ 0 & 0 \\ 0 & 1 \\ 0 & 1 \end{bmatrix}, \quad (3.9a)$$

$$[\mathbf{N}_2] = \begin{bmatrix} -1 & 0 \\ 0 & 0 \\ 0 & 1 \\ 0 & 1 \end{bmatrix}. \quad (3.9b)$$

Note that the panel displacements, w_t and w_p , have been eliminated here so that the six B.C.s in Eq. (3.7) can be simplified to four to make the dimension of the boundary condition matrices for the bonded panel case the same as the open air case. Although only two sets of boundary conditions are listed above, specifically for the cases when the poro-elastic layer is adjacent to a fluid or is bonded to a stiff panel, the boundary condition matrices in each case share the same dimensions (*i.e.*, four-by-six for $[\mathbf{M}_1]$ and $[\mathbf{M}_2]$ and four-by-two for $[\mathbf{N}_1]$ and $[\mathbf{N}_2]$), with the result that the matrix operations described next are also applicable when the poro-elastic layer is connected to other surface treatments (*e.g.*, resistive screens, limp membranes, micro-perforated panels, *etc.*). The intention of maintaining the same dimension for each boundary condition matrix is to realize a more universal applicability of the SVD and QRD procedure described in following sections. Also note that if a surface treatment is bonded to the poro-elastic layer, the boundary condition matrices will always involve the equation of motion of the surface treatment, which will further be applied in the higher-order matrix dimension reduction process. However, when a surface treatment is not directly bonded to the poro-elastic layer (*i.e.*, when it is separated from the porous layer by a fluid gap), fluid surface boundary condition matrices will be applied in the dimension reduction process, and the surface treatment (together with the fluid gap between the treatment and the poro-elastic layer, if the thickness of the gap is non-negligible) will be treated as separate layered elements and modeled using two-by-two transfer matrices, which will then be multiplied with the dimension-reduced, two-by-two transfer matrix of the poro-elastic layer after the matrix dimension reduction process.

In addition, if the rear surface ($z = d$) of the poro-elastic layer is bonded to a rigid wall, the B.C.s comprise one stress-pressure continuity condition and four motion termination conditions: *i.e.*,

$$\sigma_z + s = p, \quad (3.10a)$$

$$v_z = 0, \quad (3.10b)$$

$$u_z = 0, \quad (3.10c)$$

$$U_z = 0, \quad (3.10d)$$

$$u_x = 0. \quad (3.10e)$$

In this case, boundary condition matrices, $[\mathbf{M}_2]$ and $[\mathbf{N}_2]$, in Eq. (3.3) can be expressed as

$$[\mathbf{M}_2] = \begin{bmatrix} -1 & 0 & -1 & 0 & 0 & 0 \\ 0 & i\omega & 0 & 0 & 0 & 0 \\ 0 & 0 & 0 & i\omega & 0 & 0 \\ 0 & 0 & 0 & 0 & 0 & 1 \end{bmatrix}, \quad (3.11)$$

and

$$[\mathbf{N}_2] = \begin{bmatrix} 1 & 0 \\ 0 & 1 \\ 0 & 1 \\ 0 & 0 \end{bmatrix}. \quad (3.12)$$

Note that here u_z and U_z were made equal to v_z to keep the dimensions of the boundary condition matrices the same as in the previous cases, and the rigid termination condition is applied by setting $v_z = 0$, which results in a reflection coefficient, RC , expression shown as Eq. (2.40) instead of the Eq. (2.39), which applies to the anechoic termination case.

3.4.2 Singular Value Decomposition (SVD)

The SVD is applied in two steps. In the first step, the SVD is applied to $[\mathbf{N}_1]$,

$$[\mathbf{N}_1]_{4 \times 2} = [\mathbf{U}_1]_{4 \times 4} [\mathbf{S}_1]_{4 \times 2} [\mathbf{V}_1]_{2 \times 2}^H, \quad (3.13)$$

where $[\mathbf{U}_1]$ and $[\mathbf{V}_1]$ are orthogonal matrices containing the singular vectors, and $[\mathbf{S}_1]$ consists of the singular values, λ_1 and λ_2 , in the form

$$[\mathbf{S}_1]_{4 \times 2} = \begin{bmatrix} \lambda_1 & 0 \\ 0 & \lambda_2 \\ \hline [\mathbf{0}] \end{bmatrix}, \quad (3.14)$$

so that Eq. (3.2) can be rewritten as

$$[\mathbf{M}_1]_{4 \times 6} \begin{bmatrix} \sigma_z & u_z & s & U_z & \tau_{xz} & u_x \end{bmatrix}_{z=0}^T = [\mathbf{U}_1]_{4 \times 4} [\mathbf{S}_1]_{4 \times 2} [\mathbf{V}_1]_{2 \times 2}^H \begin{bmatrix} p & v_z \end{bmatrix}_{z=0}^T, \quad (3.15)$$

and an intermediate matrix, $[\mathbf{A}]$, is introduced here, which takes the form

$$[\mathbf{A}]_{4 \times 6} = [\mathbf{U}_1]_{4 \times 4}^H [\mathbf{M}_1]_{4 \times 6} = \begin{bmatrix} [\mathbf{A}_a]_{2 \times 6} \\ [\mathbf{A}_b]_{2 \times 6} \end{bmatrix}, \quad (3.16)$$

so that Eq. (3.2) can further be rewritten as

$$[\mathbf{A}] \begin{bmatrix} \sigma_z \\ u_z \\ s \\ U_z \\ \tau_{xz} \\ u_x \end{bmatrix}_{z=0} = \begin{bmatrix} \lambda_1 & 0 \\ 0 & \lambda_2 \\ \hline [\mathbf{0}] \end{bmatrix} [\mathbf{V}_1]^H \begin{bmatrix} p \\ v_z \end{bmatrix}_{z=0}. \quad (3.17)$$

Therefore, a coupling matrix, $[\mathbf{C}_1]$, can be defined as

$$[\mathbf{C}_1]_{4 \times 6} = \begin{bmatrix} [\mathbf{C}_{1a}]_{2 \times 6} \\ [\mathbf{C}_{1b}]_{2 \times 6} \end{bmatrix}, \quad (3.18)$$

where

$$[\mathbf{C}_{1a}] = [\mathbf{V}_1] \begin{bmatrix} \lambda_1 & 0 \\ 0 & \lambda_2 \end{bmatrix} [\mathbf{A}_a], \quad (3.19)$$

and

$$[\mathbf{C}_{1b}] = [\mathbf{A}_b], \quad (3.20)$$

so that

$$\begin{bmatrix} p \\ v_z \\ 0 \\ 0 \end{bmatrix}_{z=0} = [\mathbf{C}_1] \begin{bmatrix} \sigma_z \\ u_z \\ s \\ U_z \\ \tau_{xz} \\ u_x \end{bmatrix}_{z=0}. \quad (3.21)$$

The first two rows of $[\mathbf{C}_1]$ (*i.e.*, the rows in $[\mathbf{C}_{1a}]$) consist of two modes of the singular values and vectors, and the projection of the field variables of the poro-elastic material (*i.e.*, the state vector of $\sigma_z, u_z, s, U_z, \tau_{xz}$ and u_x) onto these singular modes results in the acoustic field variables, p and v_z . The last two rows in $[\mathbf{C}_1]$ (*i.e.*, the rows in $[\mathbf{C}_{1b}]$) can be viewed as two independent modes of the poro-elastic material state vector. From Eq. (3.21), it can be seen that the inner products of these two rows with the state vector is zero, which means that for this type of interface, the field variables should not have any components of these two modes. In a geometrical interpretation, the projection of the state vector onto these two modes is zero, which means that the field variables are orthogonal to the space spanned by these two modes. This suggests that there are certain relations among the field variables that create zero impact on the incident surface. This conclusion can be drawn equally when a poro-elastic material is exposed to open air, or for a different interface type (*e.g.*, when the interface of the poro-elastic material has a surface treatment such as a stiff panel) by following the same SVD decomposition process, but the identified modal

space to which the state is orthogonal may be different and may have a different dimension as well.

In the second step, the SVD is applied to $[\mathbf{M}_2]$, so that

$$[\mathbf{M}_2]_{4 \times 6} = [\mathbf{U}_2]_{4 \times 4} [\mathbf{S}_2]_{4 \times 6} [\mathbf{V}_2]_{6 \times 6}^H, \quad (3.22)$$

which allows Eq. (3.3) to be rewritten as

$$[\mathbf{U}_2]_{4 \times 4} [\mathbf{S}_2]_{4 \times 6} [\mathbf{V}_2]_{6 \times 6}^H \begin{bmatrix} \sigma_z & u_z & s & U_z & \tau_{xz} & u_x \end{bmatrix}_{z=d}^T = [\mathbf{N}_2]_{4 \times 2} \begin{bmatrix} p & v_z \end{bmatrix}_{z=d}^T, \quad (3.23)$$

where $[\mathbf{S}_2]$ can similarly be expressed in terms of its singular values as

$$[\mathbf{S}_2]_{4 \times 6} = \left[\begin{array}{c|c} [\boldsymbol{\Sigma}]_{4 \times 4} & [\mathbf{0}] \end{array} \right], \quad (3.24)$$

and an intermediate matrix, $[\mathbf{B}]$, can be defined as

$$[\mathbf{B}]_{4 \times 2} = [\mathbf{U}_2]_{4 \times 4}^H [\mathbf{N}_2]_{4 \times 2}, \quad (3.25)$$

so that Eq. (3.3) can be rewritten as

$$\left[\begin{array}{c|c} [\boldsymbol{\Sigma}] & [\mathbf{0}] \end{array} \right] [\mathbf{V}_2]^H \begin{bmatrix} \sigma_z \\ u_z \\ s \\ U_z \\ \tau_{xz} \\ u_x \end{bmatrix}_{z=d} = [\mathbf{B}] \begin{bmatrix} p \\ v_z \end{bmatrix}_{z=d}. \quad (3.26)$$

In contrast to splitting the matrices, as in the first step, here the matrices are given supplemental fifth and sixth rows

$$\left[\begin{array}{c|c} [\boldsymbol{\Sigma}] & [\mathbf{0}] \\ \hline [\mathbf{0}] & [\mathbf{I}]_{2 \times 2} \end{array} \right] [\mathbf{V}_2]^H \begin{bmatrix} \sigma_z \\ u_z \\ s \\ U_z \\ \tau_{xz} \\ u_x \end{bmatrix}_{z=d} = \left[\begin{array}{c|c} [\mathbf{B}] & [\mathbf{0}] \\ \hline [\mathbf{0}] & [\mathbf{I}]_{2 \times 2} \end{array} \right] \begin{bmatrix} p \\ v_z \\ X_1 \\ X_2 \end{bmatrix}_{z=d}, \quad (3.27)$$

where

$$X_1 = \mathbf{V}_2(5, 1)\sigma_z + \mathbf{V}_2(5, 2)u_z + \mathbf{V}_2(5, 3)s + \mathbf{V}_2(5, 4)U_z + \mathbf{V}_2(5, 5)\tau_{xz} + \mathbf{V}_2(5, 6)u_x, \quad (3.28)$$

and

$$X_2 = \mathbf{V}_2(6, 1)\sigma_z + \mathbf{V}_2(6, 2)u_z + \mathbf{V}_2(6, 3)s + \mathbf{V}_2(6, 4)U_z + \mathbf{V}_2(6, 5)\tau_{xz} + \mathbf{V}_2(6, 6)u_x. \quad (3.29)$$

In Eq. (3.26), when the rows of the matrix $[\mathbf{V}_2]$ are interpreted as modes for the poro-elastic material state vector at the interface on the transmission side (*i.e.*, $z = d$) of the porous material, it is noted that the coefficients of the last two modes (*i.e.*, the inner product of the last two rows of $[\mathbf{V}_2]$ to the state vector) do not produce any impact on acoustic field variables, p and v_z , in the interface equation. Those two modes can thus be identified as two free modes for the state vector, meaning that the components of these two modes in the state vector cannot be identified by just looking at this particular interface, nor do they have any impact on the acoustic field. Another reason for introducing the two unity diagonal elements in the Eq. (3.27) is to add the two arbitrary modal coefficients (*i.e.*, X_1 and X_2) to the state vector that is projected by using transfer matrix formulation. The formulation involving p and v_z is shown as the right-hand side in Eq. (3.27), and the SVD operation is then used to reduce the six-by-six poro-elastic layer transfer matrix to four-by-four, as explained below.

A second coupling matrix, $[\mathbf{C}_2]$, can then be defined as

$$[\mathbf{C}_2]_{6 \times 4} = [\mathbf{V}_2] \left[\begin{array}{c|c} [\boldsymbol{\Sigma}]_{4 \times 4}^{-1} & [\mathbf{0}] \\ \hline [\mathbf{0}] & [\mathbf{I}]_{2 \times 2} \end{array} \right] \left[\begin{array}{c|c} [\mathbf{B}]_{4 \times 2} & [\mathbf{0}] \\ \hline [\mathbf{0}] & [\mathbf{I}]_{2 \times 2} \end{array} \right], \quad (3.30)$$

so that

$$\begin{bmatrix} \sigma_z \\ u_z \\ s \\ U_z \\ \tau_{xz} \\ u_x \end{bmatrix}_{z=d} = [\mathbf{C}_2] \begin{bmatrix} p \\ v_z \\ X_1 \\ X_2 \end{bmatrix}_{z=d}. \quad (3.31)$$

Finally, based on Eqs. (3.1), (3.21) and (3.31), a relation can be found between the acoustic properties, p and v_z , on both sides of the layer, and it is expressed as

$$\begin{bmatrix} p \\ v_z \\ 0 \\ 0 \end{bmatrix}_{z=0} = [\mathbf{C}_1]_{4 \times 6} [\mathbf{T}]_{6 \times 6} [\mathbf{C}_2]_{6 \times 4} \begin{bmatrix} p \\ v_z \\ X_1 \\ X_2 \end{bmatrix}_{z=d} = [\mathbf{T}_{\text{SVD}}]_{4 \times 4} \begin{bmatrix} p \\ v_z \\ X_1 \\ X_2 \end{bmatrix}_{z=d}, \quad (3.32)$$

where $[\mathbf{T}_{\text{SVD}}]$ denotes the dimension-reduced transfer matrix of the poro-elastic layer after the SVD but before the QRD process, described in the next subsection.

Previously, it has been noted that, by looking at the two interfaces separately, two zero modes can be identified on the incident side of the layer, and two free modes can be identified on the transmission side; however, Eq. (3.32) implies that the undetermined coefficients of the two free modes can only be calculated by combining the information on both interfaces. This means that the zero modal coefficients on one interface provide the necessary information to determine the coefficients of the free modes on the other interface.

3.4.3 QR Decomposition (QRD)

The application of SVD has made it possible to reduce the six-by-six transfer matrix to a dimension of four-by-four. That is, in Eq. (3.32), a formulation relating p and v_z at $z = 0$ with those at $z = d$ has been derived but with additional zeros and free modes. In this section, QR decomposition (QRD) is applied to condense this

matrix relation, *i.e.*, to remove the additional zeros and free modes, which then gives the final transfer matrix formulation after a further reduction of the transfer matrix dimension from four-by-four to two-by-two. To achieve this further reduction, the QRD is applied to $[\mathbf{T}_{\text{SVD}}]$: *i.e.*,

$$[\mathbf{T}_{\text{SVD}}]_{4 \times 4} = [\mathbf{Q}]_{4 \times 4} [\mathbf{R}]_{4 \times 4}, \quad (3.33)$$

where $[\mathbf{Q}]$ is orthogonal, and $[\mathbf{R}]$ is upper-triangular, so that, Eq. (3.32) can be rewritten as

$$[\mathbf{D}]_{4 \times 2} \begin{bmatrix} p \\ v_z \end{bmatrix}_{z=0} = \begin{bmatrix} R_{11} & R_{12} & R_{13} & R_{14} \\ 0 & R_{22} & R_{23} & R_{24} \\ 0 & 0 & R_{33} & R_{34} \\ 0 & 0 & 0 & R_{44} \end{bmatrix} \begin{bmatrix} p \\ v_z \\ X_1 \\ X_2 \end{bmatrix}_{z=d}, \quad (3.34)$$

where

$$[\mathbf{D}] = \begin{bmatrix} [\tilde{\mathbf{D}}]_{2 \times 2} \\ \overline{[\vec{d}_3]_{1 \times 2}^T} \\ \overline{[\vec{d}_4]_{1 \times 2}^T} \end{bmatrix} = [\mathbf{Q}]_{4 \times 4}^H \begin{bmatrix} 1 & 0 \\ 0 & 1 \\ 0 & 0 \\ 0 & 0 \end{bmatrix}. \quad (3.35)$$

Further X_1 and X_2 can be expressed in terms of elements in $[\mathbf{D}]$ and $[\mathbf{R}]$, and so Eq. (3.34) can be rewritten as

$$[\mathbf{E}]_{2 \times 2} \begin{bmatrix} p \\ v_z \end{bmatrix}_{z=0} = \begin{bmatrix} R_{11} & R_{12} \\ 0 & R_{22} \end{bmatrix} \begin{bmatrix} p \\ v_z \end{bmatrix}_{z=d}, \quad (3.36)$$

where

$$[\mathbf{E}] = [\tilde{\mathbf{D}}] - \frac{1}{R_{33}} \begin{bmatrix} R_{13} \\ R_{23} \end{bmatrix} \left(\vec{d}_3 - \frac{R_{34}}{R_{44}} \vec{d}_4 \right) - \frac{1}{R_{44}} \begin{bmatrix} R_{14} \\ R_{24} \end{bmatrix} \vec{d}_4. \quad (3.37)$$

Finally, the acoustical properties on both sides of the layered structure can be connected by the dimension-reduced, two-by-two transfer matrix as

$$\begin{bmatrix} p \\ v_z \end{bmatrix}_{z=0} = [\mathbf{T}_{\text{SVDQR}}]_{2 \times 2} \begin{bmatrix} p \\ v_z \end{bmatrix}_{z=d} = \begin{bmatrix} T_{11} & T_{12} \\ T_{21} & T_{22} \end{bmatrix} \begin{bmatrix} p \\ v_z \end{bmatrix}_{z=d}, \quad (3.38)$$

where

$$\begin{bmatrix} T_{11} & T_{12} \\ T_{21} & T_{22} \end{bmatrix} = [\mathbf{E}]_{2 \times 2}^{-1} \begin{bmatrix} R_{11} & R_{12} \\ 0 & R_{22} \end{bmatrix}. \quad (3.39)$$

Note that the dimension-reduced, two-by-two matrix represents the poro-elastic layer when it has fluid on both sides; when the layer is bonded (glued) to facing panel(s), it represents the poro-elastic layer plus the stiff panel(s), which means that the higher-order element to be reduced is either the poro-elastic layer itself or the poro-elastic layer with its surface treatment(s).

3.4.4 An Alternative Matrix Dimension Reduction Method and a Comparison to the SVD+QRD Method

Recall that the main motivation of the matrix dimension reduction was to shrink the higher-order elements to two-by-two so that all the layered elements can be multiplied together as a series of two-by-two matrices. Here, an alternative calculation routine is presented, which is numerically-equivalent to the SVD+QRD method introduced in Sections 3.4.2 and 3.4.3, and which may allow more straight-forward computation. The introduction of this alternative method serves to emphasize some advantage of the SVD+QRD method, as well as to point out there is more than one way to achieve the matrix dimension reduction. This approach was originally suggested by the reviewer of an article submitted to the Journal of Applied Physics by Xue, Bolton and Liu [55].

First, Eqs. (3.2) and (3.3) can be written in matrix form as

$$[\mathbf{A}]_{8 \times 8} \mathbf{X} = \begin{bmatrix} [\mathbf{0}] \\ \hline [\mathbf{N}_2]_{4 \times 2} \end{bmatrix} \begin{bmatrix} p \\ v_z \end{bmatrix}_{z=d}, \quad (3.40)$$

where

$$\begin{bmatrix} \mathbf{A} \end{bmatrix} = \left[\begin{array}{c|c} -[\mathbf{N}_1] & [\mathbf{M}_1] \\ \hline [\mathbf{0}] & [\mathbf{M}_2][\mathbf{T}]^{-1} \end{array} \right] \quad (3.41)$$

and \mathbf{X} is a vector combining the field variables at $z = 0$: *i.e.*,

$$\mathbf{X} = \begin{bmatrix} p & v_z & \sigma_z & u_z & s & U_z & \tau_{xz} & u_x \end{bmatrix}_{z=0}^T. \quad (3.42)$$

Therefore Eq. (3.40) can be rewritten as

$$\mathbf{X} = \begin{bmatrix} \mathbf{A} \end{bmatrix}^{-1} \left[\begin{array}{c} [\mathbf{0}] \\ \hline [\mathbf{N}_2]_{4 \times 2} \end{array} \right] \begin{bmatrix} p \\ v_z \end{bmatrix}_{z=d}, \quad (3.43)$$

where

$$\begin{bmatrix} \mathbf{A} \end{bmatrix}^{-1} = \left[\begin{array}{c|c} [\mathbf{A}_{11}]_{2 \times 4} & [\mathbf{A}_{12}]_{2 \times 4} \\ \hline [\mathbf{A}_{21}]_{6 \times 4} & [\mathbf{A}_{22}]_{6 \times 4} \end{array} \right] \quad (3.44)$$

Then a relation between p and v_z at $z = 0$ and those at $z = d$ can be written as

$$\begin{bmatrix} p \\ v_z \end{bmatrix}_{z=0} = \begin{bmatrix} T_{11} & T_{12} \\ T_{21} & T_{22} \end{bmatrix} \begin{bmatrix} p \\ v_z \end{bmatrix}_{z=d}, \quad (3.45)$$

where

$$\begin{bmatrix} T_{11} & T_{12} \\ T_{21} & T_{22} \end{bmatrix} = [\mathbf{A}_{12}]_{2 \times 4} [\mathbf{N}_2]_{4 \times 2}. \quad (3.46)$$

This alternative calculation process is certainly much briefer than the SVD+QRD procedure described above. However, an important advantage of the SVD+QRD method is the ability to identify physical information including the zero and free modes on either side of the layered structure, which do not arise naturally from the alternative method.

3.4.5 Calculation of Acoustical Properties

Based on the elements in the dimension-reduced transfer matrix, $[T_{11}, T_{12}; T_{21}, T_{22}]$, the transmission coefficient, TC, reflection coefficient, RC, the absorption coefficient, AC, and transmission loss, TL, can then be calculated based on Ref. [30], and as described in Eqs. (2.38) to (2.42) of Section 2.4.1.

3.5 Transfer Matrix Dimension Reduction for an Elastic Solid Layer

The configuration shown in Figure 3.2 will help to illustrate the general approach of the matrix dimension reduction process by the SVD-QRD method for an elastic solid layer. Due to the similarity of the reduction process to that described in Section 3.4, this section is not divided into subsections.

First, the vectors of propagating waves within the layer at both surfaces of the solid layer can be connected by a four-by-four transfer matrix, $[\mathbf{T}]$: *i.e.*,

$$\begin{bmatrix} v_x^s & v_z^s & \sigma_z^s & \tau_{xz}^s \end{bmatrix}_{z=0}^T = [\mathbf{T}]_{4 \times 4} \begin{bmatrix} v_x^s & v_z^s & \sigma_z^s & \tau_{xz}^s \end{bmatrix}_{z=d}^T, \quad (3.47)$$

where v_x^s and v_z^s are the x - and z -direction velocities, respectively, and σ_z^s and τ_{xz}^s are the normal and shear stresses, respectively. The detailed expression of $[\mathbf{T}]$ for an elastic solid layer can be found in earlier literature, such as in Refs. [17, 43].

Similarly, the field variable vectors for the acoustic field and elastic solid field on both sides of the layer can be connected by boundary condition matrices, $[\mathbf{M}_1]$ and $[\mathbf{N}_1]$, on the incident side

$$[\mathbf{M}_1]_{3 \times 4} \begin{bmatrix} v_x^s & v_z^s & \sigma_z^s & \tau_{xz}^s \end{bmatrix}_{z=0}^T = [\mathbf{N}_1]_{3 \times 2} \begin{bmatrix} p & v_z \end{bmatrix}_{z=0}^T, \quad (3.48)$$

and by $[\mathbf{M}_2]$ and $[\mathbf{N}_2]$ on the transmission side

$$[\mathbf{M}_2]_{3 \times 4} \begin{bmatrix} v_x^s & v_z^s & \sigma_z^s & \tau_{xz}^s \end{bmatrix}_{z=d}^T = [\mathbf{N}_2]_{3 \times 2} \begin{bmatrix} p & v_z \end{bmatrix}_{z=d}^T. \quad (3.49)$$

To be more specific, when the layer has fluid on both its sides, the B.C.s to be satisfied are one normal stress condition, one normal velocity condition and one shear stress condition: *i.e.*,

$$\sigma_z^s = -p, \quad (3.50a)$$

$$v_z^s = v_z, \quad (3.50b)$$

$$\tau_{xz}^s = 0. \quad (3.50c)$$

Thus,

$$\begin{bmatrix} \mathbf{M}_1 \end{bmatrix} = \begin{bmatrix} \mathbf{M}_2 \end{bmatrix} = \begin{bmatrix} 0 & 1 & 0 & 0 \\ 0 & 0 & 1 & 0 \\ 0 & 0 & 0 & 1 \end{bmatrix}, \quad (3.51)$$

and

$$\begin{bmatrix} \mathbf{N}_1 \end{bmatrix} = \begin{bmatrix} \mathbf{N}_2 \end{bmatrix} = \begin{bmatrix} 0 & 1 \\ -1 & 0 \\ 0 & 0 \end{bmatrix}. \quad (3.52)$$

Further, when the layer is bonded to a stiff panel, the B.C.s to be satisfied include three motion continuity conditions, one shear stress condition, and one panel equation of motion, as per Ref. [18]: *i.e.*,

$$v_z = i\omega w_t, \quad (3.53a)$$

$$v_z^s = i\omega w_t, \quad (3.53b)$$

$$v_x^s = i\omega \left[w_p(-/+)ik_x \frac{h_p}{2} w_t \right], \quad (3.53c)$$

$$(+/-)\tau_{xz}^s = (D_p k_x^2 - m_s \omega^2) w_p, \quad (3.53d)$$

$$(+/-)p(+/-)\sigma_z^s - ik_x \frac{h_p}{2} \tau_{xz}^s = (Dk_x^4 - m_s \omega^2) w_t. \quad (3.53e)$$

Note that in B.C.s (3.53c) to (3.53e), and for the given coordinate system, the first signs are used when the panel is bonded to the incident side of the layer, and the second signs are used when the panel is bonded to the transmission side of the layer. Therefore, in this case,

$$[\mathbf{M}_1] = \begin{bmatrix} 0 & -i(Dk_x^4 - m_s \omega^2)/\omega & -1 & ik_x h_p/2 \\ -i/\omega & -k_x h_p/(2\omega) & 0 & -1/(D_p k_x^2 - m_s \omega^2) \\ 0 & 1 & 0 & 0 \end{bmatrix}, \quad (3.54a)$$

$$[\mathbf{M}_2] = \begin{bmatrix} 0 & -i(Dk_x^4 - m_s \omega^2)/\omega & 1 & ik_x h_p/2 \\ -i/\omega & k_x h_p/(2\omega) & 0 & 1/(D_p k_x^2 - m_s \omega^2) \\ 0 & 1 & 0 & 0 \end{bmatrix}, \quad (3.54b)$$

and

$$[\mathbf{N}_1] = \begin{bmatrix} 1 & 0 \\ 0 & 0 \\ 0 & 1 \end{bmatrix}, \quad (3.55a)$$

$$[\mathbf{N}_2] = \begin{bmatrix} -1 & 0 \\ 0 & 0 \\ 0 & 1 \end{bmatrix}. \quad (3.55b)$$

Then, by the application of SVD, $[\mathbf{N}_1]$ can be decomposed as follows

$$[\mathbf{N}_1]_{3 \times 2} = [\mathbf{U}_1]_{3 \times 3} [\mathbf{S}_1]_{3 \times 2} [\mathbf{V}_1]_{2 \times 2}^H, \quad (3.56)$$

and Eq. (3.48) can be rewritten as

$$\begin{aligned} [\mathbf{M}_1]_{3 \times 4} \begin{bmatrix} v_x^s & v_z^s & \sigma_z^s & \tau_{xz}^s \end{bmatrix}_{z=0}^T \\ = [\mathbf{U}_1]_{3 \times 3} [\mathbf{S}_1]_{3 \times 2} [\mathbf{V}_1]_{2 \times 2}^H \begin{bmatrix} p & v_z \end{bmatrix}_{z=0}^T, \end{aligned} \quad (3.57)$$

where $[\mathbf{S}_1]$ consists of the singular values, λ_1 and λ_2 , in the form

$$[\mathbf{S}_1]_{3 \times 2} = \begin{bmatrix} \lambda_1 & 0 \\ 0 & \lambda_2 \\ \mathbf{0} \end{bmatrix}, \quad (3.58)$$

and the intermediate matrix, $[\mathbf{A}]$, for the elastic solid case is introduced here as

$$[\mathbf{A}]_{3 \times 4} = [\mathbf{U}_1]_{3 \times 3}^H [\mathbf{M}_1]_{3 \times 4} = \begin{bmatrix} [\mathbf{A}_a]_{2 \times 4} \\ [\mathbf{A}_b]_{1 \times 4} \end{bmatrix}, \quad (3.59)$$

so that Eq. (3.48) can further be rewritten as

$$[\mathbf{A}] \begin{bmatrix} v_x^s \\ v_z^s \\ \sigma_z^s \\ \tau_{xz}^s \end{bmatrix}_{z=0} = \begin{bmatrix} \lambda_1 & 0 \\ 0 & \lambda_2 \\ \mathbf{0} \end{bmatrix} [\mathbf{V}_1]^H \begin{bmatrix} p \\ v_z \end{bmatrix}_{z=0}. \quad (3.60)$$

Therefore, the coupling matrix, $[\mathbf{C}_1]$, for the elastic solid case can be defined as

$$[\mathbf{C}_1]_{3 \times 4} = \begin{bmatrix} [\mathbf{C}_{1a}]_{2 \times 4} \\ [\mathbf{C}_{1b}]_{1 \times 4} \end{bmatrix}, \quad (3.61)$$

where

$$[\mathbf{C}_{1a}] = [\mathbf{V}_1] \begin{bmatrix} \lambda_1 & 0 \\ 0 & \lambda_2 \end{bmatrix} [\mathbf{A}_a], \quad (3.62)$$

and

$$[\mathbf{C}_{1b}] = [\mathbf{A}_b], \quad (3.63)$$

so that

$$\begin{bmatrix} p \\ v_z \\ 0 \end{bmatrix}_{z=0} = [\mathbf{C}_1]_{3 \times 4} \begin{bmatrix} v_x^s \\ v_z^s \\ \sigma_z^s \\ \tau_{xz}^s \end{bmatrix}_{z=0}. \quad (3.64)$$

Note that in contrast to poro-elastic cases, Eq. (3.64) shows that only one zero mode can be identified for the field variables (*i.e.*, v_x^s, v_z^s, σ_z^s and τ_{xz}^s) on the incident side of an elastic solid layer-involved structure.

In the second step, the SVD is applied to $[\mathbf{M}_2]$ such that

$$[\mathbf{M}_2]_{3 \times 4} = [\mathbf{U}_2]_{3 \times 3} [\mathbf{S}_2]_{3 \times 4} [\mathbf{V}_2]_{4 \times 4}^H, \quad (3.65)$$

and so that Eq. (3.49) can be rewritten as

$$[\mathbf{U}_2]_{3 \times 3} [\mathbf{S}_2]_{3 \times 4} [\mathbf{V}_2]_{4 \times 4}^H \begin{bmatrix} v_x^s & v_z^s & \sigma_z^s & \tau_{xz}^s \end{bmatrix}_{z=d}^T = [\mathbf{N}_2]_{3 \times 2} \begin{bmatrix} p & v_z \end{bmatrix}_{z=d}^T, \quad (3.66)$$

where $[\mathbf{S}_2]$ can similarly be expressed in terms of its singular values as

$$[\mathbf{S}_2]_{3 \times 4} = \left[\begin{array}{c|c} [\mathbf{\Sigma}]_{3 \times 3} & [\mathbf{0}] \end{array} \right], \quad (3.67)$$

and the intermediate matrix, $[\mathbf{B}]$, for the elastic solid case is introduced here as

$$[\mathbf{B}]_{3 \times 2} = [\mathbf{U}_2]_{3 \times 3}^H [\mathbf{N}_2]_{3 \times 2}, \quad (3.68)$$

so that Eq. (3.49) can be rewritten as

$$\left[\begin{array}{c|c} [\mathbf{\Sigma}]_{3 \times 3} & [\mathbf{0}] \end{array} \right] [\mathbf{V}_2]_{4 \times 4}^H \begin{bmatrix} v_x^s \\ v_z^s \\ \sigma_z^s \\ \tau_{xz}^s \end{bmatrix}_{z=d} = [\mathbf{B}] \begin{bmatrix} p \\ v_z \end{bmatrix}_{z=d}. \quad (3.69)$$

In contrast to splitting the matrices, as in the first step, here the matrices are given a single supplemental row: *i.e.*,

$$\left[\begin{array}{c|c} [\mathbf{\Sigma}]_{3 \times 3} & [\mathbf{0}] \\ \hline [\mathbf{0}] & 1 \end{array} \right] [\mathbf{V}_2]_{4 \times 4}^H \begin{bmatrix} v_x^s \\ v_z^s \\ \sigma_z^s \\ \tau_{xz}^s \end{bmatrix}_{z=d} = \left[\begin{array}{c|c} [\mathbf{B}] & [\mathbf{0}] \\ \hline [\mathbf{0}] & 1 \end{array} \right] \begin{bmatrix} p \\ v_z \\ X_3 \end{bmatrix}_{z=d}, \quad (3.70)$$

where X_3 , like X_1 and X_2 previously, is an intermediate value, for the QRD below, that can be expressed as

$$X_3 = \mathbf{V}_2(4, 1)v_x^s + \mathbf{V}_2(4, 2)v_z^s + \mathbf{V}_2(4, 3)\sigma_z^s + \mathbf{V}_2(4, 4)\tau_{xz}^s. \quad (3.71)$$

Also, X_3 is the one undetermined modal coefficients that can be observed on the transmission side of the solid layer. Therefore, a second coupling matrix, $[\mathbf{C}_2]$, can be defined as

$$[\mathbf{C}_2]_{4 \times 3} = [\mathbf{V}_2] \left[\begin{array}{c|c} [\boldsymbol{\Sigma}]_{3 \times 3}^{-1} & [\mathbf{0}] \\ \hline [\mathbf{0}] & 1 \end{array} \right] \left[\begin{array}{c|c} [\mathbf{B}]_{3 \times 2} & [\mathbf{0}] \\ \hline [\mathbf{0}] & 1 \end{array} \right], \quad (3.72)$$

so that

$$\begin{bmatrix} v_x^s \\ v_z^s \\ \sigma_z^s \\ \tau_{xz}^s \end{bmatrix}_{z=d} = [\mathbf{C}_2]_{4 \times 3} \begin{bmatrix} p \\ v_z \\ X_3 \end{bmatrix}_{z=d}. \quad (3.73)$$

Finally, based on Eqs. (3.47), (3.64) and (3.73), a relation can be found between the acoustic properties, p and v_z , on both sides of the layer, and it is expressed as

$$\begin{bmatrix} p \\ v_z \\ 0 \end{bmatrix}_{z=0} = [\mathbf{C}_1]_{3 \times 4} [\mathbf{T}]_{4 \times 4} [\mathbf{C}_2]_{4 \times 3} \begin{bmatrix} p \\ v_z \\ X_3 \end{bmatrix}_{z=d} = [\mathbf{T}_{\text{SVD}}]_{3 \times 3} \begin{bmatrix} p \\ v_z \\ X_3 \end{bmatrix}_{z=d}, \quad (3.74)$$

where $[\mathbf{T}_{\text{SVD}}]$ is the dimension-reduced transfer matrix of the elastic solid layer after the SVD, but before the QRD.

The QRD can then be applied to $[\mathbf{T}_{\text{SVD}}]$ of the elastic solid, and Eq. (3.74) can be rewritten as

$$[\mathbf{D}]_{3 \times 2} \begin{bmatrix} p \\ v_z \end{bmatrix}_{z=0} = \begin{bmatrix} R_{11} & R_{12} & R_{13} \\ 0 & R_{22} & R_{23} \\ 0 & 0 & R_{33} \end{bmatrix} \begin{bmatrix} p \\ v_z \\ X_3 \end{bmatrix}_{z=d}, \quad (3.75)$$

where

$$[\mathbf{D}] = \frac{\begin{bmatrix} \tilde{\mathbf{D}} \\ \vec{d}_3^T \end{bmatrix}}{\begin{bmatrix} \tilde{\mathbf{D}} \\ \vec{d}_3^T \end{bmatrix}^T} = [\mathbf{Q}]_{3 \times 3}^H \begin{bmatrix} 1 & 0 \\ 0 & 1 \\ 0 & 0 \end{bmatrix}. \quad (3.76)$$

Further X_3 can be solved for in terms of the elements in $[\mathbf{D}]$ and $[\mathbf{R}]$, and finally the acoustical properties on both sides of the elastic solid layered structure can be connected by a dimension-reduced, two-by-two transfer matrix as

$$\begin{bmatrix} p \\ v_z \end{bmatrix}_{z=0} = \begin{bmatrix} T_{11} & T_{12} \\ T_{21} & T_{22} \end{bmatrix} \begin{bmatrix} p \\ v_z \end{bmatrix}_{z=d}, \quad (3.77)$$

where

$$\begin{bmatrix} T_{11} & T_{12} \\ T_{21} & T_{22} \end{bmatrix} = [\mathbf{E}]_{2 \times 2}^{-1} \begin{bmatrix} R_{11} & R_{12} \\ 0 & R_{22} \end{bmatrix}, \quad (3.78)$$

and

$$[\mathbf{E}] = [\tilde{\mathbf{D}}] - \frac{1}{R_{33}} \begin{bmatrix} R_{13} \\ R_{23} \end{bmatrix} \vec{d}_3. \quad (3.79)$$

Further, the relation shown in Eqs. (3.77) to (3.79) can be combined with Eqs. (2.38) to (2.42) described in Section 2.4.1 to calculate the acoustical properties for cases that involve an elastic solid layer.

Note that an adhesive layer or sound insulation panel involved in an acoustical treatment can both be modeled as an elastic solid layer by using the calculation described above in Section 3.5. The elastic solid layer considered in Section 3.8 below was simply used to verify the proposed TMM model accuracy, and it does not refer to a practical treatment.

3.6 Poro-Elastic Layer Surface Treatments Coupling Methodologies

3.6.1 Impermeable Thin Treatments Coupling Methodologies

In the last chapter, different surface treatments were introduced in terms of two-by-two matrices (see Eq. (2.23) and expressions of z_m in Eqs. (2.25) to (2.34)) to couple with a rigid or limp porous layer, and previously in this chapter, the modified TMM has been introduced to allow stiff panels to be bonded to poro-elastic

layers in Section 3.4. Here, coupling methodologies can be applied similarly to other impermeable surface treatments to allow those to be bonded to a poro-elastic layer.

When a rigid or flexible resistive screen, or a limp impermeable membrane is bonded to a poro-elastic layer, the B.C.s comprise three motion continuity conditions, one normal stress-pressure condition (*i.e.*, equation of motion of the treatment), and one shear stress condition: *i.e.*,

$$v_z = i\omega w_t, \quad (3.80a)$$

$$w_t = u_z, \quad (3.80b)$$

$$w_t = U_z, \quad (3.80c)$$

$$(+/-)p(+/-)s(+/-)\sigma_z = i\omega z_m w_t, \quad (3.80d)$$

$$\tau_{xz} = 0, \quad (3.80e)$$

where the poro-elastic layer field variables, σ_z , s , τ_{xz} , u_z and U_z are as have been introduced previously in this chapter, z_m is the transfer impedance of the surface treatment, for which the expressions can be found in Eqs. (2.25), (2.26) and (2.27) for a rigid resistive screen, a limp impermeable membrane, and a flexible resistive screen, respectively, and w_t is the transverse displacement of the treatment, which can be eliminated to ensure that the dimensions of boundary condition matrices, $[\mathbf{M}_1]$, $[\mathbf{M}_2]$, $[\mathbf{N}_1]$ and $[\mathbf{N}_2]$, are consistent with previous cases: *i.e.*,

$$[\mathbf{M}_1] = \begin{bmatrix} -1 & i\omega z_m & -1 & 0 & 0 & 0 \\ 0 & 0 & 0 & 0 & 1 & 0 \\ 0 & i\omega & 0 & 0 & 0 & 0 \\ 0 & 0 & 0 & i\omega & 0 & 0 \end{bmatrix}, \quad (3.81a)$$

$$[\mathbf{M}_2] = \begin{bmatrix} 1 & i\omega z_m & 1 & 0 & 0 & 0 \\ 0 & 0 & 0 & 0 & 1 & 0 \\ 0 & i\omega & 0 & 0 & 0 & 0 \\ 0 & 0 & 0 & i\omega & 0 & 0 \end{bmatrix}, \quad (3.81b)$$

and

$$[\mathbf{N}_1] = \begin{bmatrix} 1 & 0 \\ 0 & 0 \\ 0 & 1 \\ 0 & 1 \end{bmatrix}, \quad (3.82a)$$

$$[\mathbf{N}_2] = \begin{bmatrix} -1 & 0 \\ 0 & 0 \\ 0 & 1 \\ 0 & 1 \end{bmatrix}. \quad (3.82b)$$

3.6.2 Rigid/Flexible/Stiff Micro-Perforated Panels Coupling Methodologies

Originally introduced by Maa [56] in 1975 and then extended to a more comprehensive theory [28, 57], the Micro-Perforated Panel (MPP) has been proven to be an effective sound absorber in a variety of applications, such as duct or fan noise reduction [58], or serving as acoustical liners for a vehicle engine room [59]. Similar to a porous layer, an MPP can be generally divided into three types depending on the nature of its solid part: *i.e.*, (1) a rigid MPP that does not allow the motion of the panel, while the sound absorption is achieved only by the power dissipation due to the viscous and thermal effects within the perforations (holes); (2) a flexible (limp) MPP that allows the motion of the panel, but has negligible flexural stiffness; and (3) a stiff MPP that allows motion of the panel, and has non-negligible flexural stiffness.

Previously, the coupling between each of these three types of MPP and a limp or rigid porous layer has been briefly introduced in Section 2.4.1, which was achieved

by multiplying the two-by-two transfer matrices of both layered elements together. Here, in this section, coupling methodologies are introduced to achieve bonding a rigid/flexible/stiff MPP with a poro-elastic layer.

When a rigid MPP is bonded to a poro-elastic layer, the B.C.s comprise two normal volume velocity conditions, one normal stress-pressure condition (*i.e.*, equation of motion of the fluid in the hole), one motion termination condition for the solid part of the panel, and one shear stress condition: *i.e.*,

$$v_z = \phi_{\text{mpp}} v_h, \quad (3.83a)$$

$$\phi_{\text{mpp}} v_h = i\omega\phi U_z, \quad (3.83b)$$

$$(+/-)p(+/-)\phi s(+/-)(1-\phi)\sigma_z = \phi_{\text{mpp}} z_{\text{mr}} v_h, \quad (3.83c)$$

$$u_z = 0, \quad (3.83d)$$

$$\tau_{xz} = 0, \quad (3.83e)$$

where v_h is the normal (z -direction) acoustic particle velocity of the fluid (air) in the hole, ϕ_{mpp} and ϕ are the perforation rate (porosity) of the MPP and the porosity of the poro-elastic layer, respectively, and z_{mr} is the rigid MPP transfer impedance as introduced in Eq. (2.29) of Section 2.4.1. Similarly to the bonded stiff case and the cases to be introduced in the following, and for the coordinate system specified here, the first signs in Eq. (3.83c) are used when the MPP is bonded to the incident side of the layer, and the second signs are used when the MPP is bonded to the transmission side of the layer. Therefore, in this case, v_h can be eliminated by algebra to maintain the same dimension of boundary condition matrices, and

$$[\mathbf{M}_1] = \begin{bmatrix} 0 & 1 & 0 & 0 & 0 & 0 \\ -(1-\phi) & 0 & -\phi & i\omega\phi z_{\text{mr}} & 0 & 0 \\ 0 & 0 & 0 & i\omega\phi & 0 & 0 \\ 0 & 0 & 0 & 0 & 1 & 0 \end{bmatrix}, \quad (3.84a)$$

$$[\mathbf{M}_2] = \begin{bmatrix} 0 & 1 & 0 & 0 & 0 & 0 \\ 1 - \phi & 0 & \phi & i\omega\phi z_{mr} & 0 & 0 \\ 0 & 0 & 0 & i\omega\phi & 0 & 0 \\ 0 & 0 & 0 & 0 & 1 & 0 \end{bmatrix}, \quad (3.84b)$$

and

$$[\mathbf{N}_1] = \begin{bmatrix} 0 & 0 \\ 1 & 0 \\ 0 & 1 \\ 0 & 0 \end{bmatrix}, \quad (3.85a)$$

$$[\mathbf{N}_2] = \begin{bmatrix} 0 & 0 \\ -1 & 0 \\ 0 & 1 \\ 0 & 0 \end{bmatrix}. \quad (3.85b)$$

When a flexible (limp) MPP is bonded to a poro-elastic layer, the B.C.s comprise two normal volume velocity conditions, two normal stress-pressure conditions (*i.e.*, equation of motion of the fluid in the hole, and equation of motion of the panel), one motion continuity condition between the solid part of the panel and the poro-elastic medium solid phase, and one shear stress condition: *i.e.*,

$$v_z = (1 - \phi_{\text{mpp}})v_s + \phi_{\text{mpp}}v_h, \quad (3.86a)$$

$$\phi_{\text{mpp}}v_h = i\omega(1 - \phi)u_z + i\omega\phi U_z, \quad (3.86b)$$

$$(+/-)(1 - \phi_{\text{mpp}})p(+/-)(1 - \phi_{\text{mpp}})s(+/-)(1 - \phi_{\text{mpp}})\sigma_z = i\omega m_{\text{smpp}}v_s, \quad (3.86c)$$

$$(+/-)p(+/-)\phi s(+/-)(1 - \phi)\sigma_z = \phi_{\text{mpp}}z_{mr}v_h, \quad (3.86d)$$

$$v_s = i\omega u_z, \quad (3.86e)$$

$$\tau_{xz} = 0, \quad (3.86f)$$

where v_s is the normal (z -direction) velocity of the solid part of the panel, and $m_{\text{smpp}} = \rho_{\text{mpp}} t_{\text{mpp}}$ is the mass per unit area of the panel based on its density, ρ_{mpp} , and thickness, t_{mpp} . In this case, v_h and v_s can both be eliminated by algebra to maintain consistent boundary condition matrices dimensions, and

$$[\mathbf{M}_1] = \begin{bmatrix} -(1 - \phi_{\text{mpp}}) & -m_{\text{smpp}}\omega^2 & -(1 - \phi_{\text{mpp}}) & 0 & 0 & 0 \\ -(1 - \phi) & i\omega(1 - \phi)z_{\text{mr}} & -\phi & i\omega\phi z_{\text{mr}} & 0 & 0 \\ 0 & i\omega(2 - \phi - \phi_{\text{mpp}}) & 0 & i\omega\phi & 0 & 0 \\ 0 & 0 & 0 & 0 & 1 & 0 \end{bmatrix}, \quad (3.87a)$$

$$[\mathbf{M}_2] = \begin{bmatrix} 1 - \phi_{\text{mpp}} & -m_{\text{smpp}}\omega^2 & 1 - \phi_{\text{mpp}} & 0 & 0 & 0 \\ 1 - \phi & i\omega(1 - \phi)z_{\text{mr}} & \phi & i\omega\phi z_{\text{mr}} & 0 & 0 \\ 0 & i\omega(2 - \phi - \phi_{\text{mpp}}) & 0 & i\omega\phi & 0 & 0 \\ 0 & 0 & 0 & 0 & 1 & 0 \end{bmatrix}, \quad (3.87b)$$

and

$$[\mathbf{N}_1] = \begin{bmatrix} 1 - \phi_{\text{mpp}} & 0 \\ 1 & 0 \\ 0 & 1 \\ 0 & 0 \end{bmatrix}, \quad (3.88a)$$

$$[\mathbf{N}_2] = \begin{bmatrix} -(1 - \phi_{\text{mpp}}) & 0 \\ -1 & 0 \\ 0 & 1 \\ 0 & 0 \end{bmatrix}. \quad (3.88b)$$

When a stiff MPP is bonded to a poro-elastic layer, the B.C.s are similar to the flexible MPP case except for the additional consideration of flexural and longitudinal stiffnesses in the solid part of the panel for the normal stress-pressure equation of motion, and for the shear stress condition: *i.e.*,

$$v_z = (1 - \phi_{\text{mpp}})v_s + \phi_{\text{mpp}}v_h, \quad (3.89a)$$

$$\phi_{\text{mpp}} v_h = i\omega(1 - \phi)u_z + i\omega\phi U_z, \quad (3.89b)$$

$$\begin{aligned} & (+/-)(1 - \phi_{\text{mpp}})p(+/-)(1 - \phi_{\text{mpp}})s(+/-)(1 - \phi_{\text{mpp}})\sigma_z - ik_x \frac{t_{\text{mpp}}}{2}(1 - \phi_{\text{mpp}})\tau_{xz} \\ & = (D_{\text{mpp}}k_x^4 - m_{\text{smpp}}\omega^2) \frac{v_s}{i\omega}, \end{aligned} \quad (3.89c)$$

$$(+/-)p(+/-)\phi s(+/-)(1 - \phi)\sigma_z = \phi_{\text{mpp}} z_{\text{mr}} v_h, \quad (3.89d)$$

$$v_s = i\omega u_z, \quad (3.89e)$$

$$(+/-)\tau_{xz} = (D_{\text{pmpp}}k_x^2 - m_{\text{smpp}}\omega^2) \left[u_x(+/-)ik_x \frac{t_{\text{mpp}}}{2} \frac{v_s}{i\omega} \right], \quad (3.89f)$$

where u_x is the x -direction displacement of the solid phase of the poro-elastic layer, $D_{\text{mpp}} = [t_{\text{mpp}}^3 E_{0\text{mpp}}(1 + i\eta_{\text{mpp}})] / [12(1 - \nu_{\text{mpp}}^2)]$ and $D_{\text{pmpp}} = E_{0\text{mpp}} t_{\text{mpp}}$ are the flexural and longitudinal stiffnesses of the panel per unit width in the y -direction, respectively, based on t_{mpp} , the Young's modulus, $E_{0\text{mpp}}$, the loss factor, η_{mpp} , and the Poisson's ratio, ν_{mpp} , of the MPP. In this case, v_h and v_s can both be eliminated by algebra to maintain consistent boundary condition matrices dimensions, and

$$\begin{aligned} & [\mathbf{M}_1] = \\ & \begin{bmatrix} -(1 - \phi_{\text{mpp}}) & D_{\text{mpp}}k_x^4 - \omega^2 m_{\text{smpp}} & -(1 - \phi_{\text{mpp}}) & 0 & ik_x \frac{t_{\text{mpp}}}{2}(1 - \phi_{\text{mpp}}) & 0 \\ -(1 - \phi) & i\omega(1 - \phi)z_{\text{mr}} & -\phi & i\omega\phi z_{\text{mr}} & 0 & 0 \\ 0 & i\omega(2 - \phi - \phi_{\text{mpp}}) & 0 & i\omega\phi & 0 & 0 \\ 0 & -ik_x \frac{t_{\text{mpp}}}{2} & 0 & 0 & \frac{-1}{(D_{\text{pmpp}}k_x^2 - \omega^2 m_{\text{smpp}})} & 1 \end{bmatrix}, \end{aligned} \quad (3.90a)$$

$$\begin{aligned} & [\mathbf{M}_2] = \\ & \begin{bmatrix} 1 - \phi_{\text{mpp}} & D_{\text{mpp}}k_x^4 - \omega^2 m_{\text{smpp}} & 1 - \phi_{\text{mpp}} & 0 & ik_x \frac{t_{\text{mpp}}}{2}(1 - \phi_{\text{mpp}}) & 0 \\ 1 - \phi & i\omega(1 - \phi)z_{\text{mr}} & \phi & i\omega\phi z_{\text{mr}} & 0 & 0 \\ 0 & i\omega(2 - \phi - \phi_{\text{mpp}}) & 0 & i\omega\phi & 0 & 0 \\ 0 & ik_x \frac{t_{\text{mpp}}}{2} & 0 & 0 & \frac{1}{(D_{\text{pmpp}}k_x^2 - \omega^2 m_{\text{smpp}})} & 1 \end{bmatrix}, \end{aligned} \quad (3.90b)$$

and

$$[\mathbf{N}_1] = \begin{bmatrix} 1 - \phi_{\text{mpp}} & 0 \\ 1 & 0 \\ 0 & 1 \\ 0 & 0 \end{bmatrix}, \quad (3.91\text{a})$$

$$[\mathbf{N}_2] = \begin{bmatrix} -(1 - \phi_{\text{mpp}}) & 0 \\ -1 & 0 \\ 0 & 1 \\ 0 & 0 \end{bmatrix}. \quad (3.91\text{b})$$

Note that the flexible and stiff MPPs-related B.C.s that are introduced here were developed based on the inspiration from Ref. [29],

3.7 Transversely Isotropic Poro-Elastic Layers Coupling Methodology

Previously in this chapter, the poro-elastic layer was assumed to be fully isotropic, *i.e.*, the material's elasticity and other density properties are the same for x - y - and z -directions within the material. However, a more realistic situation of transverse isotropy should be considered, where a material's properties are the same for in-plane directions, x and y , but the normal direction z has different properties. The acoustical theories of transversely isotropic poro-elastic (TIP) media have been studied and comprehensively summarized in Refs. [60] (for the study of smart foams) and [61] (for the study of honeycomb composite structures), from both of which the B.C.s were implemented by using the ACM to realize coupling of the TIP with other layered element.

For the purpose of brevity, the acoustical theories of TIP media will not be fully recalled in this thesis. None-the-less, it should be highlighted that there are also six field variables, σ_z , u_z , s , U_z , τ_{xz} and u_x , propagating within a TIP medium, which are the same variables as the fully isotropic poro-elastic medium. This is important for

the modified TMM to be implemented to couple the TIP media with either a surface treatment, a panel structure, or any other layered elements represented by two-by-two matrices, since only the six-by-six transfer matrix $[\mathbf{T}]$ needs to be swapped from the fully isotropic [17, 45] to the TIP expression, but the rest of the matrix dimension reduction process maintains exactly the same as described previously in this chapter, and the expression and derivation of $[\mathbf{T}]$ of a TIP medium can also be found in Refs. [60, 61].

3.8 The Modified TMM Model Validation

By assigning the bulk properties of the poro-elastic medium (*i.e.*, the airflow resistivity, σ , porosity, ϕ , tortuosity, α_∞ , bulk density, ρ_b , layer thickness, d , Young's modulus, E_1 , mechanical loss factor, η_m , and Poisson's ratio, ν , as listed in Table 3.1), the properties of the elastic solid layer (*i.e.*, the bulk density, ρ_b^s , layer thickness, d^s , Young's modulus, E_1^s , mechanical loss factor, η_m^s , and Poisson's ratio, ν^s , as listed in Table 3.2), the panel properties (*i.e.*, h_p , E_0 , η_p , ν_p and ρ_p as listed in Table 3.3), and the ambient properties including the dynamic viscosity of air, η , Prandtl number, B^2 , specific heat ratio, γ , plus ρ_0 , c_0 and θ , as listed in Table 3.4, the AC and TL were calculated for different layered configurations by using both the classical ACM model and the TMM model proposed here, and the results are shown in Figures 3.3 to 3.9. The comparisons for all the layered structures show excellent agreement, which confirms the accuracy of the newly-developed TMM model. At the same time, it can be observed by comparing Figures 3.5 and 3.6, that the introduction of air gaps between the panel and the poro-elastic treatment helps to increase the high frequency transmission loss. Also, it can be seen that whether an air gap is introduced, either just at the front or back of the treatment, does not significantly affect the results: compare Figures 3.6 and 3.7.

Further validation of the modified TMM model was conducted by regenerating the absorption coefficient of a classic case study described in Ref. [62], which predicted

the normal incidence sound absorption coefficient of four cases that all included a limp impermeable membrane and a poro-elastic foam with a rigid backing. By putting an 1 mm air gap (airspace) between the membrane and the foam and/or between the foam and the backing, the absorption coefficient results for the four cases: *i.e.*, (1) bonded membrane-bonded backing (BB), (2) unbonded membrane-bonded backing (UB), (3) bonded membrane-unbonded backing (BU), and (4) unbonded membrane-unbonded backing (UU), are shown in Figure 3.10. On the other hand, given the same parameters as in Ref. [62] for the poro-elastic layer ($\sigma = 1.3 \times 10^5$ Rayls/m, $\phi = 0.9$, $\alpha_\infty = 6.025$, $\rho_b = 30$ kg/m³, $d = 2.5$ cm, $E_1 = 4 \times 10^5$ Pa, $\eta_m = 0.265$ and $\nu = 0.39$), the limp membrane ($m_s = 45$ g/m²), and the ambient parameters as listed in Table 3.4 (except for $\theta = 0^\circ$ in this case), the results of those four cases were easily regenerated by using the modified TMM model, and are plotted in Figure 3.11. The regeneration of the classic results again verified the modeling efficiency and prediction accuracy of the modified TMM when coupling a poro-elastic layer with other layered elements. And by comparing the absorption among the four cases described above, an important finding, which was presented 25 years ago, should now be reemphasized here that low frequency acoustical performance can be distinctly enhanced (without sacrificing treatment depth) by separating the front surface treatment and/or rigid backing from the poro-elastic layer.

3.9 Conclusions

In this chapter, a modified transfer matrix method (TMM) has been developed for modeling and coupling multilayered acoustical systems that include higher-order elements, such as fully isotropic poro-elastic, transversely isotropic poro-elastic (TIP) and elastic solid layers. Based on the application of matrix operations, including singular value decomposition (SVD) and Q-R decomposition (QRD), to the boundary condition matrices, the four-by-four or six-by-six transfer matrix (plus bonded surface treatment(s) if applicable) can be reduced to a dimension of two-by-two, which

facilitates their coupling with other elements represented by two-by-two matrices, such as fluid (air) layers, and limp and/or rigid porous layers, limp impermeable membranes, rigid/flexible resistive screens, flexurally-stiff panels, rigid/flexible/stiff micro-perforated panels (MPPs), *etc.* The accuracy of the TMM model was verified by comparison with the classical ACM model [18] for seven different cases involving a poro-elastic layer or an elastic solid layer. And the prediction accuracy was also verified by regenerating the normal incidence absorption coefficient results of four layered systems that all involved a limp membrane and a poro-elastic layer with a rigid backing.

Potential studies can be focused in the future on the Rayleigh wave effects [63] of an elastic solid layer, which was investigated in Ref. [64], and by using the modified TMM model, it can be observed in Figure 3.12 that the Rayleigh angle (marked by a blue solid line) can be easily captured, below which structural resonances between field variables within the elastic solid layer ($\rho_b^s = 2700 \text{ kg/m}^3$, $d^s = 2.5 \text{ cm}$, $E_1^s = 7 \times 10^{10} \text{ Pa}$, $\eta_m^s = 0$, $\nu^s = 0.33$, plus $\rho_0 = 1.21 \text{ kg/m}^3$, $c_0 = 343 \text{ m/s}$, and θ ranging from 0 to 10°) can also be observed.

The most obvious advantage of the proposed TMM pertains to modeling efficiency, since every layer is treated separately and the coupling process is handled simply by multiplication, which makes the redesign or remodeling of any multilayer configuration easier compared to the classic ACM and GTM (global assembly) methods. Also, the TMM model makes it convenient to observe the physical properties of interest at any location or depth within the layered system, since the modeling process is based on physical properties (note that a pseudo-inverse operation will cause a loss of physical meaning, so it cannot be used here). On the contrary, for the recursive transfer matrix method [47] mentioned above, the multilayer system is treated globally as a single system, and the coupling is achieved through a recursive mathematical process involving the application of a series of matrix operations, so that the physical meanings of properties within the layered system are suppressed. Furthermore, the SVD process in the proposed TMM method also helps to identify the zero modes

and free modes on the boundary of the layered treatment, which provides physical insights that cannot be easily derived from the simple calculation routine introduced in Section 3.4.4, for example.

The modified TMM model with full capability of model rigid/limp/elastic porous media can now serve as an alternative method to the ACM to be used for the incorporation into the near-field damping (NFD) modeling process as showing in Figure 1.4. Note that in following chapters, rigid porous media will not be considered as an ideal damping treatment due to their heavinesses in contrast to the lightweight requirements in automotive and aerospace industries, and the TMM model was further used in combination of the NFD model to predict and optimize limp porous layers' near-field damping performance when applied to different vibrating structures in following chapters. On the other hand, the poro-elastic layer's damping performance will be examined still by using the combination of the NFD model and the ACM model instead of the TMM model introduced in this chapter, and that decision was mainly because of the numerical-stability of the ACM model and the simpleness of the target layered structure to be studied in following chapters. It should be noted that the TMM model will still be a preference when the target multilayered acoustical/damping structure is complex and when the numerical-stability criteria are less strict.

Table 3.1. Parameters for the poro-elastic layer.

σ	ϕ	α_∞	ρ_b	d	E_1	η_m	ν
40000 Rayls/m	0.9871	1.2	13.3 kg/m ³	3 cm	10 ⁶ Pa	0.005	0.3

Table 3.2. Parameters for the elastic solid layer.

ρ_b^s	d^s	E_1^s	η_m^s	ν^s
1000 kg/m ³	1 cm	10 ⁷ Pa	0.5	0.4

Table 3.3. Parameters for the aluminum panel.

h_p	E_0	η_p	ν_p	ρ_p
3 mm	7×10^{10} Pa	0.003	0.33	2700 kg/m ³

Table 3.4. Parameters for the air ambient environment when the temperature is 25 °C.

η	B^2	γ	ρ_0	c_0	θ
1.8×10^{-5} kg/(s·m)	0.71	1.402	1.21 kg/m ³	343 m/s	40°

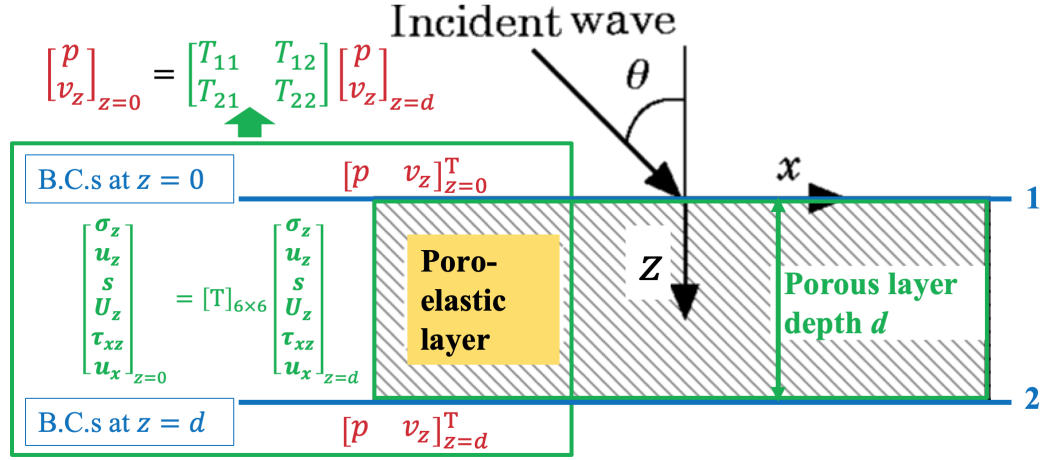


Figure 3.1. The general idea of the matrix dimension reduction process for a poro-elastic layer-involved case by using the modified Transfer Matrix Method (TMM).

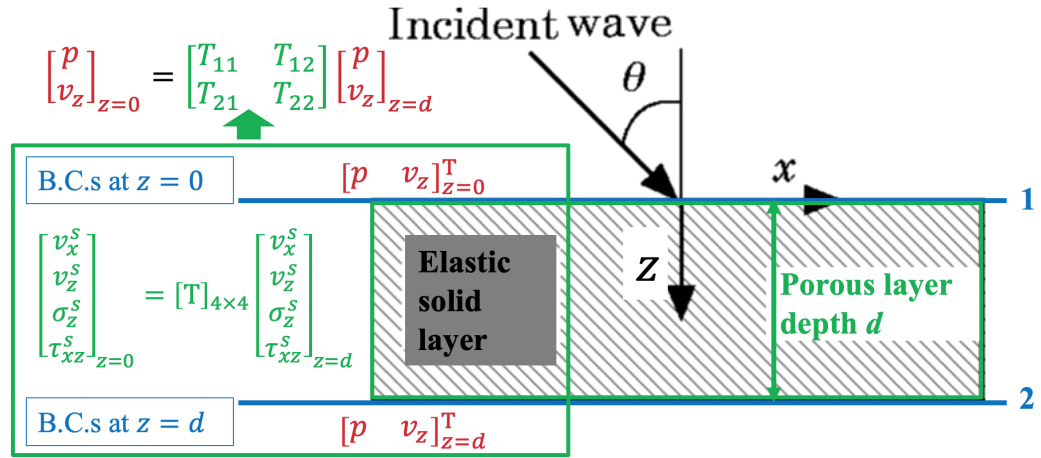


Figure 3.2. The general idea of the matrix dimension reduction process for an elastic solid layer-involved case by using the modified Transfer Matrix Method (TMM).

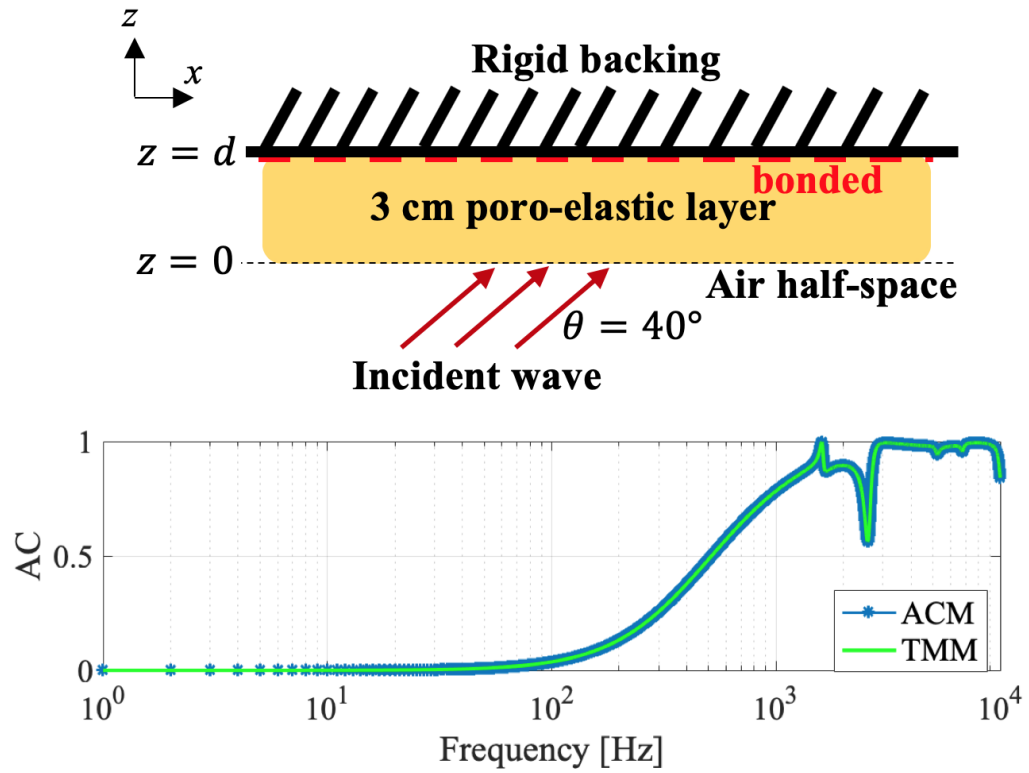


Figure 3.3. The predictions of the acoustical properties for a front-open, rigid-backed poro-elastic layer: the modified TMM *vs.* the classical ACM.

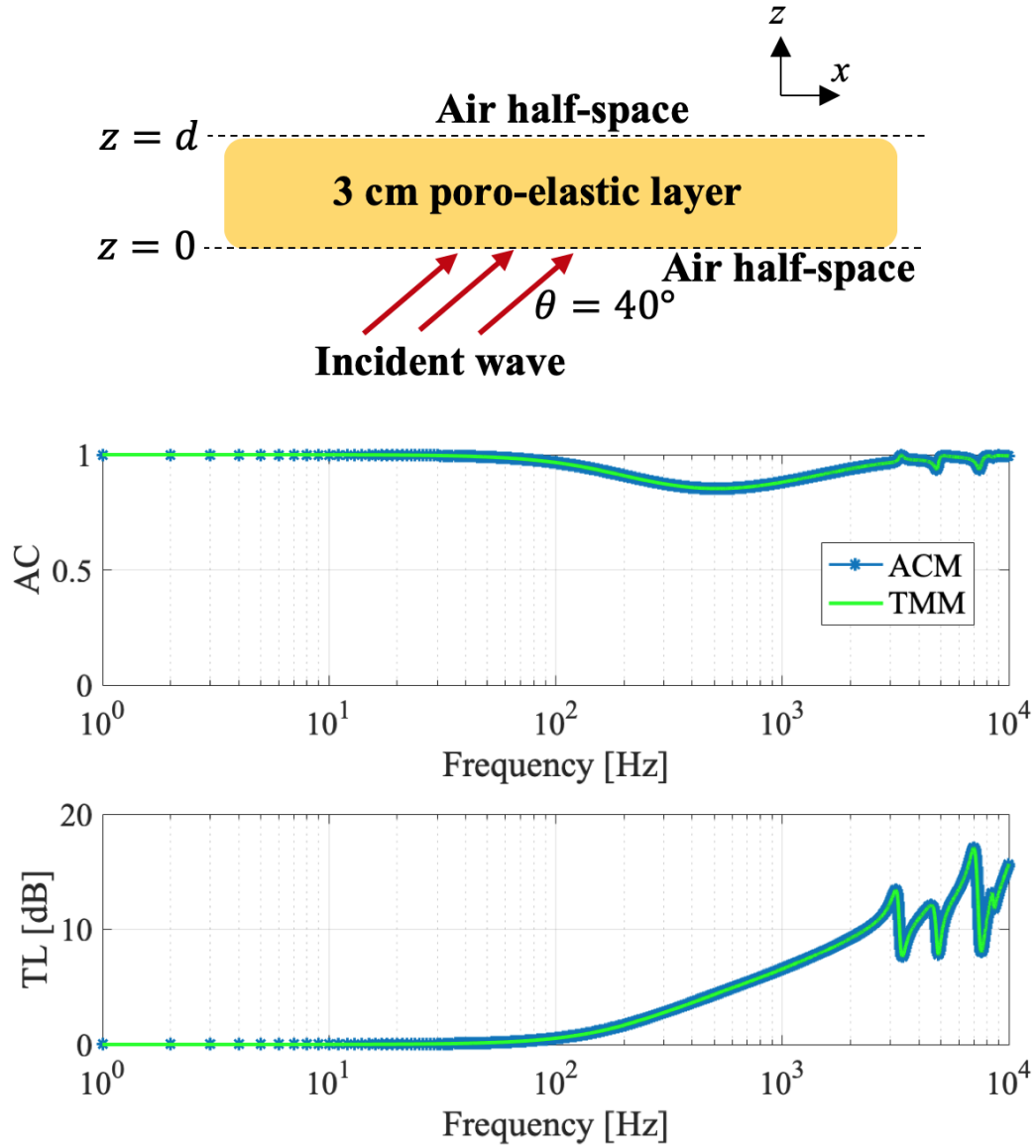


Figure 3.4. The predictions of the acoustical properties for a poro-elastic layer having open surfaces on both sides: the modified TMM *vs.* the classical ACM.

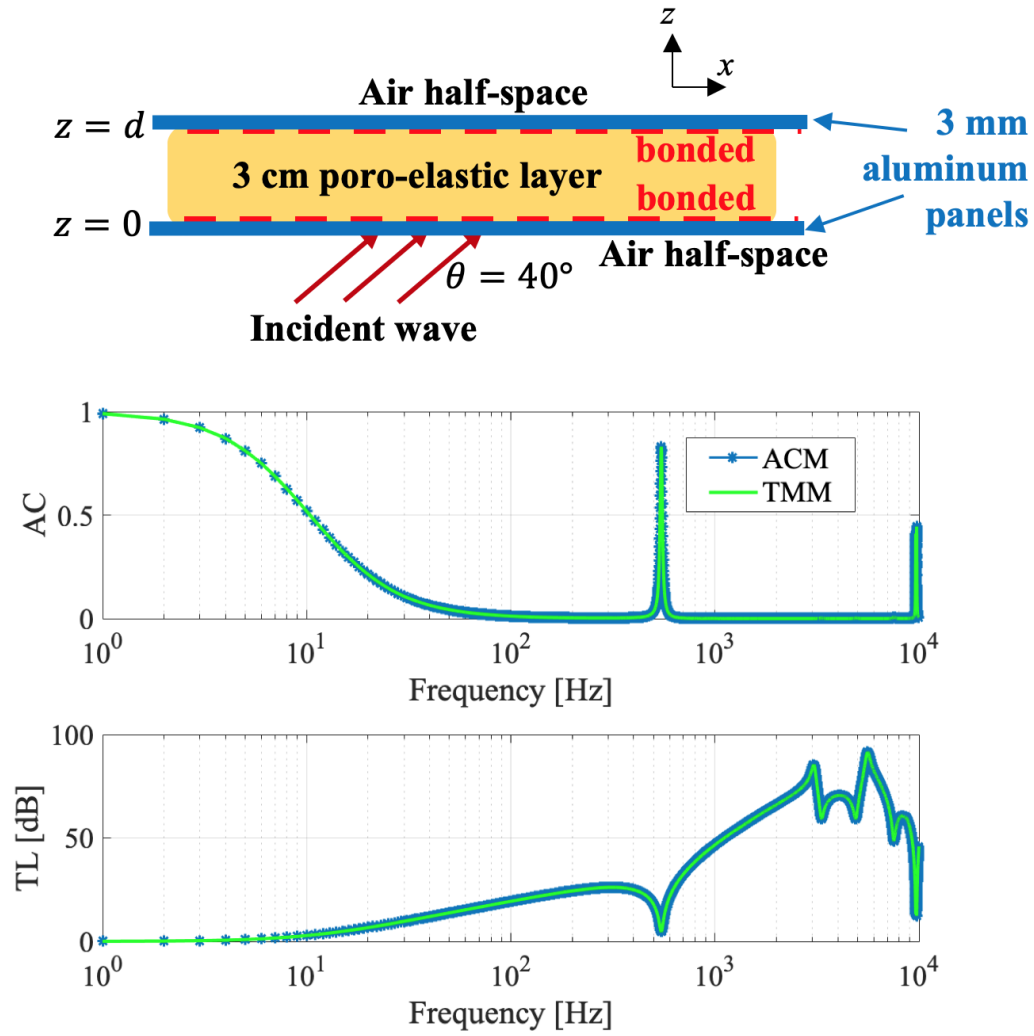


Figure 3.5. The predictions of the acoustical properties for a poro-elastic layer having bonded stiff panels on both sides: the modified TMM *vs.* the classical ACM.

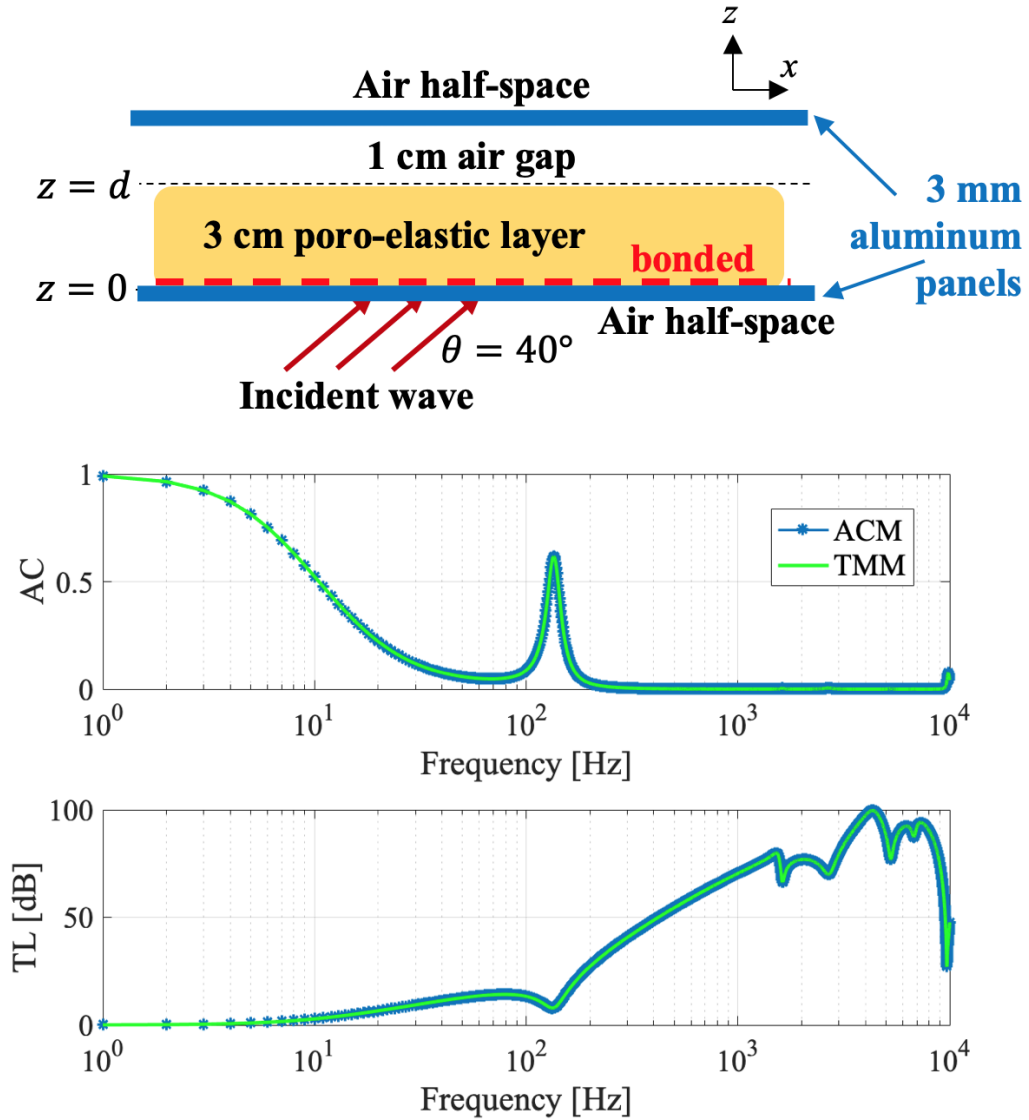


Figure 3.6. The predictions of the acoustical properties for a poro-elastic layer having a bonded stiff panel at its front surface, and an unbonded stiff panel with 1 cm air gap from its back surface: the modified TMM *vs.* the classical ACM.

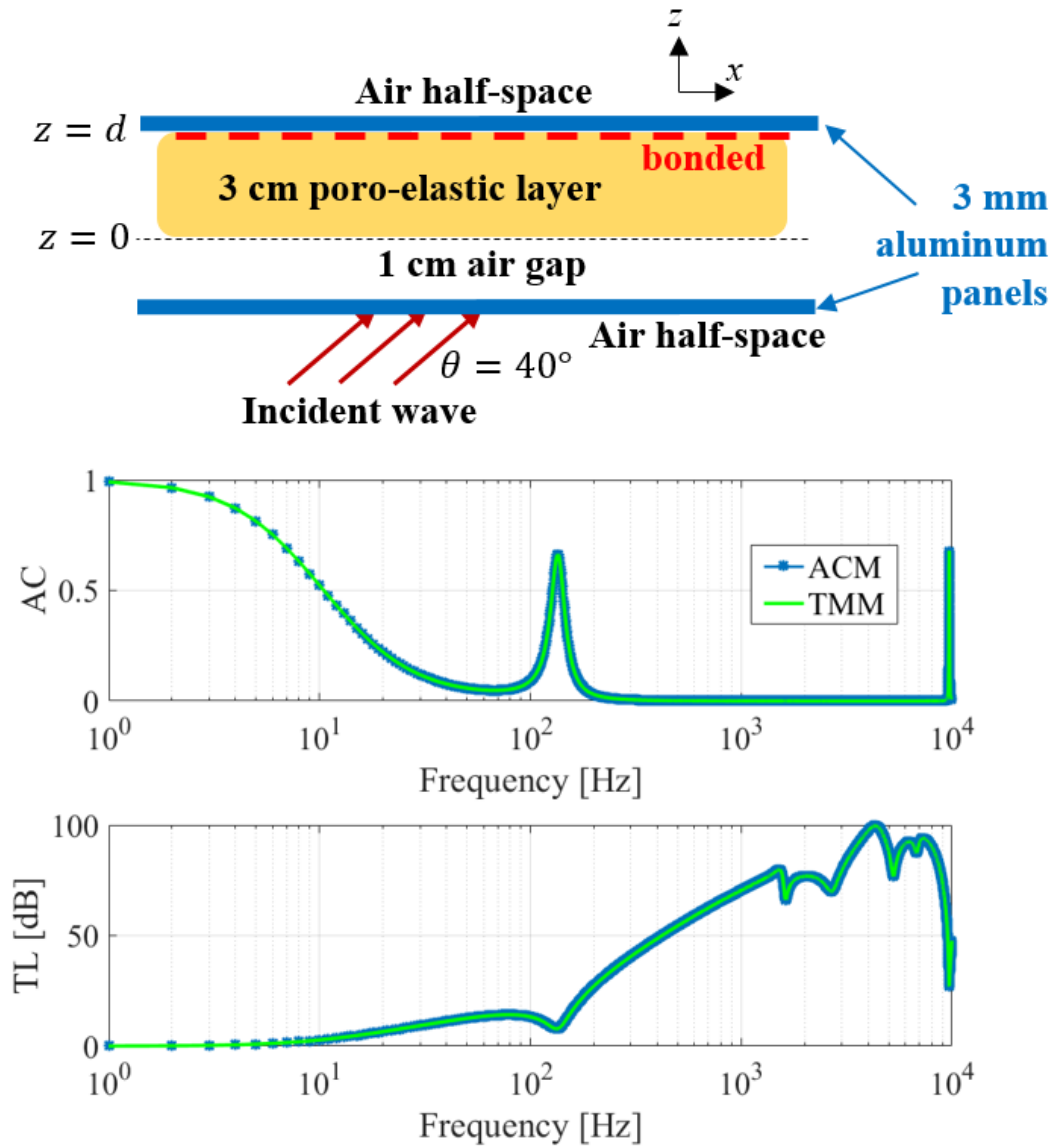


Figure 3.7. The predictions of the acoustical properties for a poro-elastic layer having an unbonded stiff panel with 1 cm air gap in front of its front surface, and a bonded stiff panel at its back surface: the modified TMM *vs.* the classical ACM.

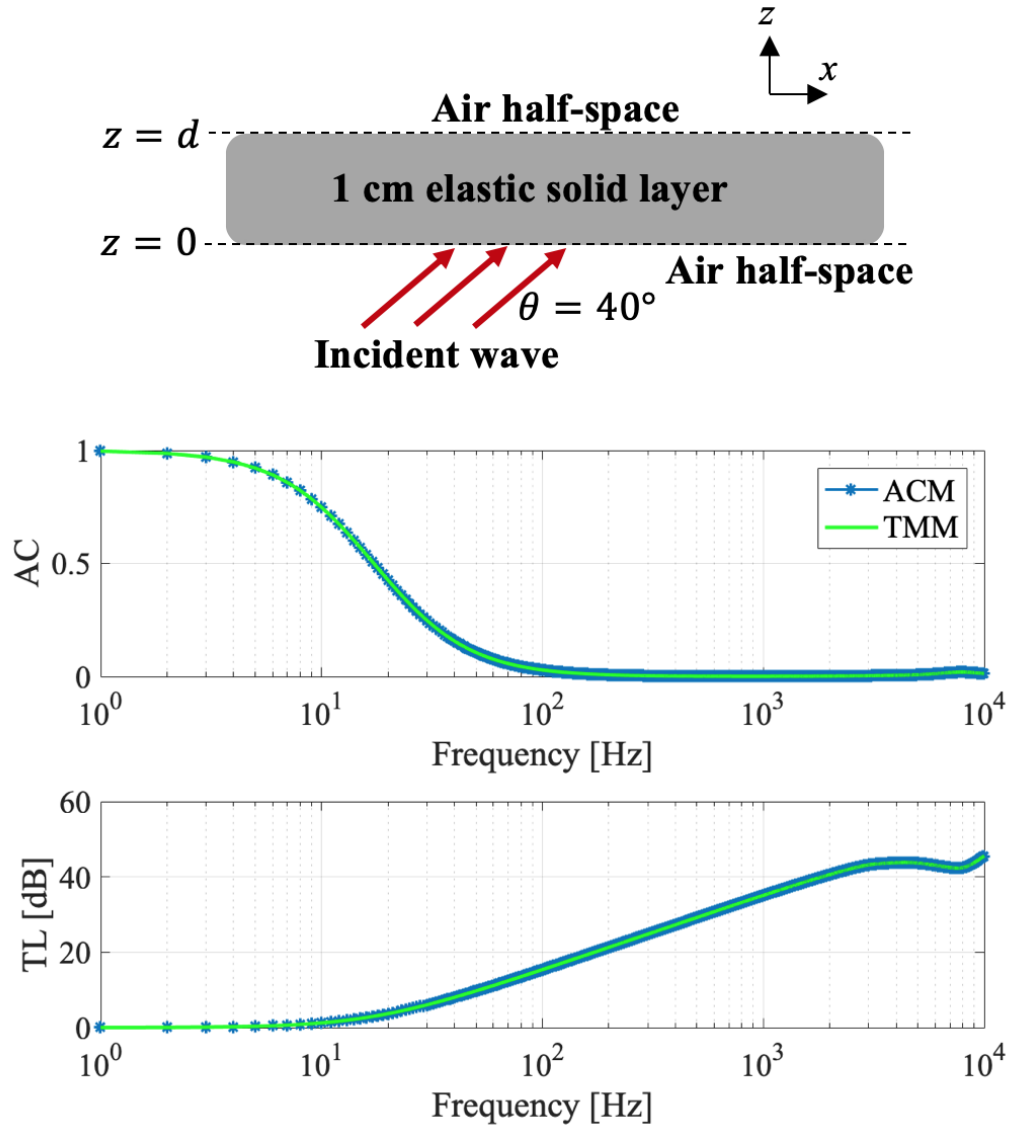


Figure 3.8. The predictions of the acoustical properties for an elastic solid layer having open surfaces on both sides: the modified TMM *vs.* the classical ACM.

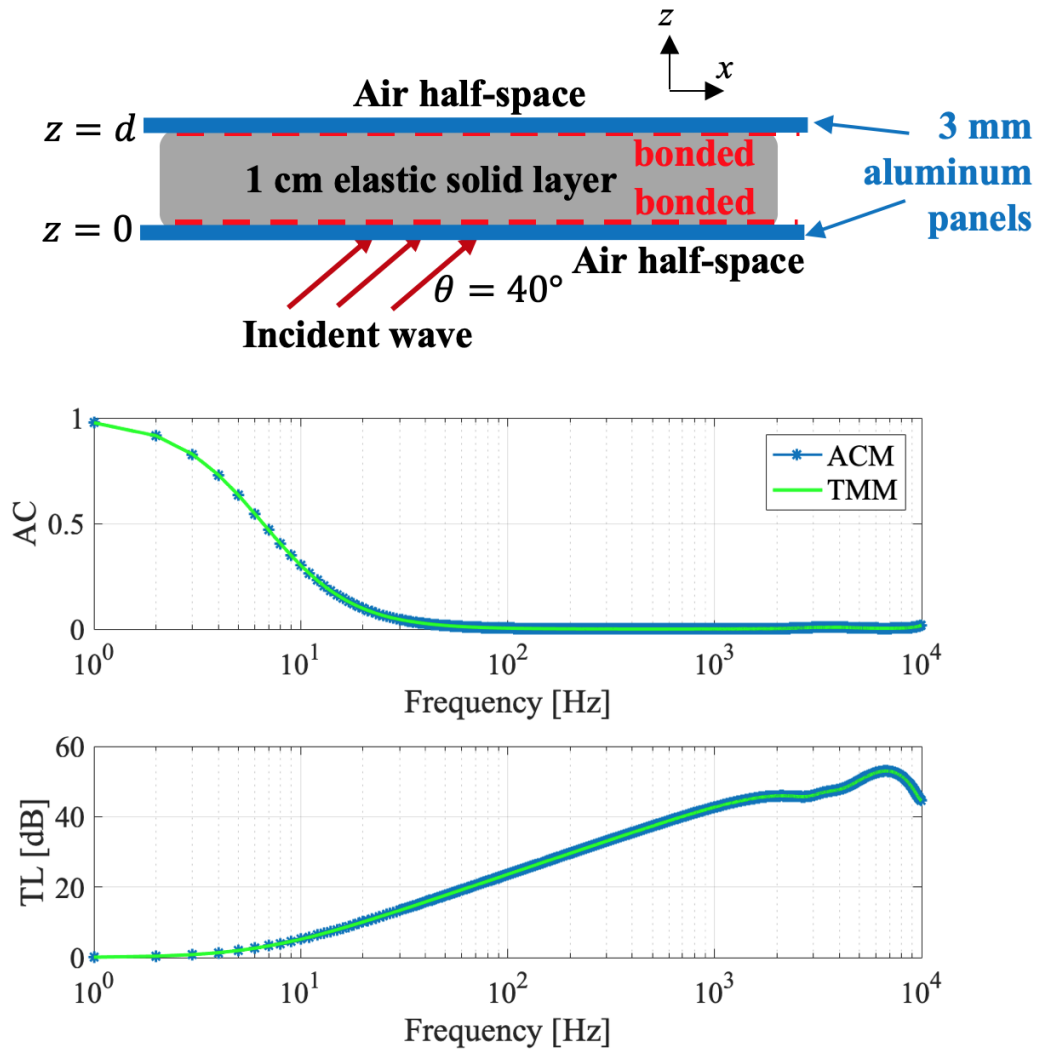
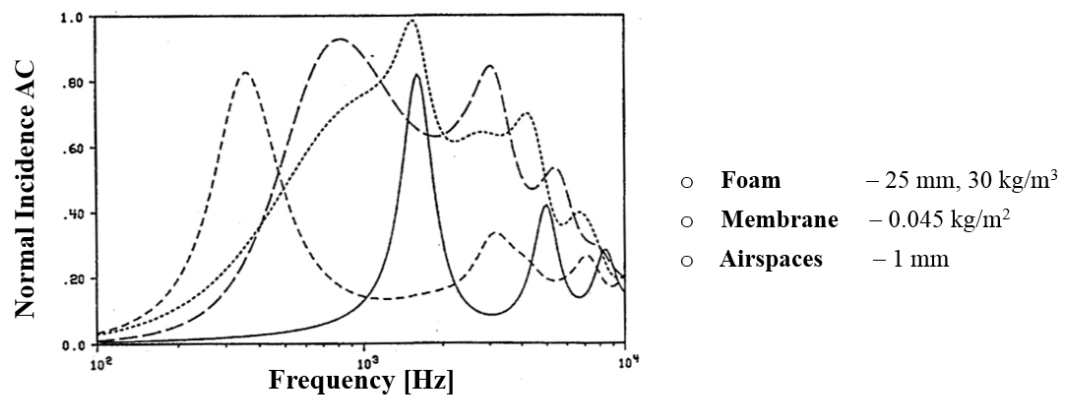


Figure 3.9. The predictions of the acoustical properties for an elastic solid layer having bonded stiff panels on both sides: the modified TMM *vs.* the classical ACM.



• **Effects of Airspace at front and rear**

- | | |
|--------------------------------------|---------|
| 1. Membrane/Foam/Backing | ————— |
| 2. Membrane /Space/Foam/Backing | |
| 3. Membrane /Foam/Space/Backing | - - - - |
| 4. Membrane/Space/Foam/Space/Backing | - . - . |

Figure 3.10. Normal incidence absorption coefficient for four cases with a limp membrane bonded/unbonded with the poro-elastic foam, and/or with the foam bonded/unbonded to the rigid backing.

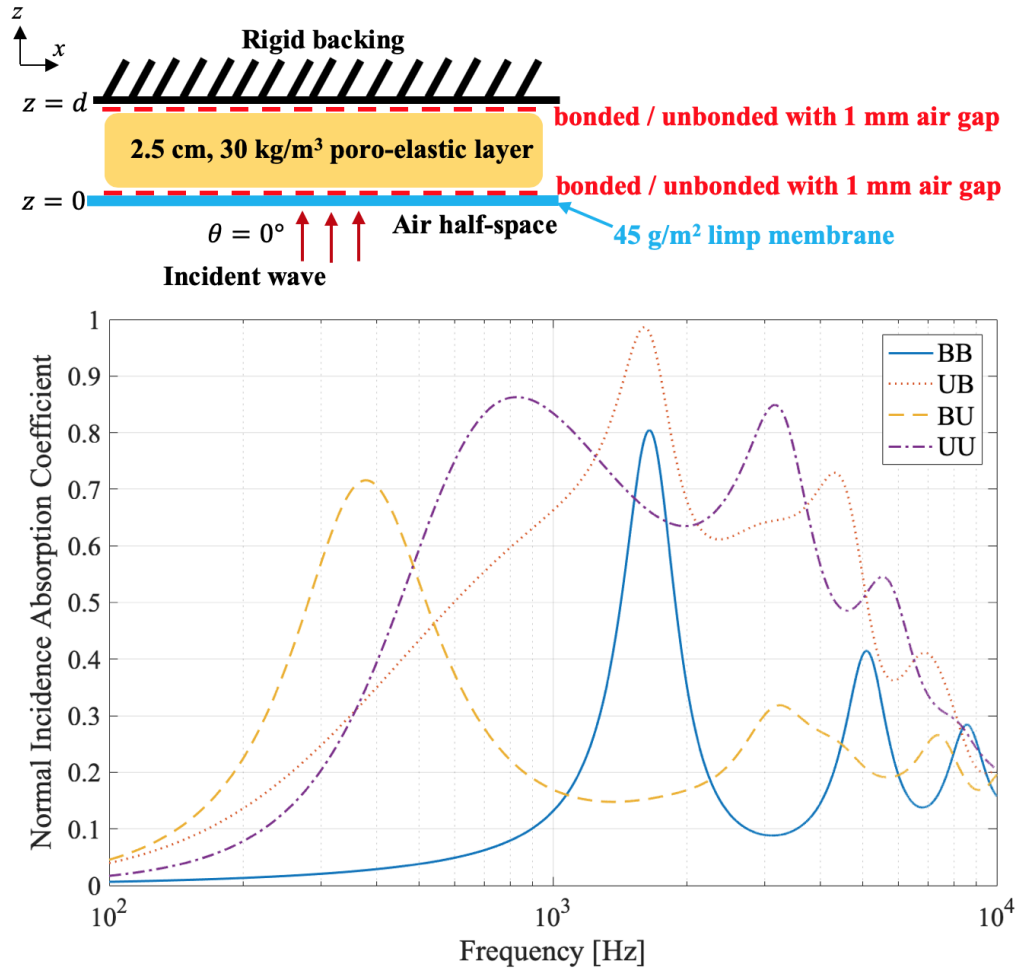


Figure 3.11. Regeneration of the normal incidence absorption coefficient for the four cases with a limp membrane bonded/unbonded with the poro-elastic foam, and/or with the foam bonded/unbonded to the rigid backing.

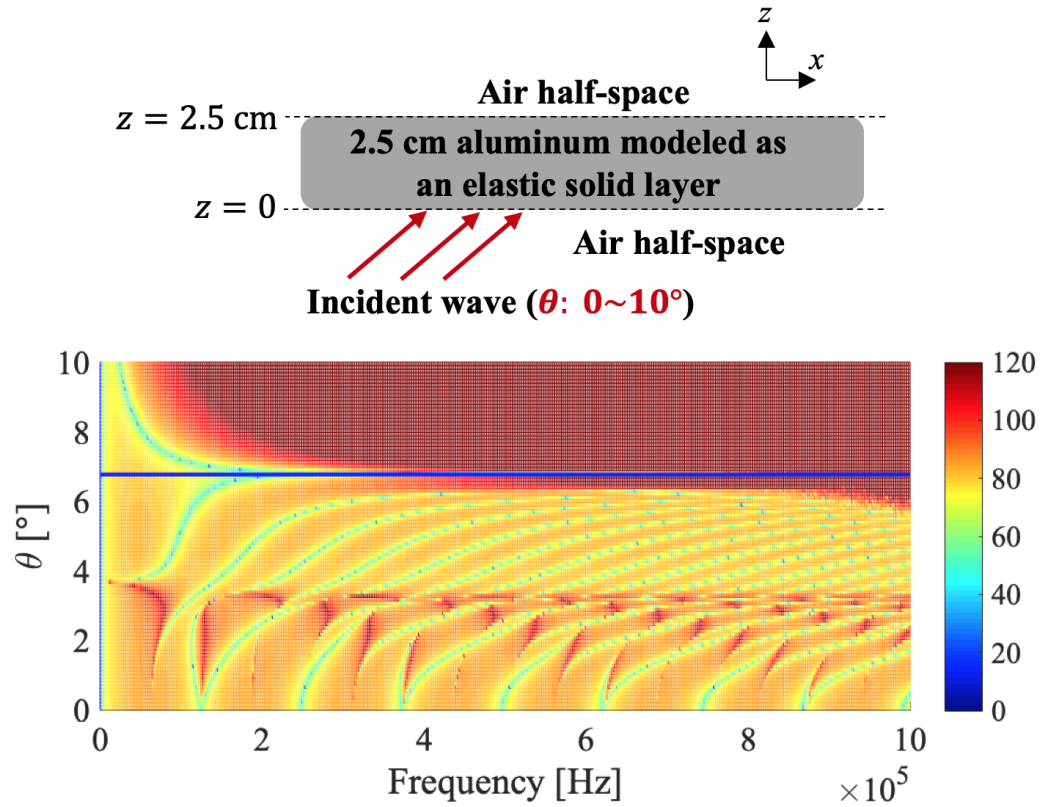


Figure 3.12. Structural resonances between Rayleigh waves below the Rayleigh angle (blue line) of an aluminum layer modeled as an elastic solid by the modified TMM model.

4. THE NEAR-FIELD DAMPING (NFD) MODEL

4.1 Introduction

In this chapter, the NFD modeling process is introduced in Sections 4.2, 4.3 and 4.4 by showing the derivation for the wavenumber and frequency domain responses of three different panel structures including an infinitely-extended (unconstrained) panel, a partially-constrained panel and a periodically-constrained panel. The process of combining the acoustical model, TMM or ACM, and the NFD model is described in Section 4.2 and Appendices B and C based on the unconstrained panel-involved configuration, which provides a connection between the bulk properties and damping performance of porous media. In Sections 4.2 and 4.3, the unconstrained and the partially-constrained panels were modeled, respectively, when driven by a harmonic line force excitation and with either a layer of limp porous or a poro-elastic damping treatment. In Section 4.4, the periodically-constrained panel was modeled as being driven by a distributed convective pressure wave excitation and with a layer of limp porous damping treatment to simulate a porous damping layer-treated aircraft fuselage structure. The process of Fourier transforming the wavenumber domain response to the spatial domain is introduced in Section 4.5, and the power analysis based on either wavenumber or spatial domain response is introduced in Section 4.6. Further, the NFD model validation process is shown in Section 4.7 based on the partially-constrained and periodically-constrained panel-involved cases.

4.2 A Layered Structure with a Harmonic Line Force-Driven, Infinitely-Extended Panel: the Incorporation of Acoustical Models

For unconstrained panel structures, as shown in Figures 4.1, 4.2 and 4.3 (*i.e.*, panels loaded by an acoustical medium on top and driven by a harmonic line force in

a vacuum beneath), the governing equation of motion for the transverse displacement, w_t , can be expressed in the time and space domain as

$$D \frac{\partial^4 w_t(x, t)}{\partial x^4} + m_s \frac{\partial^2 w_t(x, t)}{\partial t^2} = -p_1(x, t) + F e^{i\omega t} \delta(x). \quad (4.1)$$

where $m_s = \rho_p h_p$ is the mass per unit area of the panel based on its density, ρ_p , and thickness, h_p , and $D = [h_p^3 E_0 (1 + i\eta_p)] / [12(1 - \nu_p^2)]$ is the flexural stiffness per unit length in the y -direction of the panel based on h_p , the Young's modulus, E_0 , the loss factor, η_p , and the Poisson's ratio, ν_p . Note that η_p is the mechanical loss factor of the panel, which is distinct from either η_m or η_e mentioned in the Introduction. In addition, F is the forcing magnitude per unit length in the y -direction, and $\omega = 2\pi f$ is the excitation frequency. Further, the governing equation can be Fourier transformed to the frequency and wavenumber domain, and can be expressed in terms of ω and trace wavenumber, k_x , as

$$(Dk_x^4 - m_s \omega^2) w_t(k_x, \omega) = -p_1(k_x, \omega) + F, \quad (4.2)$$

At $z = 0$, the relation between the acoustic pressure, p_1 , and the acoustic particle velocity, v_{z1} , can be expressed as

$$p_1 = Z_{a1} v_{z1}, \quad (4.3)$$

where Z_{a1} is the normal acoustic impedance looking into the porous treatment: *i.e.*, a layer of limp porous or poro-elastic medium. At $z = d$, a similar relation relates the acoustic pressure, p_2 , and the acoustic particle velocity, v_{z2} : *i.e.*,

$$p_2 = Z_{a2} v_{z2}, \quad (4.4)$$

where Z_{a2} is the normal acoustic impedance looking into the acoustic half-space, *i.e.*, air, above the porous layer, which can be expressed as

$$Z_{a2}(k_x, \omega) = \frac{\omega \rho_0}{\sqrt{k_a^2 - k_x^2}}, \quad (4.5)$$

where ρ_0 is the density of air, and k_a is the complex wavenumber in the air expressed as

$$k_a = \frac{\omega(1 - i\eta_a)}{c_0}, \quad (4.6)$$

in terms of the angular frequency, ω , the speed of sound in the air, c_0 , and the loss factor of the air, η_a . Note that the air is here made slightly lossy to avoid a numerical issue, which will be discussed in Section 4.5.1 in connection with an example involving a unconstrained stiff panel that is directly loaded by an air half-space.

Therefore, the governing equation can be rewritten as

$$Z_m(k_x, \omega)v_t(k_x, \omega) = -Z_{a1}(k_x, \omega)v_{z1}(k_x, \omega) + F, \quad (4.7)$$

where Z_m is the mechanical impedance of the panel, which can be expressed as

$$Z_m(k_x, \omega) = i [\omega m_s - (D/\omega)k_x^4]. \quad (4.8)$$

Note that $v_{z1} = v_t = i\omega w_t$, due to the motion continuity between the panel and the porous layer.

When an unconstrained panel is loaded by a limp porous layer plus an air half-space as shown in Figure 4.1, the wavenumber domain velocity response of the panel can be expressed as

$$v_t(k_x, \omega) = v_{z1}(k_x, \omega) = \frac{F}{Z_m(k_x, \omega) + Z_{a1}(k_x, \omega)}, \quad (4.9)$$

where $v_t(k_x, \omega)$ together with $Z_{a1}(k_x, \omega)$ and $v_{z2}(k_x, \omega)$ can be implicitly solved by using the TMM model [21] given the bulk properties (σ , ϕ , ρ_b , d and α_∞) of the limp porous medium and the ambient properties (ρ_0 , η_a , c_0 , Prandtl number, B^2 , specific heat ratio, γ , and the dynamic viscosity of air, η). The details of that solution process are given in Appendix B.

If the limp porous layer is replaced by a poro-elastic layer as shown in Figure 4.2, and the layer is assumed to be bonded to the panel, then p_1 at $z = 0$ in Eq. (4.2) can be expressed as

$$p_1 = -s - \sigma_z + ik_x \frac{h_p}{2} \tau_{xz}, \quad (4.10)$$

and the boundary conditions at $z = 0$ can be expressed as

$$u_z = w_t, \quad (4.11a)$$

$$U_z = w_t, \quad (4.11b)$$

$$u_x = w_p + ik_x \frac{h_p}{2} w_t, \quad (4.11c)$$

$$\tau_{xz} = (D_p k_x^2 - m_s \omega^2) w_p, \quad (4.11d)$$

$$s + \sigma_z - ik_x \frac{h_p}{2} \tau_{xz} + F = (Dk_x^4 - m_s \omega^2) w_t, \quad (4.11e)$$

and at $z = d$ as

$$s = -\phi p_b, \quad (4.11f)$$

$$\sigma_z = -(1 - \phi) p_b, \quad (4.11g)$$

$$i\omega(1 - \phi)u_z + i\omega\phi U_z = v_{zb}, \quad (4.11h)$$

$$\tau_{xz} = 0, \quad (4.11i)$$

where w_t and w_p are the transverse and longitudinal displacements of the panel, respectively, $D_p = E_0 h_p$ is the longitudinal stiffness per unit length in the y -direction of the panel, u_z and U_z are the z -direction displacements for the solid and fluid phases of the poro-elastic medium, respectively, u_x is the x -direction displacement for the solid phase, τ_{xz} is the shear force per unit material area acting on the solid phase in the x - z plane, s is the force per unit material area acting on the fluid phase of the poro-elastic medium (opposite in sign to a pressure), σ_z is the force per unit material area acting on the solid phase of the poro-elastic medium in the z -direction,

and p_b and v_{zb} are the acoustic pressure and acoustic particle velocity when $z \geq d$, respectively.

If the connection between the poro-elastic layer and the panel is changed from “bonded” to “unbonded” as shown in Figure 4.3, and assuming that the layer is resting on the panel without any additional means of connection (*i.e.*, when it is assumed that the panel and poro-elastic layer are separated by a zero-depth airspace), then p_1 at $z = 0$ in Eq. (4.2) can be expressed as

$$p_1 = p_a, \quad (4.12)$$

and the boundary conditions at $z = 0$ can be expressed as

$$-p_a + F = (Dk_x^4 - m_s\omega^2) w_t, \quad (4.13a)$$

$$v_{za} = i\omega w_t, \quad (4.13b)$$

$$s = -\phi p_a, \quad (4.13c)$$

$$\sigma_z = -(1 - \phi)p_a, \quad (4.13d)$$

$$i\omega(1 - \phi)u_z + i\omega\phi U_z = v_{za}, \quad (4.13e)$$

$$\tau_{xz} = 0, \quad (4.13f)$$

and at $z = d$ as

$$s = -\phi p_b, \quad (4.13g)$$

$$\sigma_z = -(1 - \phi)p_b, \quad (4.13h)$$

$$i\omega(1 - \phi)u_z + i\omega\phi U_z = v_{zb}, \quad (4.13i)$$

$$\tau_{xz} = 0, \quad (4.13j)$$

where p_a and v_{za} are the acoustic pressure and acoustic particle velocity, respectively, in the infinitesimal space between the panel and the poro-elastic layer when they are unbonded.

The wavenumber domain velocity response of the panel for a poro-elastic medium-involved case (either bonded or unbonded) can then be expressed as

$$v_t(k_x, \omega) = v_{z1}(k_x, \omega) = i\omega w_t(k_x, \omega), \quad (4.14)$$

where $w_t(k_x, \omega)$ together with $Z_{a1}(k_x, \omega)$ and $v_{z2}(k_x, \omega)$ can be evaluated explicitly by using the ACM model [18] given the bulk properties (σ , ϕ , ρ_b , d , α_∞ , E_1 , ν and η_m) of the poro-elastic medium and the ambient properties (ρ_0 , η_a , c_0 , B^2 , γ and η). The details of that solution process are included in Appendix C.

4.3 A More Realistic Structure with a Harmonic Line Force-Driven, Partially-Constrained Panel

To create a more realistic scenario, two identical constraints both with finite translational inertia, m_l , and finite rotational inertia, J_l , were then added to the panel structure to make it partially-constrained as shown in Figures 4.4 and 4.5. The governing equation of the partially-constrained layered structure can then be formed by adding the reaction force term, f_r , to Eq. (4.1), as in

$$D \frac{\partial^4 w_t(x, t)}{\partial x^4} + m_s \frac{\partial^2 w_t(x, t)}{\partial t^2} = -p_1(x, t) + F e^{i\omega t} \delta(x) + f_r(x, t), \quad (4.15)$$

where f_r can be expressed as a summation of the reaction forces due to the translational and rotational inertias of the two identical constraints as

$$f_r(x, t) = \sum_{j=1}^2 \left(-m_l \frac{\partial^2 w_t(x, t)}{\partial t^2} \right) \delta(x - x_{l,j}) + \sum_{j=1}^2 \left(-J_l \frac{\partial^2 \theta(x, t)}{\partial t^2} \right) \delta'(x - x_{l,j}), \quad (4.16)$$

and where $x_{l,j}$ is the location of each constraint, and $\theta = \partial w_t / \partial x = -ik_x w_t$ is the angular displacement of the panel.

By Fourier transforming Eq. (4.15) from the time and space domain to the frequency and wavenumber domain, the governing equation can be expressed as

$$Z_m(k_x, \omega) v_t(k_x, \omega) = -Z_{a1}(k_x, \omega) v_{z1}(k_x, \omega) + F + f_r(k_x, \omega), \quad (4.17)$$

where Z_m (by using Eq. (4.8)) and Z_{a1} (either by using Eq. (B.2) for the limp layer case, or by using Eq. (C.19) for the elastic layer case) can both be evaluated based on the unconstrained calculation routine described in Section 4.2. Then the motion continuity: *i.e.*, $v_t = v_{z1}$, and the relation between the linear and angular velocities of the panel: *i.e.*, $\dot{\theta} = -ik_x v_t$, can be applied to Eq. (4.17) to derive the wavenumber domain linear and angular velocity responses of the panel

$$v_t(k_x, \omega) = v_{z1}(k_x, \omega) = \frac{F + f_r(k_x, \omega)}{Z_m(k_x, \omega) + Z_{a1}(k_x, \omega)}, \quad (4.18a)$$

$$\dot{\theta}(k_x, \omega) = -ik_x v_t(k_x, \omega) = -ik_x \frac{F + f_r(k_x, \omega)}{Z_m(k_x, \omega) + Z_{a1}(k_x, \omega)}, \quad (4.18b)$$

with

$$f_r(k_x, \omega) = -i\omega m_l \sum_{j=1}^2 v_t(x_{l,j}, \omega) e^{ik_x x_{l,j}} - k_x \omega J_l \sum_{j=1}^2 \dot{\theta}(x_{l,j}, \omega) e^{ik_x x_{l,j}}. \quad (4.19)$$

Equations (4.18a) and (4.18b) can be inverse wavenumber Fourier transformed at $x = x_{l,1}$ and $x = x_{l,2}$ to obtain

$$v_t(x_{l,1}, \omega) = \frac{1}{2\pi} \int_{-\infty}^{+\infty} \frac{F + f_r(k_x, \omega)}{Z_m(k_x, \omega) + Z_{a1}(k_x, \omega)} e^{-ik_x x_{l,1}} dk_x, \quad (4.20a)$$

$$v_t(x_{l,2}, \omega) = \frac{1}{2\pi} \int_{-\infty}^{+\infty} \frac{F + f_r(k_x, \omega)}{Z_m(k_x, \omega) + Z_{a1}(k_x, \omega)} e^{-ik_x x_{l,2}} dk_x, \quad (4.20b)$$

$$\dot{\theta}(x_{l,1}, \omega) = \frac{-i}{2\pi} \int_{-\infty}^{+\infty} k_x \frac{F + f_r(k_x, \omega)}{Z_m(k_x, \omega) + Z_{a1}(k_x, \omega)} e^{-ik_x x_{l,1}} dk_x, \quad (4.20c)$$

$$\dot{\theta}(x_{l,2}, \omega) = \frac{-i}{2\pi} \int_{-\infty}^{+\infty} k_x \frac{F + f_r(k_x, \omega)}{Z_m(k_x, \omega) + Z_{a1}(k_x, \omega)} e^{-ik_x x_{l,2}} dk_x, \quad (4.20d)$$

then a system of equations can be formed by substituting Eq. (4.19) into Eqs. (4.20) to obtain

$$[\mathbf{N}] [\mathbf{Y}] = [\mathbf{K}]. \quad (4.21)$$

Here $[\mathbf{Y}]$ is a 4×1 vector of unknown constraint responses, and

$$[\mathbf{Y}]^T = \begin{bmatrix} v_t(x_{l,1}, \omega) & v_t(x_{l,2}, \omega) & \dot{\theta}(x_{l,1}, \omega) & \dot{\theta}(x_{l,2}, \omega) \end{bmatrix}, \quad (4.22)$$

and $[\mathbf{N}]$ is a 4×4 coefficient matrix, where

$$\mathbf{N}(1, 1) = -i\omega m_l \int_{-\infty}^{+\infty} \frac{1}{Z_m(k_x, \omega) + Z_{a1}(k_x, \omega)} dk_x - 2\pi, \quad (4.23a)$$

$$\mathbf{N}(1, 2) = -i\omega m_l \int_{-\infty}^{+\infty} \frac{e^{ik_x(x_{l,2}-x_{l,1})}}{Z_m(k_x, \omega) + Z_{a1}(k_x, \omega)} dk_x, \quad (4.23b)$$

$$\mathbf{N}(1, 3) = -\omega J_l \int_{-\infty}^{+\infty} \frac{k_x}{Z_m(k_x, \omega) + Z_{a1}(k_x, \omega)} dk_x, \quad (4.23c)$$

$$\mathbf{N}(1, 4) = -\omega J_l \int_{-\infty}^{+\infty} \frac{k_x e^{ik_x(x_{l,2}-x_{l,1})}}{Z_m(k_x, \omega) + Z_{a1}(k_x, \omega)} dk_x, \quad (4.23d)$$

$$\mathbf{N}(2, 1) = -i\omega m_l \int_{-\infty}^{+\infty} \frac{e^{-ik_x(x_{l,2}-x_{l,1})}}{Z_m(k_x, \omega) + Z_{a1}(k_x, \omega)} dk_x, \quad (4.23e)$$

$$\mathbf{N}(2, 2) = -i\omega m_l \int_{-\infty}^{+\infty} \frac{1}{Z_m(k_x, \omega) + Z_{a1}(k_x, \omega)} dk_x - 2\pi, \quad (4.23f)$$

$$\mathbf{N}(2, 3) = -\omega J_l \int_{-\infty}^{+\infty} \frac{k_x e^{-ik_x(x_{l,2}-x_{l,1})}}{Z_m(k_x, \omega) + Z_{a1}(k_x, \omega)} dk_x, \quad (4.23g)$$

$$\mathbf{N}(2, 4) = -\omega J_l \int_{-\infty}^{+\infty} \frac{k_x}{Z_m(k_x, \omega) + Z_{a1}(k_x, \omega)} dk_x, \quad (4.23h)$$

$$\mathbf{N}(3, 1) = -\omega m_l \int_{-\infty}^{+\infty} \frac{k_x}{Z_m(k_x, \omega) + Z_{a1}(k_x, \omega)} dk_x, \quad (4.23i)$$

$$\mathbf{N}(3, 2) = -\omega m_l \int_{-\infty}^{+\infty} \frac{k_x e^{ik_x(x_{l,2}-x_{l,1})}}{Z_m(k_x, \omega) + Z_{a1}(k_x, \omega)} dk_x, \quad (4.23j)$$

$$\mathbf{N}(3, 3) = i\omega J_l \int_{-\infty}^{+\infty} \frac{k_x^2}{Z_m(k_x, \omega) + Z_{a1}(k_x, \omega)} dk_x - 2\pi, \quad (4.23k)$$

$$\mathbf{N}(3, 4) = i\omega J_l \int_{-\infty}^{+\infty} \frac{k_x^2 e^{ik_x(x_{l,2}-x_{l,1})}}{Z_m(k_x, \omega) + Z_{a1}(k_x, \omega)} dk_x, \quad (4.23l)$$

$$\mathbf{N}(4, 1) = -\omega m_l \int_{-\infty}^{+\infty} \frac{k_x e^{-ik_x(x_{l,2}-x_{l,1})}}{Z_m(k_x, \omega) + Z_{a1}(k_x, \omega)} dk_x, \quad (4.23m)$$

$$\mathbf{N}(4, 2) = -\omega m_l \int_{-\infty}^{+\infty} \frac{k_x}{Z_m(k_x, \omega) + Z_{a1}(k_x, \omega)} dk_x, \quad (4.23n)$$

$$\mathbf{N}(4, 3) = i\omega J_l \int_{-\infty}^{+\infty} \frac{k_x^2 e^{-ik_x(x_{l,2}-x_{l,1})}}{Z_m(k_x, \omega) + Z_{a1}(k_x, \omega)} dk_x, \quad (4.23o)$$

$$\mathbf{N}(4, 4) = i\omega J_l \int_{-\infty}^{+\infty} \frac{k_x^2}{Z_m(k_x, \omega) + Z_{a1}(k_x, \omega)} dk_x - 2\pi. \quad (4.23p)$$

Also $[\mathbf{K}]$ is a 4×1 forcing vector, and

$$\mathbf{K}(1, 1) = -F \int_{-\infty}^{+\infty} \frac{e^{-ik_x x_{l,1}}}{Z_m(k_x, \omega) + Z_{a1}(k_x, \omega)} dk_x, \quad (4.24a)$$

$$\mathbf{K}(2, 1) = -F \int_{-\infty}^{+\infty} \frac{e^{-ik_x x_{l,2}}}{Z_m(k_x, \omega) + Z_{a1}(k_x, \omega)} dk_x, \quad (4.24b)$$

$$\mathbf{K}(3, 1) = iF \int_{-\infty}^{+\infty} \frac{k_x e^{-ik_x x_{l,1}}}{Z_m(k_x, \omega) + Z_{a1}(k_x, \omega)} dk_x, \quad (4.24c)$$

$$\mathbf{K}(4, 1) = iF \int_{-\infty}^{+\infty} \frac{k_x e^{-ik_x x_{l,2}}}{Z_m(k_x, \omega) + Z_{a1}(k_x, \omega)} dk_x. \quad (4.24d)$$

The constraint responses in $[\mathbf{Y}]$ can be evaluated as

$$[\mathbf{Y}] = [\mathbf{N}]^{-1} [\mathbf{K}], \quad (4.25)$$

and the wavenumber domain velocity response of the partially-constrained structure can be evaluated by substituting the constraint responses into Eqs. (4.19) and (4.18a).

4.4 A Fuselage-Like Structure with a Convective Pressure-Driven, Periodically-Constrained Panel

Previously, the NFD modeling has been demonstrated for line-driven, infinite panels and panels with isolated constraints. In this section, the focus is instead on presenting the modeling process of periodically-constrained panels driven into motion by a distributed convective pressure wave as shown in Figure 4.6. The constraints were allowed to have finite translational and rotational inertias and stiffnesses, and were uniformly distributed along the panel to create a panel with frames. This arrangement was intended to represent a very simple model of an aircraft fuselage structure like the one shown in Figure 4.7(a) [5]. And the fuselage acoustical treatment as shown in Figure 4.7(b) [65] was modeled here as limp porous layer for near-field damping purposes. Note that previous studies [66–69] have relied on modeling a periodic structure by using various different methods, such as the principle of virtual work, for example, while here the periodic structure was modeled based on the equation of motion of the panel in order both to conveniently incorporate the NFD model and to allow the use of the Inverse Discrete Fourier Transform (IDFT) in the analysis [22], which has already proven to be an efficient tool when analyzing the spatial and frequency responses of layered vibrating structures.

Based on the configurations shown in Figure 4.6, the periodically-constrained panel was modeled being loaded by a layer of limp porous material, and a half-space of air above the layer. Instead of a harmonic line force as used previously, a convective pressure was considered to exist below the panel to simulate a boundary layer excitation of the outer surface of the fuselage. The constraints were modeled as having identical translational inertias per unit length in the y -direction, m_l , translational stiffnesses per unit length in the y -direction, k_l , rotational inertias per unit length in the y -direction, J_l , and rotational stiffnesses per unit length in the y -direction, s_l . Based on the Euler-Bernoulli beam theory and the acoustical theory applied in the

NFD model, the governing equation of motion for the panel transverse displacement can now be expressed as

$$D \frac{\partial^4 w_t(x, t)}{\partial x^4} + m_s \frac{\partial^2 w_t(x, t)}{\partial t^2} = -p_1(x, t) + f_{\text{in}}(x, t) + f_{\text{re}}(x, t), \quad (4.26)$$

where the input forcing term, f_{in} , due to the convective pressure excitation can be expressed as

$$f_{\text{in}}(x, t) = P e^{+i\omega t} e^{-ik_v x}, \quad (4.27)$$

where P is the forcing magnitude per unit area of the panel, ω is the angular frequency, and k_v the convective wavenumber, which is expressed as

$$k_v = \frac{\omega}{Mc_0}, \quad (4.28)$$

indicating a subsonic excitation when the Mach number, $M < 1$, and a supersonic excitation when $M > 1$. The reaction force term, f_{re} , can be expressed as a summation of the reaction forces due to the translational and rotational inertias and stiffnesses of the periodic constraints as

$$\begin{aligned} f_{\text{re}}(x, t) = & \sum_{j=1}^{N_l} \left[-m_l \frac{\partial^2 w_t(x, t)}{\partial t^2} - k_l w_t(x, t) \right] \delta(x - x_{l,j}) \\ & + \sum_{j=1}^{N_l} \left[-J_l \frac{\partial^2 \theta(x, t)}{\partial t^2} - s_l \theta(x, t) \right] \delta'(x - x_{l,j}), \end{aligned} \quad (4.29)$$

where N_l is the total number of the constraints, $x_{l,j}$ is the location of each constraint, and $\theta = \partial w_t / \partial x = -ik_x w_t$.

By substituting equations (4.27) and (4.29) into equation (4.26), the governing equation can then be rewritten as

$$\begin{aligned} D \frac{\partial^4 w_t(x, t)}{\partial x^4} + m_s \frac{\partial^2 w_t(x, t)}{\partial t^2} = & -p_1(x, t) + P e^{+i\omega t} e^{-ik_v x} \\ & + \sum_{j=1}^{N_l} \left[-m_l \frac{\partial^2 w_t(x, t)}{\partial t^2} - k_l w_t(x, t) \right] \delta(x - x_{l,j}) \\ & + \sum_{j=1}^{N_l} \left[-J_l \frac{\partial^2 \theta(x, t)}{\partial t^2} - s_l \theta(x, t) \right] \delta'(x - x_{l,j}). \end{aligned} \quad (4.30)$$

Then by Fourier transforming equation (4.30) from the time domain to the frequency domain, and forward wavenumber Fourier transforming from the spatial domain to the wavenumber domain, the governing equation can be expressed as

$$Z_m(k_x, \omega)v_t(k_x, \omega) = -Z_{a1}(k_x, \omega)v_{z1}(k_x, \omega) + 2\pi P\delta(k_x - k_v) - i\left(\omega m_l - \frac{k_l}{\omega}\right) \sum_{j=1}^{N_l} v_t(x_{l,j}, \omega)e^{ik_x x_{l,j}} - k_x \left(\omega J_l - \frac{s_l}{\omega}\right) \sum_{j=1}^{N_l} \dot{\theta}(x_{l,j}, \omega)e^{ik_x x_{l,j}}, \quad (4.31)$$

where Z_m (by using Eq. (4.8)) and Z_{a1} (by using Eq. (B.2) for the limp layer case) can both be evaluated based on the unconstrained calculation routine described in Section 4.2.

The relation between the linear and angular velocities of the panel, $\dot{\theta} = -ik_x v_t$, and the motion continuity, $v_{z1} = v_t$, can then be applied to Eq. (4.31), and the wavenumber domain linear and angular velocity responses of the panel can be expressed as

$$v_t(k_x, \omega) = \frac{2\pi P\delta(k_x - k_v) + f_{\text{re}}(k_x, \omega)}{Z_m(k_x, \omega) + Z_{a1}(k_x, \omega)}, \quad (4.32a)$$

$$\dot{\theta}(k_x, \omega) = -ik_x \frac{2\pi P\delta(k_x - k_v) + f_{\text{re}}(k_x, \omega)}{Z_m(k_x, \omega) + Z_{a1}(k_x, \omega)}, \quad (4.32b)$$

with

$$f_{\text{re}}(k_x, \omega) = -i\left(\omega m_l - \frac{k_l}{\omega}\right) \sum_{j=1}^{N_l} v_t(x_{l,j}, \omega)e^{ik_x x_{l,j}} - k_x \left(\omega J_l - \frac{s_l}{\omega}\right) \sum_{j=1}^{N_l} \dot{\theta}(x_{l,j}, \omega)e^{ik_x x_{l,j}}. \quad (4.33)$$

In order to evaluate $v_t(k_x, \omega)$, all the constraint responses, $v_t(x_{l,j}, \omega)$ and $\dot{\theta}(x_{l,j}, \omega)$, need to be evaluated first. Since the periodic structure has uniformly-spaced, identical constraints, it can be assumed that the responses of all the constraints must have the

same amplitude, but any two adjacent constraint responses differ in phase by $e^{-ik_v l}$, with l being the constraint separation [66]. Equation (4.33) can then be rewritten as

$$f_{\text{re}}(k_x, \omega) = \left[-i \left(\omega m_l - \frac{k_l}{\omega} \right) v_t(x_{l,1}, \omega) - k_x \left(\omega J_l - \frac{s_l}{\omega} \right) \dot{\theta}(x_{l,1}, \omega) \right] \sum_{j=1}^{N_l} e^{ik_x x_{l,j} - ik_v(x_{l,j} - x_{l,1})}, \quad (4.34)$$

with the constraint at $x = x_{l,1}$ being the base point to which all the other constraints are referred: thus, there are just two unknown constraint responses, $v_t(x_{l,1}, \omega)$ and $\dot{\theta}(x_{l,1}, \omega)$.

Further, Eqs. (4.32a) and (4.32b) can be inverse Fourier transformed at $x = x_{l,1}$ to obtain

$$v_t(x_{l,1}, \omega) = \frac{1}{2\pi} \int_{-\infty}^{+\infty} \frac{2\pi P \delta(k_x - k_v) + f_{\text{re}}(k_x, \omega)}{Z_m(k_x, \omega) + Z_{a1}(k_x, \omega)} e^{-ik_x x_{l,1}} dk_x, \quad (4.35a)$$

$$\dot{\theta}(x_{l,1}, \omega) = \frac{-i}{2\pi} \int_{-\infty}^{+\infty} k_x \frac{2\pi P \delta(k_x - k_v) + f_{\text{re}}(k_x, \omega)}{Z_m(k_x, \omega) + Z_{a1}(k_x, \omega)} e^{-ik_x x_{l,1}} dk_x. \quad (4.35b)$$

Then a system of equations can be formed by substituting Eq. (4.34) into Eqs. (4.35) to obtain

$$N_{11} v_t(x_{l,1}, \omega) + N_{12} \dot{\theta}(x_{l,1}, \omega) = K_1, \quad (4.36a)$$

$$N_{21} v_t(x_{l,1}, \omega) + N_{22} \dot{\theta}(x_{l,1}, \omega) = K_2, \quad (4.36b)$$

with

$$N_{11} = -i \left(\omega m_l - \frac{k_l}{\omega} \right) \int_{-\infty}^{+\infty} \frac{\sum_{j=1}^{N_l} e^{i(k_x - k_v)(x_{l,j} - x_{l,1})}}{Z_m(k_x, \omega) + Z_{a1}(k_x, \omega)} dk_x - 2\pi, \quad (4.37a)$$

$$N_{12} = - \left(\omega J_l - \frac{s_l}{\omega} \right) \int_{-\infty}^{+\infty} \frac{k_x \sum_{j=1}^{N_l} e^{i(k_x - k_v)(x_{l,j} - x_{l,1})}}{Z_m(k_x, \omega) + Z_{a1}(k_x, \omega)} dk_x, \quad (4.37b)$$

$$N_{21} = - \left(\omega m_l - \frac{k_l}{\omega} \right) \int_{-\infty}^{+\infty} \frac{k_x \sum_{j=1}^{N_l} e^{i(k_x - k_v)(x_{l,j} - x_{l,1})}}{Z_m(k_x, \omega) + Z_{a1}(k_x, \omega)} dk_x, \quad (4.37c)$$

$$N_{22} = i \left(\omega J_l - \frac{s_l}{\omega} \right) \int_{-\infty}^{+\infty} \frac{k_x^2 \sum_{j=1}^{N_l} e^{i(k_x - k_v)(x_{l,j} - x_{l,1})}}{Z_m(k_x, \omega) + Z_{a1}(k_x, \omega)} dk_x - 2\pi, \quad (4.37d)$$

$$K_1 = -2\pi P \int_{-\infty}^{+\infty} \frac{e^{-ik_x x_{l,1}}}{Z_m(k_x, \omega) + Z_{a1}(k_x, \omega)} \delta(k_x - k_v) dk_x, \quad (4.37e)$$

$$K_2 = i2\pi P \int_{-\infty}^{+\infty} \frac{k_x e^{-ik_x x_{l,1}}}{Z_m(k_x, \omega) + Z_{a1}(k_x, \omega)} \delta(k_x - k_v) dk_x. \quad (4.37f)$$

Now, $v_t(x_{l,1}, \omega)$ and $\dot{\theta}(x_{l,1}, \omega)$ can be evaluated by calculating all the coefficients in Eq. (4.37), and by substituting those coefficients into Eq. (4.36). Finally, the wavenumber domain transverse velocity response, $v_t(k_x, \omega)$, can be evaluated by using Eqs. (4.32a) and (4.34) along with the constraint responses, $v_t(x_{l,1}, \omega)$ and $\dot{\theta}(x_{l,1}, \omega)$.

4.5 Wavenumber Response Inverse Discrete Fourier Transform (IDFT) for the Spatial Response of the Panel

Based on the wavenumber domain response acquired in previous sections, the spatial domain response can be evaluated by using the IDFT [22], given properly-chosen sampling rates, γ_s 's, and number of sampling points, N_s , at each frequency, as

$$G(m\Delta x, \omega) = \frac{1}{N_s \Delta x} \sum_{n=0}^{N_s-1} G(n\Delta k_x, \omega) e^{\frac{-i2\pi mn}{N_s}}, \quad (4.38)$$

where

$$\Delta x = \frac{2\pi}{\gamma_s}, \quad (4.39)$$

and

$$\Delta k_x = \frac{\gamma_s}{N_s}. \quad (4.40)$$

Note that G can be a discretized function of v_t , Z_m , v_{z1} , v_{z2} , Z_{a1} , Z_{a2} , p_1 or p_2 depending on the actual requirements. Also note that $N_s = 2^{14}$ for all the calculations in this thesis to ensure a large enough sampling points number, and γ_s 's were chosen

based on appropriate cutoff levels at each frequency, which is further introduced in Section 4.5.1 based on the evaluation of the wavenumber domain velocity levels of three different kinds of panel structures.

4.5.1 Choices of Sampling Rates

According to Ref. [22], different γ_s 's should be chosen at different driving frequencies for the evaluation of the IDFT to avoid windowing or truncation effects. The NFD model was developed here to be capable of automatically adjusting the sampling rates when the input driving frequency is varied over a wide range, so that the spatial response of the panel can be observe at dispersive frequencies without significant bias.

Based on the configuration as shown in Figure 4.8, an example based on a 3 mm thick, harmonic line force-driven, unconstrained aluminum panel is presented here to address the sampling rates self-adjusting process. In this case, the panel was directly loaded by an air half-space, which means the normal acoustic impedance at $z = 0$ is equal to the normal acoustic impedance of the air: *i.e.*, $Z_{a1} = Z_{a2}$. Given $h_p = 3$ mm, $F = 1$ N/m, and the input properties listed in Tables 4.1 and 4.2, the wavenumber domain velocity response, $v_t(k_x, \omega)$, of the panel was evaluated by using Eqs. (4.9) and (4.5) over a wide range of trace wavenumbers, k_x (*i.e.*, evenly-discretized into 2^{14} points from -500 to 500 rad/m), and over a wide range of temporal frequencies, f (*i.e.*, at 500 different frequencies equally-spaced from 10 to 10000 Hz), and the result in terms of the velocity level, $20 \log_{10} |v_t(k_x, \omega)|$, is plotted in Figure 4.9, based on which a cutoff level (*e.g.*, -130 dB) can be selected as shown in Figure 4.10. The values of the required γ_s 's can finally be selected based on the cutoff level for each frequency as shown in Figure 4.11.

The example here also helps to explain the reason why the air was made slightly dissipative by including η_a (which is usually much smaller than unity) in k_a . Without η_a , $k_a = \omega/c_0$ will be purely real, and the z -direction wavenumber in the air, $k_{za} = (k_a^2 - k_x^2)^{1/2}$, will be purely imaginary when $k_a < k_x$. In this case, a negative sign of

the square root must be selected for k_{za} so that $k_{za} = -i(k_x^2 - k_a^2)^{1/2}$ to ensure that the disturbance decays (rather than grows) exponentially in the panel near-field [70]. By adding the loss factor, k_a and k_{za} are both made complex in such a way that a decay in the positive z -direction is ensured.

The sampling rates self-adjusting process was then repeated for another example with a 1 mm thick, harmonic line force-driven, partially-clamped panel (by assigning two large and heavy constraints) directly loaded by an air half-space. To be more specific, given $h_p = 1$ mm, $F = 1$ N/m, and the input properties listed in Tables 4.1, 4.2 and 4.3, the wavenumber domain velocity response, $v_t(k_x, \omega)$, of the panel was evaluated by using Eq. (4.18a) over a wide range of trace wavenumbers, k_x (*i.e.*, evenly-discretized into 2^{14} points from -500 to 500 rad/m), and over a wide range of temporal frequencies, f (*i.e.*, at 500 different frequencies equally-spaced from 10 to 10000 Hz), and the wavenumber domain velocity level, $20 \log_{10} |v_t(k_x, \omega)|$, is plotted in Figure 4.13, from which the sampling rates, γ_s 's, at each frequency were selected based on a fixed cutoff level, *e.g.*, -200 dB, are marked as the magenta solid line.

A similar sampling rates self-adjusting process was further conducted for an example with a 1 mm thick, subsonic convective pressure-driven, periodically-clamped panel (by assigning periodic large and heavy constraints) directly loaded by an air half-space. To be more specific, given $h_p = 1$ mm, $P = 1$ N/m², $M = 0.8$, and the input properties listed in Tables 4.1, 4.2 and 4.4, the wavenumber domain velocity response, $v_t(k_x, \omega)$, of the panel was evaluated by using Eq. (4.32a) over a wide range of trace wavenumbers, k_x (*i.e.*, evenly-discretized into 2^{14} points from -6000 to 6000 rad/m), and over a wide range of temporal frequencies, f (*i.e.*, at 500 different frequencies equally-spaced from 10 to 10000 Hz), and the wavenumber domain velocity level, $20 \log_{10} |v_t(k_x, \omega)|$, is plotted in Figure 4.15, based on which the original wavenumber domain sampling rates, γ_{or} 's (black solid line), at each frequency were based on a fixed cutoff level, *e.g.*, -300 dB, but the γ_{or} 's were just raw estimates of the sampling rates needed to minimize bias due to windowing and truncation effects. These sampling rates were then further adjusted to the closest sampling rates that

corresponded to an integer spatial span, x_{span} (*i.e.*, a multiple of the constraint separation), which ensures that the IDFT is conducted on a complete periodic structure. The adjusted sampling rates, γ_s 's, are marked as the magenta dashed line in Figure 4.15. According to the adjusted x_{span} , the constraint locations, $x_{l,j}$, were assigned at ± 0.5 m, ± 1.5 m, ..., $\pm(|x_{\text{span}}|/2 - 0.5)$ m. Note that in all the calculation routines used in this model, k_v is always first evaluated by using Eq. (4.28), and is then approximated by the closest wavenumber from the sampled k_x array. This approximation also ensures that the IDFT is conducted on a complete periodic structure by making x_{span} an integer multiple of the excitation wavelength. And in this case, Eqs. (4.39) and (4.40) can be rewritten as

$$\Delta x = \frac{2\pi}{\gamma_s} = \frac{x_{\text{span}}}{N_s}, \quad (4.41)$$

and

$$\Delta k_x = \frac{\gamma_s}{N_s} = \frac{2\pi}{x_{\text{span}}}. \quad (4.42)$$

4.5.2 Identification of Conventional Panel Critical Frequencies

The conventional critical frequency, f_c , for the panel (regardless if the panel is constrained or unconstrained) can be evaluated as

$$f_c = \frac{(c_0)^2}{2\pi} \sqrt{\frac{m_s}{\text{Re}(D)}}. \quad (4.43)$$

and is identified as shown in Figure 4.16 (*i.e.*, for a 3 mm aluminum panel in this example, $f_c = 4008.4$ Hz). The conventional critical frequency separates the supersonic and sub-critical regions. Note that the damping provided by the porous layer was mainly due to the viscous interaction between the near-field evanescent acoustical motion that results from the sub-critical panel motion. Thus, the panel damping is mainly effective within the sub-critical frequency region. On the other hand, a spatial resonance occurs in the supersonic region when the trace wave speed in the air and the free flexural wave speed of the panel match each other. Therefore, the identifi-

cation of f_c helps to verify and understand the acoustical and damping phenomena observed in different frequency regions (see Section 5.2).

Besides, if the panel is excited by a convective pressure wave, the intersection between the excitation line and the panel wavenumber domain dispersion curves corresponds to the convective critical frequency, f_{cv} , which shifts with the increase of M , and which can be calculated using the equation

$$f_{cv} = \frac{(Mc_0)^2}{2\pi} \sqrt{\frac{m_s}{\text{Re}(D)}}. \quad (4.44)$$

The comparison between f_c and f_{cv} will be discussed in Section 5.4.1.

4.6 Power Analysis

4.6.1 Power Distribution in a Layered Structure

The power distribution within the layered structure can be analyzed based on either spatial or wavenumber domain responses.

The input power per unit length in the y -direction for a line-driven structure can be evaluated as

$$P_{\text{inp}}(\omega) = \frac{1}{2} \text{Re} (Fv_t^*(x=0, \omega)) = \frac{1}{4\pi} \text{Re} \left(\sum_{j=1}^{N_s} Fv_t^*(k_{x,j}, \omega) \right) \Delta k_x. \quad (4.45)$$

For a convective pressure-driven structure, the input power per unit length in the y -direction, on the other hand, can be evaluated as

$$\begin{aligned} P_{\text{inp}}(\omega) &= \frac{1}{2} \text{Re} \left(\sum_{j=1}^{N_s} P e^{-ik_v x_j} v_t^*(x_j, \omega) \right) \Delta x = \frac{1}{4\pi} \text{Re} (2\pi P v_t(k_v, \omega)) \\ &= \frac{1}{4\pi} \text{Re} \left(\sum_{j=1}^{N_s} [Z_{a1}(k_{x,j}, \omega) + Z_m(k_{x,j}, \omega)] |v_t(k_{x,j}, \omega)|^2 \right) \Delta k_x. \end{aligned} \quad (4.46)$$

The power radiation per unit length in the y -direction from the panel to the (limp or elastic) porous layer above it can be evaluated by using either spatial or the wavenumber domain integrations as

$$P_1(\omega) = \frac{1}{2} \text{Re} \left(\sum_{j=1}^{N_s} p_1(x_j, \omega) v_{z1}^*(x_j, \omega) \right) \Delta x, \quad (4.47a)$$

or

$$\begin{aligned} P_1(\omega) &= \frac{1}{4\pi} \operatorname{Re} \left(\sum_{j=1}^{N_s} p_1(k_{x,j}, \omega) v_{z1}^*(k_{x,j}, \omega) \right) \Delta k_x \\ &= \frac{1}{4\pi} \operatorname{Re} \left(\sum_{j=1}^{N_s} Z_{a1}(k_{x,j}, \omega) |v_{z1}(k_{x,j}, \omega)|^2 \right) \Delta k_x. \end{aligned} \quad (4.47b)$$

To be more specific, P_1 for a bonded poro-elastic layer case can be divided into three parts, and be expressed as

$$P_1(\omega) = P_{1,s}(\omega) + P_{1,\sigma}(\omega) + P_{1,\tau}(\omega), \quad (4.48)$$

where

$$P_{1,s}(\omega) = \frac{1}{4\pi} \operatorname{Re} \left(\sum_{j=1}^{N_s} -s(k_{x,j}, \omega) v_{z1}^*(k_{x,j}, \omega) \right) \Delta k_x, \quad (4.49)$$

is the power radiating into the fluid phase of the poro-elastic medium,

$$P_{1,\sigma}(\omega) = \frac{1}{4\pi} \operatorname{Re} \left[\sum_{j=1}^{N_s} \left(-\sigma_z(k_{x,j}, \omega) + ik_x \frac{h_p}{2} \tau_{xz}(k_{x,j}, \omega) \right) v_{z1}^*(k_{x,j}, \omega) \right] \Delta k_x, \quad (4.50)$$

is the power radiating into the solid phase of the poro-elastic medium *via* normal direction motion, and

$$P_{1,\tau}(\omega) = \frac{1}{4\pi} \operatorname{Re} \left[\sum_{j=1}^{N_s} \tau_{xz}(k_{x,j}, \omega) (i\omega u_x(k_{x,j}, \omega))^* \right] \Delta k_x, \quad (4.51)$$

is the power radiating into the solid phase of the poro-elastic medium *via* in-plane panel motion. The frequency and wavenumber domain field variables u_x , τ_{xz} , s , and σ_z , can all be evaluated at $z = 0$ by substituting the ACM-solved complex amplitude coefficients (C_1 to C_6) into Eqs. (C.3), (C.4), (C.5) and (C.6), respectively. The power radiation per unit length in the y -direction from the top surface of the (limp or elastic) porous layer to the acoustic half-space above it can be evaluated by using either spatial or wavenumber domain integrations as

$$P_2(\omega) = \frac{1}{2} \operatorname{Re} \left(\sum_{j=1}^{N_s} p_2(x_j, \omega) v_{z2}^*(x_j, \omega) \right) \Delta x, \quad (4.52a)$$

or

$$\begin{aligned}
 P_2(\omega) &= \frac{1}{4\pi} \operatorname{Re} \left(\sum_{j=1}^{N_s} p_2(k_{x,j}, \omega) v_{z2}^*(k_{x,j}, \omega) \right) \Delta k_x \\
 &= \frac{1}{4\pi} \operatorname{Re} \left(\sum_{j=1}^{N_s} Z_{a2}(k_{x,j}, \omega) |v_{z2}(k_{x,j}, \omega)|^2 \right) \Delta k_x.
 \end{aligned} \tag{4.52b}$$

The power staying in the panel can then be evaluated as

$$P_p(\omega) = P_{\text{inp}}(\omega) - P_1(\omega), \tag{4.53}$$

and the power dissipation within the porous (either limp or elastic) layer can be evaluated as

$$P_d(\omega) = P_1(\omega) - P_2(\omega). \tag{4.54}$$

4.6.2 System Equivalent Damping Loss Factor

Based on the spatial domain response and the power injection method (PIM) [23], the system equivalent damping loss factor can be calculated as

$$\eta_e(\omega) = \frac{E_{\text{inj}}(\omega)}{E_{\text{tot}}(\omega)}, \tag{4.55}$$

where the energy injected into the panel per cycle, E_{inj} , can be expressed as

$$E_{\text{inj}}(\omega) = \frac{P_{\text{inp}}(\omega) - P_2(\omega)}{\omega}, \tag{4.56}$$

and the total energy of the panel, E_{tot} , can be expressed as

$$E_{\text{tot}}(\omega) = \text{PE}(\omega) + \text{KE}(\omega) = 2\text{KE}(\omega) = 2 \left(\frac{1}{2} \sum_{j=1}^{N_s} m_j \frac{|v_t(x_j, \omega)|^2}{2} \right), \tag{4.57}$$

where $m_j = \rho_p h_p \Delta x$ is the discretized mass of each panel element. The potential energy, PE, and the kinetic energy, KE, are assumed to be equal to each other.

4.7 Model Validations

4.7.1 Model Validation for a Partially-Constrained Structure by Using a Finite Element Model

A finite element model developed by using COMSOL Multiphysics was applied to validate the NFD analytical model used for the current study. The validation was based on three different configurations: (1) a 1 mm thick aluminum panel clamped at the ends and directly loaded by an air half-space as shown in Figure 4.12; (2) a 1 mm thick aluminum panel clamped at the ends and loaded by a limp porous layer plus an air half-space as shown in Figure 4.17; (3) a 1 mm thick aluminum panel clamped at the ends and loaded by a poro-elastic layer plus an air half-space as shown in Figure 4.18. The finite element cases that correspond to (1), (2) and (3) are shown in Figures 4.19, 4.20 and 4.21, respectively. For the NFD model, the clamped boundary conditions were created by assigning two large and heavy discontinuities (*i.e.*, $m_l = 200$ kg/m, $J_l = 0.7083$ kg·m, located at $x_{l,1} = -0.5$ m and $x_{l,2} = 0.5$ m), to the 1 mm thick panel. For the COMSOL model, a 1 mm thick, 1 m long panel (modeled using 2-D elastic elements with a 1 mm triangular mesh) was clamped by specifying zero deflection and zero rotation at the ends for all three configurations. Given $h_p = 1$ mm, $F = 1$ N/m and the parameters of the air (Table 4.1), the panel (Table 4.2), the constraints (Table 4.3), the limp porous (Table 4.5) and the poro-elastic (Table 4.6) treatments, the velocity response spectrum at the driving point ($x = 0$ m) was evaluated using both models for each configuration at 500 equally-spaced frequencies ranging from 1 to 1000 Hz, and the comparisons of responses are plotted in Figures 4.22, 4.23 and 4.24 for configurations (1) to (3), respectively, from which excellent agreement can be observed, which verifies the calculation accuracy of the NFD model.

4.7.2 Model Validation for a Periodically-Constrained Structure by Using a Finite Element Model

Another finite element model was implemented to validate the NFD model for the periodically-constrained structure. The parameters as shown in Tables 4.1, 4.2, 4.4 and 4.5 together with $h_p = 1$ mm, $P = 1$ N/m² and $M = 0.8$ were input to the NFD model to create the case of a 1 mm thick, convective pressure-driven, periodically-clamped aluminum panel treated with a 3 cm thick limp fibrous layer as shown in Figure 4.25. The finite element model consisted of a baffled 1 mm thick, 1 m long aluminum panel modeled using 2-D elastic elements with a 1 mm triangular mesh, and clamped (*i.e.*, zero deflection and zero rotation) at both ends with the same limp fibrous layer on top as in the periodic case, along with the air half-space (see Figure 4.26). The comparison of the velocity response spectrum from 20 to 1000 Hz at $x = 0$ m for this subsonic convective excitation case is shown in Figure 4.27, which shows reasonable agreement, especially given that the COMSOL model represents a stand-alone fully-clamped structure in contrast to the configuration in the NFD model in which the panel is one channel of a periodically-constrained structure distributed with constraints having large but finite inertias and stiffnesses to approximate fully-clamped boundary conditions at the constraints. Furthermore, inspired by the idea of mode localization [71], the NFD model was rerun with the periodic constraints all shifted to nearby locations to break the symmetry, however, the “wiggling” between peaks did not disappear after the addition of this slight randomness, which means the unstable results between natural frequencies was not due to numerical errors, and the reason for it can be potentially studied in the future.

4.7.3 Model Validation for a Periodically-Constrained Structure by Using an Analytical Model

Due to the fact that the COMSOL validation introduced in Section 4.7.2 did not perfectly match the NFD results especially when comparing the results between

the peaks, the periodically-constrained case was further validated by using Mead's space harmonic model described in Ref. [66] (also introduced here in Appendix D) to reconfirm the prediction accuracy of the NFD model on the periodically-constrained cases. Since the Mead's model was derived for a periodically-supported beam in a vacuum, the NFD model was also changed to remove the air half-space from the layered system as shown in Figure 4.14. Given $c_0 = 343$ m/s, $h_p = 3$ mm, $P = 1$ N/m², $M = 0.8$, and the panel parameters listed in Table 4.2, plus $l = 1$ m and $k_l = 1.77 \times 10^9$ kg/(s²·m) ($m_l = J_l = s_l = 0$), the velocity response spectra from 10 to 10000 Hz (500 logarithm-spaced frequencies) at $x = 0.61$ were calculated by using Mead's rigid or flexible model, and by using the NFD model with adjustable γ_s 's (chosen based on -300 dB cutoff level on a -6000 rad/m to 6000 rad/m range of k_x 's) or a fixed γ_s for each frequency. The results are shown in Figure 4.28. It can be observed that the results from Mead's rigid support model (green dashed line) generally repeated the flexible support model (blue solid line) except for at high frequencies. This is reasonable since the translational stiffness assigned to the supports were extremely high, which created a nearly-rigid support condition at the periodic constraint locations, and note that the flexible model was more accurate in the high frequency region per Mead's 1971 paper [66]. Also, both lines from the NFD periodically-constrained model showed good agreement with Mead's model especially at peak locations, and the agreements between peaks are seen to be better than in Section 4.7.2, which reconfirmed the prediction accuracy of the NFD model. Further, a fixed γ_s for some cases will stabilize the results between the peaks.

4.8 Conclusions

Near-field damping (NFD) modeling methodologies were presented in this chapter based on three different panel structures. First, a layered structure that involves a harmonic line force-driven, infinitely-extended (unconstrained) panel was introduced to demonstrate the coupling process between the limp or elastic porous treatment

and the vibrating panel based on the Transfer Matrix Method (TMM) [21] (to couple the limp porous layer), and the Arbitrary Coefficient Method (ACM) [18] (to couple the poro-elastic layer), so that the near-field acoustical properties can be interpreted in terms of the damping properties for acquiring the wavenumber domain response of the panel. Then two identical discontinuities (constraints) were added to the unconstrained panel to create a more realistic structure with a harmonic line force-driven, partially-constrained panel coupled with either a limp porous or a poro-elastic layer. Further, periodic constraints were assigned to the panel, and a convective pressure wave was used to replace the line-driven excitation to create an aircraft fuselage-like structure.

Based on the wavenumber domain velocity response of either an unconstrained, a partially-constrained or a periodically constrained structure, a self-adjusting process was introduced to choose the sampling rates of the inverse discrete Fourier transform (IDFT) [22], and it was made adaptive to the change of the excitation frequency, so that the IDFT accurately returns the spatial response of the panel from the wavenumber domain response. Also, the conventional critical frequency of the panel can be identified and used to separate the wavenumber or spatial domain response into sub-critical and super-critical frequency regions.

Power distributions can then be calculated based on either the wavenumber domain or the spatial domain response of the panel, and the system equivalent damping loss factor can also be evaluated for the porous damping treatment by using the power injection method (PIM) [23].

Finally, the calculation accuracy of the NFD model was validated by using finite element models based on three cases each involving partially-constrained and periodically-constrained (fuselage-like) structure(s). The prediction and optimization results based on the validated NFD model will be introduced in Chapters 5 and 7.

Table 4.1. Parameters for the air ambient environment when the temperature is 25 °C.

η	B^2	γ	η_a	ρ_0	c_0
$1.846 \times 10^{-5} \text{ kg}/(\text{s} \cdot \text{m})$	0.71	1.402	0.0005	$1.21 \text{ kg}/\text{m}^3$	343 m/s

Table 4.2. Parameters for the aluminum panel.

E_0	η_p	ν_p	ρ_p
$7 \times 10^{10} \text{ Pa}$	0.003	0.33	$2700 \text{ kg}/\text{m}^3$

Table 4.3. Parameters of the discontinuity (constraint) having a dimension of $20 \text{ cm} \times 5 \text{ cm}$ and a density of $20000 \text{ kg}/\text{m}^3$ to create a partially-clamped condition.

$x_{l,1}$	$x_{l,2}$	m_l	J_l
-0.5 m	0.5 m	$200 \text{ kg}/\text{m}$	$0.7083 \text{ kg} \cdot \text{m}$

Table 4.4. Parameters of the discontinuity (constraint)the discontinuity (constraint) having a dimension of $20 \text{ cm} \times 5 \text{ cm}$ and a density of $20000 \text{ kg}/\text{m}^3$ to create a periodically-clamped condition.

l	m_l	k_l	J_l	s_l
1 m	$200 \text{ kg}/\text{m}$	0	$0.7083 \text{ kg} \cdot \text{m}$	0

Table 4.5. Parameters for the limp porous layer.

σ	ϕ	α_∞	ρ_b	d
$20000 \text{ Rayls}/\text{m}$	0.9871	1.2	$10 \text{ kg}/\text{m}^3$	3 cm

Table 4.6. Parameters for the poro-elastic layer.

σ	ϕ	α_∞	ρ_b	d	E_1	η_m	ν
20000 Rayls/m	0.9871	1.2	10 kg/m ³	3 cm	10 ⁶ Pa	0.3	0.3

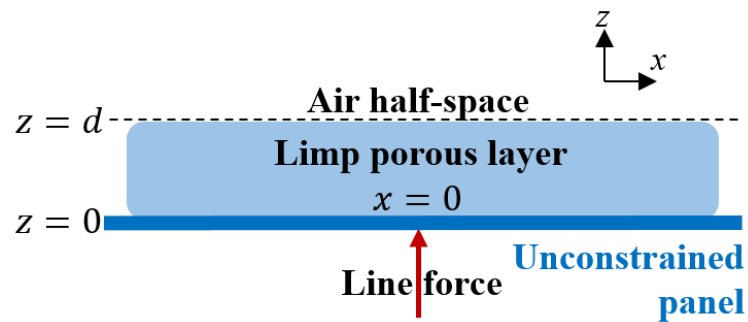


Figure 4.1. A harmonic line force-driven, infinitely-extended aluminum panel treated with a limp porous damping layer.

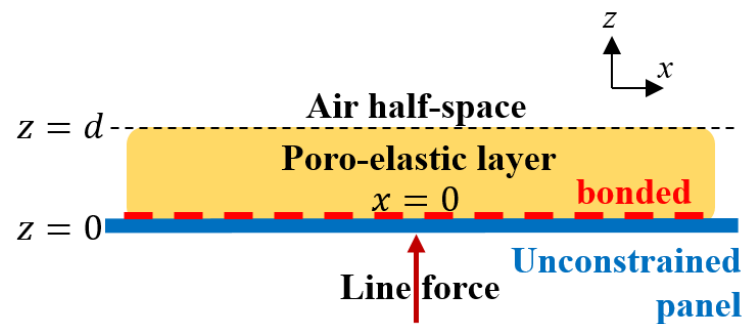


Figure 4.2. A harmonic line force-driven, infinitely-extended panel treated with a bonded poro-elastic damping layer.

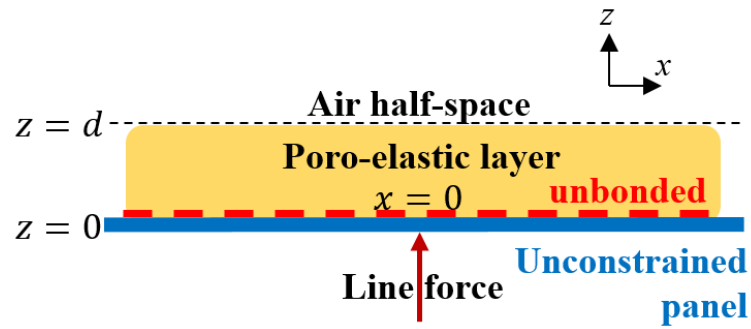


Figure 4.3. A harmonic line force-driven, infinitely-extended panel treated with an unbonded poro-elastic damping layer.

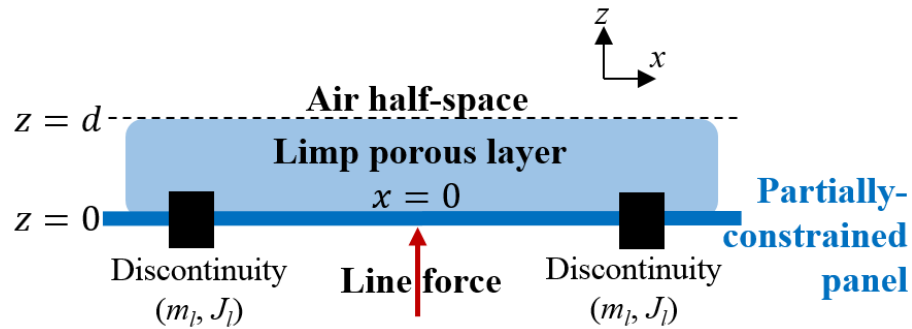


Figure 4.4. A harmonic line force-driven, partially-constrained panel treated with a limp porous damping layer.

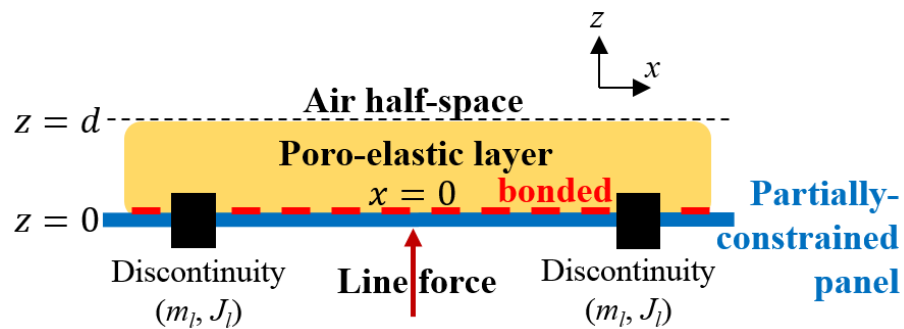


Figure 4.5. A harmonic line force-driven, partially-constrained panel treated with a bonded poro-elastic damping layer.

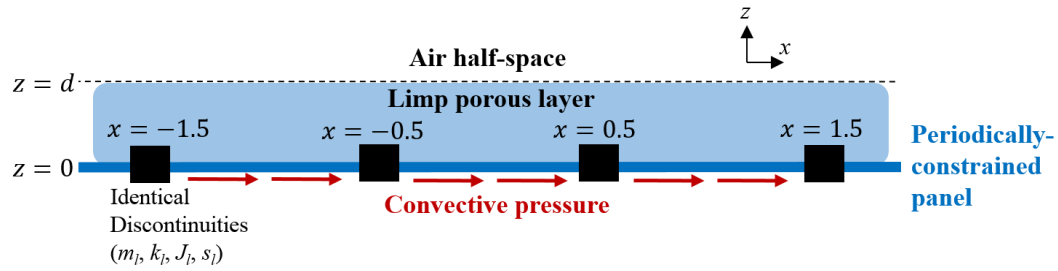
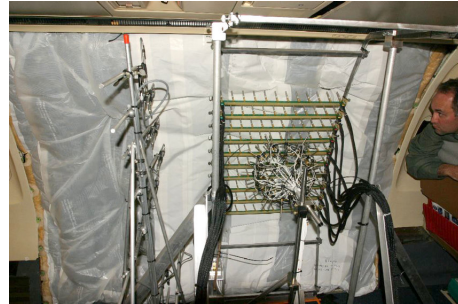


Figure 4.6. Aircraft fuselage-like structure modeled for the current study.



(a)



(b)

Figure 4.7. A typical aircraft fuselage structure as shown in Nadeau *et al.*'s study [5] and a fuselage acoustical treatment as shown in Klos *et al.*'s study [65].

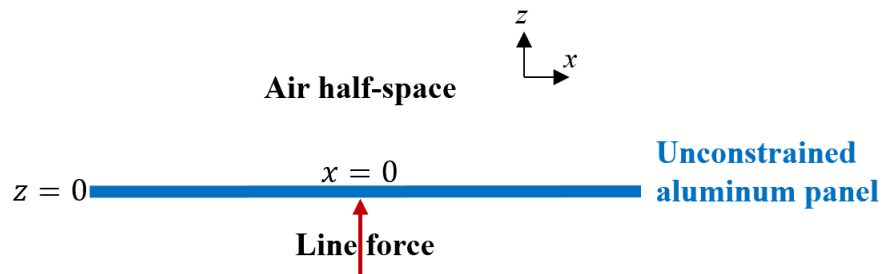


Figure 4.8. A harmonic line force-driven, unconstrained aluminum panel directly loaded by an air half-space.

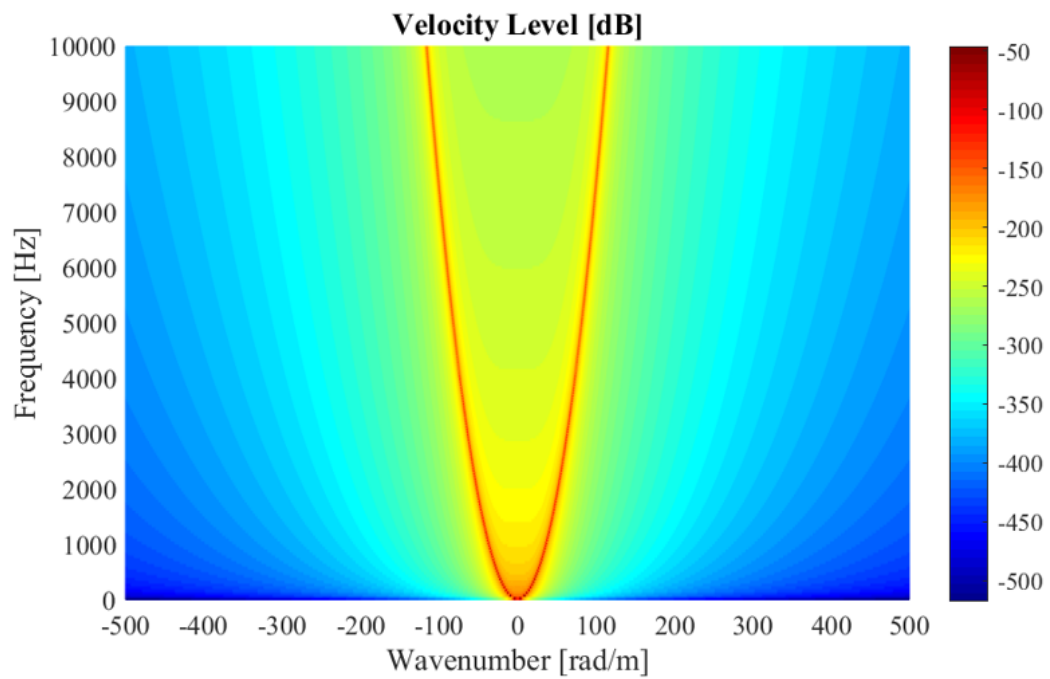


Figure 4.9. Evaluation of the wavenumber/frequency domain response for a 3 mm thick aluminum panel driven by a harmonic line force and loaded by an air half-space as shown in Figure 4.8.

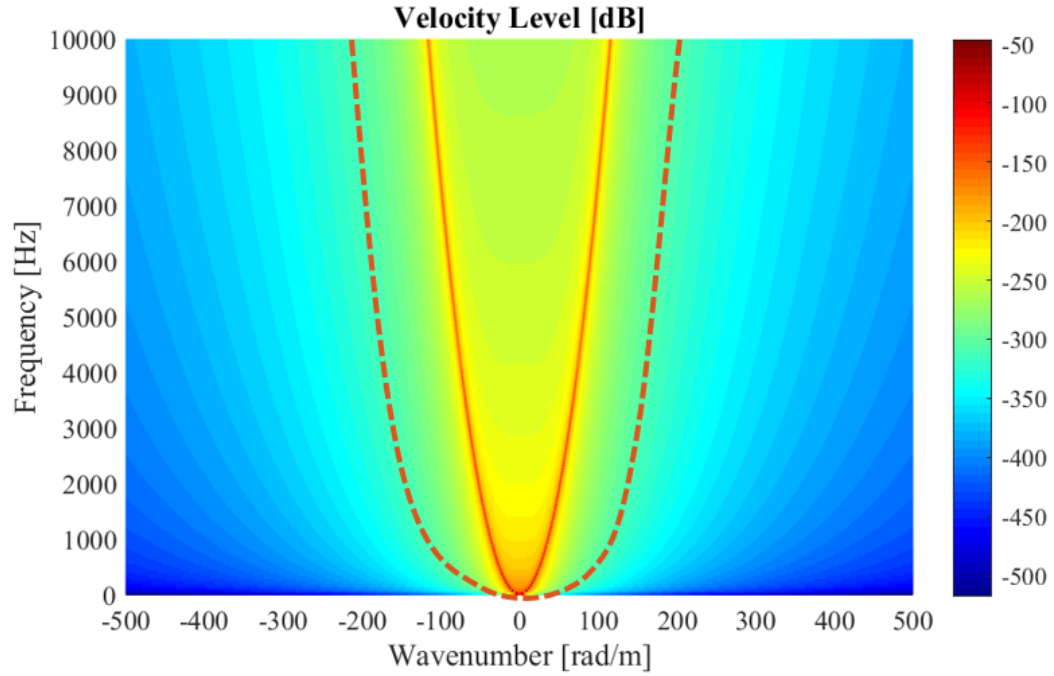


Figure 4.10. Selection of the cutoff level of -130 dB based on the evaluation as shown in Figure 4.9.

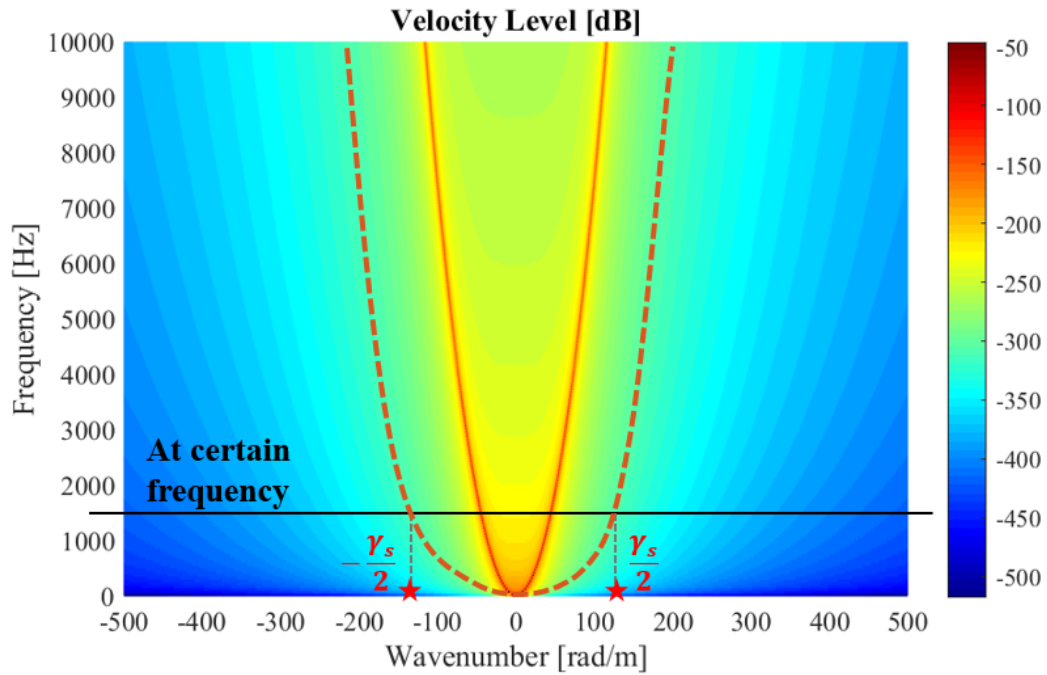


Figure 4.11. Choice of the sampling rate for a certain frequency based on the cutoff level of -130 dB as marked in Figure 4.10.

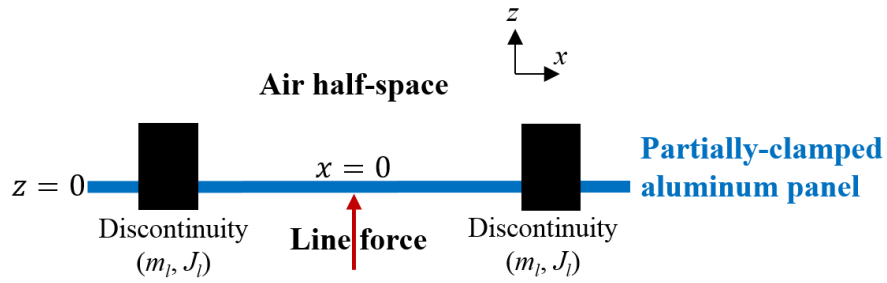


Figure 4.12. A 1 mm thick, harmonic line force-driven, partially-clamped aluminum panel directly loaded by an air half-space in the NFD model.

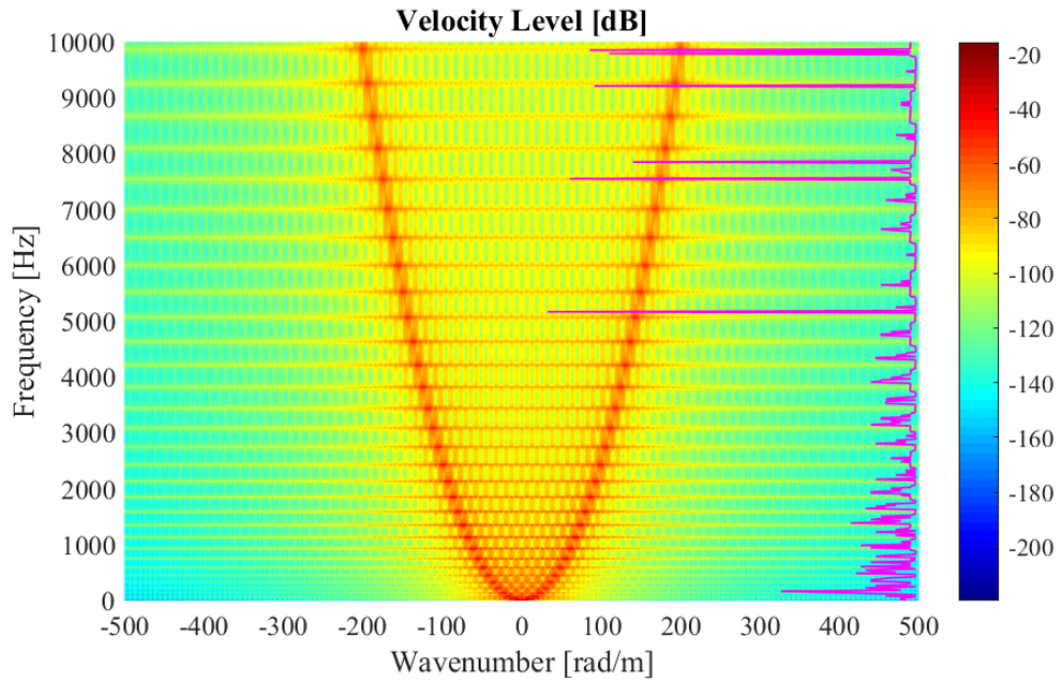


Figure 4.13. Choices of the sampling rates (marked as the magenta curve) based on the wavenumber/frequency response for the panel shown in Figure 4.12 at a cutoff level of -200 dB.

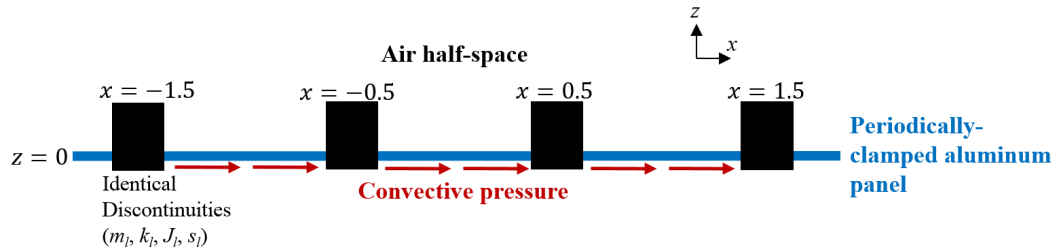


Figure 4.14. A 1 mm thick, harmonic line force-driven, periodically-clamped aluminum panel directly loaded by an air half-space in the NFD model.

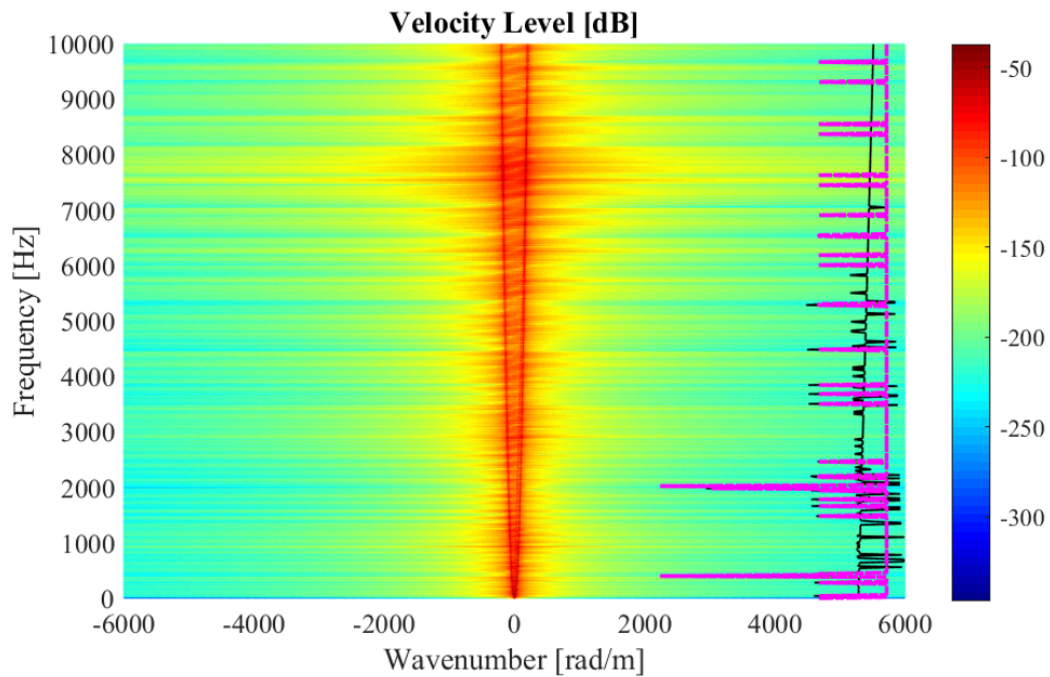


Figure 4.15. Choices of the original sampling rates (marked as the black curve) based on the wavenumber/frequency response for the panel shown in Figure 4.14 at a cutoff level of -300 dB, and further adjusted sampling rates (marked as the magenta curve) to ensure a complete periodic structure.

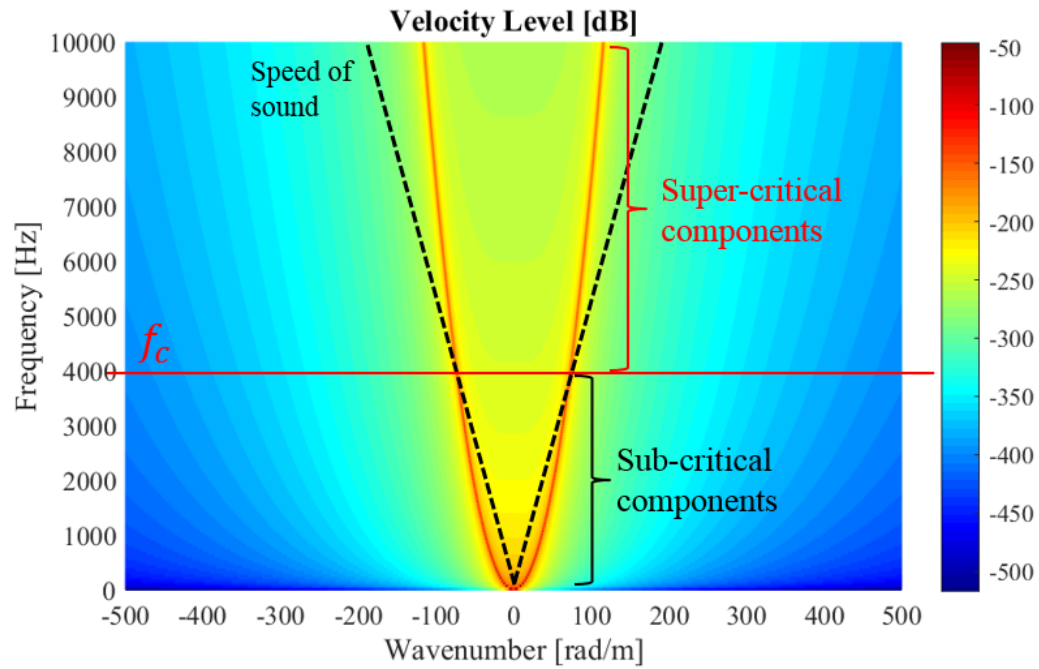


Figure 4.16. Identification of the critical frequency of a 3 mm aluminum panel in the NFD model.

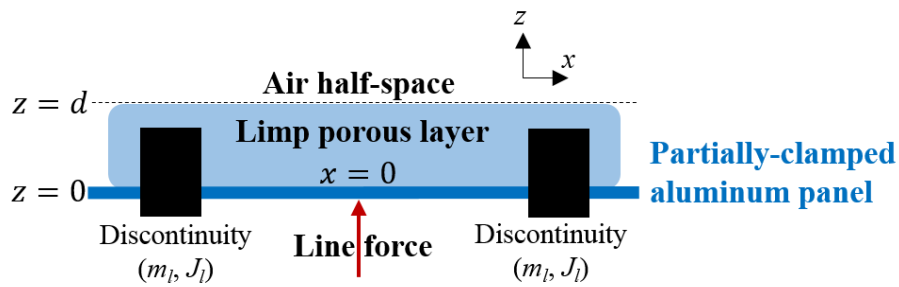


Figure 4.17. A 1 mm thick, harmonic line force-driven, partially-clamped aluminum panel loaded by a limp porous layer plus an air half-space in the NFD model.

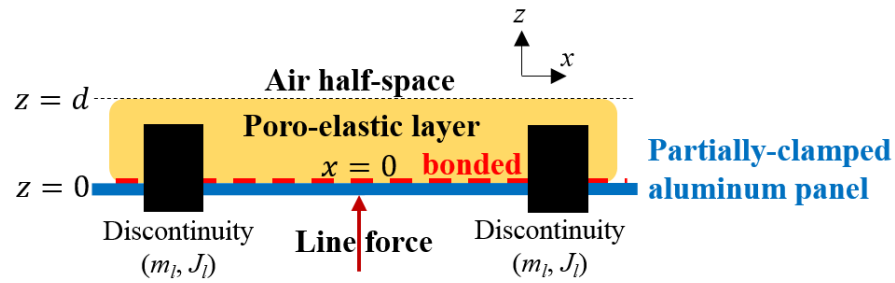


Figure 4.18. A 1 mm thick, harmonic line force-driven, partially-clamped aluminum panel loaded by a poro-elastic layer plus an air half-space in the NFD model.

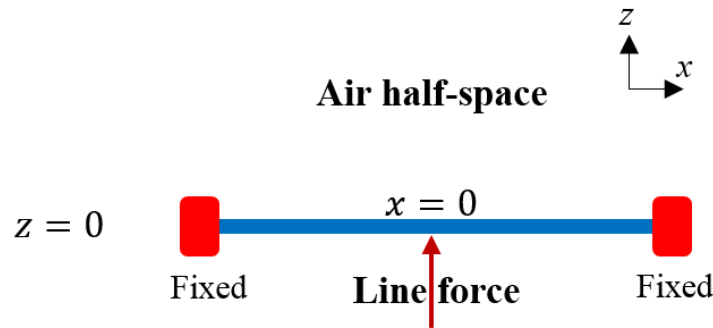


Figure 4.19. A 1 mm thick, 1 m long, harmonic line force-driven, aluminum panel directly loaded by an air half-space, and fixed at the ends in COMSOL model.

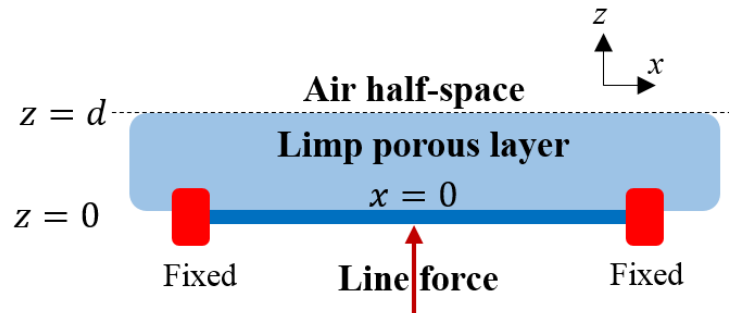


Figure 4.20. A 1 mm thick, 1 m long, harmonic line force-driven, aluminum panel loaded by a limp porous layer plus an air half-space, and fixed at the ends in COMSOL model.

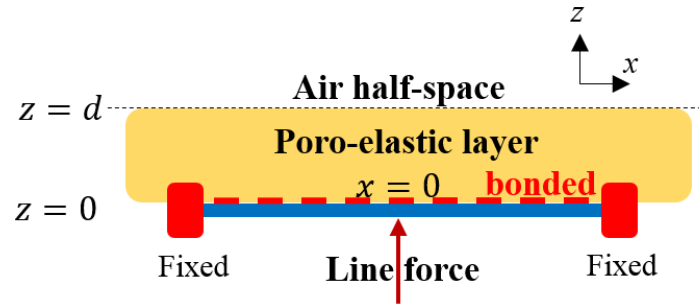


Figure 4.21. A 1 mm thick, 1 m long, harmonic line force-driven, aluminum panel loaded by a poro-elastic layer plus an air half-space, and fixed at the ends in COMSOL model.

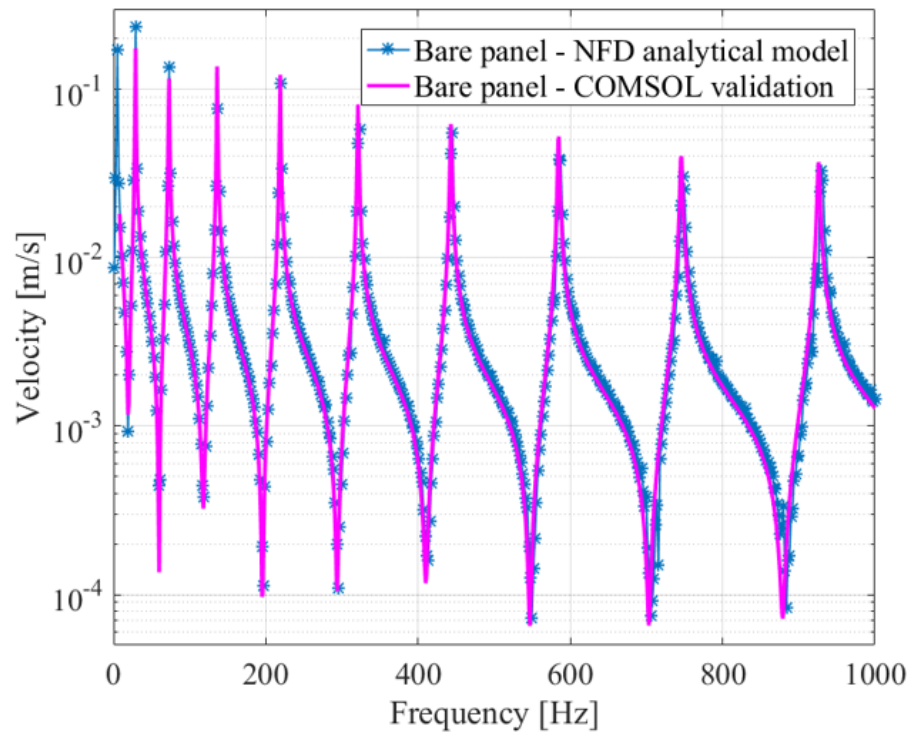


Figure 4.22. NFD *vs.* COMSOL of the velocity response spectrum at the driving point ($x = 0$ m) for configuration (1): a bare clamped panel.

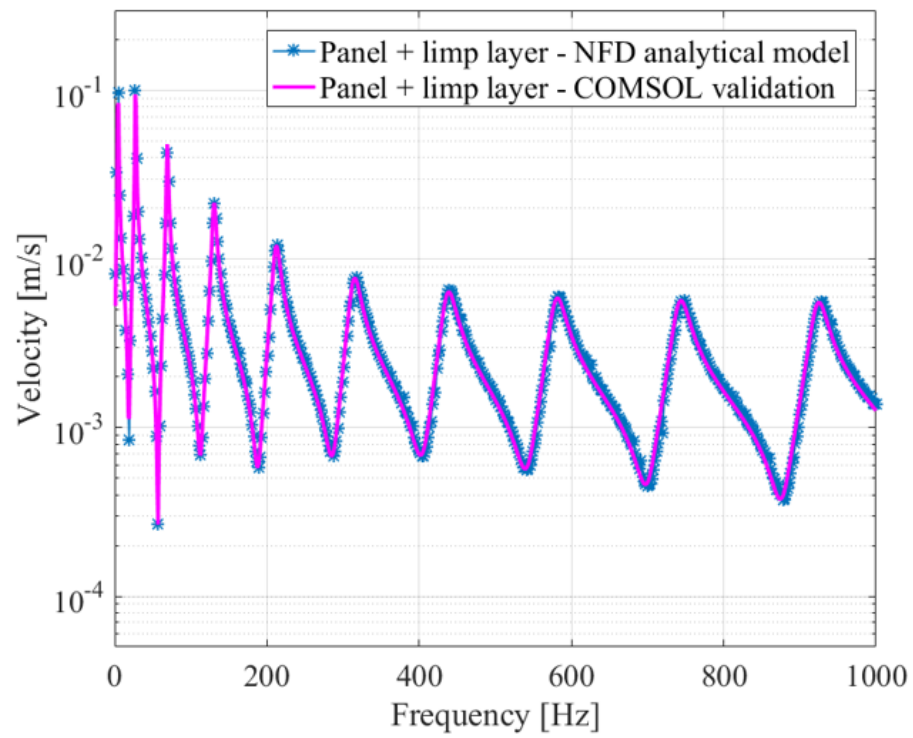


Figure 4.23. NFD *vs.* COMSOL of the velocity response spectrum at the driving point ($x = 0$ m) for configuration (2): a clamped panel treated by a limp porous layer.

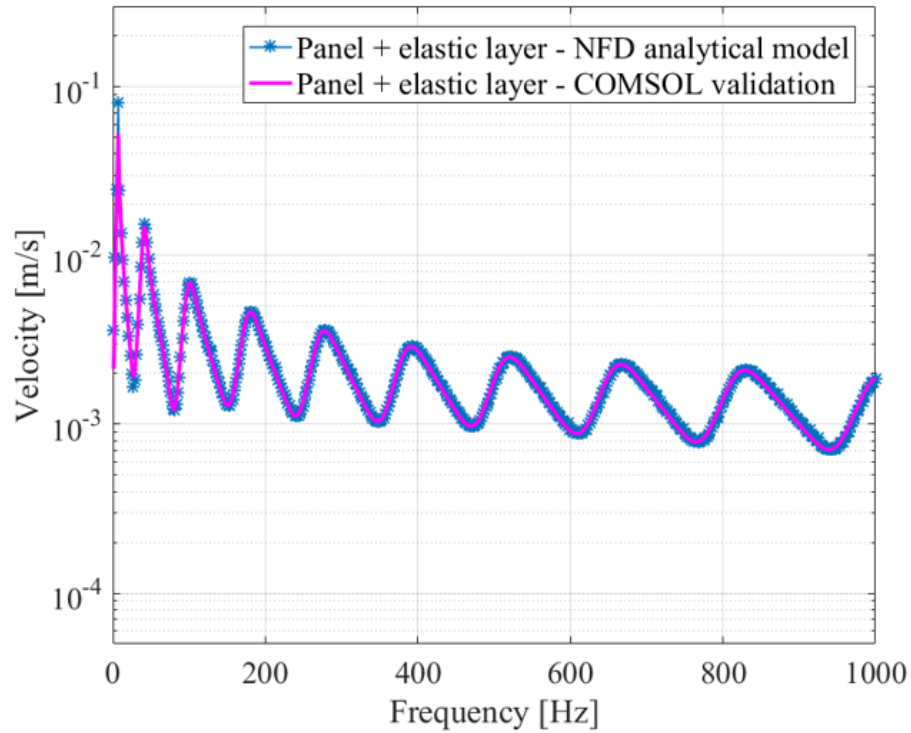


Figure 4.24. NFD *vs.* COMSOL of the velocity response spectrum at the driving point ($x = 0$ m) for configuration (3): a clamped panel treated by a poro-elastic layer.

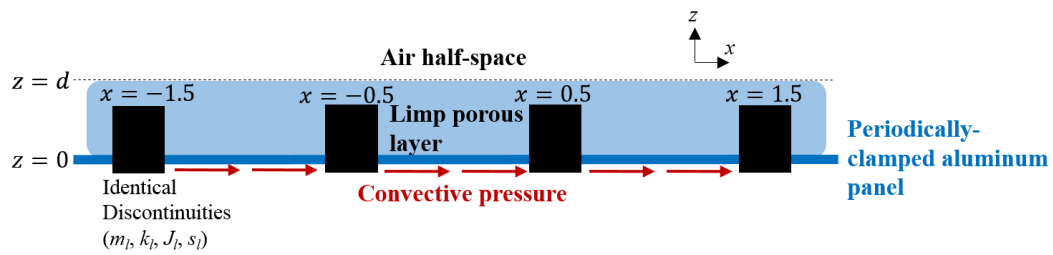


Figure 4.25. A 1 mm thick, convective pressure-driven, periodically-clamped aluminum panel loaded by a limp porous layer plus an air half-space in the NFD model.

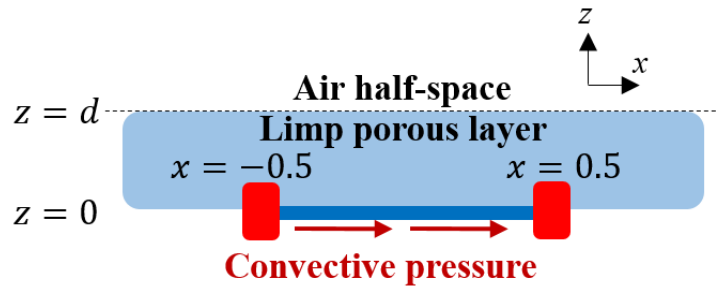


Figure 4.26. A 1 mm thick, 1 m long, convective pressure-driven, aluminum panel loaded by a limp porous layer plus an air half-space, and fixed at the ends in COMSOL model.

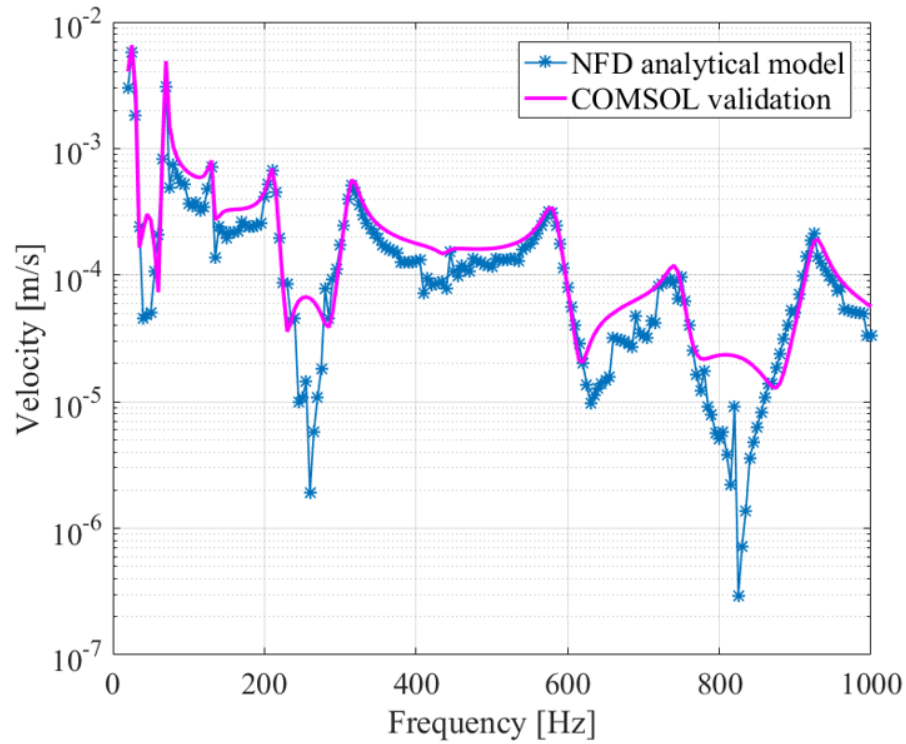


Figure 4.27. NFD *vs.* COMSOL of the velocity response spectrum at $x = 0$ m for the convective pressure-driven, periodically-clamped structure.

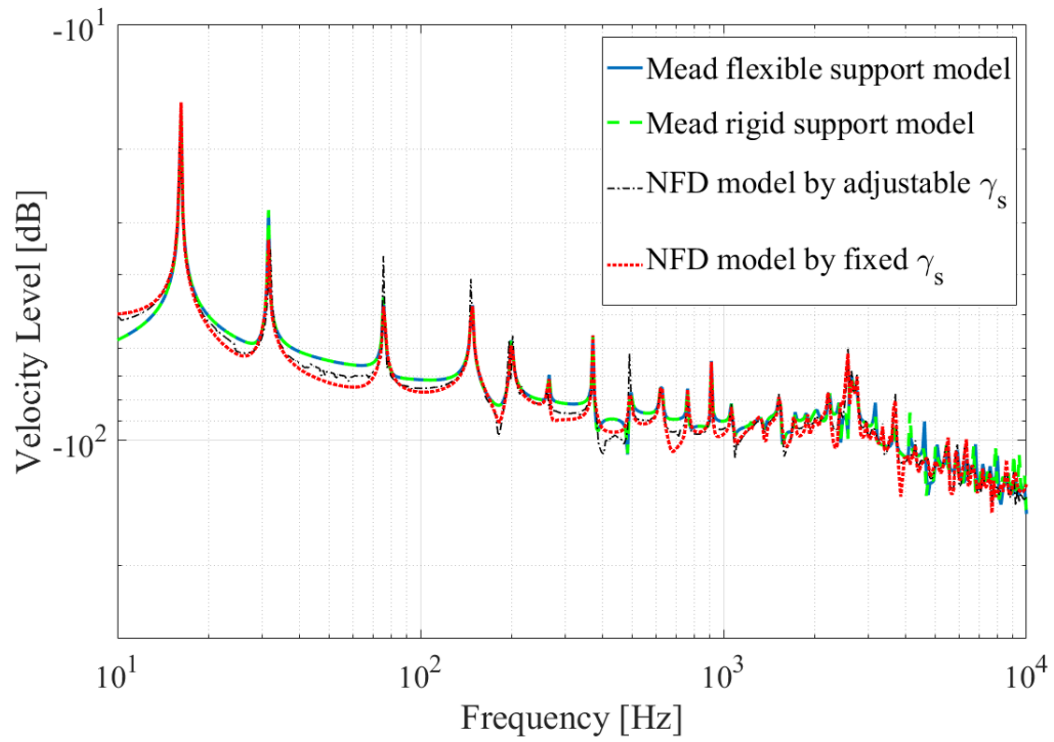


Figure 4.28. NFD *vs.* Mead's space harmonic model of the velocity response spectrum at $x = 0.11$ m for the convective pressure-driven, periodically-clamped structure in a vacuum.

5. PREDICTIONS OF DAMPING PERFORMANCE FOR POROUS DAMPING TREATMENTS BASED ON THE NFD MODEL

5.1 Introduction

The prediction of the damping performance starts in Section 5.2, with an unconstrained structure involving an infinitely-extended vibrating panel and a layer of limp porous medium plus an air-half space above it, which was used to prove the damping effectiveness of the limp porous layer. Parametric studies are also described in this section, performed on the same configuration to study the connection between the treatment's bulk properties and its damping performance, in terms of η_e 's at different frequencies. The porous treatment was then made poro-elastic in Section 5.3, by adding bulk elasticity to the solid phase of the material, based on which the reason why a poro-elastic damping layer outperforms a limp porous layer was analyzed, and the importance of bonding the poro-elastic layer to the vibrating panel was emphasized for maintaining this better performance. Also, the damping performance between the poro-elastic and limp porous layers was compared based on a partially-constrained panel. In Section 5.4, the damping effectiveness of a limp porous treatment was further verified based on a periodically-constrained (fuselage-like) structure.

5.2 Limp Porous Damping Treatments Applied to an Infinitely-Extended Vibrating Panel

The results shown here are mainly based on two cases: (1) a harmonic line force-driven, unconstrained panel loaded by an air half-space (*i.e.*, the same configuration as shown in Figure 4.8 of Section 4.5.1); and (2) a harmonic line force-driven, un-

constrained panel with a limp porous layer adjacent to it, and then loaded by an air half-space (*i.e.*, the same configuration as shown in Figure 4.1 of Section 4.2).

5.2.1 Spatial Response: Treated *vs.* Untreated Panels

Based on the NFD model, the spatial velocity response of the panel was evaluated based on the IDFT (by using Eq. (4.38)) of the wavenumber domain response of the panel for the two cases mentioned above. For case (1), the inputs for air and panel were set as listed in Tables 4.1 and 4.2 plus $h_p = 3$ mm and $F = 1$ N/m, and the wavenumber domain evaluation was based on Eqs. (4.9), (4.5) and $Z_{a1} = Z_{a2}$. For case (2), the inputs for the air and panel ($h_p = 3$ mm) were also set as listed in Tables 4.1 and 4.2, and the inputs for the limp porous layer were set as listed in Table 4.5, and the wavenumber domain evaluation was based on Eqs. (4.9) and (B.2). To begin with, a comparison of the spatial velocity level, $20 \log_{10} |v_t(x, \omega)|$ (dB), between case (1) (solid lines) and case (2) (dashed lines) is shown in Figure 5.1 at five randomly-picked driving frequencies: 10 Hz, 56 Hz, 316 Hz, 1778 Hz and 10000 Hz. Note that only half of the spatial response is shown here due to the spatial symmetry to the results (*i.e.*, the harmonic force was driving at $x = 0$ m), and the spatial span is only shown up to 10 m. It can be observed that the porous layer causes the velocity level to generally decay more quickly than in the bare panel case (indicating the damping effect), but this is especially true in the sub-critical frequency region. Note, for example, that at 10 kHz, *i.e.*, in the super-critical region, there is essentially no difference between the two cases, while in the sub-critical region, the differences are relatively large.

Next, the spatial velocity level was calculated for cases (1) and (2) at a finer input frequency resolution, and the results are shown separately in Figures 5.2 and 5.3, respectively. At each frequency, the velocity level differences at 10 m between the case (1) and case (2) (*i.e.*, case (1) minus case (2)) are shown in Figure 5.4(a). There, it can be observed that below the panel critical frequency $f_c = 4008.4$ Hz,

the differences are all positive (*i.e.*, case (1) shows the higher velocity level in the sub-critical region), while above the panel critical frequency $f_c = 4008.4$ Hz, the differences are negative except at the highest frequency considered (*i.e.*, case (2) shows the higher velocity level in the super-critical region). This observation reconfirmed that significant attenuation can be achieved in the sub-critical region by adding the porous layer. In the super-critical region, the velocity level was lower without the porous layer because of the relatively large acoustic loading applied by the radiating sound field at, and above, the critical frequency; this effect is reduced by the addition of the porous layer. Therefore, the porous layer does not add damping in the super-critical region, but note, nevertheless, that the sound power radiation is reduced in the super-critical region by the addition of the porous layer (see the power analysis in Section 5.2.2).

For all the results shown above, the panel thickness was 3 mm (with the critical frequency being 4008.4 Hz). To see the effect of changing the critical frequency, the panel thickness was then changed to 1.5 mm or 6 mm. It can be observed in Figure 5.4(b) that the critical frequency is shifted up to 8016.9 Hz when the thickness of the panel is 1.5 mm, and in Figure 5.4(c), the critical frequency is shifted down to 2004.2 Hz when the thickness of the panel is 6 mm. It can be seen in both cases that the damping action is effective below the critical frequency, and that, as might be expected, the damping effectiveness (*i.e.*, the decrease in velocity level caused by the layer in the sub-critical region) increases as the panel thickness decreases.

5.2.2 Power Distribution: Treated *vs.* Untreated Panels

Given the parameters as listed in Tables 4.1, 4.2 and 4.5 plus $h_p = 3$ mm and $F = 1$ N/m, the power distributions within the layered system were calculated by using Eqs. (4.45), (4.47), (4.52), (4.53) and (4.54) for the same two cases mentioned above. The results for cases (1) and (2) are shown in Figures 5.5 and 5.6, respectively. For the bare panel, it can be observed in Figure 5.5 that most of the input power

(blue) remains in the panel (purple) in the sub-critical region, while the greater part of the input power radiates into the air (red) in the super-critical region above 4 kHz. On the other hand, when there was a porous layer adjacent to the panel, it can be observed in Figure 5.6 that a large fraction of input power (blue) was taken out of the panel (orange), and that most of that power was dissipated within the layer (green). At the same time, the porous layer reduced the power (red) radiating from the surface of the porous layer into the adjacent air space in the super-critical region. Thus, the addition of the porous layer acts both to reduce the panel vibration and the radiated sound.

5.2.3 Damping Loss Factor: Parametric Studies on Limp Fibrous Treatments

To understand the connection between the bulk properties and damping performance for limp porous damping treatments, parametric studies were then conducted on case (2) mentioned above with an harmonic line force-driven ($F = 1$ N/m), unconstrained aluminum panel ($h_p = 1$ mm, other parameters as listed in Table 4.2) and a limp porous layer ($\alpha_\infty = 1.2$, $\phi = 0.9871$), by changing one or two of the input bulk properties (layer thickness, d , airflow resistivity, σ , and bulk density, ρ_b) of the porous layer while fixing the others, and by observing the η_e 's (evaluated by Eq. (4.55)) resulting from different bulk property combinations to compare their damping performance. Note that there are three groups of studies, and that the limp porous layer was assumed to be made of fibers in all of these three groups in order to provide a more specific and figurative impression.

In group 1, d was fixed as 3 cm, σ as MKS 20000 Rayls/m, and ρ_b was increased from 10 kg/m³ (*i.e.*, a typical bulk density of polymeric fiber) to 30 kg/m³ (*i.e.*, a typical bulk density of glass fiber with the same microstructure as the polymer fiber). The resulting η_e 's for a frequency range of 10–10000 Hz are shown in Figure 5.7, which indicates that with the same micro-geometry details (indicated by the fixed σ)

and the same layer depth (indicated by the fixed d), an increase of the bulk density of the fibrous layer (*e.g.*, making the fibers from a heavier solid material like glass) will increase the peak value of the equivalent loss factor and move the peak to a lower frequency region.

In group 2, σ was fixed at 20000 Rayls/m, and ρ_b was gradually increased from 10 kg/m³ to 30 kg/m³ while decreasing d from 3 cm to 1 cm, which kept the mass per unit area constant. Based on the η_e 's shown in Figure 5.8, it can be observed that with the same micro-geometry details (indicated by the fixed σ) and the same bulk weight (indicated by the combinations of ρ_b and d), increasing the bulk density of the fibrous layer (*e.g.*, making the fibers from a heavier solid material like glass) while decreasing the layer thickness moves the peak equivalent loss factor to a lower frequency region.

In group 3, d was chosen to be 3 cm, ρ_b to be 10 kg/m³, and σ was varied from 10000 Rayls/m to 50000 Rayls/m. It can be observed from the η_e 's shown in Figure 5.9 that with the same bulk weight and the same layer depth (indicated by the fixed ρ_b and d), the fibrous layer with relatively low airflow resistivity (*e.g.*, made of sparse, coarse glass fibers) provides better damping in the low frequency region, while the fibrous layer with relatively high airflow resistivity (*e.g.*, made of dense, fine polymeric fibers) provides better damping in the high frequency region.

5.3 The Effects of Adding Bulk Elasticity to the Porous Media

To examine the effect of adding bulk elasticity to the porous media on its near-field damping, a comparison of the damping performance of limp porous and bonded poro-elastic treatments based on an unconstrained panel structure was performed first, and the comparison is illustrated in Section 5.3.1 in terms of power dissipation. The power dissipation was also evaluated for the unbonded poro-elastic treatment case, and the bonding effect on a poro-elastic layer's damping performance is analyzed in Section 5.3.2. Further, the damping performance in terms of loss factor, η_e , was evaluated

based on the partially-constrained structure of Section 4.2), and is compared between the limp porous and the bonded poro-elastic cases in Section 5.3.3.

5.3.1 Power Dissipation: Limp Layer *vs.* Elastic Layer

The power dissipation, P_d , was calculated (by using Eq. (4.54)) and normalized by the power input, P_{inp} , (evaluated by using Eq. (4.45)) at 50 log-spaced frequencies within the 10 Hz to 10000 Hz range, given $F = 1$ N/m, $h_p = 1$ or 3 mm and the parameters listed in Tables 4.1, 4.2, 4.5 and 4.6, to represent harmonic line force-driven, unconstrained aluminum panels treated by either a limp porous layer as shown in Figure 4.1 or a bonded poro-elastic layer as shown in Figure 4.2, and the results are shown in Figure 5.10, from which the poro-elastic treatment (red solid lines) was found to have a generally larger ratio of power dissipation than the limp porous layer (green dashed lines) for either a 1 mm (lines with circles) or 3 mm (lines with stars) panel, especially in the frequency regions that are below 100 Hz and above 1000 Hz; the better performance is also more obvious when the panel structure is thinner. It is believed that the improved performance results from the additional structural dissipation within the solid phase of the porous medium when the porous layer is elastic and is bonded to the panel, in contrast to the case when there is only viscous and thermal dissipation within a limp porous layer.

5.3.2 Bonding Effect for Poro-Elastic Damping Media

The normalized power dissipations were then calculated for the configuration as shown in Figure 4.3 with either a 1 mm or 3 mm thick line-driven, unconstrained aluminum panel treated by an unbonded poro-elastic layer given $F = 1$ N/m, $h_p = 1$ or 3 mm and the parameters listed in Tables 4.1, 4.2 and 4.6, and the results are plotted as blue-dotted lines in Figure 5.11 in addition to the previous bonded poro-elastic cases and limp porous cases. It can be seen that for both 1 mm (blue dotted line with circles) and 3 mm (blue dotted line with stars) panels, the unbonded poro-

elastic layer still outperforms the limp porous layer in the low frequency region, but provides a similar amount of power dissipation to that of the limp porous layer above 300 Hz. This finding indicates that bonding the layer to the panel is very important (especially in the high frequency region) if the poro-elastic layer is to perform better than the limp porous layer, which also makes sense in that the power radiation in the high frequency region mostly depends on the solid phase of the poro-elastic medium, and bonding the poro-elastic layer to the panel will ensure better power radiation efficiencies through both $P_{1,\sigma}$ and $P_{1,\tau}$, so that the structural dissipation can be enhanced.

5.3.3 Damping Loss Factor: Limp Layer *vs.* Elastic Layer

The system equivalent damping loss factor, η_e , was calculated at 500 equally-spaced frequencies ranging from 1 Hz to 1000 Hz for configurations as shown in Figures 4.4 and 4.5, which includes a 1 mm thick, line-driven and partially-constrained aluminum panel treated by either a limp porous layer or a bonded poro-elastic layer, given $F = 1$ N/m, $h_p = 1$ mm and the parameters listed in Tables 4.1, 4.2, 4.5 and 4.6 together with discontinuity parameters as listed in Table 5.1, and the comparison between the limp layer and the elastic layer in terms of damping performance based on the η_e 's is shown in Figure 5.12, from which the overall superior damping of the bonded poro-elastic treatment can be observed.

5.4 Limp Porous Damping Treatments Applied to a Fuselage-Like Structure

The results to be presented in this section were primarily based on a fuselage-like configuration: *i.e.*, a 3 mm thick periodically-constrained aluminum panel as shown in Figure 4.6. The input parameters for this configuration are listed in Tables 4.1, 4.2, 4.5 together with the discontinuity parameter as listed in Tables 5.2, plus $h_p = 3$ mm and $P = 1$ N/m². The wavenumber domain velocity level responses are presented

in Section 5.4.1 for different M 's in order to illustrate the shift of the convective excitation critical frequency. And a comparison of the frequency and spatial responses for a bare fuselage-like panel *vs.* a panel treated with a limp porous layer on top are presented in Sections 5.4.2 and 5.4.3, respectively, to show the damping effectiveness of the treatment. Finally, the damping loss factor evaluation is presented in Section 5.4.4.

5.4.1 Wavenumber Response and the Identification of Convective Excitation Critical Frequencies

The wavenumber domain velocity level (based on Eq. (4.32a)) was calculated over a range of k_x from -500 rad/m to 500 rad/m, and a range of f from 10 to 10000 Hz for $M = 0.8$ (subsonic excitation), $M = 1.0$ (sonic excitation) and $M = 1.2$ (supersonic excitation). The results are plotted in Figure 5.13, and it can be observed that the excitation (black dashed line) and the panel dispersion curves intersects at the convective critical frequency, f_{cv} , which shifts with the increase of M . Also, of course, for the sonic excitation case, f_{cv} is the same as the conventional critical frequency, f_c , of the panel.

5.4.2 Velocity Response Spectrum: Treated *vs.* Untreated Panels

A comparison of the velocity response spectrum from 10 Hz to 10000 Hz at $x = 0.11$ m (a randomly-selected point between two adjacent constraints at $x = \pm 0.5$ m) between a bare fuselage-like structure and a fuselage-like structure treated with the 3 cm limp porous layer is shown in Figure 5.14 for both subsonic ($M = 0.8$) and supersonic ($M = 1.2$) convective pressure excitation cases. It can be observed that vibration peaks below f_c were reduced by 5 to 15 dB by the porous layer. This observation is in-line with the previous finding that the porous near-field damping is primarily effective below the critical frequency, in which case the panel motion creates a strong, evanescent, acoustical near-field.

5.4.3 Spatial Response: Treated *vs.* Untreated Panels

To show in greater detail, Figure 5.14 was then replotted as Figure 5.15 over the frequency range from 100 Hz to 1200 Hz. The reduction in vibration level at the peaks is more easily discernible in this view. Two vibration peak frequencies, 420 Hz and 531 Hz, were selected for further observation of the spatial velocity response between the constraints at $x = \pm 0.5$ m for both subsonic ($M = 0.8$) and supersonic ($M = 1.2$) convective pressure excitation cases, respectively. The spatial responses are plotted in Figure 5.16, from which a 10 to 15 dB reduction of vibration can be observed at the peak frequencies (420 Hz, 531 Hz) across the observation area.

5.4.4 Damping Loss Factor: Parametric Studies on Limp Fibrous Treatments

A parametric study on airflow resistivity was conducted, where the system damping loss factor, η_e , was calculated for the fuselage-like structure treated by a limp porous layer at three different input σ 's, which represent three different types of porous media's microstructures (here all assumed to be fibrous media for a more figurative impression): the results are plotted in Figure 5.17. A general trend that can be observed from both the subsonic and supersonic cases is that a fibrous layer with a relatively low airflow resistivity effectively reduces lower frequency vibration, while a layer with a relatively high airflow resistivity effectively reduces higher frequency vibration. This general trend is consistent with what was observed in Figure 5.9 on Section 5.2.3 for the unconstrained structure.

5.5 Conclusions

In this chapter, damping performance was predicted for both limp porous and poro-elastic damping treatments given their bulk properties.

In Section 5.2, the prediction started with the simplest and the most general configuration with a harmonic line force-driven, unconstrained aluminum panel treated by a layer of limp porous medium. Spatial responses and power distributions were acquired for both a treated and an untreated (bare) panels, and the comparison between these two cases shows that the porous layer's damping primarily corresponds to the power dissipation within the layer, which is effective below the critical frequency, and that the level of damping increases as the panel thickness decreases. Also, the multi-functionality of the porous media comes from the sub-critical damping and super-critical absorbing based on the power distributions.

In Section 5.3, the damping was compared mainly between limp porous and poro-elastic treatments. With the same micro-/macro-geometries, poro-elastic media give better damping than limp porous media over a broad range of excitation frequencies (10–10000 Hz), and this overall advantage results from the additional structural dissipation due to the bulk elasticity of the solid material of a poro-elastic medium, but bonding the poro-elastic layer to the vibrating substrate is very important to maintain this outperformance.

The damping performance in terms of both spatial response of the panel was then evaluated in Section 5.4 based on a fuselage-like (periodically-constrained) structure, and a significant level of damping of the vibration peaks was observed below the sub-critical frequency of the structure.

Last but not least, given different combinations of bulk properties, the damping performance in terms of system equivalent damping loss factor, η_e , was evaluated for limp porous treatments that were assumed to be made of fibers, which helped the understanding of the connections between a material's parameters and its damping performance. In both unconstrained and periodically-constrained cases, the general trend shows that certain combinations of bulk properties contribute to the largest damping (also referred to as the “optimal damping”) at certain excitation frequency for a given structure. This finding led to the following studies (shown in Chapters 6 and 7) to design the optimal micro-/macro-geometry for fibrous damping media.

Table 5.1. Parameters of discontinuity (constraint) to create a partially-constrained condition.

$x_{l,1}$	$x_{l,2}$	m_l	J_l
-0.5 m	0.5 m	6.75 kg/m	0.0028 kg·m

Table 5.2. Parameters of discontinuity (constraint) to create a periodically-clamped condition.

l	m_l	k_l	J_l	s_l
1 m	6.75 kg/m	2.66×10^8 kg/(s ² ·m)	0.0028 kg·m	1.11×10^5 kg· m/s ²

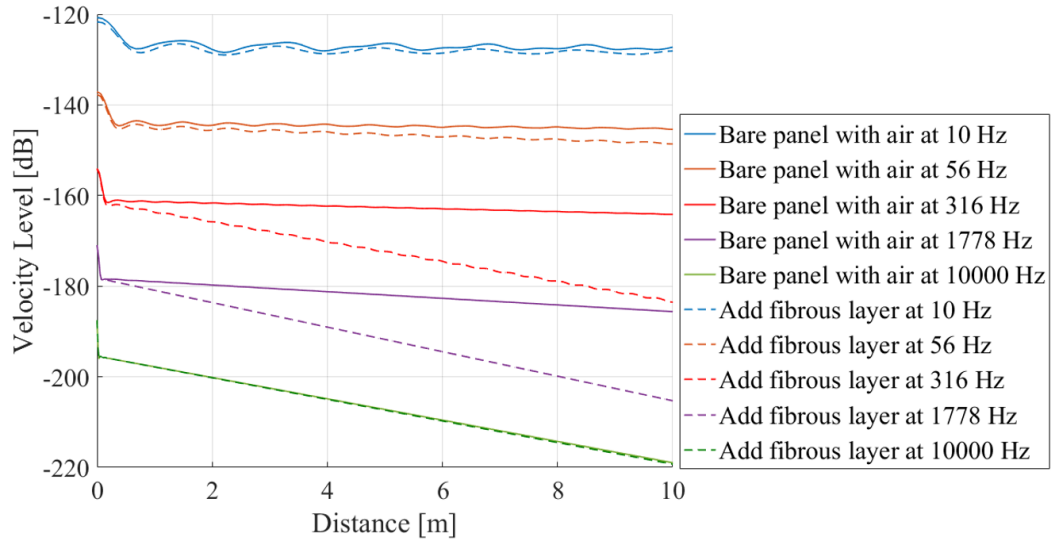


Figure 5.1. Spatial velocity level comparison between case (1): a bare 3 mm thick, unconstrained aluminum panel (solid lines) and case (2): a 3 mm thick, unconstrained aluminum panel with a 3 cm layer of limp porous media (dashed lines), both driven by the harmonic force under different frequencies: 10 Hz, 56 Hz, 316 Hz, 1778 Hz and 10000 Hz.

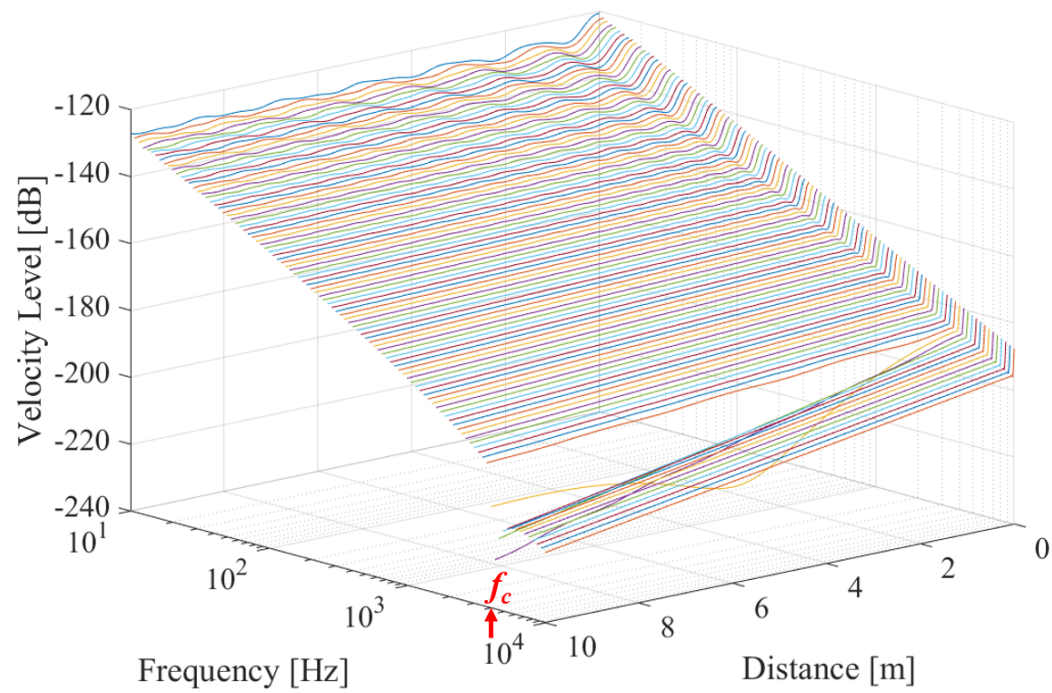


Figure 5.2. Spatial velocity level for case (1): a bare 3 mm thick, unconstrained aluminum panel, driven by a harmonic force under 100 different frequencies: log-spaced within 10–10000 Hz.

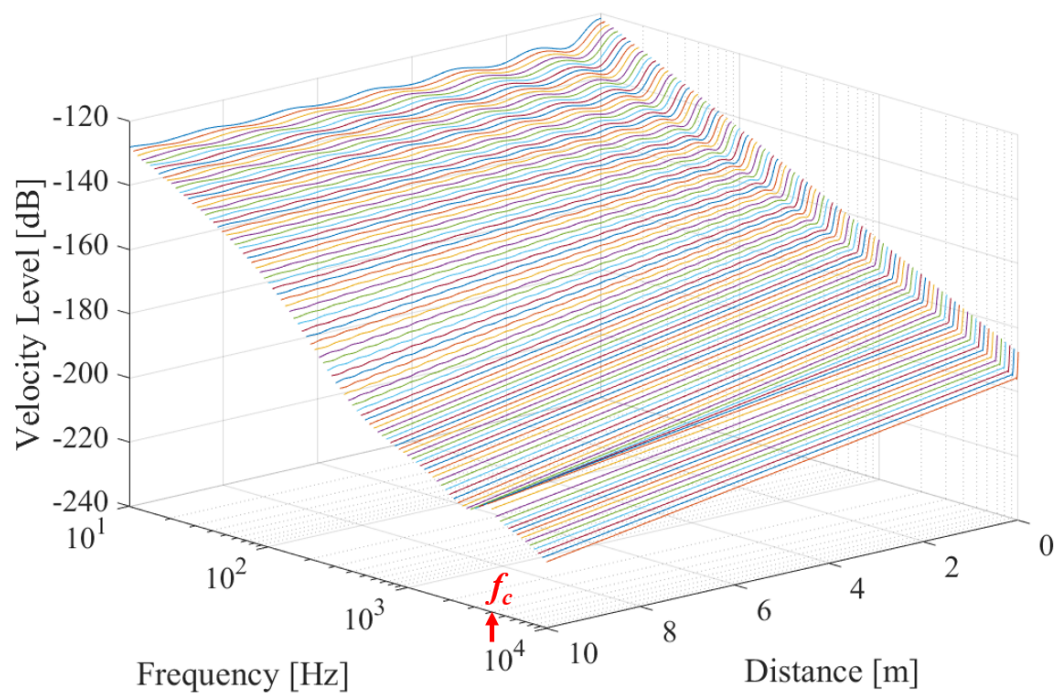


Figure 5.3. Spatial velocity level for case (2): a 3 mm thick, unconstrained aluminum panel with a 3 cm layer of limp porous media, driven by a harmonic force under 100 different frequencies: log-spaced within 10–10000 Hz.

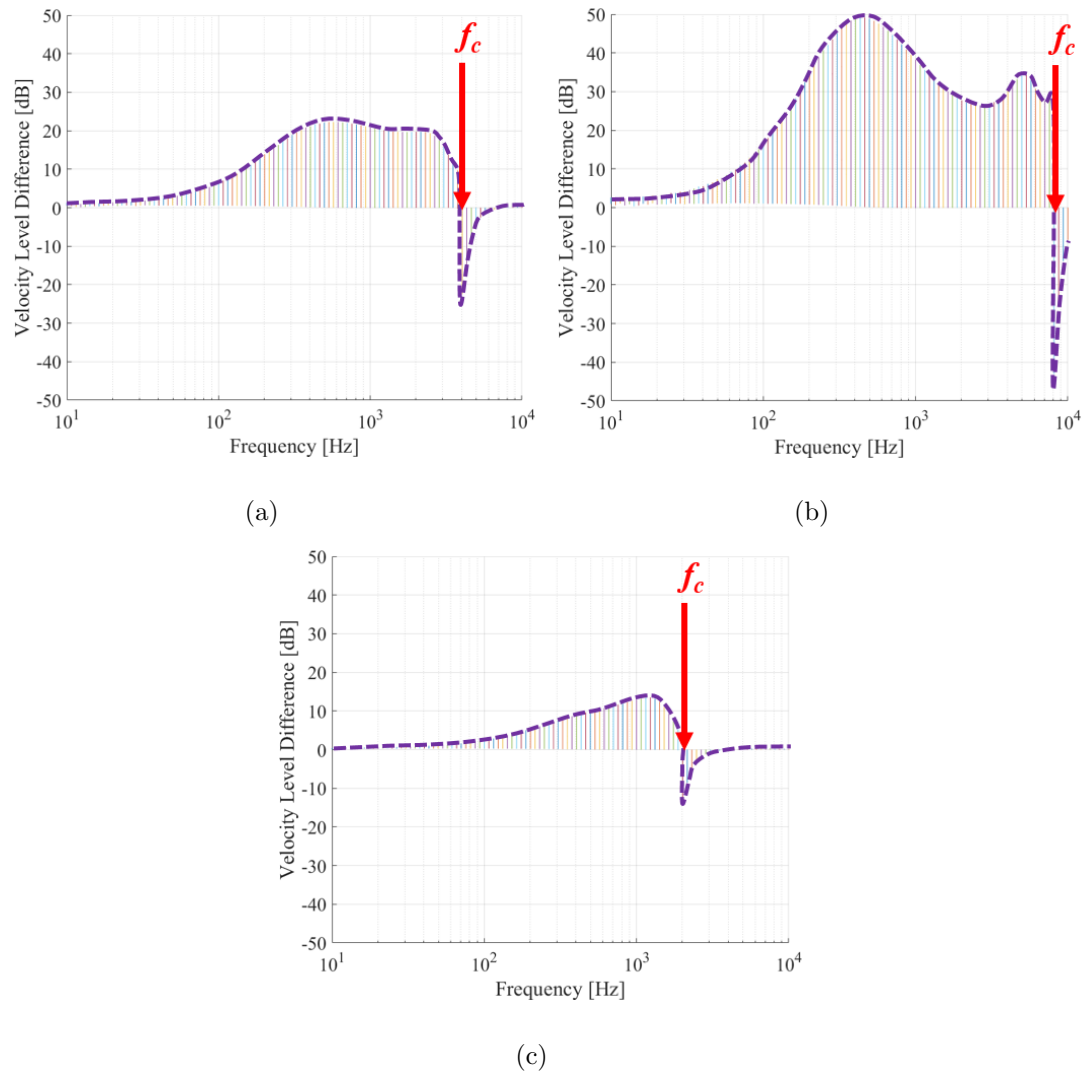


Figure 5.4. A side view of the spatial velocity level differences at $x = 10$ m between case (1): an unconstrained aluminum panel driven by a harmonic force under 100 different frequencies (log-spaced within 10–10000 Hz), and case (2): the panel treated with a 3 cm layer of limp porous medium with (a) 3 mm, (b) 1.5 mm and (c) 6 mm as panel thicknesses.

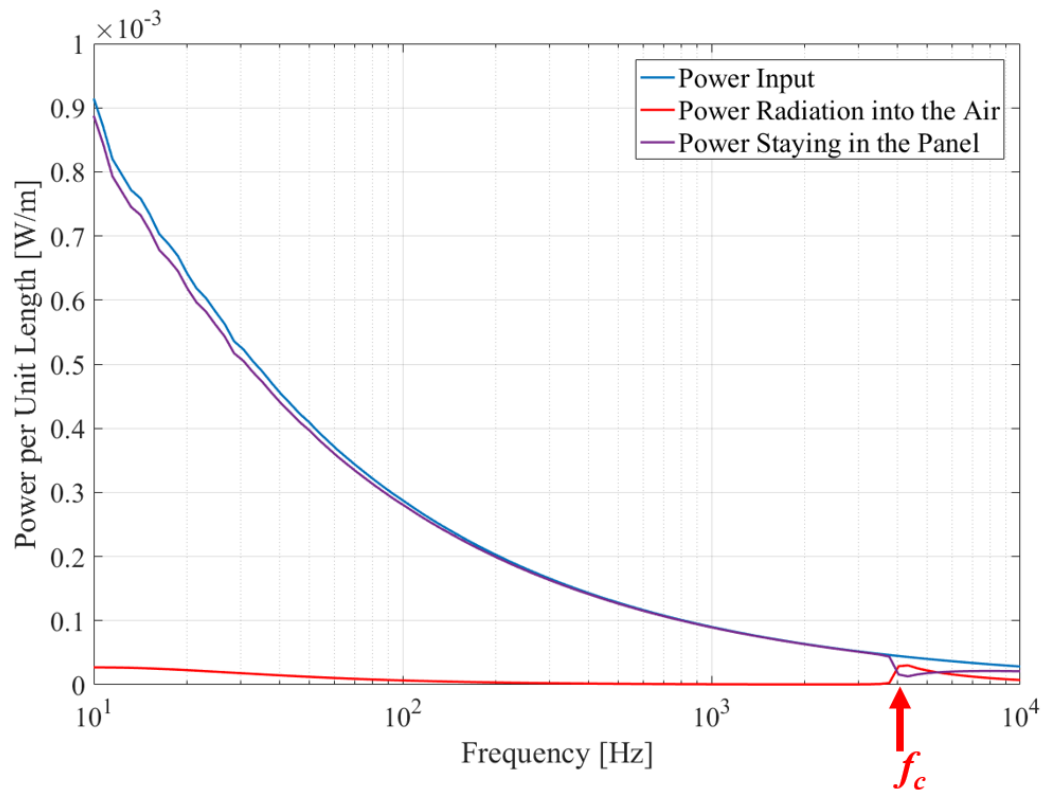


Figure 5.5. Power distribution for case (1): a bare 3 mm thick, unconstrained aluminum panel, driven by a harmonic force under 100 different frequencies: log-spaced within 10–10000 Hz.

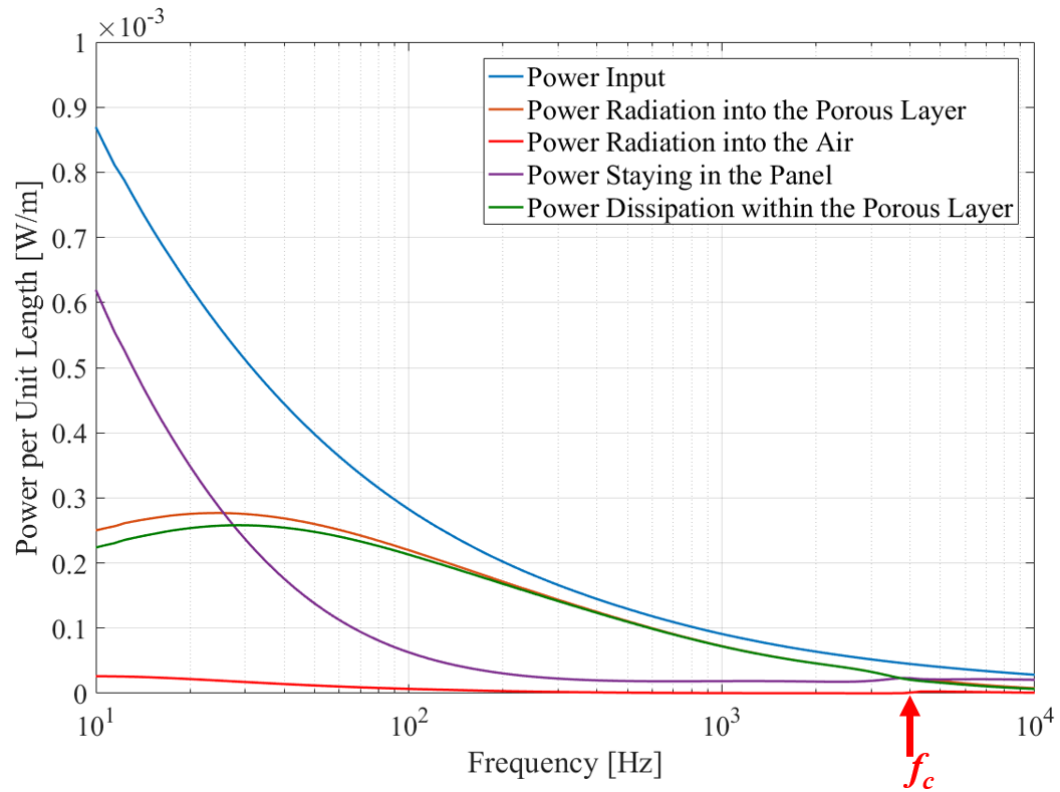


Figure 5.6. Power distribution for case (2): a 3 mm thick, unconstrained aluminum panel with a 3 cm layer of limp porous medium, driven by a harmonic force under 100 different frequencies: log-spaced within 10–10000 Hz.

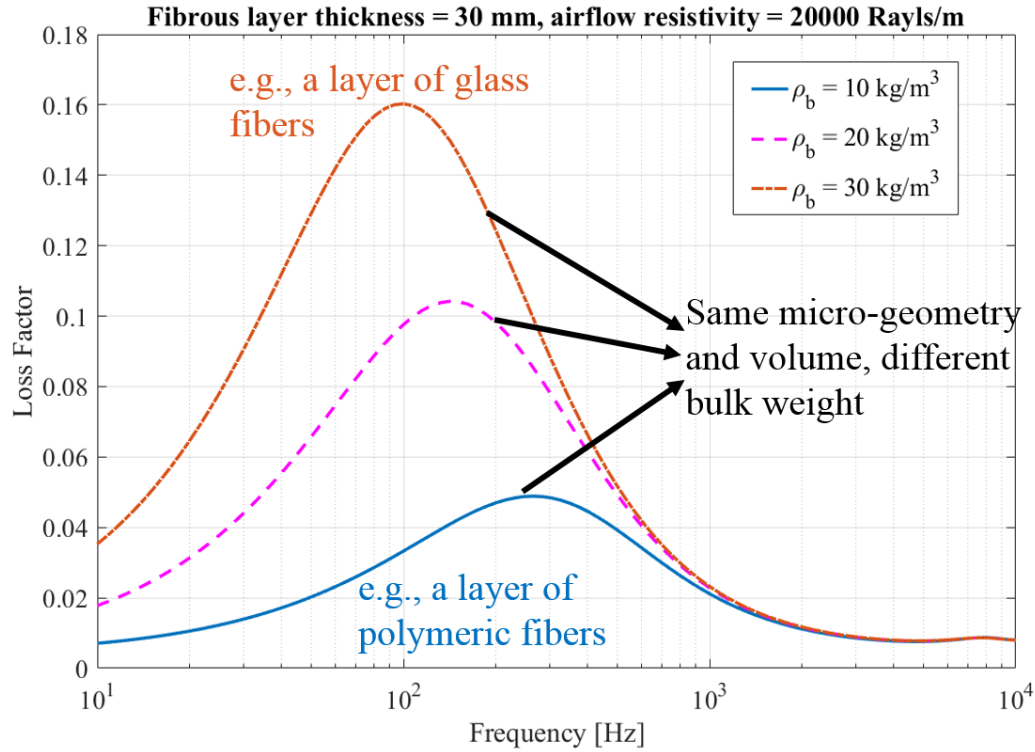


Figure 5.7. System equivalent damping loss factor of a 1 mm thick, unconstrained aluminum panel treated with limp fibrous layers with the same thickness and airflow resistivity but different bulk densities, driven by a harmonic force under 100 different frequencies: log-spaced within 10–10000 Hz.

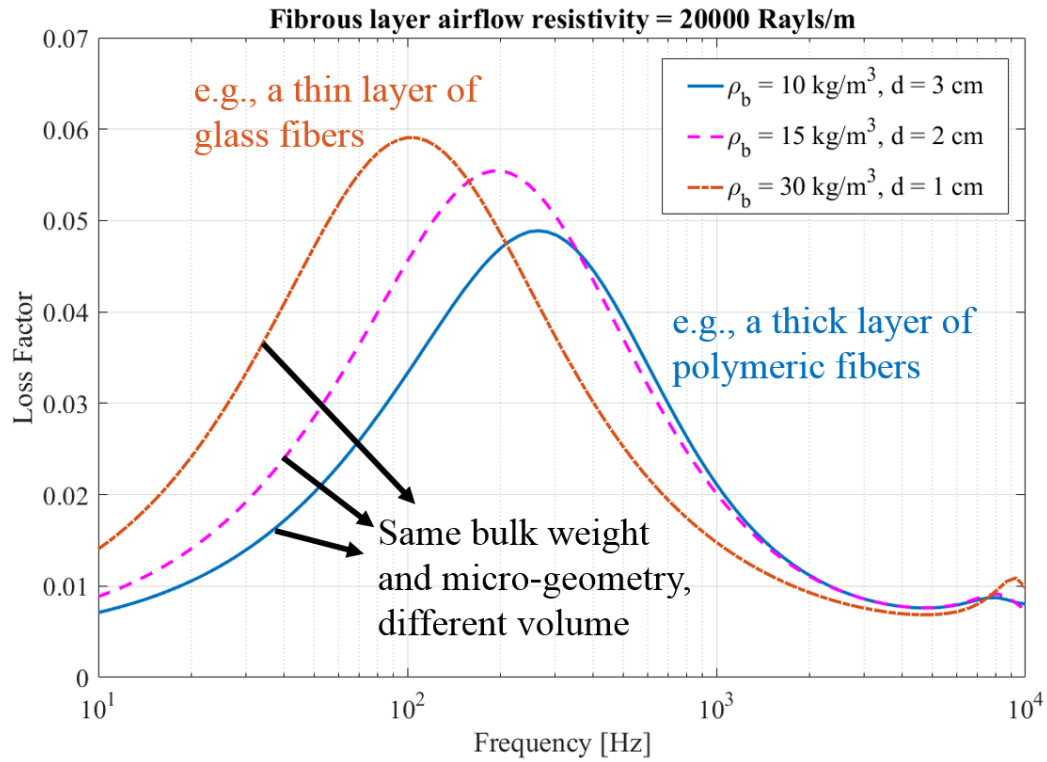


Figure 5.8. System equivalent damping loss factor of a 1 mm thick, unconstrained aluminum panel treated with limp fibrous layers with the same airflow resistivity but different combinations of thicknesses and bulk densities, driven by a harmonic force under 100 different frequencies: log-spaced within 10–10000 Hz.

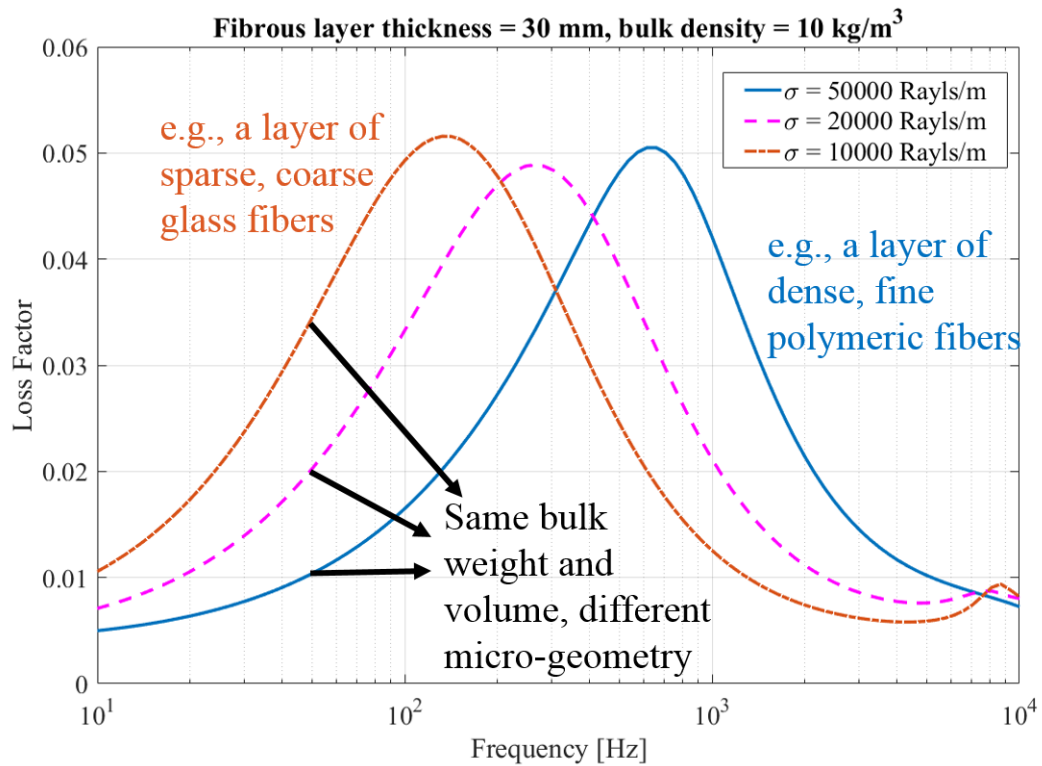


Figure 5.9. System equivalent damping loss factor of a 1 mm thick, unconstrained aluminum panel treated with limp fibrous layers with the same thickness and bulk density but different airflow resistivities, driven by a harmonic force under 100 different frequencies: log-spaced within 10–10000 Hz.

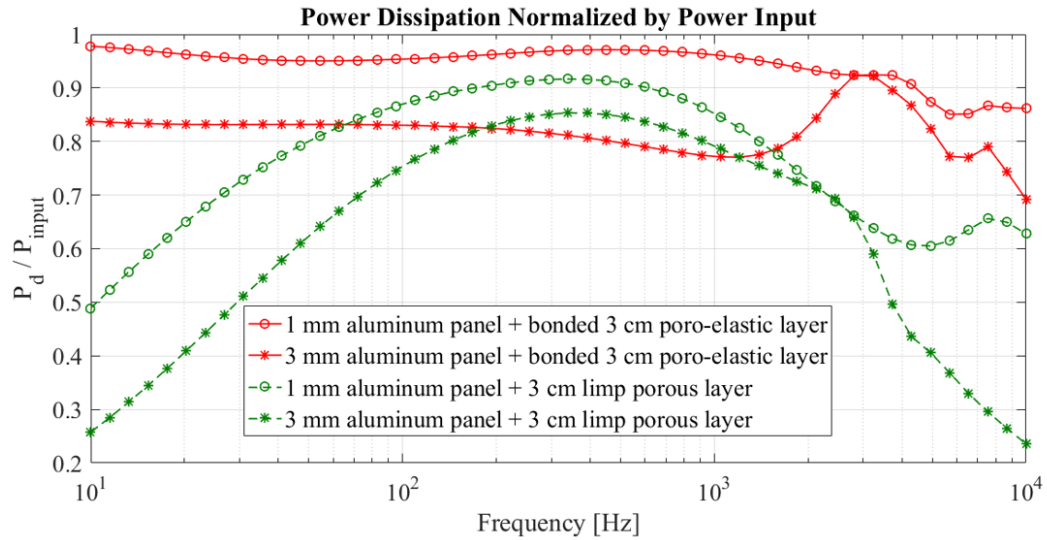


Figure 5.10. Normalized power dissipations within either a bonded poro-elastic layer (red solid lines) or a limp porous layer (green dashed lines) acting on a 1 mm (circled lines) or a 3 mm (starred lines) thick, unconstrained aluminum panel, driven by a harmonic force under 50 different frequencies: log-spaced within 10–10000 Hz.

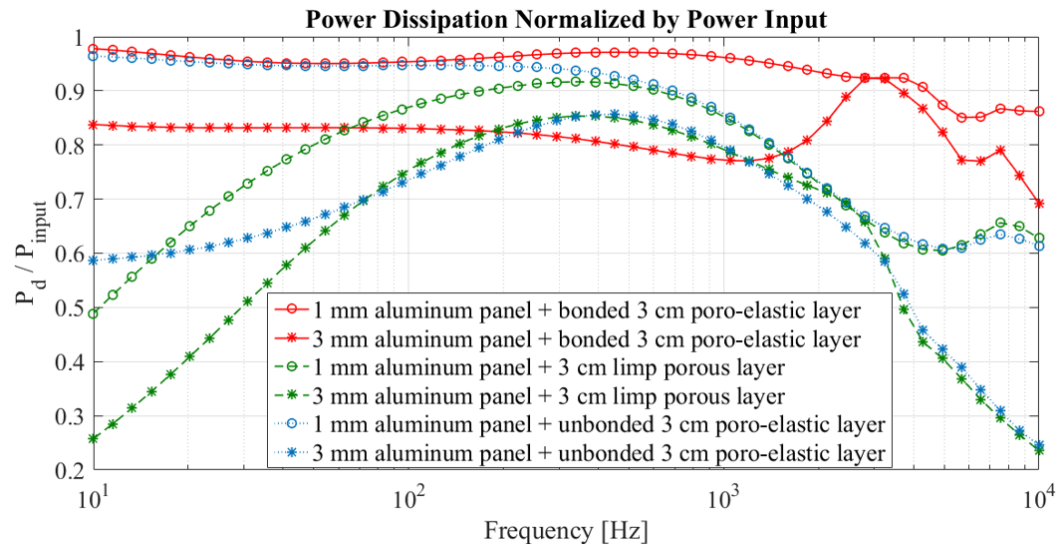


Figure 5.11. Adding normalized power dissipations within an unbonded poro-elastic layer acting on a 1 mm (blue dotted-circled line) or a 3 mm (blue dotted-starred line) thick, unconstrained aluminum panel, driven by a harmonic force under 50 different frequencies: log-spaced within 10–10000 Hz.

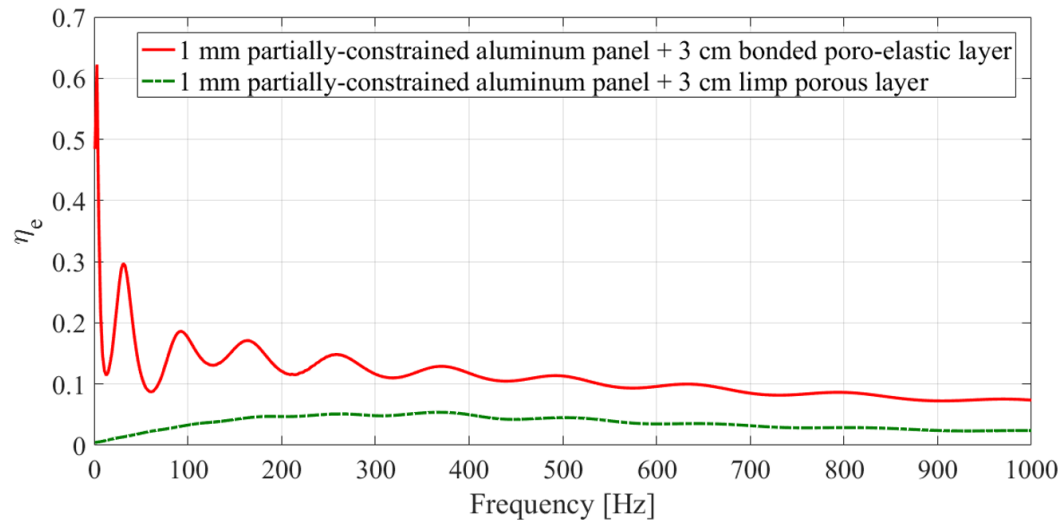


Figure 5.12. System equivalent damping loss factor for a 1 mm thick, partially-constrained aluminum panel treated either by a bonded poro-elastic layer (red solid line) or a limp porous layer (green dashed line), driven by a harmonic force under 500 different frequencies: log-spaced within 1–1000 Hz.

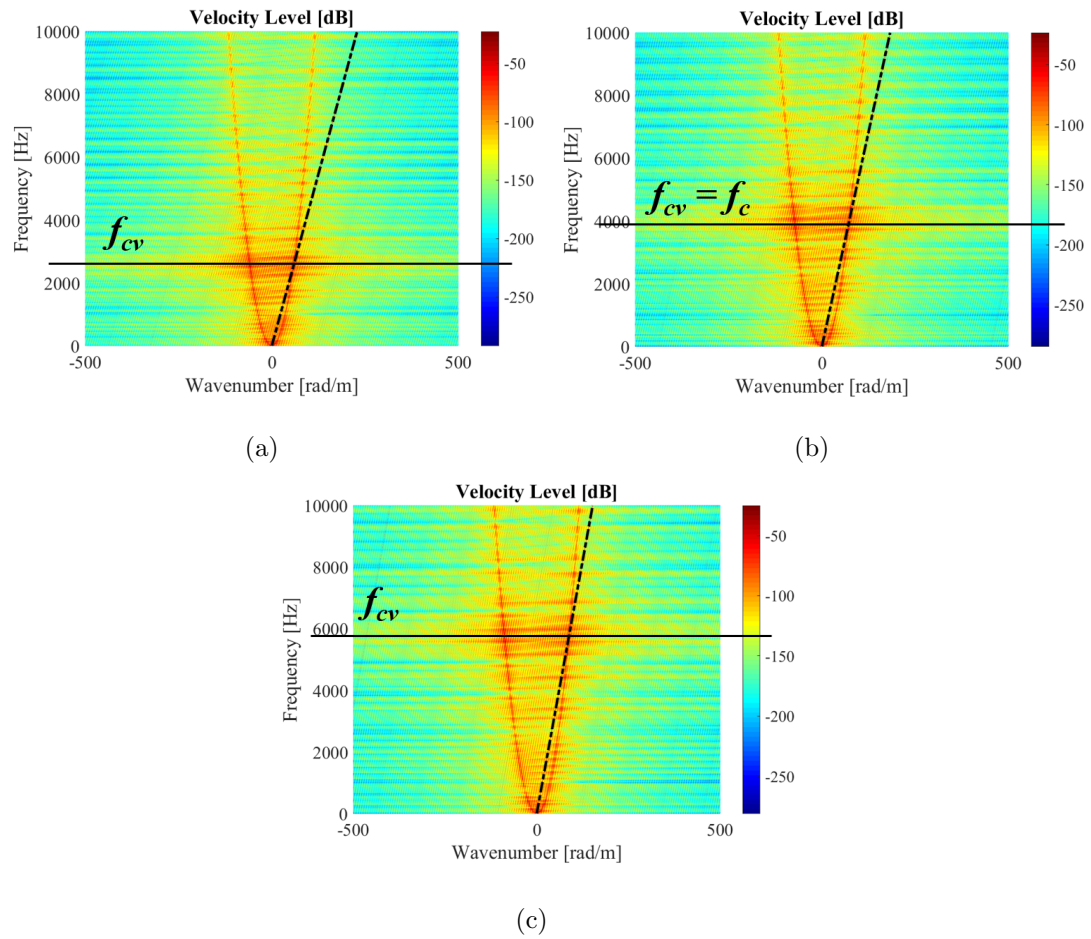


Figure 5.13. Wavenumber domain velocity level for a 3 mm thick, fuselage-like structure treated by a 3 cm thick, limp porous layer, driven by (a) subsonic convective pressure ($M = 0.8$), (b) sonic convective pressure ($M = 1.0$), (c) supersonic convective pressure ($M = 1.2$), with the convective excitations marked as black dashed lines.

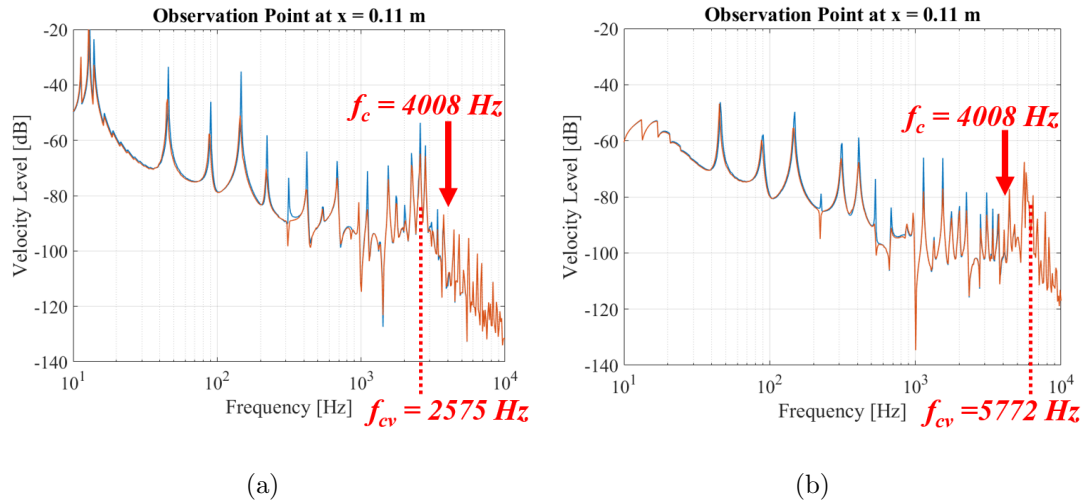


Figure 5.14. Velocity response spectrum from 10 Hz to 10000 Hz of the velocity at $x = 0.11$ for the 3 mm thick, bare fuselage-like structure (blue line) or the limp porous layer-treated, fuselage-like structure (orange line) both driven by (a) subsonic ($M = 0.8$), (b) supersonic ($M = 1.2$) convective pressure, both with conventional and convective critical frequencies marked by red arrows.

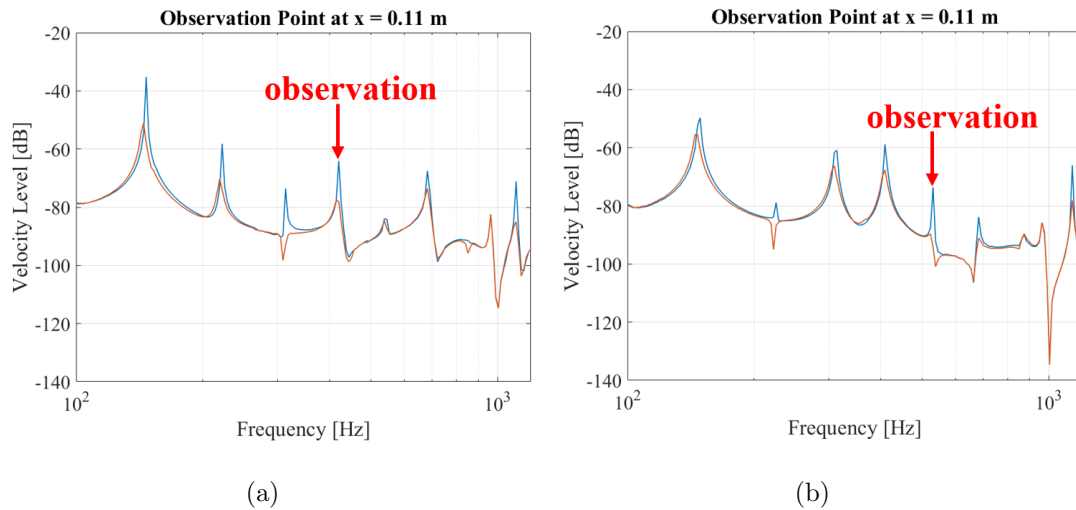


Figure 5.15. Velocity response spectrum from 100 Hz to 1200 Hz of the velocity at $x = 0.11$ for the 3 mm thick, bare fuselage-like structure (blue line) or the limp porous layer-treated, fuselage-like structure (orange line) both driven by (a) subsonic ($M = 0.8$, with 420 Hz selected as a spatial response observation frequency), (b) supersonic convective pressure ($M = 1.2$, with 521 Hz selected as a spatial response observation frequency).

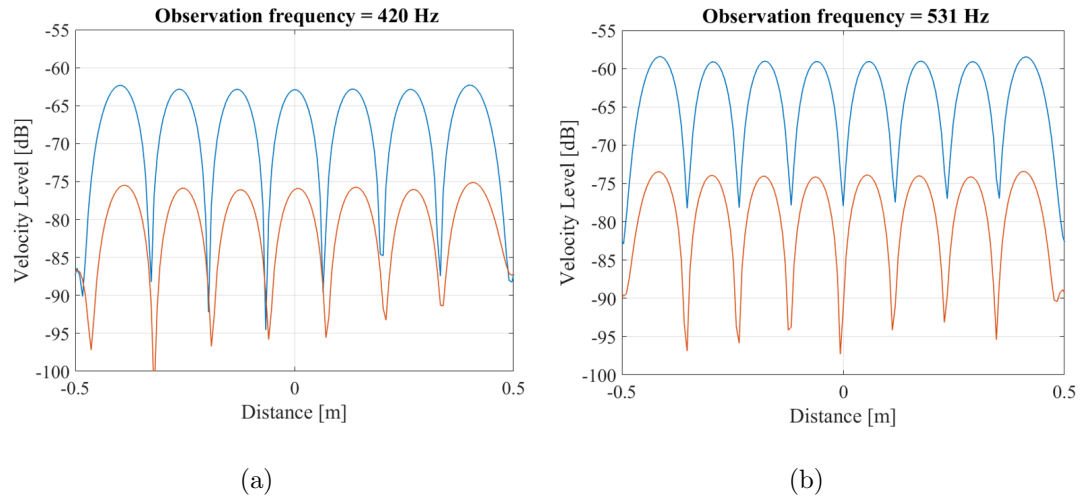


Figure 5.16. Spatial responses between the constraints at $x = \pm 0.5$ m for the 3 mm thick, bare fuselage-like structure (blue line) or the limp porous layer-treated fuselage-like structure (orange line) both driven by (a) subsonic convective pressure ($M = 0.8$) at 420 Hz, (b) supersonic convective pressure ($M = 1.2$) at 521 Hz.

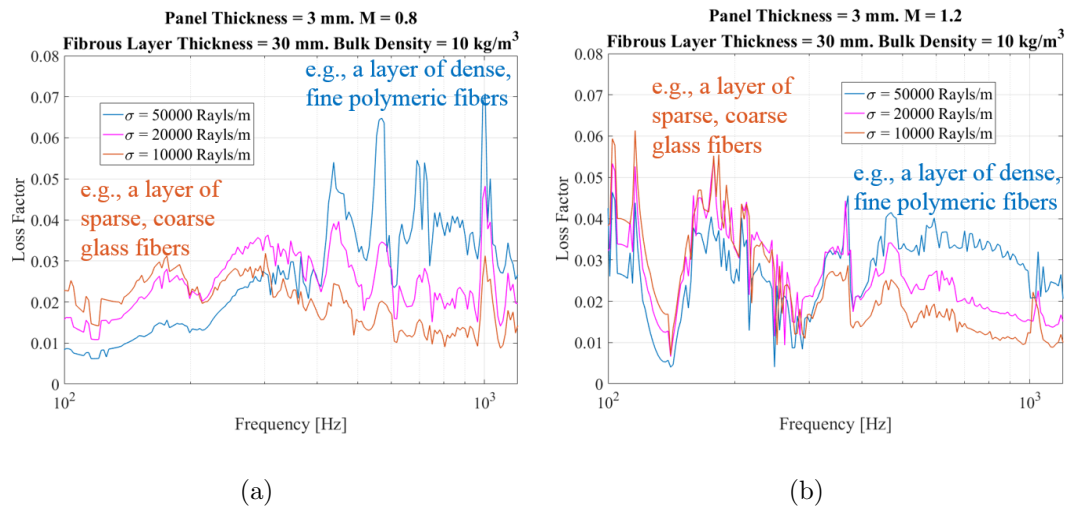


Figure 5.17. System equivalent damping loss factor for the 3 mm thick, fibrous layer-treated fuselage-like structure driven by (a) subsonic convective pressure ($M = 0.8$), (b) supersonic convective pressure ($M = 1.2$), with input fibrous layer's airflow resistivity as 10000 Rayls/m (orange line), 20000 Rayls/m (magenta line), 50000 Rayls/m (blue line).

6. THE AIRFLOW RESISTIVITY (AFR) MODEL TO BUILD THE MICRO-BULK RELATIONS FOR FIBROUS MEDIA

6.1 Introduction

The predictions shown in the last chapter were all based on porous media's bulk properties inputs, and the results indicated that for a specified vibrating structure, the optimal damping performance at certain excitation frequencies results from certain bulk property combinations of the treatment, and that the optimal bulk property combinations at different frequencies could be easily identified by parametric studies.

Inspired by the previous findings, the studies presented in this chapter focus on building the relations between the microstructure and bulk properties (also referred to as “micro-bulk relations”) of porous media that are made of fibers, so that the identified optimal bulk properties can be further translated into optimal microstructure details in terms of fiber sizes, based on which fibrous layers can be designed to maximize their damping performances.

For both limp porous and poro-elastic media, there are five geometry-related macroscopic properties to be taken account of: layer thickness, d , porosity, ϕ , tortuosity, α_∞ , bulk density, ρ_b , and airflow resistivity, σ . All of these bulk properties can be easily characterized by analytical, experimental or numerical methods [72–77]. For certain types of fibers, the first four bulk properties do not change very much when changing the microstructural parameters such as the fiber size: so they can be treated as empirical or fixed values. In contrast, the airflow resistivity results from the viscous drag exerted on the fibers by the oscillatory fluid flow, and it is very sensitive to microstructure variations. That behavior makes the airflow resistivity the most significant bulk property when building the dynamic connections between microscopic geometries and damping properties of fibrous layers.

Presented here is a new airflow resistivity (AFR) prediction model that accounts for situations in which a fibrous medium comprises more than one fiber component, and when the radius of each fiber component varies within a certain range. The intention of developing this model was to broaden the airflow resistivity prediction capability, since most of the existing models are only able to predict AFR for single component fibrous medium uniform fiber size, but there are novel fibrous material having multiple fiber components and varying fiber radii. Therefore, the target fibrous material selected for the current study (as shown in Figure 6.1) consists of one fiber component with relatively small and varying radius, here referred to as fiber component 1, and a second fiber component with relatively large and nearly uniform radius, here referred to as fiber component 2.

6.2 Single-Component Fibrous Media with Uniform Fiber Radius (SCUR)

The study started with the evaluation of existing AFR models, which were mostly developed for single-component fibrous media with uniform radius (SCUR). After comparing the SCUR prediction results with AFR measurements of single-component fiber samples, a model of Tarnow's [78] was shown to yield reasonable and accurate predictions and was chosen as the starting point for further development.

6.2.1 AFR-SCUR Models Review and General Comparison

All of the AFR-SCUR models that could be found in the literature were identified including Carman's model [79, 80], Langmuir's model [81], Davies' model [82], Happel's [83], Kuwabara's model [84], Pich's model [85], Tarnow's models [78], the BAL-semi-empirical model [19], Lind-Nordgren and Goransson's model [86], Doutres *et al.*'s model [87], and Pelegrinis *et al.*'s model [88]. The mathematical expressions of the models from 1997 and earlier were taken from Ref. [19], and all of the formulae are summarized in the Appendix E. In the literature, these AFR-SCUR models were originally developed for different kinds of porous media based on different assump-

tions of material microstructure. To explain this, a general view of the microstructure difference between two different porous media is shown in Figures 6.2(a)–fibers [89] and 6.2(b)–foams [90]. In the former case, the visco-thermal boundary layers are assumed to form around the exterior of the cylindrical fibers, while in the latter case, the boundary layers are assumed to form on the interior surface of pores of the partially or fully open foam cells. Despite being developed for different porous media, the reviewed AFR-SCUR models were found to be capable of predicting AFR for SCUR fibrous media due to their similarity in microscopically defining AFR, as they all defined the AFR of a porous layer as the cross-sectional drag force per mean spacing per unit mean flow velocity. This definition is physically reasonable since it corresponds with the AFR arising due to viscous drag from the solid phase of the porous material on the fluid flow. The definition is also mathematically reasonable since it has the same dimensions as the macro-definition of the airflow resistivity: the pressure drop per unit thickness per unit mean flow velocity. Due to that definition similarity, it can be seen that all the models mentioned above are similar in form. That is, all of these models allow us to calculate σ given the material's solidity, C , and the mean spacing, b^2 , of the Voronoi cells (shown in Figure 6.2(c)) [91].

To illustrate the calculation process, an example is presented here involving Tarnow's model [78] for the case of perpendicular airflow through a random fiber lattice (also referred to as the Tarnow Perpendicular-Random model). In that model, the AFR is expressed as

$$\sigma = \frac{4\pi\eta}{b^2(-0.64 \ln C - 0.737 + C)}, \quad (6.1)$$

where recall $\eta = 1.846 \times 10^{-5}$ kg/(s·m) is the dynamic viscosity of air when the temperature is 25 °C. In addition, the solidity, C , can be expressed as

$$C = \frac{\rho_b}{\rho}, \quad (6.2)$$

where ρ_b is the bulk density of the porous material and ρ is the density of the solid material of which the porous material is made. Furthermore, b^2 is a function of C and fiber radius (or strut radius of foams).

To fix the relation between C and b^2 , two assumptions need to be made. The first assumption is that the solid part of the porous material contributes all of the mass of the bulk porous material. The second assumption is that the fiber cylinders are uniformly distributed in an average sense within the porous material space. Then from the definition of solidity in Eq. (6.2), C is the ratio of the bulk density and the solid density, which, based on the first assumption, can be written as the total volume occupied by the fibers over the total volume of the porous material. Then for any cross-sectional area of a porous material sample, based on the second assumption, the ratio can be written as the total cross-sectional area of cylindrical fibers over the total cross-sectional area (or the fiber cross-sectional circle area per unit area). For SCUR fibrous media with a fiber radius, r , Eq. (6.2) can thus be written as

$$C = \frac{\pi r^2}{b^2}, \quad (6.3)$$

which also explains why the sum of the solidity and porosity equals 1; and further, the mean spacing, b^2 , of the Voronoi cells is

$$b^2 = \frac{\pi r^2}{C}. \quad (6.4)$$

Given the porous material microstructure details, C and b^2 can be easily calculated by using Eqs. (6.2) and (6.4), respectively, and their values can then be substituted into Eq. (6.1) to evaluate σ . Note that for SCUR fibrous media, Eq. (6.1) can also be written as

$$\sigma = \frac{4\eta C}{r^2 (-0.64 \ln C - 0.737 + C)}. \quad (6.5)$$

Based on the calculation routine mentioned in this example, all the AFR-SCUR models were first evaluated by calculating σ given C in the range of 0 to 0.03 (*i.e.*, porosities from 1 to 0.97 since fibrous media typically have high porosities), and r was set equal to 24.8 μm : the AFR results given by each model are plotted in Figure 6.3.

First note the very wide spread of the results, the spread being almost an order of magnitude. But, from the general comparison, some of the results can be numerically

grouped together. For example, the BAL-semi-empirical model gives results similar to Carman's model. Lind-Nordgren and Goransson's calculation is close to Doutres *et al.*'s, the Tarnow Perpendicular-Random model results are numerically similar to Langmuir's, Davies' and Pich's, and the Tarnow Perpendicular-Square model gives the same results as Kuwabara's. This general comparison provides a first view of where certain models stand compared to all the others.

6.2.2 AFR-SCUR Models Prediction Accuracy Evaluated by Comparison to Measurements

To help evaluate the accuracy of the various models, measurements of σ were made on six samples according to ASTM C522-03 [92] using the Gas Permeameter GP-05A-C-522 shown in Figure 6.4(a). All of the samples were made of the fiber component 2 mentioned above. A scanning electron micrograph view of this component is shown in Figure 6.4(b) to illustrate the uniformity of the fiber radii, and to confirm that they matched the SCUR case. Several pieces of material were gradually compressed to create different samples, which then differed in bulk density and solidity. In the measurements, the SCUR fiber AFR was estimated as

$$\sigma = \frac{\Delta p}{v_m d}, \quad (6.6)$$

where Δp was the measured pressure drop, v_m was the measured mean velocity of the airflow, and d was the thickness of the sample. Five measurements were made on each sample to show the measurement repeatability. For each sample, ρ_b could be measured. Then ρ and r could be specified so that C and b^2 could be calculated. For all of the samples, ρ was set equal to 1380 kg/m³, and r was set equal to 25 μ m.

Based on the calculation routine mentioned in Section 6.2.1, the corresponding σ 's were then predicted for each of the six samples using the different AFR-SCUR models. Then the predicted σ results from each model were plotted and compared to the measured σ results: see Figure 6.5. Due to the numerical similarity discussed in Section 6.2.1, only certain of the AFR-SCUR models are plotted in Figure 6.5.

From Figure 6.5, it can be seen that the measured results (consisting of five different measurements at each value of solidity) together with their least square fit lie between the Tarnow Perpendicular-Random model and Tarnow Parallel-Square model. Based on that result, it was decided to use the former model as a basis for further development for a number of reasons. First, that model is free of empirical or phenomenological parameters. Secondly, the case described in that model was considered to be closest to the actual situation when sound propagates through SCUR fiber. Thus, based on its prediction accuracy and these other factors, the Tarnow Perpendicular-Random model was chosen to be the candidate for further development.

6.3 Two-Component Fibrous Media with Various Fiber Radii (TCVR)

The Tarnow Perpendicular-Random (SCUR) model was then modified to make it capable of predicting the AFR for two-component fibrous media with various radii (TCVR) or uniform radii (TCUR) by adding the effect of multiple fiber components and fiber radii distributions. The AFR-TCVR model prediction accuracy was again verified by comparing predictions and repeated measurements.

6.3.1 AFR-TCVR Model Development

Previously, different approaches were proposed in the literature, Refs. [19, 72, 74, 75, 77], for taking account of the presence of multiple fiber components and/or fiber size distributions. The most appropriate approach for the current case was proposed in Ref. [19] and was applied here. As described in Section 6.2.1, σ can be predicted given C and b^2 by using the Tarnow Perpendicular-Random model. That is also true for the modified models, which means that modifications can be made to C and b^2 to account for the presence of multiple fiber components without changing the expression for σ given in Eq. (6.1).

The first modification converts C and b^2 from SCUR to TCUR by adding one more component to the model. For a TCUR fibrous media, the solidity is the sum of the fractional solidities of each component. Therefore, Eq. (6.2) can be written as

$$C = \frac{X_1 \rho_b}{\rho_1} + \frac{X_2 \rho_b}{\rho_2}, \quad (6.7)$$

where X_1 and ρ_1 are the weight fraction and solid phase density of fiber component 1, and X_2 ($X_2 = 1 - X_1$) and ρ_2 are the weight fraction and solid phase density of fiber component 2. Then based on the same assumptions mentioned in Section 6.2.1, Eq. (6.3) can be written as

$$C = \frac{n_1 \pi r_1^2 + n_2 \pi r_2^2}{b^2(n_1 + n_2)}, \quad (6.8)$$

where r_1 and r_2 are the fiber radii of TCUR fiber components 1 and 2, respectively, and n_1 and n_2 are the corresponding fiber counts. The fiber count for the TCUR fibrous media is defined as the number of fibers per unit cross-sectional area with the same radius (or the number of fibers of each fiber component). It follows that the ratio of the weight fractions of the two fiber components can then be written as

$$\frac{X_1}{X_2} = \frac{\rho_1 n_1 r_1^2}{\rho_2 n_2 r_2^2}. \quad (6.9)$$

By using Eqs. (6.8) and (6.9), the mean spacing, b^2 , of the Voronoi cells for a TCUR fibrous medium becomes

$$b^2 = \frac{\pi(X_1 \rho_2 + X_2 \rho_1) r_1^2 r_2^2}{C(X_1 \rho_2 r_1^2 + X_2 \rho_1 r_2^2)}. \quad (6.10)$$

Given the inputs of fiber radii r_1 and r_2 , densities ρ_1 and ρ_2 , and weight fractions X_1 and X_2 , the σ predictions can be made using the Tarnow Perpendicular-Random model by substituting C from Eq. (6.7) and b^2 from Eq. (6.10) into Eq. (6.1).

The second modification converts C and b^2 from TCUR to TCVR by adding discrete radii distributions to each component. The expression of C for a TCVR fibrous medium remains the same as Eq. (6.7) because it is calculated macroscopically and covers both the TCUR and TCVR cases. However, since the radii for each

component are not uniform for TCVR fibers, b^2 must be evaluated in a different way so that the variation of the fiber radii for each component is taken into account. Therefore, Eqs. (6.8) and (6.9) must now be written as

$$C = \frac{\pi \left(\sum_{p=1}^j n_{1,p} r_{1,p}^2 + \sum_{q=1}^k n_{2,q} r_{2,q}^2 \right)}{b^2 \left(\sum_{p=1}^j n_{1,p} + \sum_{q=1}^k n_{2,q} \right)}, \quad (6.11)$$

$$\frac{X_1}{X_2} = \frac{\rho_1 \sum_{p=1}^j n_{1,p} r_{1,p}^2}{\rho_2 \sum_{q=1}^k n_{2,q} r_{2,q}^2}, \quad (6.12)$$

and then the mean spacing, b^2 , of the Voronoi cells for a TCVR fibrous medium is

$$b^2 = \frac{\pi \left(\sum_{p=1}^j n_{1,p} r_{1,p}^2 + \sum_{q=1}^k n_{2,q} r_{2,q}^2 \right)}{C \left(\sum_{p=1}^j n_{1,p} + \sum_{q=1}^k n_{2,q} \right)}, \quad (6.13)$$

where the fiber component 1 has discretized fibers radii ranging from $r_{1,1}$, $r_{1,2}$, $r_{1,3}$, \dots , to $r_{1,j}$ ($r_{1,1} < r_{1,2} < r_{1,3} < \dots < r_{1,j}$), and corresponding fiber counts of $n_{1,1}$, $n_{1,2}$, $n_{1,3}$, \dots , to $n_{1,j}$, respectively. Similarly, the fiber component 2 has discretized fiber radii ranging from $r_{2,1}$, $r_{2,2}$, $r_{2,3}$, \dots , to $r_{2,k}$ ($r_{2,1} < r_{2,2} < r_{2,3} < \dots < r_{2,k}$), and corresponding fiber counts of $n_{2,1}$, $n_{2,2}$, $n_{2,3}$, \dots , to $n_{2,k}$, respectively. Here, the fiber count, $n_{1,1}$, means the number of fibers whose radii lie in the radius range $[0, r_{1,1} + 0.5(r_{1,2} - r_{1,1})]$, and the fiber count, $n_{1,2}$, means the number of fibers whose radii lie in the radius range $[r_{1,1} + 0.5(r_{1,2} - r_{1,1}), r_{1,2} + 0.5(r_{1,3} - r_{1,2})]$, *etc.*

To evaluate b^2 by using Eq. (6.13) in the AFR-TCVR model, recall r_1 and r_2 that appear in Eqs. (6.8), (6.9) and (6.10) of the AFR-TCUR model. Here, distribution parameters were first applied to r_1 and r_2 to generate random numbers obeying certain types of distributions. Then for each component, the discretized fiber radii with their corresponding fiber counts can be quantified by the histogram-estimated probability density function of the random numbers. The histogram is referred to as the fiber radii distribution function. And r_1 and r_2 are referred to as the peak fiber radii in the fiber radii distribution functions.

To be more specific, based on the weight fraction criterion expressed in Eqs. (6.7), (6.8) and (6.9), the raw estimation of total fiber counts, n_{ii} , for component ii ($ii = 1, 2$) can be first calculated from

$$n_{ii} = \frac{X_{ii}\rho_b}{\rho_{ii}(\pi r_{ii}^2)}. \quad (6.14)$$

Then, random numbers obeying a gamma distribution can be generated based on component 1 fiber total counts, n_1 , peak fiber radius, r_1 , the shape factor, s_1 and the scale factor, θ (*i.e.*, $\theta = r_1/s_1$), and the fibers of radii ranging from $r_{1,1}$, $r_{1,2}$, $r_{1,3}$, \dots , to $r_{1,j}$, and corresponding fiber counts of $n_{1,1}$, $n_{1,2}$, $n_{1,3}$, \dots , to $n_{1,j}$, can be estimated from the histogram of the probability density function of the gamma distributed random numbers. Similarly, random numbers obeying a normal distribution can be generated based on component 2 fiber total counts, n_2 , peak fiber radius, r_2 , the standard deviation, s_2 and the expectation, μ (*i.e.*, $\mu = r_2$), and the fibers of radii ranging from $r_{2,1}$, $r_{2,2}$, $r_{2,3}$, \dots , to $r_{2,k}$, and corresponding fiber counts of $n_{2,1}$, $n_{2,2}$, $n_{2,3}$, \dots , to $n_{2,k}$, can be estimated from the histogram of the probability density function of the normally distributed random numbers. Finally, by substituting C from Eq. (6.7) and b^2 from Eq. (6.13) into Eq. (6.1), the σ prediction can be made using the Tarnow Perpendicular-Random model for TCVR fibers.

6.3.2 AFR-TCVR Model Validation by Measurements

The validation focused on demonstrating the model prediction accuracy when all the fiber parameters, including the distribution of the fiber radii, were known. First, σ , together with ρ_b , X_1 , ρ_1 , r_1 , X_2 , ρ_2 , r_2 were measured or known for six TCVR samples. It should be noted that these samples are slightly different in ρ_b based on their basis weight (mass per unit area) measurements, but in this case these samples' X_1 's, ρ_1 's, r_1 's, X_2 's, ρ_2 's and r_2 's were all the same since they were composed of the same kind of fibrous components. And similar to the SCUR sample measurements, five groups of measurements were made on each sample to show the measurement repeatability. In addition, the fiber radii distributions were verified for all of the

samples based on micro-CT measurements. The micro-CT scanned distribution is shown in Figure 6.6(a). The regenerated distributions are shown in Figure 6.6(b), and the parameters used to regenerate the distributions are shown in Table 6.1. Now consider the fiber radii characteristics of the two-component fibrous medium captured by the micro-CT scan. During the distribution regeneration process, the gamma distributed random numbers mentioned in Section 6.3.1 were used for component 1, with a relatively large variation of fiber radius, and the normally distributed random numbers mentioned in Section 6.3.1 were used for component 2, with a nearly uniform fiber radius generated by setting the standard deviation to be very small. Thus, it should be noted that the predictions are based on repeated realizations of the model for a range of ρ_b that covered all the samples' bulk densities, so the n_1 and n_2 are different numbers in ranges corresponding to each realization from a single bulk density input. Given the samples' ρ_b , X_1 , ρ_1 , r_1 , X_2 , ρ_2 , r_2 as well as the distribution parameters corresponding to the regenerated fiber radii characteristics, the values of σ for the various samples were then predicted using Eqs. (6.1), (6.7) and (6.13), and the results are plotted in Figure 6.7. The blue dots show the predicted results of repeated realizations of the model for a range of bulk densities, and at the same time, allowing some randomness on the fiber radius distribution. The green dots show the predicted results of repeated realizations of the model for a range of bulk densities and certain verified fiber radii distribution shown in Table 6.1. In addition, the red crosses show the repeated measured σ 's for six different samples and the black dashed line is the least square fitting of the measured results. Thus finally, the prediction accuracy of the Tarnow Perpendicular-Random AFR-TCVR model was verified by the good agreement between the predictions (green dots) and the measurements (black line).

6.4 Conclusions

In this chapter, representative AFR-SCUR models were chosen for review and evaluation because of their similar form and micro-definition of AFR. On the one

hand, these models could be divided into different groups due to their implicit difference (fiber model, foam model, *etc.*). On the other hand, they could be divided into several groups due to the numerical similarity of the σ calculation.

The Tarnow Perpendicular-Random SCUR model was chosen to be the starting point of the AFR-TCVR model development because of its SCUR fiber AFR prediction accuracy, physical reasonableness, modernity, and its non-empirical nature.

By adding a second fiber component and radii distributions, the Tarnow Perpendicular Random SCUR model was modified to the Tarnow Perpendicular-Random TCVR model, and its TCVR fiber AFR prediction accuracy was also verified. The modified AFR-TCVR model provides us with a powerful tool to understand the micro-macro connections for fibrous acoustical materials including SCUR, TCUR and TCVR fibers. Combined with the acoustical and NFD models, the AFR-TCVR model will be beneficial for both performance prediction and microstructural optimization for porous acoustical plus damping treatments.

Table 6.1. Inputs for regenerating the measured TCVR fiber radii distributions.

ρ_1	n_1	r_1	s_1	θ
910 kg/m ³	7760–9830	5.5 μm	5	1.1×10^{-6}
ρ_2	n_2	r_2	s_2	μ
1380 kg/m ³	912–1155	13.1 μm	2.8×10^{-7}	13.1×10^{-6}

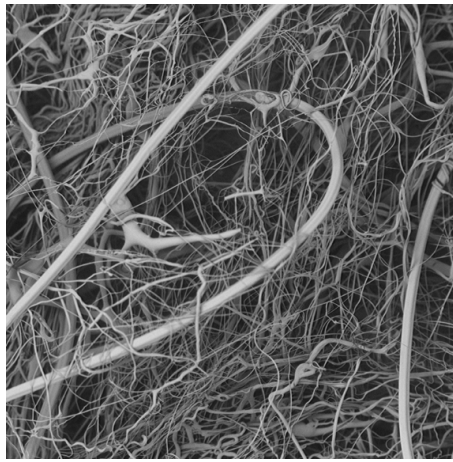


Figure 6.1. Target fibrous material of the current study with two fiber components and varying fiber radii.

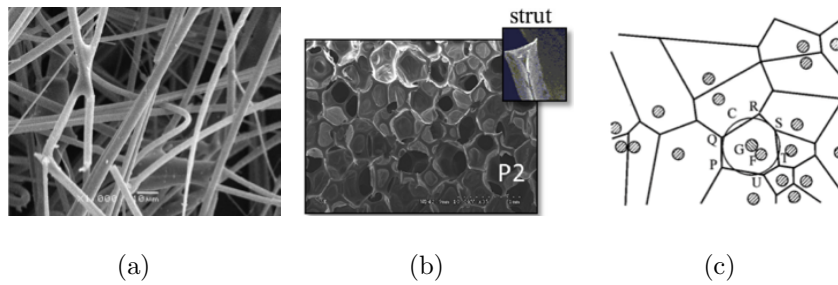


Figure 6.2. (a) Fibrous material microstructure [89], (b) partially-reticulated foam microstructure [90], (c) Voronoi cells [91].

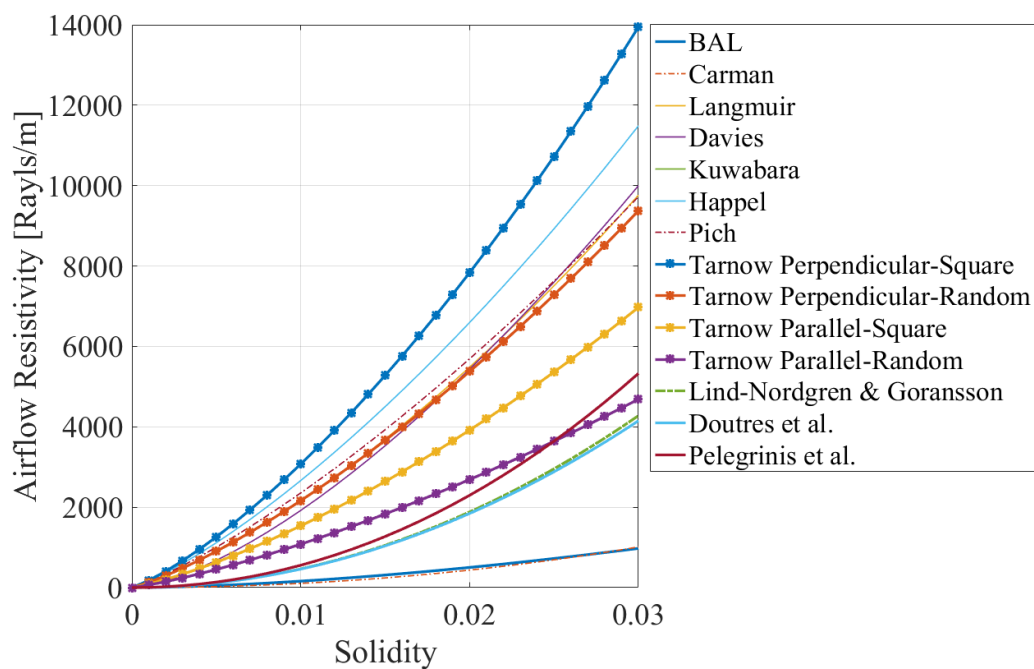
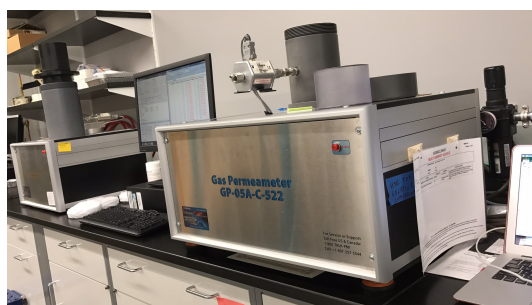
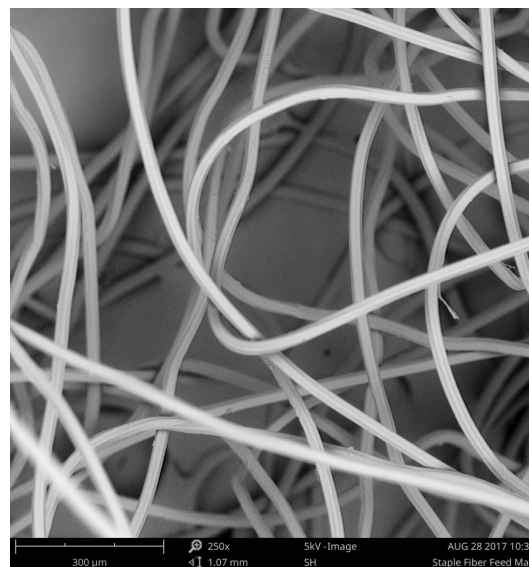


Figure 6.3. General comparison among AFR-SCUR models.



(a)



(b)

Figure 6.4. (a) Gas Permeameter GP-05A-C-522 for ASTM-C522-03 AFR measurements, (b) SEM view of fiber component 2.

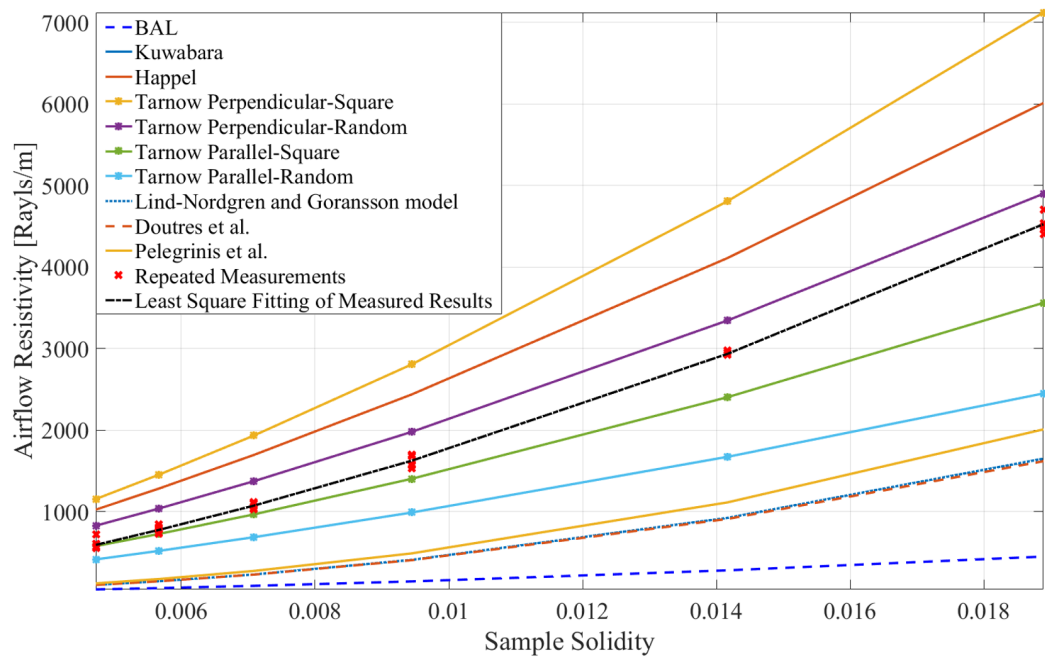
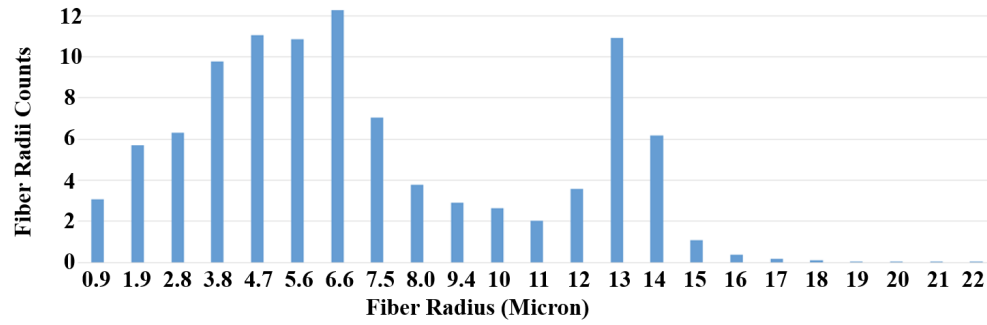
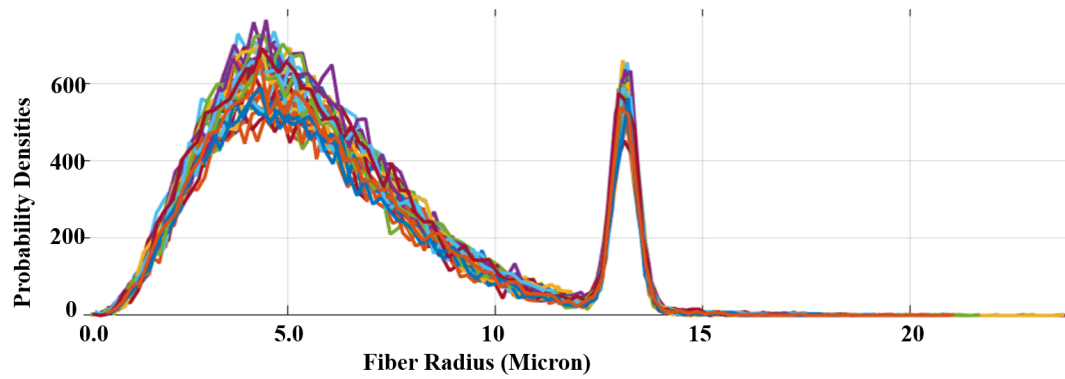


Figure 6.5. AFR-SCUR models predictions compared to measurements.



(a)



(b)

Figure 6.6. (a) Micro-CT scanned TCVR fiber radii distributions, (b) regenerated TCVR fiber radii distributions as inputs.

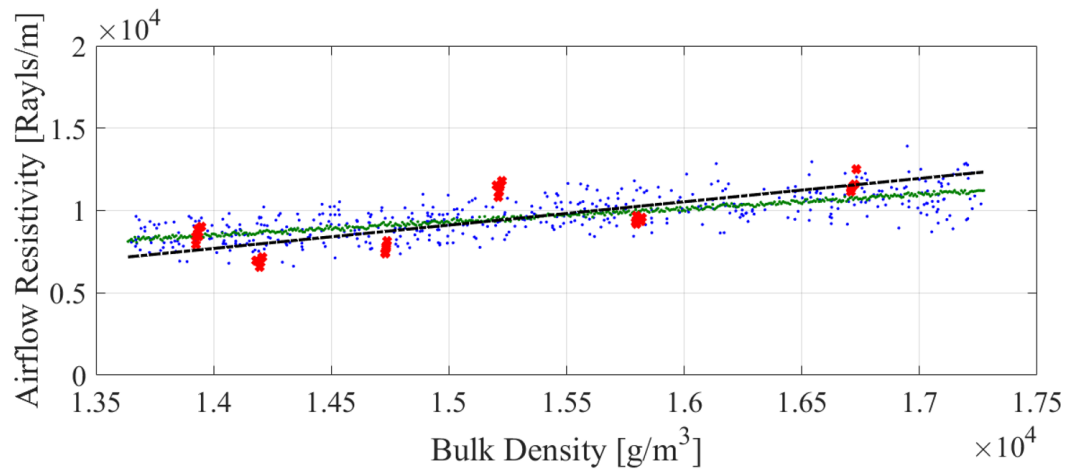


Figure 6.7. AFR-TCVR model predictions (marked as the blue dots) based on 500 normally-distributed (with mean value of $5.5 \mu\text{m}$ and standard deviation of $0.2 \mu\text{m}$) inputs of r_1 's corresponding to 500 uniformly-distributed (within $0.3\text{--}0.38 \text{ kg/m}^2$) inputs of basis weights, or (marked as the green line) based on a constant input of r_1 as $5.5 \mu\text{m}$ corresponding to 500 line-spaced (within $0.3\text{--}0.38 \text{ kg/m}^2$) inputs of basis weights, compared to the repeated measurements (marked as the red crosses) for six samples with verified microstructure details, and the 1st-degree polynomial fitting of the measured results (marked as the black line).

7. MICROSTRUCTURAL OPTIMIZATIONS FOR FIBROUS DAMPING TREATMENTS BASED ON THE AFR MODEL

7.1 Introduction

Based on the TMM/ACM, NFD and AFR models, an optimization process is introduced in Section 7.2 to find the optimal airflow resistivity and its corresponding optimal fiber radius which contribute to the largest damping given a specific frequency and panel of interest, and the optimized results of various types of fibrous damping media applied to different kinds of vibrating substrates are introduced in Sections 7.3, 7.4 and 7.5.

Finally, a practical case study is introduced in Section 7.6 to show the application of the validated NFD model and the Fourier transform technique to investigate limp porous media's damping performance when applied on a vibrating vehicle floor pan-like structure represented by a harmonic line force-driven, arbitrarily-shaped aluminum panel.

7.2 Finding Optimal Fiber Radii of Fibrous Damping Treatments

With well-developed micro-bulk relations based on the AFR model, a typical process for using analytical models to calculate the acoustical and damping properties of fibrous materials can be summarized as shown in Figure 7.1. After the characterization of the microstructure of the material, σ can be predicted by using an airflow resistivity (AFR) model. Then, the acoustical properties of the fibrous material can be predicted given the ambient properties (*e.g.*, the sound speed, air density, *etc.*) and the material bulk properties (including σ) by using the Transfer Matrix Method (TMM) [21] (for limp fibrous media) or Arbitrary Coefficient Method (ACM) [18] (for elastic fibrous media), which here incorporate the Johnson-Champoux-Allard (JCA)

model [16] (for calculating the viscous and thermal characteristic lengths, effective density and bulk modulus of the fluid phase of the material), the Biot theory, with either a limp [19–21] or elastic [15, 16, 18] frame approximation (for calculating the fundamental acoustical properties such as the complex density and complex wave number(s) of the material) and the layered structure Boundary Conditions (B.C.'s). Furthermore, the structural damping that the fibrous layer exerts on a nearby stiff panel due to the near-field damping (NFD) effect can be predicted using a specific beam theory (*e.g.*, Euler-Bernoulli beam theory) and numerical methods such as the inverse discrete Fourier transform (IDFT).

The process just described provides an approach for predicting acoustical and damping properties given the material's microstructural details. On the other hand, to realize the design of the microstructure, which means, in the first instance, that the microstructural details are assumed unknown, the process shown in Figure 7.1 must be reorganized as shown in Figure 7.2. For design purposes, first, the airflow resistivity, together with other bulk properties, are input as fixed values to the TMM/ACM and NFD models in a range, which returns a range of damping property predictions. Then the optimal damping property is selected together with its corresponding input airflow resistivity (referred to as the optimal airflow resistivity). Finally, based on the selected optimal airflow resistivity, a numerical optimization method performed by least squares fitting is applied, combined with the AFR model, to identify the microstructure that will create this optimal airflow resistivity, which means, with this microstructure, the optimal damping performance of the fibrous layer will be realized. Note that there were mainly two reasons for the airflow resistivity to be chosen among all the bulk properties as the connection between fibrous media's microstructure and their damping performance: (1) fibrous materials' acoustical/damping performance is highly sensitive to the variation of the airflow resistivity so that it serves as a good optimization variable; and (2) the microstructure of a fibrous material in terms of the fiber size has a linear relation with its airflow resistivity, which ensures that a global instead of local optimal point can be found.

Thus, according to this design process, given any frequency and panel of interest, there are four objectives: (1) find an appropriate property to evaluate the damping performance; (2) find the optimal damping and the corresponding optimal airflow resistivity; (3) translate the optimal airflow resistivity into the optimal microstructure to realize the microstructure design; and (4) understand the relation between optimal microstructure and optimal damping performance, and summarize the design insights related to damping-oriented fibrous materials. It should be noted that the optimal airflow resistivity and corresponding microstructure provide the optimal damping by taking energy out of the oscillatory, evanescent, short-wavelength near-field. Though it has been found that the designed material also helps with the acoustical performance (as shown in Section 5.2.2), it is unlikely that the material would provide the optimal acoustical performance at the same time since the acoustical attenuation is achieved by taking energy out of a propagating, relatively long-wavelength sound field. The acoustical properties referred to here primarily serves as intermediate properties in the design process.

Based on the prediction and parametric studies described in Chapter 5, both the power dissipation, P_d , within the porous layer and the system equivalent damping loss factor, η_e , can be used as an appropriate property to evaluate the damping performance. In this chapter, the optimization process is introduced based on finding the optimal airflow resistivity and optimal fiber radius that contribute to the largest η_e for certain frequencies and panels of interest. At a specific frequency, ω_0 , when we input an array of σ 's over a relatively wide range (*e.g.*, 500–5000000 MKS Rayls/m), each of those σ 's will return a corresponding η_e calculated using the TMM/ACM and NFD models given the other material bulk properties, panel-related properties and properties of the air. Then amongst all the returned η_e 's, the largest value can be easily found and referred to as $\eta_{eo}(\omega_0)$, which then identifies the optimal damping performance at ω_0 . Thus, among the input σ 's, the one corresponding to $\eta_{eo}(\omega_0)$ is the optimal airflow resistivity, σ_o , at ω_0 .

Further, if the microstructure of certain type of fibers is to be designed, then the AFR model can be used in an inverse sense to find the optimal material microstructure based on the optimal airflow resistivity. To be more specific, a microstructure design target should be chosen first (*e.g.*, r_1 of TCVR fibers, since it was found that component 1 was the main contributor to the airflow resistivity). Then instead of inputting one value of r_1 as for the prediction, one can input an array of r_1 's covering a reasonable range. Each of these r_1 's will return a corresponding σ by use of the AFR model given the other microstructural details including the fiber radii distribution parameters. Among all the σ results, the value closest to the σ_o can be found by least squares fitting and will be referred to as σ_{fit} . Finally, amongst the input r_1 's, the one corresponding to σ_{fit} is chosen as the fibrous medium's optimal fiber radius.

This optimization procedure is illustrated in Section 7.3 for the design of a TCVR fibrous damping treatment applied to an unconstrained aluminum panel. Note that TCVR fibrous media are the target materials studied here due to their novel microstructure, but the AFR model prediction capability and the microstructure design procedure are not limited to TCVR fibers but are also applicable to fibers with simpler (*e.g.*, SCUR fibers) or more complicated microstructure (*e.g.*, multiple components). The optimization procedure for SCUR fibers applied to more realistic structures including a partially-constrained structure and a fuselage-like structure is introduced in Section 7.4 and 7.5, respectively.

7.3 Optimized Limp Fibrous Damping Treatments for an Infinitely-Extended Vibrating Panel

For a 3 mm thick, harmonic line force-driven, unconstrained aluminum panel treated by a 3 cm limp TCVR fibrous layer (as shown in Figure 4.1), the η_{eo} 's and σ_o 's were identified based on the procedure described above at 10 different frequencies within the range from 100 to 1000 Hz, given $h_p = 3$ mm, $F = 1$ N/m and the bulk property inputs for the air, the panel and the treatment as listed in Tables 4.1, 4.2 and

4.5, respectively, except that there were 200 log-spaced σ 's being input in a range from 500 to 500000 Rayls/m for each frequency. The microstructural parameters shown in Table 7.1 (including 100 r_1 's ranging from 0.11 to 11 μm) were then input to the AFR model to return 50 predictions of σ 's as the optimization candidates. Recall that s_1 and s_2 that appear in Table 7.1 are parameters that characterize the fiber radii distributions. Then based on the σ_o 's (plotted as blue stars in Figure 7.3) found previously, the least-squares-fitted σ_{fit} 's were selected from the candidates and plotted as orange stars in Figure 7.3. Finally, the optimal r_1 's corresponding to the σ_{fit} 's were found and are shown in Figure 7.4.

Further, four optimal r_1 's designed at 100 Hz (blue dashed circle), 300 Hz (red dashed circle), 500 Hz (green dashed circle) and 700 Hz (purple dashed circle) are highlighted in Figure 7.4. The fiber radii distributions corresponding to these frequencies were regenerated based on the AFR model and are shown in Figure 7.5. It can be seen clearly from the results that the optimal r_1 's tend to be smaller when considering higher frequency excitation, which conversely means that relatively large fibers are more effective at damping lower frequency vibration.

7.4 Optimized Limp *vs.* Elastic Fibrous Damping Treatments for a Partially-Constrained Vibrating Panel

For a 1 mm thick, harmonic line force-driven, partially-constrained aluminum panel treated by a 3 cm limp or elastic SCUR fibrous layer (as shown in Figure 4.4 or 4.5, respectively), the η_{eo} 's and σ_o 's were identified, given $h_p = 1$ mm, $F = 1$ N/m and the parameters listed in Tables 4.1, 4.2 and 4.5, 4.6 and 5.1, except for an array of 200 log-spaced σ candidates ranging from 500 to 500000 Rayls/m, the optimal σ 's that result in the largest η_e 's at ten frequencies (equally-spaced from 100 to 1000 Hz) were found for either a limp porous or a poro-elastic layer. The optimal σ 's are plotted in Figure 7.6, from which it can be observed that larger σ 's are better at reducing higher frequency vibration. The resulting largest η_e 's at each frequencies

are plotted in Figure 7.7, which shows that a layer of properly-designed poro-elastic layer can achieve larger optimal damping than the corresponding limp porous layer.

Furthermore, the microstructural design for a specific type of porous medium can be realized by translating the optimal airflow resistivity into the optimal microstructure of the SCUR fibrous medium based on a given micro-bulk relation. In the current study, the optimal σ 's shown above were translated into the optimal fiber radii, r_1 's, based on the AFR model previously described in Chapter 6, and an assumption that both the poro-elastic and limp porous media comprised single component, uniformly-sized fibers, with a solid material density of 910 kg/m^3 (typical of a polymer fiber). Similar to the unconstrained panel case described above, the optimal r_1 's for either a limp or elastic fibrous layer were chosen from a range of $0.11\text{--}11 \text{ }\mu\text{m}$, and are shown in Figure 7.8, which generally shows that relatively large fibers are required to achieve optimal damping at lower frequencies (the same trend as observed in Section 7.3). Also, it can be observed the optimal damping for elastic fibers is achieved at a larger fiber size than is required for limp fibers. That finding could translate into a potential manufacturing benefit from using a stiffer fibrous medium as a damping treatment, since it is generally easier and less costly to manufacture relatively large fibers.

7.5 Optimized Glass *vs.* Polymeric Fibrous Damping Treatments for a Fuselage-Like Structure

The optimal microstructure of the fibrous layer expressed in terms of the optimal fiber radius, r_1 , is then introduced based on a 3 mm thick, fuselage-like structure in this section. Given fibrous layer microstructural parameters as listed in Table 7.2 and the same parameters as described in Section 7.3 plus the constraint parameters as listed in Table 5.2, together with $h_p = 1 \text{ mm}$ and $P = 1 \text{ N/m}^2$, r_1 was optimized for both polymeric and glass fibers at ten different equally-spaced frequencies between 100 and 1000 Hz through the optimal damping selection process. The largest η_{eo} achieved by the two kinds of fibers' optimal fiber radii at each frequency under both

subsonic and supersonic convective excitations is shown in Figures 7.9, which shows that an equivalent level of damping can be achieved by the two kinds of fibers after the microstructural optimization. Note that the sudden rise of η_{eo} corresponds to the “dip” at 1000 Hz shown in Figures 5.14 and 5.15.

Further, the optimal fiber radii are shown in Figure 7.10, which generally shows that relatively large fibers are required to achieve optimal damping at lower frequency. Also it can be observed that a larger fiber size is required for polymeric fibers than for glass fibers to achieve an equivalent optimal damping (the same trend as observed in Sections 7.3 and 7.4). That finding could contribute to a potential benefit from using polymeric fibers (with fiber material density of 910 kg/m³) instead of glass fibers (with fiber material density of 2730 kg/m³) as a damping treatment for a aircraft fuselage due to manufacturing benefit.

7.6 Practical Case Study: A Vehicle Floor Pan-Like Structure with a Harmonic Line Force-Driven, Arbitrarily-Shaped Panel

Based on the validated TMM, NFD and AFR models, and on the idea that vibrating structures exhibit a certain wavenumber/frequency response spectrum such as the ones shown in Figures 4.9, 4.13 and 4.15, a case study is demonstrated in this section in order to extend the applications of the NFD model from vibrating structures with regular shapes to arbitrarily-shaped panel, which makes the modeling scenario more realistic. The objective in this case study was to optimize the damping performance of porous (fibrous) treatments when applied to this more realistic structure than the regular structures mentioned above. Therefore, the analytical models were combined with a numerical simulation based on a finite element model, owing to the fact that a finite element model is more flexible in creating realistic (irregular) geometries. It should be noted that the damping optimization process introduced here can be applied to different realistic structures, although only one representative example is shown in the following sections to illustrate this design and optimization approach.

7.6.1 General Approach

The first step of this approach was to build a irregular structure, like the very simple two-dimensional vehicle floor pan-like structure studied in this section, by using the finite element model, and to identify a target region from the wavenumber/frequency response of the structure, within which the response was to be reduced. At the same time, the damping performance of a fibrous layer was evaluated in terms of power dissipation in the wavenumber/frequency domain, and based on those results, the fibrous layer's damping was maximized within the target region, and the microstructure in terms of fiber radius that provides the maximum damping was found by using the design process mentioned above. Also, note that all the fibrous media studied here were assumed to be limp-framed and to consist of a single fiber component with a uniform fiber size.

Recall the flow chart shown in Figure 7.2 illustrates the analytical design process used to find the fiber radius that provides the largest damping (here referred to as the optimal damping) for a specific vibrating structure. There are two basic steps in this process: (1) evaluating the damping property of a fibrous layer by conducting a parametric variation of its bulk properties (typically based on its airflow resistivity); and (2) identifying the optimal damping and translating the corresponding optimal airflow resistivity into the optimal fiber radius. The details of this process are omitted from this thesis since they have been introduced and described several times previously. Also, when previously studying fibrous damping for regular vibrating structures, the optimal damping property was evaluated based on identifying either the largest power dissipation or the largest system equivalent damping loss factor at different excitation frequencies, without particular regard to the spatial effect of the damping.

In the current study, a wavenumber/frequency domain velocity response was calculated for a floor pan-like structure by applying the spatial Fourier transform to the output of the finite element model, and a certain wavenumber/frequency region of the response that showed a salient response was specified as the “strong vibration region”.

The energy dissipation per cycle was integrated within the strong vibration region to evaluate a fibrous layer's damping performance. By following the analytical design process shown in Figure 7.2, the damping performance of a specific fibrous layer was maximized within that strong vibration region, and the corresponding optimal fiber radius that contributed to the optimal damping was finally identified.

7.6.2 Identification of the Strong Vibration Region for a Floor Pan-like Structure

A simple line-driven, two-dimensional (2D) floor pan-like structure was created by using 2D beam elements and triangular mesh in COMSOL Multiphysics, and it is shown in Figure 7.11. The whole structure was a 1 meter long, baffled panel, clamped at both ends, made of 1 mm thick aluminum, loaded by an air half-space above it, and driven by a harmonic line force beneath it (in a vacuum) at $x = 0.382$ m. The input parameters for the panel and ambient medium (air) are as listed in Tables 4.2 and 4.1 plus $F = 1$ N/m. By changing the excitation frequency, the panel's transverse velocity response spectra can be calculated at different spatial points, and the responses at two points are shown as velocity amplitudes in Figure 7.12. Also, at different excitation frequencies, the panel's response can be plotted as a functions of space, giving the so-called "spatial response", and three spatial responses are shown in terms of the real parts of the transverse velocities in Figure 7.13.

The spatial response of the panel at any excitation frequency can then be Fourier transformed to the wavenumber domain. It should be noted that the 3148 spatial points output directly from COMSOL were not evenly distributed from $x = 0$ m to $x = 1$ m. Therefore, these 3148 spatial points were cubic-interpolated to give 213 evenly-spaced response points and were further zero-padded to 216 points to ensure good resolution and accuracy of the Fourier transform. The wavenumber/frequency domain velocity level (dB) of the line-driven, floor pan-like structure was evaluated at 1000 evenly-spaced frequencies ranging from 10 to 10000 Hz, and the resulting

wavenumber/frequency spectrum is shown in Figure 7.14. It can be observed that the response of this structure is largely subsonic by comparing the response curve and the sonic lines (marked in magenta): *i.e.*, the response that lies outside the sonic lines are created by waves propagating more slowly than the speed of sound in the ambient medium. This observation indicates that the velocity response spectrum up to 10000 Hz of this floor pan-like panel is sub-critical (*i.e.*, the critical frequency of this structure is above 10000 Hz). Finally, based on the observation of the velocity level of the spectrum (*i.e.*, areas in red show salient vibration, and areas in blue show relatively weak vibration), a wavenumber/frequency region showing prominent vibration was selected, and it is shown as a blue rectangle (500 to 1000 rad/m, 900 to 1600 Hz) in Figure 7.14. The objective is then to design a porous (fibrous) layer that effectively damps the motion within that region.

7.6.3 Evaluation of the Damping Performance for a Limp Fibrous Layer

The wavenumber/frequency response of the floor pan-like structure was evaluated to first identify the strong vibration region: *i.e.*, the target region. Then, for an infinitely-extended limp fibrous layer driven by a harmonic line force at $x = 0$ m (as shown in Figure 7.15), the near field damping performance of the layer can be evaluated based on the NFD model and power analysis as described in Chapter 4.

According to the TMM and NFD analytical models, the acoustic particle velocity at $z = 0$ for a bare limp layer can be expressed as

$$v_{z1}(k_x, \omega) = \frac{F}{Z_{a1}(k_x, \omega)}, \quad (7.1)$$

where F is the amplitude of the harmonic force per unit length in the y -direction, and Z_{a1} is the normal acoustic impedance at $z = 0$. Then, the acoustic particle velocity at $z = d$ can be expressed, per Eq. B.4 in Appendix B, as

$$v_{z2}(k_x, \omega) = \frac{v_{z1}(k_x, \omega)}{T_{21}Z_{a2}(k_x, \omega) + T_{22}}. \quad (7.2)$$

where Z_{a2} is the normal acoustic impedance at $z = d$, and T_{21} and T_{22} are the elements of the transfer matrix, $[T_{11}, T_{12}; T_{21}, T_{22}]$, for a limp fibrous layer, which can all be evaluated by using the TMM model as described in Appendix B, so that v_{z1} and v_{z2} can both be evaluated as functions of trace wavenumber, k_x , and angular frequency, $\omega = 2\pi f$. Then the power input into the system by the harmonic line force that was mapped as a function of k_x and ω can be expressed as

$$P_{\text{inp}}(k_x, \omega) = \frac{1}{4\pi} \text{Re} (F v_{z1}^*(k_x, \omega)), \quad (7.3)$$

the power radiation at $z = 0$ can be expressed as

$$P_1(k_x, \omega) = \frac{1}{4\pi} \text{Re} (Z_{a1}(k_{x,j}, \omega) |v_{z1}(k_{x,j}, \omega)|^2), \quad (7.4)$$

and the power radiation at $z = d$ can be expressed as

$$P_2(k_x, \omega) = \frac{1}{4\pi} \text{Re} (Z_{a2}(k_{x,j}, \omega) |v_{z2}(k_{x,j}, \omega)|^2). \quad (7.5)$$

Given the bulk properties of the limp fibrous layer together with the ambient (air) properties as listed in Tables 4.5 (except for layer depth $d = 5$ cm instead of 3 cm in this case study) and 4.1, the power dissipation within the fibrous layer could then be evaluated as

$$P_d(\omega) = P_1(k_x, \omega) - P_2(k_x, \omega), \quad (7.6)$$

and that function is mapped in Figure 7.16 over 2^{16} evenly-spaced k_x 's ranging from -250 to 250 rad/m and 1000 evenly-spaced f 's ranging from 10 to 10000 Hz. Note that the strong vibration region and the sonic lines are also marked in Figure 7.16 for reference. The energy dissipation per cycle per unit length in the y -direction can also be integrated within the strong vibration region to give

$$E_d = \sum_{f=900}^{1600} \frac{\sum_{k_x=50}^{100} P_d(k_x, 2\pi f) \Delta k_x}{2\pi f}, \quad (7.7)$$

7.7 Optimization of the Limp Fibrous Damping Treatment for a Vehicle Floor Pan-Like Structure

By following the forward design process shown in Figure 7.2, instead of a single airflow resistivity input, an array of 64 log-spaced airflow resistivities ranging from 5000 to 500000 Rayls/m were input to the analytical model, and the power dissipation within the fibrous layer corresponding to 16 of these airflow resistivities are plotted together in Figure 7.17. Also, E_d can be evaluated for each airflow resistivity, and that result is plotted in Figure 7.18, from which a peak value can be identified with a corresponding optimal airflow resistivity around 12000 Rayls/m. By using the AFR model described in Chapter 6 for a fibrous medium that has a single fiber component and uniform fiber size, the optimal airflow resistivity can then be translated into an optimal fiber radius of 3.6 μm . Further, to show the damping effectiveness of the microstructurally-optimized fibrous treatment, the wavenumber/frequency spectra within the strong vibration region for the untreated and treated panels are plotted in Figures 7.19(a) and 7.19(b), respectively, and the velocity level difference between an untreated and a treated panel within the strong vibration region is plotted in Figure 7.19(c), which shows vibration level reductions of up to 10 dB (especially at peak locations) when the floor pan-like panel was treated by the optimized fibers. A comparison between the treated and untreated panel in terms of spatial response at peak frequencies within the strong vibration target region is also shown in Figure 7.20 for the observation of the vibration reduction.

7.8 Conclusions

Based on the TMM/ACM, NFD and AFR models, predictions of near-field damping performance can now start with porous layers' microstructures. On the other hand, the microstructures of porous media can also be designed to maximize the material's damping performance. The microstructural design process based on the AFR model of fibrous media and optimization was first shown in Section 7.2.

The design process was then applied to three different cases: (1) an unconstrained panel treated by limp TCVR fibrous layer, (2) a partially-constrained panel treated by either a limp or elastic SCUR fibrous layer, and (3) a periodically-constrained panel (fuselage-like structure) treated by a limp SCUR fibers made of either glass or polymer. All three cases showed that relatively large fibers were found to be better at reducing lower frequency vibrations, while relatively small fibers were better at higher frequency damping. In addition, the elastic fibers were found to have not only damping but also manufacturing advantages over limp fibers after optimization, because the optimal damping for elastic fibers is achieved at a larger fiber size than is required for limp fibers, but the optimal damping level achieved by the optimized elastic fibers was higher than it was for limp fibers. A similar manufacturing benefit was also found for limp fibers made of polymer compared to the situation when it was made of glass, which could be a valuable design concept for aerospace industries.

Finally, based on the idea that vibrating structures exhibit a certain wavenumber/frequency response spectrum, the NFD model plus the optimization process was further applied to evaluate the power dissipated by a fibrous treatment as a function of wavenumber and frequency, and on identifying the material microstructure (*i.e.*, fiber size) required to maximize the power dissipation, and hence damping, in a specific wavenumber/frequency range. To demonstrate the wavenumber/frequency-matching procedure, an example involving a simplified model of a vehicle component was considered here, which showed how a fibrous layer can be designed to maximize its damping effectiveness when applied to a realistic base structure, such as an automotive floor pan.

Table 7.1. Parameters for the limp TCVR fibrous layer applied to the unconstrained structure.

ρ_1	X_1	r_1	s_1
910 kg/m ³	0.5	0.11–11 μm	5
ρ_2	X_2	r_2	s_2
1380 kg/m ³	0.5	13.1 μm	2.8×10^{-7}

Table 7.2. Parameters for the limp SCUR fibrous layer applied to the fuselage-like structure.

r_1	ρ_1 (polymeric fiber)	ρ_1 (glass fiber)
0.01–11 μm	910 kg/m ³	2730 kg/m ³

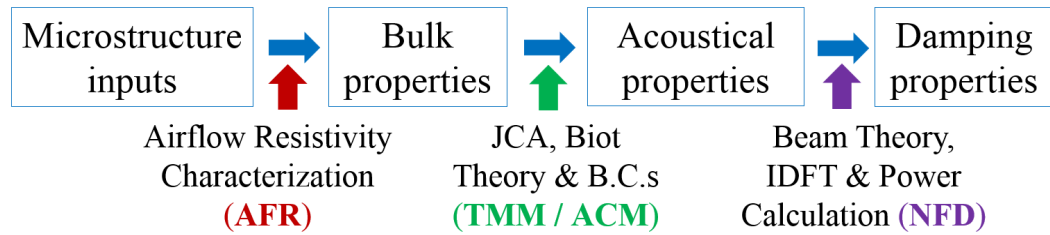


Figure 7.1. Fibrous material acoustical and damping properties prediction by an analytical approach.

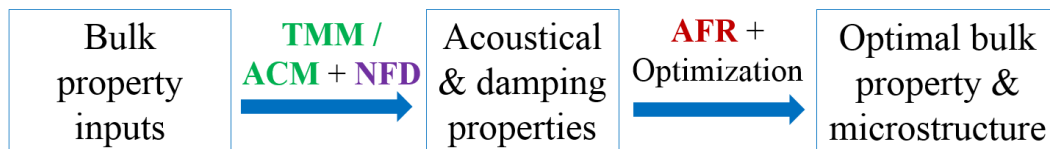


Figure 7.2. Fibrous material microstructure design by an analytical approach.

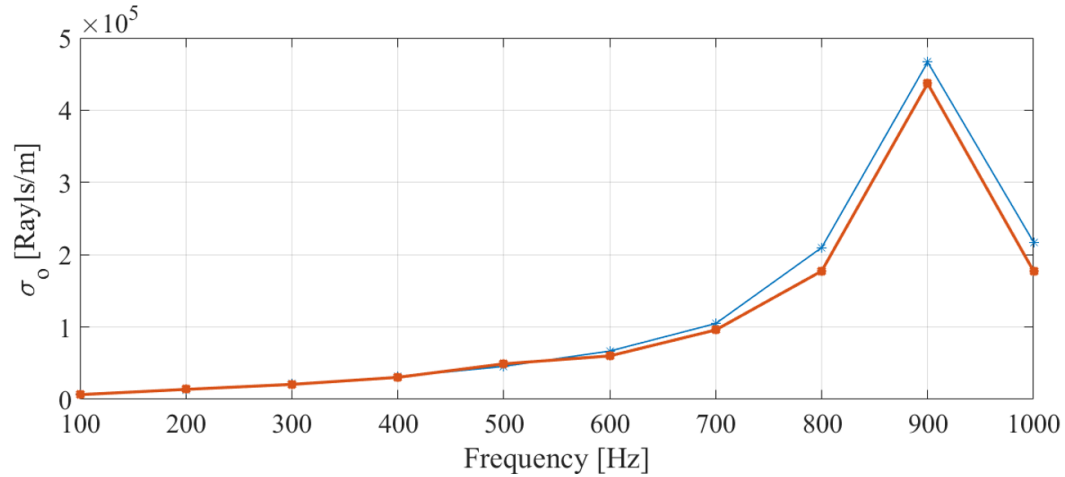


Figure 7.3. Optimal airflow resistivity, σ_o 's (blue stars) selected from 200 log-spaced σ candidates ranging from 500 to 500000 Rayls/m, and the AFR-TCVR model-fitted airflow resistivity, σ_{fit} 's (orange stars) corresponding to the optimal r_1 shown in Figure 7.4 for a 3 mm thick, unconstrained aluminum panel with a 3 cm layer of limp fibers, driven by a harmonic force under 10 different frequencies: line-spaced within 100–1000 Hz.

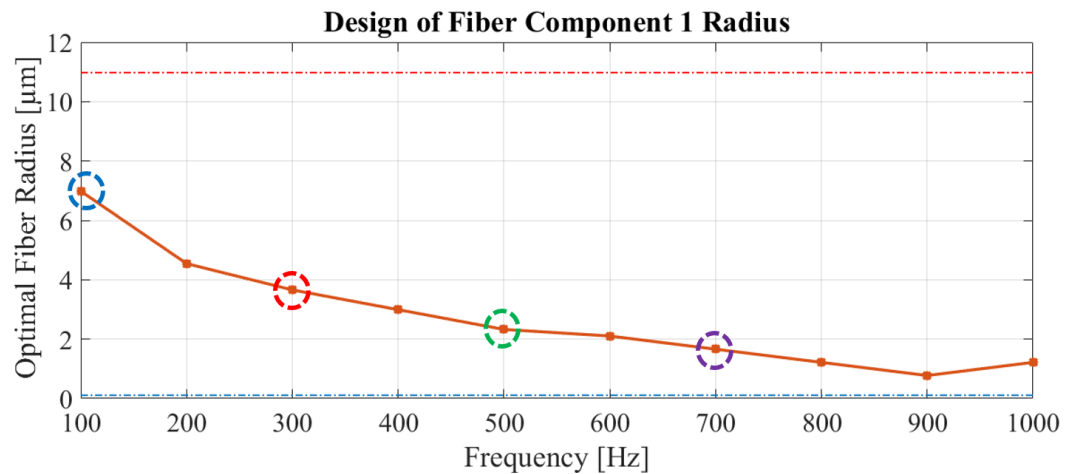


Figure 7.4. σ_{fit} -corresponded optimal r_1 (orange stars) identified from 100 line-spaced r_1 candidates ranging from 0.01 μm (blue dashed line) to 11 μm (red dashed line) for a 3 mm thick, unconstrained aluminum panel with a 3 cm layer of limp fibers, driven by a harmonic force under 10 different frequencies: line-spaced within 100–1000 Hz, with the optimal r_1 at four different frequencies: 100 Hz (in blue circle), 300 Hz (in red circle), 500 Hz (in green line) and 700 Hz (in purple line) being selected for radii distribution observation.

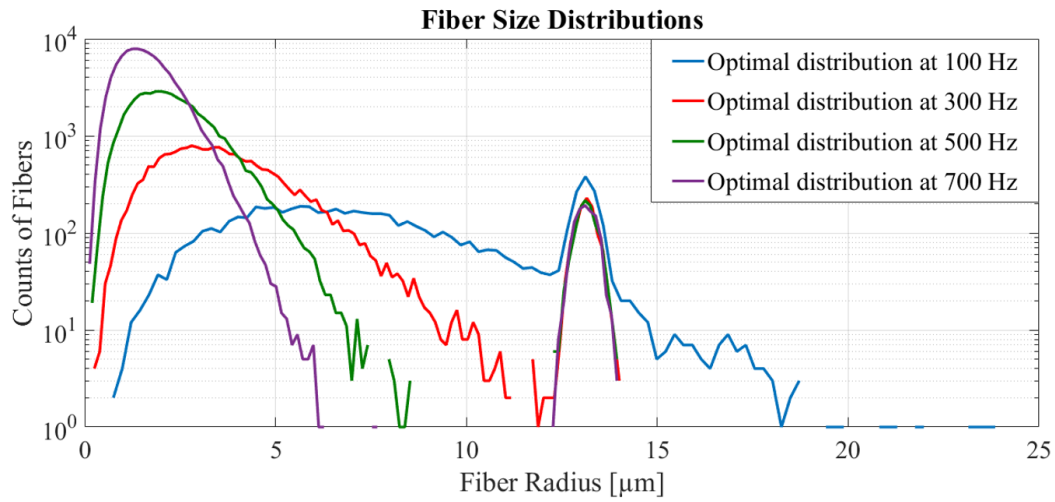


Figure 7.5. Regenerated fiber radii distributions corresponding to the optimal r_1 's designed for TCVR fibers for a 3 mm thick, unconstrained aluminum panel with a 3 cm layer of limp fibers (σ ranging from 500 to 500000 Rayls/m), driven by a harmonic force under four different frequencies: 100 Hz (blue line), 300 Hz (red line), 500 Hz (green line) and 700 Hz (purple line).

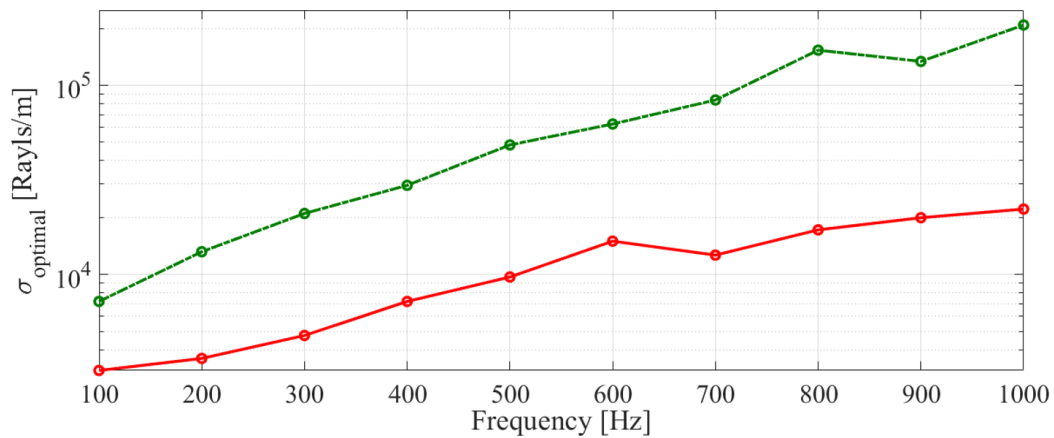


Figure 7.6. Optimal σ 's for either a 3 cm thick bonded poro-elastic layer (red solid line) or a limp porous layer (green solid line) to achieve the largest η_e 's when acting on a 1 mm thick, partially-constrained aluminum panel, driven by a line force at ten equally-spaced frequencies ranging from 100 to 1000 Hz.

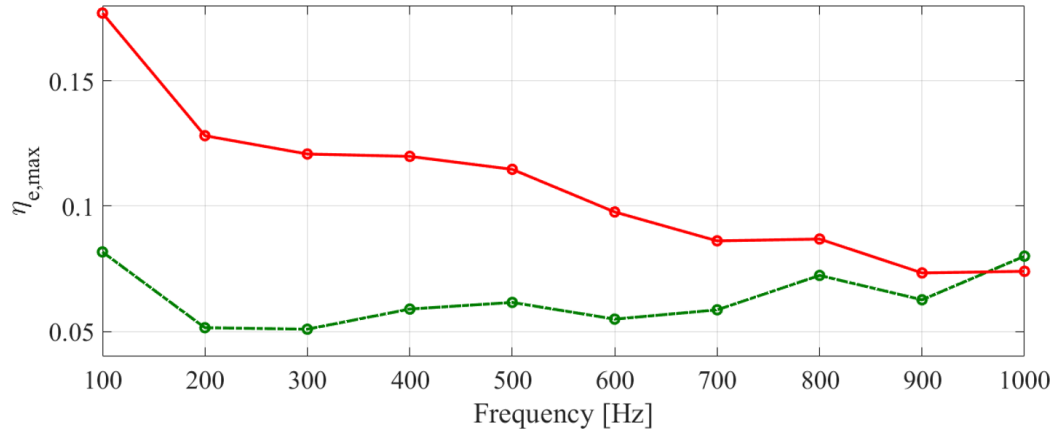


Figure 7.7. The largest η_e 's achieved by either a 3 cm thick bonded poro-elastic layer (red solid line) or a limp porous layer (green solid line) applied to a 1 mm thick, partially-constrained aluminum panel, driven by a line force at ten equally-spaced frequencies ranging from 100 to 1000 Hz.

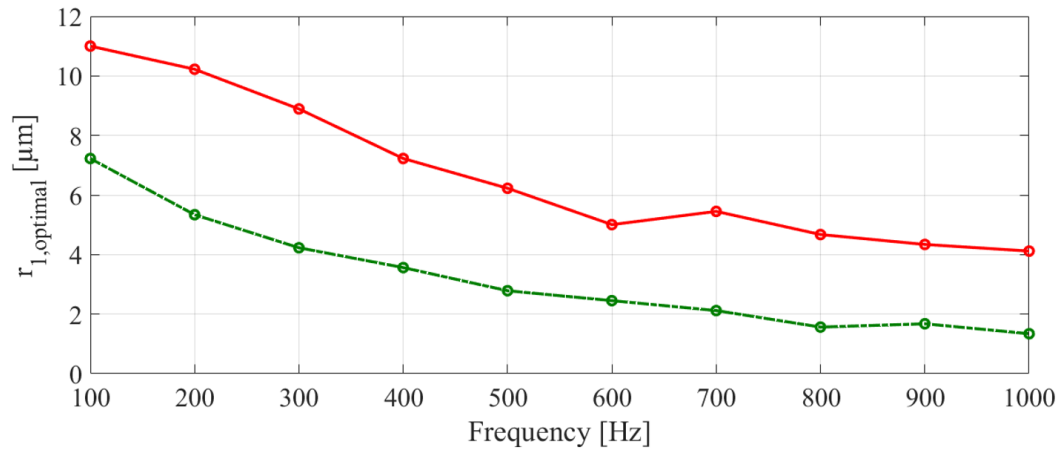


Figure 7.8. Optimal r_1 's for either a 3 cm thick bonded poro-elastic layer (red solid line) or a limp porous layer (green solid line) to achieve the largest η_e 's when acting on a 1 mm thick, partially-constrained aluminum panel, driven by a line force at ten equally-spaced frequencies ranging from 100 to 1000 Hz.

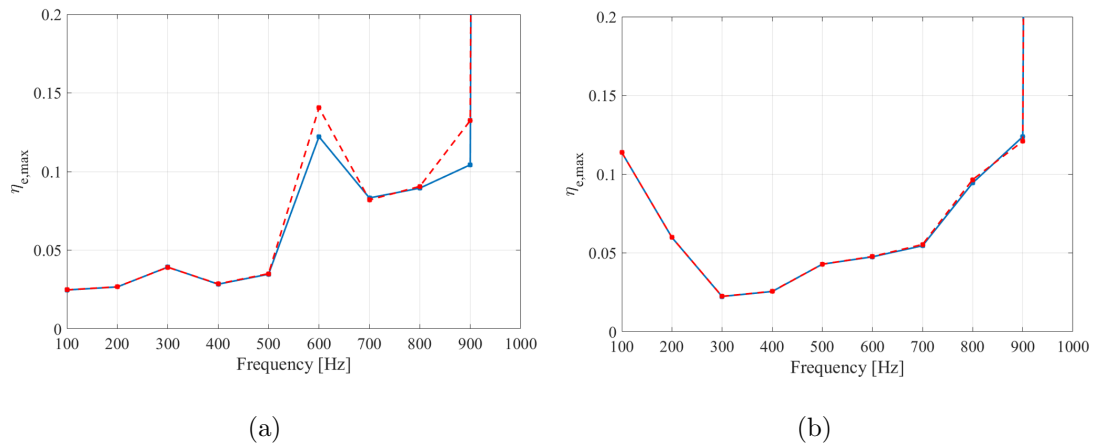


Figure 7.9. Optimal damping in terms of η_e achieved by a 3 cm thick layer of microstructural-optimized polymeric fibers (blue solid line) or glass fibers (red dashed line) for a 3 mm thick fuselage-like structure driven by (a) subsonic convective pressure ($M = 0.8$), (b) supersonic convective pressure ($M = 1.2$) at ten equally-spaced frequencies ranging from 100 to 1000 Hz.

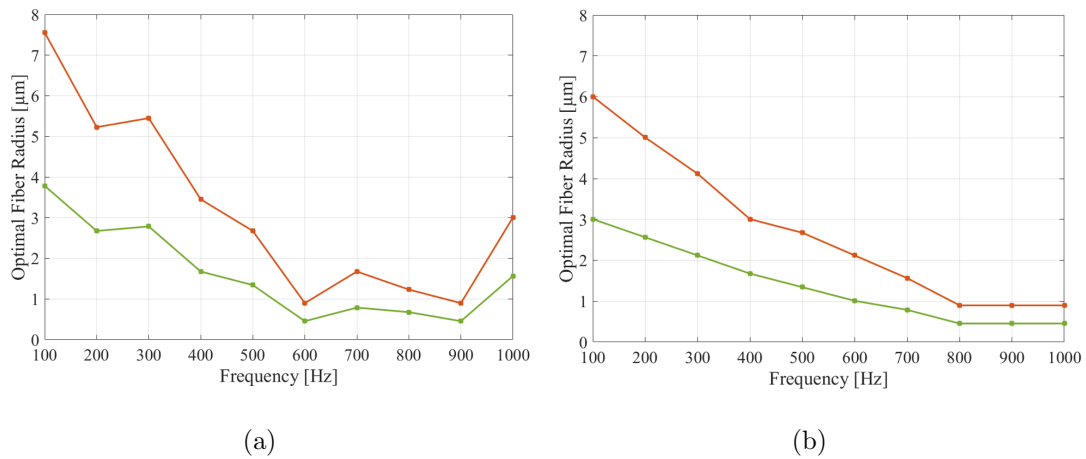


Figure 7.10. Optimal fiber radii, r_1 , designed for a 3 cm thick layer of polymeric fibers (orange line) or glass fibers (green line) to achieve the optimal damping for a fuselage-like structure driven by (a) subsonic convective pressure ($M = 0.8$), (b) supersonic convective pressure ($M = 1.2$) at ten equally-spaced frequencies ranging from 100 to 1000 Hz.



Figure 7.11. A 1 mm thick, harmonic line force-driven, arbitrarily-shaped aluminum panel to model a vehicle floor pan-like structure.

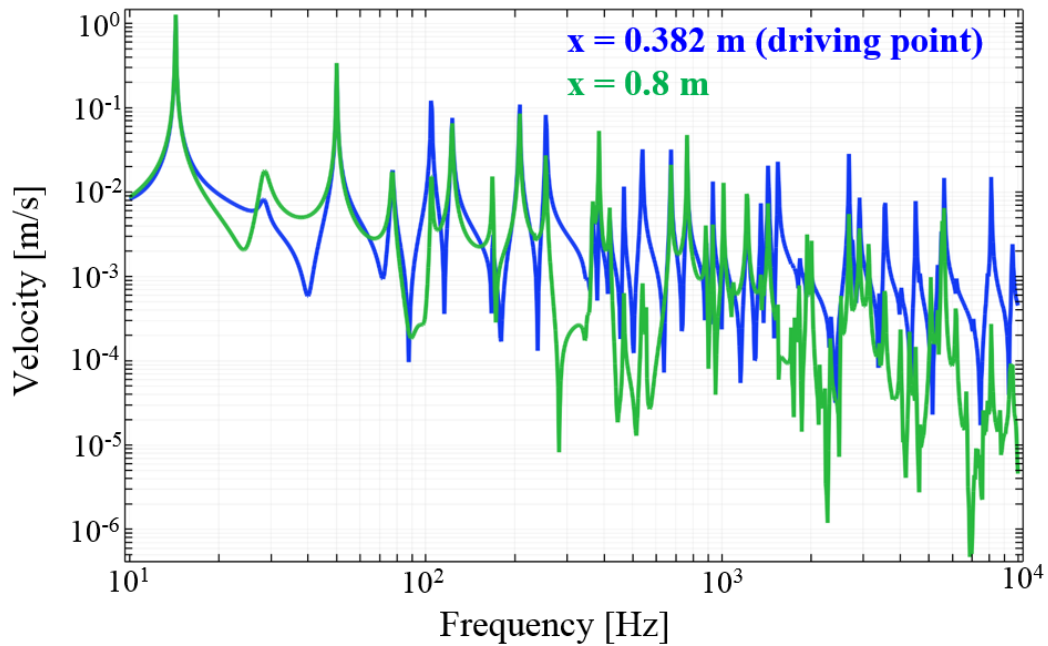


Figure 7.12. Transverse velocity response spectra at $x = 0.382 \text{ m}$ (blue line) and $x = 0.8 \text{ m}$ (green line) returned by the COMSOL finite element model.

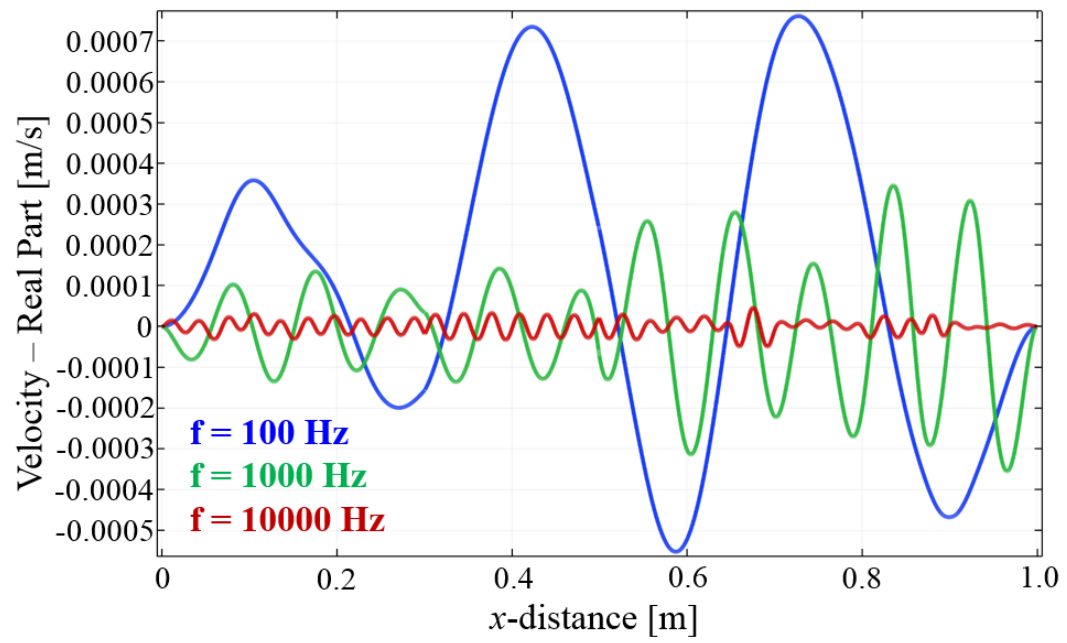


Figure 7.13. Transverse velocity (real part) spatial response at $f = 100 \text{ Hz}$ (blue line), $f = 1000 \text{ Hz}$ (green line) and $f = 10000 \text{ Hz}$ (red line).

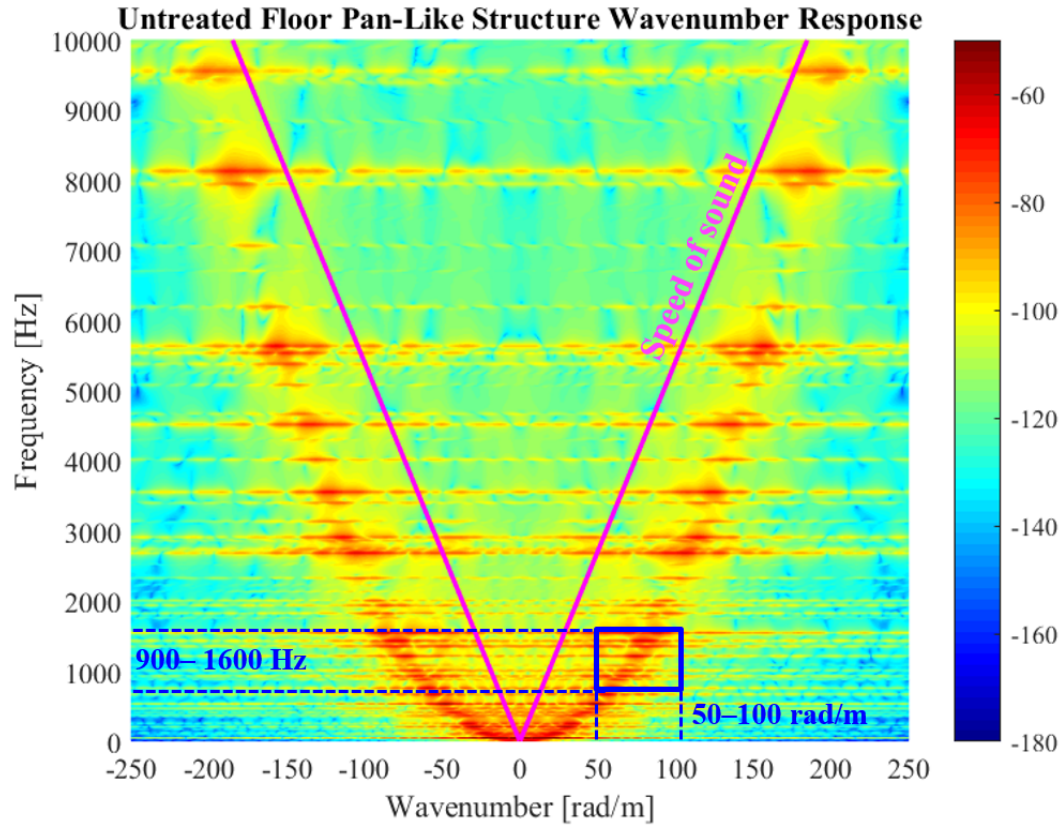


Figure 7.14. Wavenumber/frequency domain transverse velocity level (dB) of the bare (untreated) floor pan-like structure, with the strong vibration region marked in blue rectangle, and speed of sound (sonic) lines mark in magenta.

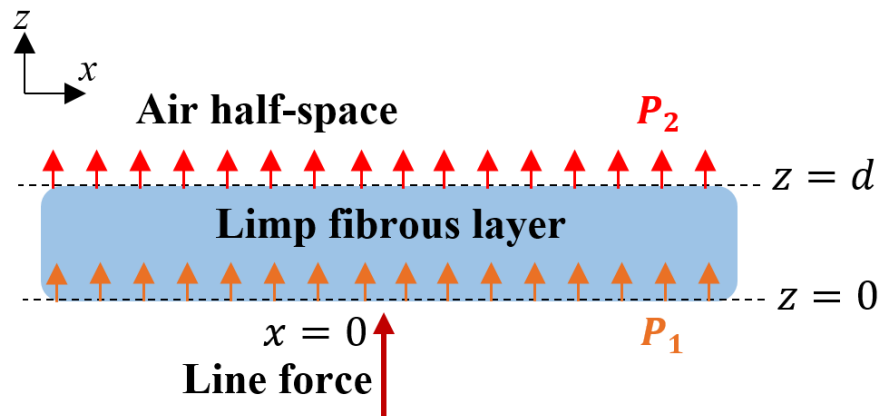


Figure 7.15. A line-driven, infinitely-extended bare limp fibrous layer for damping evaluation based on the NFD analytical model.

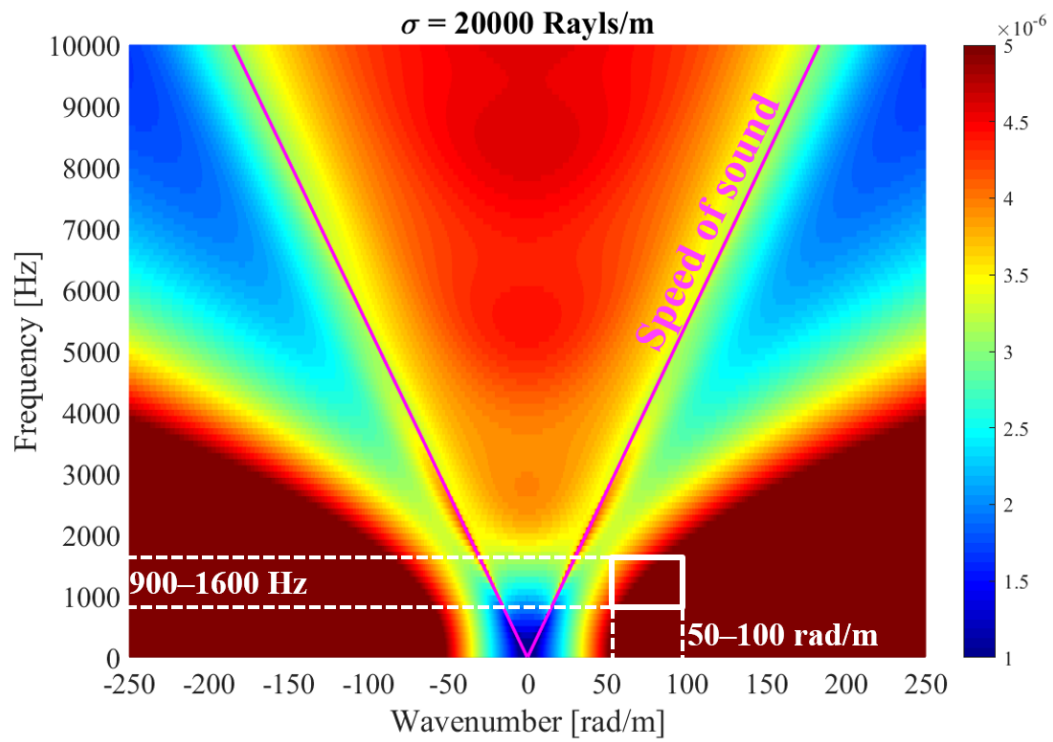


Figure 7.16. Power dissipation [W/m^2] within a line-driven, infinitely-extended limp fibrous layer.

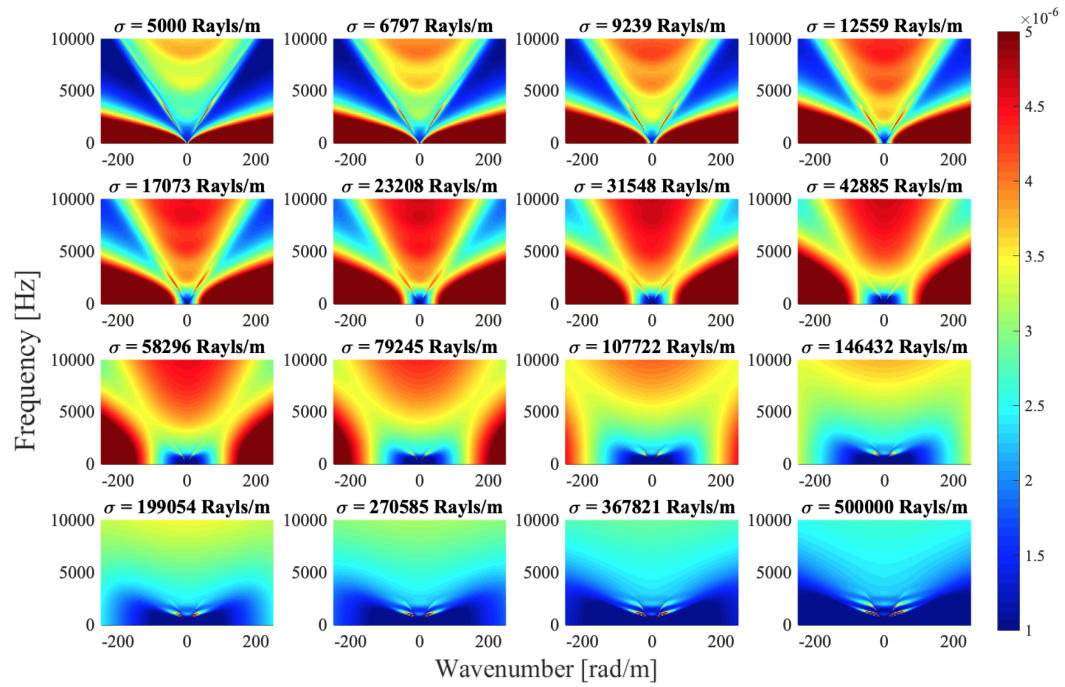


Figure 7.17. Parametric study of the effect of airflow resistivity on the fibrous layer's damping performance in terms of the power dissipation [W/m^2].

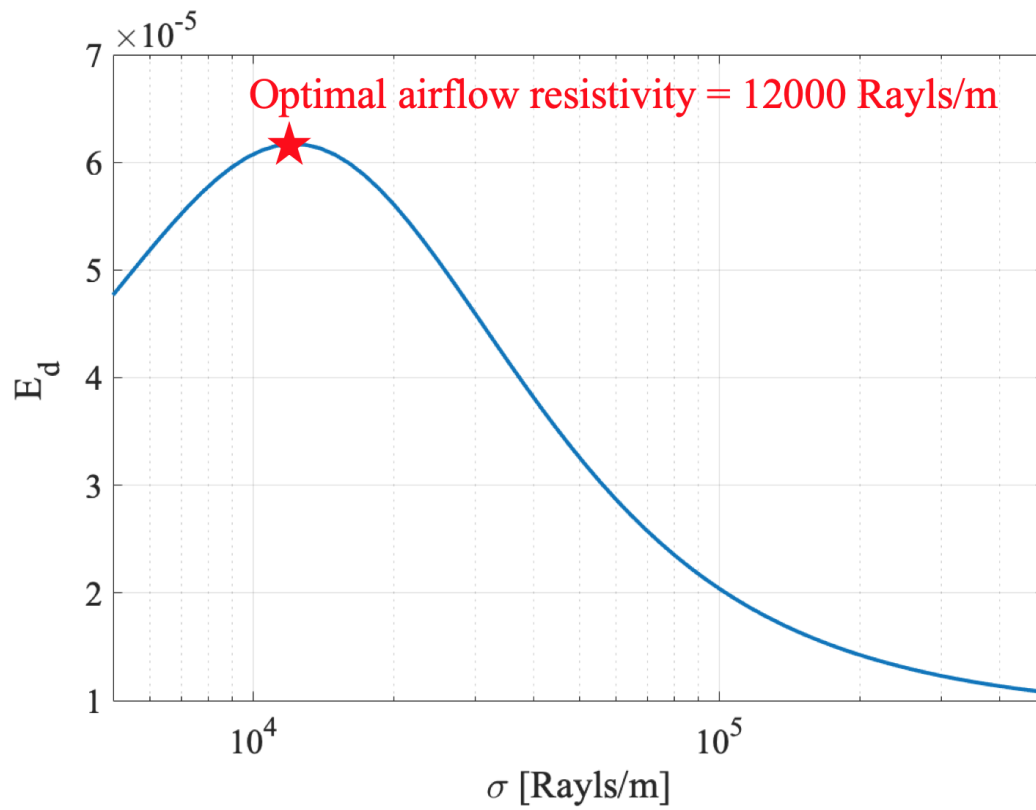


Figure 7.18. Energy dissipation per cycle per unit length of y -direction [J/m] within the strong vibration region under different airflow resistivities to identify the optimal airflow resistivity for the limp fibrous damping treatment.

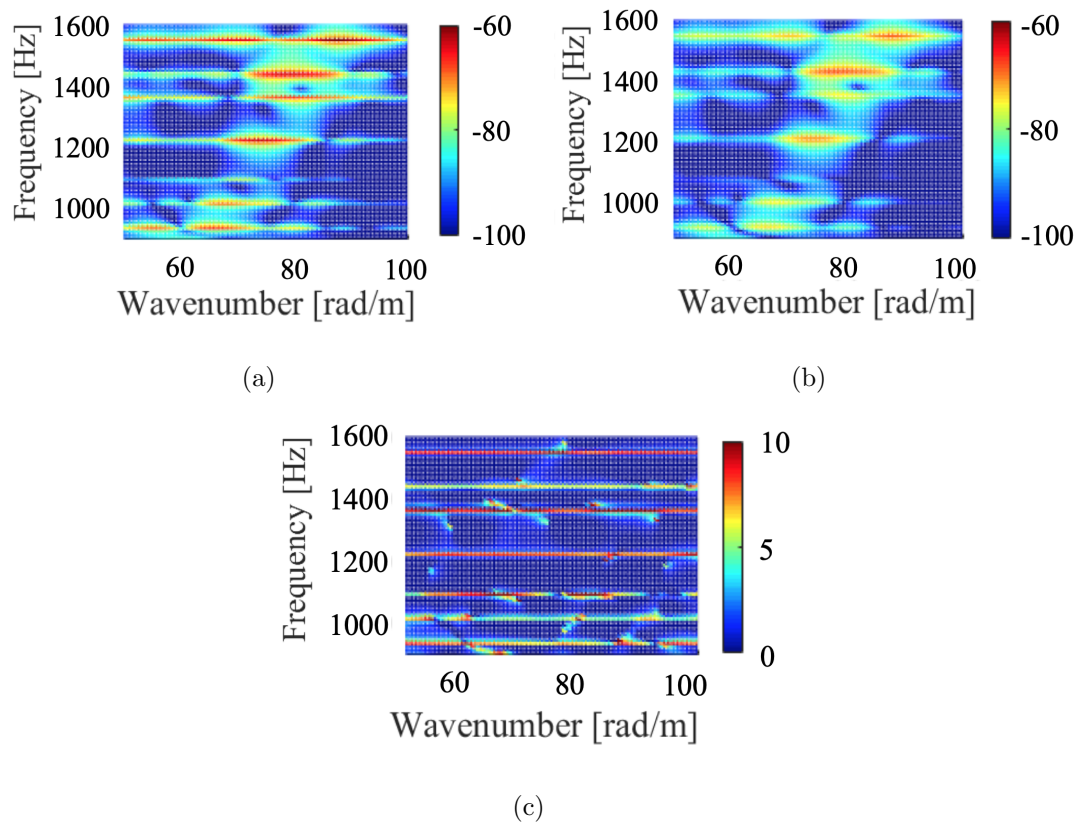
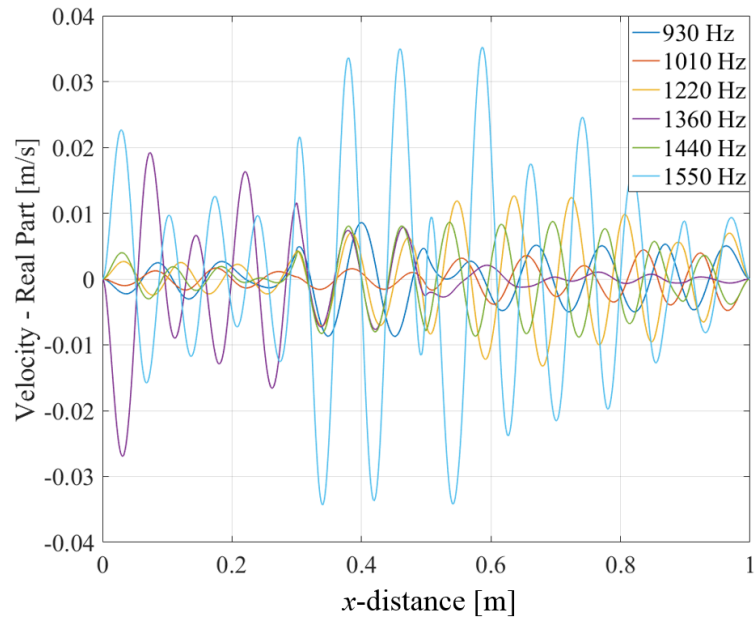
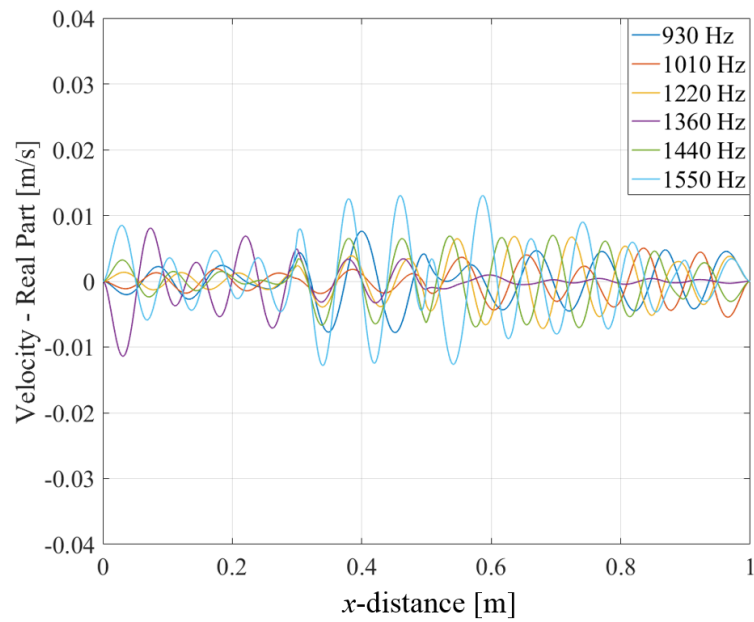


Figure 7.19. Wavenumber/frequency velocity level (dB) spectrum within the strong vibration region of (a) the untreated floor pan-like structure, (b) the floor pan-like structure treated by the optimized fibrous damping layer, (c) the difference between (a) and (b) to show the vibration reduction.



(a)



(b)

Figure 7.20. Spatial responses at peak frequencies within the target region of (a) the untreated floor pan-like structure, and (b) the floor pan-structure treated by the optimized fibrous damping layer.

8. CONCLUSIONS AND NEXT STEPS

8.1 Summary of Conclusions

Based on the state-of-the-art and classic theories of acoustics, modeling methodologies have been developed here into a comprehensive toolbox to model multilayer systems that involve acoustical and/or damping treatments, as well as to optimize the performance of those treatments by designing their geometrical structures, which allows the understanding, prediction and optimization of the near-field damping performance for porous media. Thus, the damping effectiveness can be maximized for porous materials, and that attribute can be exploited in combination with their conventional sound absorption features, lightness, and the advantage of temperature independence in contrast to conventional visco-elastic damping layer. The important conclusions based on the near-field damping studies on different porous damping treatments applied to various vibrating structures are summarized here.

There were three kinds of analytical models involved in this study: (1) the acoustical models including the Johnson-Champoux-Allard model introduced in Section 2.2, the Biot theory introduced in Section 2.3, the Transfer Matrix Method (TMM) for limp porous media introduced in Section 2.4.1 and Appendix B, the Arbitrary Coefficient Method (ACM) for poro-elastic media introduced in Section 2.4.2 and Appendix C and the TMM for the poro-elastic media introduced in Chapter 3, (2) the near-field damping (NFD) model (introduced in Chapter 4 and its incorporation with the TMM-limp model in Appendix B and ACM-poro-elastic model in Appendix C), mainly consisting of Euler-Bernoulli beam theory, inverse discrete Fourier transform (IDFT), and power analysis (power distribution and system equivalent damping loss factor); and (3) the micro-bulk relations in terms of the AFR model (introduced in Chapter 6, for SCUR, TCUR and TCVR fibers).

There were two types of porous damping treatments that were studied: limp porous media with negligible bulk elasticity of their solid frames, and poro-elastic media with non-negligible bulk elasticity of their solid frames, and they were studied based on four different kinds of vibrating structures (also referred to as “panels” or “substrates” in the thesis): (1) a harmonic line force-driven, infinitely-extended (unconstrained) panel; (2) a partially-constrained panel with two identical discontinuities (constraints); (3) a convective pressure-driven, periodically-constrained (fuselage-like) panel with uniformly-distributed discontinuities (constraints); and (4) a harmonic line force-driven, arbitrarily-shaped (vehicle floor pan-like) finite panel.

First, connections were built between porous media’s bulk properties and their fundamental acoustical properties, based on which, different acoustical models were then introduced for coupling and modeling multilayer acoustical systems that involve porous media. Given a specified layered structure consisting of a vibrating panel and a porous damping treatment, the acoustical models that include the Transfer Matrix Method (TMM) and the Arbitrary Coefficient Method (ACM) were then applied to characterize the acoustical properties of the panel’s acoustical near-field. Then, the incorporation of these acoustical models into the near-field damping (NFD) model makes it possible to predict the spatial response of the panel and the damping performance of the porous layer. Additional studies were also conducted during the near-field damping modeling process; for example, the relations between a porous medium’s bulk properties and acoustical properties were also modified to be applied for modeling double-phase porous media: *i.e.*, materials consisting of two different components such as fibers plus particles. In that case, the TMM model originally used for limp porous media was modified to be capable of coupling with poro-elastic layers or elastic solid layers in order to improve multilayer systems modeling efficiency. In addition, layered acoustical elements including various kinds of surface treatments, micro-perforated panels (MPP) and transversely isotropic poro-elastic (TIP) layers were also built into this toolbox to extend its modeling capability.

The application of the TMM/ACM plus NFD models provides a prediction toolbox to help us evaluate the damping performance of certain limp porous or poro-elastic layers acting on the specified panels. First, for both unconstrained and periodically-constrained panels, the toolbox verified that a limp porous layer provided significant attenuation of the panel motion, but primarily in the sub-critical frequency region, and that the damping effectiveness increased when the panel thickness decreased. And the layer also proved effective at controlling the sound radiation from the panel in the super-critical region (see Section 5.2 and 5.4). Also, the prediction toolbox was used to compare the normalized power dissipations within a poro-elastic and a limp porous layer when acting on an unconstrained panel structure, which revealed that a poro-elastic layer results in greater power dissipation than the limp porous layer due to the additional structural dissipation in the former medium, but that this superior performance could not be maintained when the poro-elastic layer was not directly bonded to the vibrating panel. The bonded poro-elastic layer was further shown to possess an overall damping advantage over the limp porous layer based on the system equivalent damping loss factor, η_e (see Section 5.3), when applied to a partially-constrained harmonic line-driven panel. Furthermore, the prediction models were used to study the damping performance of different layered porous media resting on either an unconstrained or a periodically-constrained panel (see Sections 5.2 and 5.4), according to which, limp porous damping treatment application guidelines can be summarized in three main findings: (1) with limited space and the same microstructure, a layer of glass fiber is heavier compared to a layer of polymeric fiber, but will improve the low frequency damping; (2) with limited weight and the same microstructure, a thin layer of glass fiber gives better low frequency damping, while a thick layer of polymeric fiber gives better high frequency damping; and (3) with limited space, limited weight and different microstructures, a layer of sparse, coarse glass fibers is better at reducing low frequency vibration, while a layer of dense, fine polymeric fibers is better at reducing high frequency vibration. These findings can thus be used as guidelines when applying these media in structural damping

applications. In addition, limp porous (fibrous) media's damping effectiveness were proven on both the fuselage-like and floor pan-like structures.

On the other hand, the process of microstructural design on the fibrous damping media was introduced in Section 7.2, and can be conducted based on using the AFR model in combination with the TMM/ACM and NFD models, in order to maximize a fibrous treatment's damping performance for a certain frequency and panel of interest. Limp TCVR fibers were designed for a harmonic line force-driven, unconstrained panel; limp and elastic SCUR fibers were designed for a partially-constrained panel (fuselage structure, see Section 7.5) and an arbitrarily-shaped panel (floor pan structure, see Section 7.7); and limp SCUR fibers that were made of either polymer or glass were both designed based on a fuselage-like panel. From the observation of the designed microstructures, design concepts for fibrous dampers can be summarized as: (1) larger fibers (*i.e.*, smaller airflow resistivities) were found to be more effective at reducing lower frequency vibrations; (2) elastic fibers have advantages with respect to both optimal damping and manufacturing over limp fibers, and (3) polymeric fibers were found to have a potential manufacturing benefit over glass fibers due to the larger fiber size required by the former material to achieve the optimal damping for a fuselage-like structure.

8.2 Recommendation of Next Steps

There are several potential studies that can be focused on in the future:

(1) Micro-bulk relations can be further developed for porous media with different types of microstructures: *e.g.*, open- or closed-cell foams, or for fibrous media taking the orientation of fibers into account by using numerical simulation and statistical methods.

(2) Sensitivity study can be conducted on the JCA inputs to understand and to modify the relations between porous media's bulk properties and their fundamental

acoustical properties especially for trendy materials such as nano-fibers and double-porosity materials.

(3) Adhesives can be modeled as elastic solid layers to bond a poro-elastic layer with a panel, and Rayleigh waves effect can be studied by using the TMM model proposed in Chapter 3 to make it more comprehensive.

(4) Zero modes and free modes appeared during the SVD process in Chapter 3 can be studied in combination with the conditioning of the TMM-poro-elastic model to make the package more numerically-stable and comprehensive especially for large layer depth, high frequencies and special case, such as double poro-elastic layers with a stiff panel bonded in between.

(5) Joint optimization can be applied to multilayered treatments considering practical limitations and materials' randomness to maximize both their acoustical and damping performance.

(6) A finite element periodic structure can be built for further validating, and mode localization literatures can be reviewed to understand and stabilize the results for the NFD fuselage-like cases. Three-dimensional (point excitation) NFD cases involving poro-elastic treatments can be modeled as a comparison of finite panel power injection method damping loss factor measurements.

REFERENCES

REFERENCES

- [1] C. Bruer and J. S. Bolton. Vibro-acoustic damping of extended vibrating systems. *Proceedings of AIAA Aeroacoustics Conference*, AIAA-87-2661, 7 pages, 1987.
- [2] H.-Y. Lai, J. S. Bolton, and J. H. Alexander. Structural damping by the use of fibrous blankets. *Proceedings of Noise-Con*, pages 403–408, 1998.
- [3] R. W. Gerdes, J. H. Alexander, B. K. Gardner, H.-Y. Lai, and J. S. Bolton. The use of poro-elastic finite elements to model the structural damping effect of fibrous acoustical treatments. *Proceedings of Noise-Con*, pages 409–414, 1998.
- [4] R. W. Gerdes, J. H. Alexander, B. K. Gardner, H.-Y. Lai, and J. S. Bolton. Numerical modeling of the damping effect of fibrous acoustical treatments. *SAE Technical Paper*, 2001-01-1462, 2001.
- [5] S. Nadeau, Y. Champoux, and L. Mongeau. Trim and floor influence on vibrational response of an aircraft model. *Journal of Aircraft*, 36(3):591–595, 1999.
- [6] A. Cummings, H. J. Rice, and R. Wilson. Radiation damping in plates, induced by porous media. *Journal of Sound and Vibration*, 221:143–167, 1999.
- [7] D. Tomlinson, R. J. M. Craik, and R. Wilson. Acoustic radiation from a plate into a porous medium. *Journal of Sound and Vibration*, 273:33–49, 2004.
- [8] J. R. Fricke. Lodengraf damping – an advanced vibration damping technology. *Sound and Vibration*, 34(7):22–27, 2000.
- [9] K. K. Varanasi and S. A. Nayfeh. Damping of flexural vibration using low-density, low-wave-speed media. *Journal of Sound and Vibration*, 292:402–414, 2006.
- [10] N. Kim, S. Lee, J. S. Bolton, S. Hollands, and T. Yoo. Structural damping by the use of fibrous materials. *SAE Technical Paper*, 2015-01-2239, 2015.
- [11] D. Ross, E. E. Ungar, and E. M. Kerwin Jr. Damping of plate flexural vibrations by means of viscoelastic laminae. *Structural Damping, ASME Publication, New York*, page 4988, 1959.
- [12] E. M. Kerwin Jr. Damping of flexural waves by a constrained viscoelastic layer. *The Journal of the Acoustical Society of America*, 31(7):952–962, 1959.
- [13] E. E. Ungar and E. M. Kerwin Jr. Plate damping due to thickness deformations in attached viscoelastic layers. *The Journal of the Acoustical Society of America*, 36(2):386–392, 1964.
- [14] J. S. Bolton. Porous materials for sound absorption and transmission control. *Proceedings of Inter-Noise*, paper 2084, 20 pages, 2005.

- [15] M. A. Biot. Theory of propagation of elastic waves in a fluid-saturated porous solid. *The Journal of the Acoustical Society of America*, 28(2):168–191, 1956.
- [16] J.-F. Allard. *Propagation of Sound in Porous Media: Modeling Sound Absorbing Materials*. Elsevier, New York, New York, first edition, 1993.
- [17] J.-F. Allard and N. Atalla. *Propagation of Sound in Porous Media: Modeling Sound Absorbing Materials*. Wiley, United Kingdom, second edition, 2009.
- [18] J. S. Bolton, N. M. Shiau, and Y. J. Kang. Sound transmission through multi-panel structures lined with elastic porous materials. *Journal of Sound and Vibration*, 191(3):317–347, 1996.
- [19] H.-Y. Lai. Modeling of acoustical properties of limp fibrous materials. *Purdue University*, Ph.D. Thesis, 1997.
- [20] R. Panneton. Comments on the limp frame equivalent fluid model porous media. *The Journal of the Acoustical Society of America*, 122:EL217–222, 2007.
- [21] H.-Y. Lai, S. Katragadda, J. S. Bolton, and J. H. Alexander. Layered fibrous treatments for a sound absorption and sound transmission. *SAE Technical Paper*, 972064, 1997.
- [22] T. J. Wahl and J. S. Bolton. The use of the discrete fourier transform to calculate the spatial and temporal response of line-driven, layer-wise homogeneous acoustically loaded panels. *The Journal of the Acoustical Society of America*, 92(3):1473–1488, 1992.
- [23] B. C. Bloss and M. D. Rao. Estimation of frequency-averaged loss factors by the power injection and the impulse response decay methods. *The Journal of the Acoustical Society of America*, 177(1):240–249, 2005.
- [24] D. L. Johnson, J. Koplik, and R. Dashen. Theory of dynamic permeability and tortuosity in fluid-saturated porous media. *Journal of Fluid Mechanics*, 176:379–402, 1987.
- [25] Y. Champoux and J.-F. Allard. Dynamic tortuosity and bulk modulus in air-saturated porous media. *Journal of Applied Physics*, 70(4):1975–1979, 1991.
- [26] J. S. Bolton. Poro-elastic material characterization methods by using standing wave tubes: history and current issues related to biot parameter estimation. *Conference Keynote Address of the 2nd Symposium on the Acoustics of Poro-Elastic Materials (SAPEM) 2008, Bradford, UK*, 2008.
- [27] F.-X. Becot and L. Jaouen. An alternative Biot’s formulation for dissipative porous media with skeleton deformation. *The Journal of the Acoustical Society of America*, 134(6):4801–4807, 2013.
- [28] D.-Y. Maa. Potential of microperforated panel absorber. *The Journal of the Acoustical Society of America*, 104(5):2861–2866, 1998.
- [29] T. Yoo, J. S. Bolton, D. F. Slama, and J. H. Alexander. Absorption of finite-sized microperforated panels with finite flexural stiffness at normal incidence. *Proceedings of Noise-Con*, pages 1102–1113, 2008.

- [30] B. H. Song and J. S. Bolton. A transfer-matrix approach for estimating the characteristic impedance and wave numbers of limp and rigid porous materials. *The Journal of the Acoustical Society of America*, 107(3):1131–1152, 2000.
- [31] R. Venegas and O. Umnova. Influence of sorption on sound propagation in granular activated carbon. *The Journal of the Acoustical Society of America*, 140(2):755–766, 2016.
- [32] ASTM E1050-12. Standard test method for impedance and absorption of acoustical materials using a tube, two microphones and a digital frequency analysis system. *American Society for Testing and Materials, West Conshohocken, PA, USA*, 2012.
- [33] W. T. Thompson. Transmission of elastic waves through a stratified solid medium. *Journal of Applied Physics*, 21:89–93, 1950.
- [34] J. S. Bolton and N. M. Shiau. Oblique incidence sound transmission through multi-panel structures lined with elastic porous materials. *Proceedings of AIAA 11th Aeroacoustic Conference*, AIAA-87-2660, 1987.
- [35] Y. Xue, J. S. Bolton, R. W. Gerdes, S. Lee, and T. Herdtle. Prediction of airflow resistivity of fibrous acoustical media having two fiber components and a distribution of fiber radii. *Applied Acoustics*, 134:145–153, 2018.
- [36] Y. Xue and J. S. Bolton. Fibrous material microstructure design for optimal structural damping. *The Journal of the Acoustical Society of America, Proceedings of 175th ASA Meeting, Minneapolis, MN*, 143(3):1715, 2018.
- [37] Y. Xue, J. S. Bolton, T. Herdtle, S. Lee, and R. W. Gerdes. Structural damping by lightweight poro-elastic media. *Journal of Sound and Vibration*, 459:114866, 19 pages, 2019.
- [38] Y. Xue, J. S. Bolton, and T. Herdtle. Design of lightweight fibrous vibration damping treatments to achieve optimal performance in realistic applications. *SAE Technical Paper*, 2019-01-1524, 2019.
- [39] B. Brouard, D. Lafarge, and J.-F. Allard. A general method of modeling sound propagation in layered media. *Journal of Sound and Vibration*, 183(1):129–142, 1995.
- [40] W. P. Mason. A study of the regular combination of acoustic elements, with applications to recurrent acoustic filters, tapered acoustic filters, and horns. *Bell System Technical Journal*, 6:258–294, 1927.
- [41] A. D. Pierce. *Acoustics An Introduction to its Physical Principles and Applications*. Acoustical Society of America, Melville, NY, 1989.
- [42] L. M. Brekhovskikh. *Waves in Layered Media*. Academic Press, New York, NY, 1960.
- [43] D. L. Folds and C. D. Loggins. Transmission and reflection of ultrasonic waves in layered media. *The Journal of the Acoustical Society of America*, 62:1102–1109, 1977.

- [44] K. P. Scharnhorst. Properties of acoustic and electromagnetic transmission coefficients and transfer matrices of multilayered plates. *The Journal of the Acoustical Society of America*, 74:1883–1886, 1983.
- [45] J.-F. Allard, C. Depollier, P. Rebillard, W. Lauriks, and A. Cops. Inhomogeneous Biot waves in layered media. *Journal of Applied Physics*, 66:2278–2284, 1989.
- [46] W. Lauriks, P. Mees, and J.-F. Allard. The acoustic transmission through layered systems. *Journal of Sound and Vibration*, 15(1):125–132, 1992.
- [47] O. Dazel, J.-P. Groby, B. Brouard, and C. Potel. A stable method to model the acoustic response of multilayered structures. *Journal of Applied Physics*, 113:083506, 2013.
- [48] Y. Xue, J. S. Bolton, R. W. Gerdes, S. Lee, and T. Herdtle. Prediction of airflow resistivity of fibrous acoustical media having double fiber components and a distribution of fiber radii. *Proceedings of Inter-Noise 2017, Hong Kong, China*, pages 5649–5657, 2017.
- [49] Y. Xue, J. S. Bolton, T. Herdtle, S. Lee, and R. W. Gerdes. Structural damping by layers of fibrous media applied to a periodically-constrained vibrating panel. *Journal of Physics: Conference Series*, 1264:012043, 15 pages, 2019.
- [50] Y. Xue, J. S. Bolton, T. Herdtle, S. Lee, and R. W. Gerdes. A comparison between glass fibers and polymeric fibers when serving as a structural damping medium for fuselage-like structures. *Proceedings of Inter-Noise 2018, Chicago, IL, USA*, paper 1478, 12 pages, 2018.
- [51] Y. Xue and J. S. Bolton. Microstructure design of lightweight fibrous material acting as a layered damper for a vibrating stiff panel. *The Journal of the Acoustical Society of America*, 143(6):3254–3265, 2018.
- [52] Y. Xue and J. S. Bolton. Fibrous material microstructure design for optimal damping performance. *Proceedings of the 5th Symposium on the Acoustics of Poro-Elastic Materials (SAPEM) 2017, Le Mans, France*, 2017.
- [53] D. Lafarge, P. Lemarinier, J.-F. Allard, and V. Tarnow. Dynamic compressibility of air in porous structures at audible frequencies. *Journal of the Acoustical Society of America*, 102(4):1995–2006, 1997.
- [54] S. R. Pride, F. D. Morgan, and A. F. Gangi. Drag forces of porous-medium acoustics. *Physical Review B: Condensed Matter and Materials Physics*, 47:4964–4978, 1993.
- [55] Y. Xue, J. S. Bolton, and Y. Liu. Modeling and coupling of acoustical layered systems that consist of elements having different transfer matrix dimensions. *Journal of Applied Physics*, in press, 2019.
- [56] D.-Y. Maa. Theory and design of microperforated panel sound-absorbing constructions. *Scientia Sinica*, 18(1):55–71, 1975.
- [57] D.-Y. Maa. Microperforated-panel wideband absorbers. *Noise Control Engineering Journal*, 29(3):77–84, 1987.

- [58] S. Lee. Application of microperforated elements in axial fan noise control and silencer design. *Purdue University*, Ph.D. Thesis, 2015.
- [59] H. Shin. Weight minimization of sound packages by balancing absorption and transmission performance. *Purdue University*, Ph.D. Thesis, 2019.
- [60] Y. J. Kang. Studies of sound absorption by and transmission through layers of elastic noise control foams: finite element modeling and effects of anisotropy. *Purdue University*, Ph.D. Thesis, 1994.
- [61] J.-W. Kim. Sound transmission through lined, composite panel structures: transversely isotropic poro-elastic model. *Purdue University*, Ph.D. Thesis, 2005.
- [62] J. S. Bolton. Normal incidence absorption properties of single layers of elastic porous materials. *Journal of the Acoustical Society of America, Proceedings of 110th ASA Meeting, Nashville, TN*, 78(S1):S60, 1985.
- [63] F.R.S. Lord Rayleigh D.C.L. On waves propagated along the plane surface of an elastic solid. *Proceedings of the London Mathematical Society*, S1-17(1):4–11, 1885.
- [64] D. Woods. On the use of mechanical and acoustical excitations for selective heat generation in polymer-bonded energetic materials. *Purdue University*, Ph.D. Thesis, 2016.
- [65] J. Klos, D. L. Palumbo, R. D. Buehrle, E. G. Williams, N. Valdivia, P. C. Herdic, and B. Sklanka. Comparison of different measurement technologies for the in-flight assessment of radiated acoustic intensity. *Proceedings of Noise-Con*, 2005.
- [66] D. J. Mead and K. K. Pujara. Space-harmonic analysis of periodically supported beams: response to convected random loading. *Journal of Sound and Vibration*, 14(4):525–541, 1971.
- [67] D. J. Mead. A general theory of harmonic wave propagation in linear periodic systems with multiple coupling. *Journal of Sound and Vibration*, 27(2):235–260, 1973.
- [68] H. Qiao, Z. He, W. Jiang, and W. Peng. Sound transmission of periodic composite structure lined with porous core: Rib-stiffened double panel case. *Journal of Sound and Vibration*, 440:256–276, 2018.
- [69] P. Fossat, C. Boutin, and M. Ichchou. Dynamics of periodic ribbed plates with inner resonance: Analytical homogenized model and dispersion features. *International Journal of Solids and Structures*, 152-153:85–103, 2018.
- [70] F. J. Fahy and P. Gardonio. *Sound and Structural Vibration: Radiation, Transmission and Response*. Elsevier, Netherlands, second edition, 2007.
- [71] D. J. Mead and S. M. Lee. Receptance methods and the dynamics of disordered one-dimensional lattices. *Journal of Sound and Vibration*, 92(3):427–445, 1984.
- [72] R. C. Brown. A many-fibre model of airflow through a fibrous filter. *Journal of Aerosol Science*, 15(5):583–593, 1984.

- [73] V. Tarnow. Measured anisotropic air flow resistivity and sound attenuation of glass wool. *The Journal of Acoustical Society of America*, 111(6):2735–2739, 2002.
- [74] K. Verdiere, R. Panneton, and S. Elkoun. Prediction of the acoustic behavior of a parallel assembly of hollow cylinders. *Applied Acoustics*, 102:100–107, 2016.
- [75] H. T. Luu, R. Panneton, and C. Perrot. Effective diameter for modeling the acoustic properties of polydisperse fiber networks. *The Journal of Acoustical Society of America*, 141(2):EL96–101, 2017.
- [76] K. Hirosawa and H. Nakagawa. Formulae for predicting non-acoustical parameters of deformed fibrous porous materials. *The Journal of Acoustical Society of America*, 141(6):4301–4313, 2017.
- [77] T. Herdtle, Y. Xue, and J. S. Bolton. Numerical modeling of the acoustics of low density fibrous media having a distribution of fiber sizes. *Proceedings of the 5th Symposium on the Acoustics of Poro-Elastic Materials (SAPEM) 2017, Le Mans, France*, 2017.
- [78] V. Tarnow. Airflow resistivity of models of fibrous material. *The Journal of Acoustical Society of America*, 100(6):3706–3713, 1997.
- [79] P. C. Carman. Fluid flow through granular beds. *Transactions of the American Institute of Chemical Engineers*, 15:S32–S48, 1937.
- [80] P. C. Carman. Permeability of saturated sands, soils and clays. *The Journal of Agricultural Science*, 29(02):262–273, 1939.
- [81] I. Langmuir. Theory of filtration of smokes. *Report on Smokes and Filters*, OSRD 865 Section IV, 1942.
- [82] C. N. Davies. The sedimentation and diffusion of small particles. *Proceedings of the Royal Society of London Series A-Mathematical and Physical Sciences*, 200(1060):100–113, 1949.
- [83] J. Happel. Viscous flow relative to arrays of cylinders. *The American Institute of Chemical Engineers Journal*, 5:174–177, 1959.
- [84] S. Kuwabara. The force experienced by randomly distributed parallel circular cylinders or spheres in a viscous flow at small reynolds numbers. *Journal of the Physical Society of Japan*, 14(4):527–532, 1959.
- [85] J. Pich. *Aerosol science*. Academic Press, London, edited by C. N. Davies edition, 1966.
- [86] E. Lind-Nordgren and P. Goransson. Optimising open porous foam for acoustical and vibrational performance. *Journal of Sound and Vibration*, 329:753–767, 2010.
- [87] O. Doutres, N. Atalla, and K. Dong. Effect of the microstructure closed pore content on the acoustic behavior of polyurethane foams. *Journal of Applied Physics*, 110:064901, 2011.

- [88] M. T. Pelegrinis, K. V. Horoshenkov, and A. Burnett. An application of kozeny-carman flow resistivity model to predict the acoustical properties of polyester fibre. *Applied Acoustics*, 101:1–4, 2016.
- [89] Y. Yang and Z. Chen. A model for calculating the air flow resistivity of glass fiber felt. *Applied Acoustics*, 91:6–11, 2015.
- [90] O. Doutres, N. Atalla, and K. Dong. A semi-phenomenological model to predict the acoustic behavior of fully and partially reticulated polyurethane foams. *Journal of Applied Physics*, 113:054901, 2013.
- [91] F. Aurenhammer. Voronoi diagrams – a survey of a fundamental geometric data structure. *Association for Computing Machinery Computing Surveys*, 23(3):345–405, 1991.
- [92] ASTM C522-03. Standard test method for airflow resistance of acoustical materials. *American Society for Testing and Materials, West Conshohocken, PA, USA*, 2016.
- [93] B. Noble and J. W. Daniel. *Applied Linear Algebra*. Prentice-Hall, Inc., Englewood Cliffs, New Jersey, second edition, 1977.
- [94] Z. Hu. Measurement and prediction of sound propagation over an absorbing plane. *Purdue University*, Ph.D. Thesis, 1992.
- [95] E. R. Green. An examination of “smart” foams for active noise control. *Purdue University*, Ph.D. Thesis, 1995.

APPENDICES

A. THE GRANULAR ACTIVATED CARBON (GAC) MODEL USED TO COUPLE BULK MODULI FROM DIFFERENT SCALES OF PORES OF THE DOUBLE-COMPONENT FIBER-PARTICLE POROUS MEDIUM

The process for calculating the micro-scale and nano-scale bulk moduli attributable to an activated carbon particle, and coupling those with the intergranular-scale bulk modulus by using the GAC model is described in Ref. [31] and is summarized here for the sake of completeness.

First, the bulk moduli resulting from three different scales of porosity were combined as

$$K'_f = \left(\frac{1}{E_p} + \frac{(1 - \phi_p) F_d}{E_u} \right)^{-1}, \quad (\text{A.1})$$

where E_p is the bulk modulus calculated by using the JCA model described in Chapter 2 for the fiber plus particle on the intergranular scale, which is coupled by the factor, F_d , and the intergranular-scale porosity, ϕ_p , with the micro-scale plus nano-scale, E_u . And ϕ_p , F_d and E_u can be expressed as

$$\phi_p = \frac{\phi_{tb} - (\phi_m + (1 - \phi_m) \phi_n)}{1 - (\phi_m + (1 - \phi_m) \phi_n)}, \quad (\text{A.2})$$

$$F_d = 3z_d^{-2}(1 - z_d \cot z_d), \quad (\text{A.3})$$

and

$$E_u = \left(\frac{1}{E_m} + \frac{(1 - \phi_m) F_{nm}}{E_n} \right)^{-1}. \quad (\text{A.4})$$

In Eq. (A.2), ϕ_{tb} , ϕ_m and ϕ_n are the overall porosity, the micro-scale porosity and the nano-scale porosity, respectively, where $\phi_{tb} = 1 - \rho_{bc}/\rho_{sc}$ can be calculated given the solid density of the carbon material, $\rho_{sc} = 2200 \text{ kg/m}^3$, and the bulk density of the particle component, $\rho_{bc} = 214.5 \text{ kg/m}^3$ (based on particle component weight

fraction, 0.78, and bulk density, ρ_b , of the double-component porous medium, 275 kg/m³), and $\phi_m = 0.71$ and $\phi_n = 0.26$ were previously characterized in Ref. [31].

In Eq. (A.3), interscale coupling, z_d , was calculated given a particle radius, $r_p = 0.74$ mm, micro-scale pore radius, $r_m = 0.41$ μ m, micro-scale bulk modulus, E_m , and dynamic viscous permeability, k_m : *i.e.*,

$$z_d = r_p \omega \sqrt{\eta / (i \omega k_m E_m)}, \quad (\text{A.5})$$

where

$$k_m = -i \phi_m \eta (1 - G_c) / (\rho_0 \omega), \quad (\text{A.6})$$

$$G_c = \frac{2J_1(s_c)}{s_c [J_0(s_c) - \text{Kn} s_c J_1(s_c)]}, \quad (\text{A.7})$$

$$s_c = \frac{i^{3/2} r_m}{\sqrt{\eta / \rho_0 \omega}}, \quad (\text{A.8})$$

and the Knudsen number in terms of specific gas constant, $R_g = 287.05$ J/(kg · K), and temperature, $T_g = 293.15$ K (20°C) is,

$$\text{Kn} = \frac{\eta \sqrt{\pi R_g T_g / 2}}{P_0 r_m}. \quad (\text{A.9})$$

In Eq. (A.4), another interscale coupling factor, F_{nm} , was calculated given the configurational diffusivity of air, $D_c = 1.35 \times 10^{-10}$ m²/s, by

$$F_{nm} = 1 - \frac{i \omega_s}{i \omega_s + \sqrt{1 + i \omega_s M_b / 2}}, \quad (\text{A.10})$$

where

$$\omega_s = \frac{\omega}{\omega_{dnm}}, \quad (\text{A.11})$$

$$M_b = \frac{8B_0}{\Lambda_d^2 (1 - \phi_m)}, \quad (\text{A.12})$$

$$\omega_{dnm} = \frac{D_c (1 - \phi_m)}{B_0}, \quad (\text{A.13})$$

$$B_0 = \frac{r_m^2 (-\ln \phi_m - 3/2 + 2\phi_m - \phi_m^2/2)}{4\phi_m}, \quad (\text{A.14})$$

$$\Lambda_d = \frac{r_m(1 - \phi_m)}{\phi_m}. \quad (\text{A.15})$$

The micro-scale bulk modulus, E_m , was calculated given the thermal permeability, k'_m , constant pressure heat capacity, $C_p = 1006.1$ J/K, and thermal conductivity, $\kappa = 0.02587$ W/(m · K) (Note that the Prandtl number $B^2 = C_p\eta/\kappa = 0.71$), by

$$E_m = \frac{\gamma P_0}{\phi_m} \left(\gamma - i\omega\rho_0 C_p (\gamma - 1) \frac{k'_m}{\phi_m \kappa} \right)^{-1}, \quad (\text{A.16})$$

where

$$k'_m = -i\phi_m B^2 \eta (1 - G'_c) / (\rho_0 \omega), \quad (\text{A.17})$$

$$G'_c = \frac{2J_1(s_t)}{s_t [J_0(s_t) - \text{Kn}' s_t J_1(s_t)]}, \quad (\text{A.18})$$

$$s_t = \frac{i^{3/2} r_m B}{\sqrt{\eta/\rho_0 \omega}}, \quad (\text{A.19})$$

and the Knudsen number was rewritten in thermal effect form as

$$\text{Kn}' = \frac{2\gamma \text{Kn}}{(\gamma + 1)B^2}. \quad (\text{A.20})$$

Also, the nano-scale bulk modulus, E_n , was calculated given nano-scale pore radius, $r_n = 0.33$ nm, Langmuir constant, $L_b = 3.47 \times 10^{-6}$ Pa⁻¹, mass of the saturating fluid (air) molecule, $m_m = 4.8 \times 10^{-26}$ kg, and area occupied by each molecule, $S_m = 4.3 \times 10^{-19}$ m², by

$$E_n = \frac{P_0}{\phi_n (1 + \rho_n \Psi / \rho_0)}, \quad (\text{A.21})$$

where

$$\Psi = \frac{P_0 L_b}{(1 + P_0 L_b)^2}, \quad (\text{A.22})$$

and

$$\rho_n = \frac{2\phi_n m_m}{r_n S_m}. \quad (\text{A.23})$$

B. THE TRANSFER MATRIX METHOD (TMM) USED TO PREDICT ACOUSTICAL PROPERTIES FOR LIMP POROUS MEDIA

The process for calculating acoustical properties including Z_{a1} , v_{z1} , Z_{a2} and v_{z2} by using the TMM model is summarized here for the sake of completeness.

The near-field acoustical properties and the far-field acoustical properties can be connected by the transfer matrix of the limp porous layer, and that relation can be expressed as

$$\begin{bmatrix} Z_{a1}v_{z1} \\ v_{z1} \end{bmatrix} = \begin{bmatrix} T_{11} & T_{12} \\ T_{21} & T_{22} \end{bmatrix} \begin{bmatrix} Z_{a2}v_{z2} \\ v_{z2} \end{bmatrix}, \quad (\text{B.1})$$

based on which the normal acoustic impedance at $z = 0$ looking into the acoustic medium, $Z_{a1}(k_x, \omega)$, can be expressed as

$$Z_{a1}(k_x, \omega) = \frac{T_{11}Z_{a2}(k_x, \omega) + T_{12}}{T_{21}Z_{a2}(k_x, \omega) + T_{22}}. \quad (\text{B.2})$$

The transfer matrix of the limp porous layer can be expressed as

$$\begin{bmatrix} T_{11} & T_{12} \\ T_{21} & T_{22} \end{bmatrix} = \begin{bmatrix} \cos \sqrt{k_c^2 - k_x^2}d & i \frac{\rho_c \omega}{\sqrt{k_c^2 - k_x^2}} \sin \sqrt{k_c^2 - k_x^2}d \\ i \frac{\sqrt{k_c^2 - k_x^2}}{\rho_c \omega} \sin \sqrt{k_c^2 - k_x^2}d & \cos \sqrt{k_c^2 - k_x^2}d \end{bmatrix}, \quad (\text{B.3})$$

where the k_c is the complex wavenumber, and ρ_c is the complex density of the limp porous layer. Both of these values can be evaluated at each frequency based on the Johnson-Champoux-Allard (JCA) model [16] and the Biot limp porous medium theory [19–21], given the properties that include the limp porous layer's σ , ϕ , α_∞ and ρ_b , in addition to ρ_0 , c_0 , B^2 , γ and η . The elements of the matrix can then be evaluated as functions of ω and k_x , given k_c , ρ_c and the porous layer thickness, d , by using Eq. (B.3). Finally, $Z_{a1}(k_x, \omega)$ can be evaluated by using Eq. (B.2), and

$v_t(k_x, \omega) = v_{z1}(k_x, \omega)$ can then be evaluated by using Eq. (4.9). In addition, $v_{z2}(k_x, \omega)$ can be evaluated as

$$v_{z2}(k_x, \omega) = \frac{v_{z1}(k_x, \omega)}{T_{21}Z_{a2}(k_x, \omega) + T_{22}}. \quad (\text{B.4})$$

Note that $Z_{a1} = Z_{a2}$ when there is no porous layer but only a bare panel loaded by the acoustic half-space.

C. THE ARBITRARY COEFFICIENT METHOD (ACM) USED TO PREDICT ACOUSTICAL PROPERTIES FOR PORO-ELASTIC MEDIA

The calculation process that gives the acoustical properties of the poro-elastic medium and the wavenumber domain response of the panel by using the ACM model is summarized here.

The main idea of the ACM model is to construct the equation system resulting from the boundary conditions of a layered structure, then to solve the matrix equation for all the arbitrary complex amplitude coefficients (C_1 – C_6 , W_t , A_2 , W_p , A_1 and B_1) of the propagating waves in the frequency and wavenumber domain. These propagating waves (also referred to as “field variables”) include the z -direction displacement for the solid phase of the poro-elastic medium

$$\begin{aligned} u_z(k_x, \omega) = & i \frac{k_{1z}}{k_1^2} (C_1 e^{-ik_{1z}z} - C_2 e^{ik_{1z}z}) + i \frac{k_{2z}}{k_2^2} (C_3 e^{-ik_{2z}z} - C_4 e^{ik_{2z}z}) \\ & + i \frac{k_x}{k_3^2} (C_5 e^{-ik_{3z}z} + C_6 e^{ik_{3z}z}), \end{aligned} \quad (\text{C.1})$$

the z -direction displacement for the fluid phase of the poro-elastic medium

$$\begin{aligned} U_z(k_x, \omega) = & ib_1 \frac{k_{1z}}{k_1^2} (C_1 e^{-ik_{1z}z} - C_2 e^{ik_{1z}z}) + ib_2 \frac{k_{2z}}{k_2^2} (C_3 e^{-ik_{2z}z} - C_4 e^{ik_{2z}z}) \\ & + ig \frac{k_x}{k_3^2} (C_5 e^{-ik_{3z}z} + C_6 e^{ik_{3z}z}), \end{aligned} \quad (\text{C.2})$$

the x -direction displacement for the solid phase of the poro-elastic medium

$$\begin{aligned} u_x(k_x, \omega) = & i \frac{k_x}{k_1^2} (C_1 e^{-ik_{1z}z} + C_2 e^{ik_{1z}z}) + i \frac{k_x}{k_2^2} (C_3 e^{-ik_{2z}z} + C_4 e^{ik_{2z}z}) \\ & - i \frac{k_{3z}}{k_3^2} (C_5 e^{-ik_{3z}z} - C_6 e^{ik_{3z}z}), \end{aligned} \quad (\text{C.3})$$

the shear force per unit material area acting on the solid phase in the x - z plane

$$\begin{aligned}\tau_{xz}(k_x, \omega) = & 2N \frac{k_x k_{1z}}{k_1^2} (C_1 e^{-ik_{1z}z} - C_2 e^{ik_{1z}z}) \\ & + 2N \frac{k_x k_{2z}}{k_2^2} (C_3 e^{-ik_{2z}z} - C_4 e^{ik_{2z}z}) \\ & + N \frac{k_x^2 - k_{3z}^2}{k_3^2} (C_5 e^{-ik_{3z}z} + C_6 e^{ik_{3z}z}),\end{aligned}\quad (\text{C.4})$$

the force per unit material area acting on the fluid phase of the poro-elastic medium

$$\begin{aligned}s(k_x, \omega) = & (Q + b_1 R) (C_1 e^{-ik_{1z}z} + C_2 e^{ik_{1z}z}) \\ & + (Q + b_2 R) (C_3 e^{-ik_{2z}z} + C_4 e^{ik_{2z}z}),\end{aligned}\quad (\text{C.5})$$

the force per unit material area acting on the solid phase of the poro-elastic medium

$$\begin{aligned}\sigma_z(k_x, \omega) = & \left(2N \frac{k_{1z}^2}{k_1^2} + A + b_1 Q \right) (C_1 e^{-ik_{1z}z} + C_2 e^{ik_{1z}z}) \\ & + \left(2N \frac{k_{2z}^2}{k_2^2} + A + b_2 Q \right) (C_3 e^{-ik_{2z}z} + C_4 e^{ik_{2z}z}) \\ & + \left(2N \frac{k_x k_{3z}}{k_3^2} \right) (C_5 e^{-ik_{3z}z} - C_6 e^{ik_{3z}z}),\end{aligned}\quad (\text{C.6})$$

the transverse displacement of the panel

$$w_t(k_x, \omega) = W_t, \quad (\text{C.7})$$

the longitudinal displacement of the panel

$$w_p(k_x, \omega) = W_p, \quad (\text{C.8})$$

the acoustic pressure above the poro-elastic layer ($z \geq d$)

$$p_b(k_x, \omega) = i\omega \rho_0 A_2 e^{-ik_z z}, \quad (\text{C.9})$$

the acoustic particle velocity above the poro-elastic layer ($z \geq d$)

$$v_{zb}(k_x, \omega) = ik_z A_2 e^{-ik_z z}, \quad (\text{C.10})$$

the acoustic pressure between the panel and the poro-elastic layer when they are unbonded

$$p_a(k_x, \omega) = i\omega\rho_0 (A_1 e^{-ik_z z} + B_1 e^{ik_z z}), \quad (\text{C.11})$$

and the acoustic particle velocity between the panel and the poro-elastic layer when they are unbonded

$$v_{za}(k_x, \omega) = ik_z (A_1 e^{-ik_z z} - B_1 e^{ik_z z}), \quad (\text{C.12})$$

where $k_z = \sqrt{[\omega(1 - i\eta_a)/c_0]^2 - k_x^2}$ is the z -direction wavenumber in the air expressed in terms of ω and k_x given ρ_0 , η_a and c_0 , and where the stress-strain relation constants, A , N , Q , R , the complex wavenumbers, k_1 , k_2 , k_3 , and the velocity or displacement ratios, b_1 , b_2 , g , can all be found by using the JCA model [16] and the Biot poro-elastic medium theory [15, 16, 18], given the poro-elastic layer's σ , ϕ , α_∞ , ρ_b , E_1 , ν and η_m , in addition to ρ_0 , c_0 , B^2 , γ and η . The z -direction wavenumbers $k_{1z} = \sqrt{k_1^2 - k_x^2}$, $k_{2z} = \sqrt{k_2^2 - k_x^2}$, $k_{3z} = \sqrt{k_3^2 - k_x^2}$, can then be evaluated in terms of ω and k_x . Note that the harmonic time dependence, $e^{i\omega t}$, and the x -direction harmonic spatial dependence, $e^{-ik_x x}$, are both eliminated for all the field variables mentioned above after Fourier transferring them from the time and space domain to the frequency and wavenumber domain. These frequency and wavenumber domain field variables can be combined with appropriate boundary conditions to construct the matrix equation system

$$[\mathbf{M}] [\mathbf{X}] = [\mathbf{J}]. \quad (\text{C.13})$$

Based on the boundary conditions (B.C.s) listed in Eqs. (4.11): *i.e.*, (4.11)(a)–(i) interpreted as B.C. (1)–(9) here for the bonded layered structure as shown in 4.2, $[\mathbf{X}]$ is a 9×1 vector of unknown amplitudes, and

$$[\mathbf{X}]^T = [C_1 \ C_2 \ C_3 \ C_4 \ C_5 \ C_6 \ W_t \ A_2 \ W_p]. \quad (\text{C.14})$$

$[\mathbf{M}]$ is a 9×9 coefficient matrix with row number, p , corresponding to the p^{th} B.C., and with column number, q , corresponding to the q^{th} element in $[\mathbf{X}]$. The elements in $[\mathbf{M}]$ are

$$\begin{aligned}
\mathbf{M}(1, 1) &= k_{1z}/k_1^2, \quad \mathbf{M}(1, 2) = -k_{1z}/k_1^2, \quad \mathbf{M}(1, 3) = k_{2z}/k_2^2, \\
\mathbf{M}(1, 4) &= -k_{2z}/k_2^2, \quad \mathbf{M}(1, 5) = k_x/k_3^2, \quad \mathbf{M}(1, 6) = k_x/k_3^2, \quad \mathbf{M}(1, 7) = i, \\
\mathbf{M}(2, 1) &= b_1 k_{1z}/k_1^2, \quad \mathbf{M}(2, 2) = -b_1 k_{1z}/k_1^2, \quad \mathbf{M}(2, 3) = b_2 k_{2z}/k_2^2, \\
\mathbf{M}(2, 4) &= -b_2 k_{2z}/k_2^2, \quad \mathbf{M}(2, 5) = g k_x/k_3^2, \quad \mathbf{M}(2, 6) = g k_x/k_3^2, \quad \mathbf{M}(2, 7) = i, \\
\mathbf{M}(3, 1) &= k_x/k_1^2, \quad \mathbf{M}(3, 2) = k_x/k_1^2, \quad \mathbf{M}(3, 3) = k_x/k_2^2, \quad \mathbf{M}(3, 4) = k_x/k_2^2, \\
\mathbf{M}(3, 5) &= -k_{3z}/k_3^2, \quad \mathbf{M}(3, 6) = k_{3z}/k_3^2, \quad \mathbf{M}(3, 7) = -h_p k_x/2, \quad \mathbf{M}(3, 9) = i, \\
\mathbf{M}(4, 1) &= 2N k_x k_{1z}/k_1^2, \quad \mathbf{M}(4, 2) = -2N k_x k_{1z}/k_1^2, \quad \mathbf{M}(4, 3) = 2N k_x k_{2z}/k_2^2, \\
\mathbf{M}(4, 4) &= -2N k_x k_{2z}/k_2^2, \quad \mathbf{M}(4, 5) = N (k_x^2 - k_{3z}^2) / k_3^2, \\
\mathbf{M}(4, 6) &= N (k_x^2 - k_{3z}^2) / k_3^2, \quad \mathbf{M}(4, 9) = - (D_p k_x^2 - m_s \omega^2), \\
\mathbf{M}(5, 1) &= 2N k_{1z}^2/k_1^2 + A + b_1 Q + Q + b_1 R - i h_p N k_x^2 k_{1z}/k_1^2, \\
\mathbf{M}(5, 2) &= 2N k_{1z}^2/k_1^2 + A + b_1 Q + Q + b_1 R + i h_p N k_x^2 k_{1z}/k_1^2, \\
\mathbf{M}(5, 3) &= 2N k_{2z}^2/k_2^2 + A + b_2 Q + Q + b_2 R - i h_p N k_x^2 k_{2z}/k_2^2, \\
\mathbf{M}(5, 4) &= 2N k_{2z}^2/k_2^2 + A + b_2 Q + Q + b_2 R + i h_p N k_x^2 k_{2z}/k_2^2, \\
\mathbf{M}(5, 5) &= 2N k_x k_{3z}/k_3^2 - i h_p N k_x (k_x^2 - k_{3z}^2) / k_3^2/2, \\
\mathbf{M}(5, 6) &= -2N k_x k_{3z}/k_3^2 - i h_p N k_x (k_x^2 - k_{3z}^2) / k_3^2/2, \\
\mathbf{M}(5, 7) &= - (D k_x^4 - m_s \omega^2), \\
\mathbf{M}(6, 1) &= (Q + b_1 R) e^{-i k_{1z} d}, \quad \mathbf{M}(6, 2) = (Q + b_1 R) e^{i k_{1z} d}, \\
\mathbf{M}(6, 3) &= (Q + b_2 R) e^{-i k_{2z} d}, \quad \mathbf{M}(6, 4) = (Q + b_2 R) e^{i k_{2z} d}, \\
\mathbf{M}(6, 8) &= i \omega \rho_0 \phi e^{-i k_z d},
\end{aligned}$$

$$\begin{aligned}
\mathbf{M}(7, 1) &= (2Nk_{1z}^2/k_1^2 + A + b_1Q) e^{-ik_{1z}d}, \\
\mathbf{M}(7, 2) &= (2Nk_{1z}^2/k_1^2 + A + b_1Q) e^{ik_{1z}d}, \\
\mathbf{M}(7, 3) &= (2Nk_{2z}^2/k_2^2 + A + b_2Q) e^{-ik_{2z}d}, \\
\mathbf{M}(7, 4) &= (2Nk_{2z}^2/k_2^2 + A + b_2Q) e^{ik_{2z}d}, \\
\mathbf{M}(7, 5) &= (2Nk_x k_{3z}/k_3^2) e^{-ik_{3z}d}, \\
\mathbf{M}(7, 6) &= (-2Nk_x k_{3z}/k_3^2) e^{ik_{3z}d}, \quad \mathbf{M}(7, 8) = i\omega\rho_0(1 - \phi)e^{-ik_zd}, \\
\mathbf{M}(8, 1) &= (-\omega(1 - \phi + \phi b_1)k_{1z}/k_1^2) e^{-ik_{1z}d}, \\
\mathbf{M}(8, 2) &= (\omega(1 - \phi + \phi b_1)k_{1z}/k_1^2) e^{ik_{1z}d}, \\
\mathbf{M}(8, 3) &= (-\omega(1 - \phi + \phi b_2)k_{2z}/k_2^2) e^{-ik_{2z}d}, \\
\mathbf{M}(8, 4) &= (\omega(1 - \phi + \phi b_2)k_{2z}/k_2^2) e^{ik_{2z}d}, \\
\mathbf{M}(8, 5) &= (-\omega(1 - \phi + \phi g)k_x/k_3^2) e^{-ik_{3z}d}, \\
\mathbf{M}(8, 6) &= (-\omega(1 - \phi + \phi g)k_x/k_3^2) e^{ik_{3z}d}, \quad \mathbf{M}(8, 8) = -ik_z e^{-ik_zd}, \\
\mathbf{M}(9, 1) &= (2Nk_x k_{1z}/k_1^2) e^{-ik_{1z}d}, \quad \mathbf{M}(9, 2) = (-2Nk_x k_{1z}/k_1^2) e^{ik_{1z}d}, \\
\mathbf{M}(9, 3) &= (2Nk_x k_{2z}/k_2^2) e^{-ik_{2z}d}, \quad \mathbf{M}(9, 4) = (-2Nk_x k_{2z}/k_2^2) e^{ik_{2z}d}, \\
\mathbf{M}(9, 5) &= [N(k_x^2 - k_{3z}^2)/k_3^2] e^{-ik_{3z}d}, \quad \mathbf{M}(9, 6) = [N(k_x^2 - k_{3z}^2)/k_3^2] e^{ik_{3z}d}.
\end{aligned}$$

$[\mathbf{J}]$ is a 9×1 forcing vector with row number, p , corresponding to the p^{th} B.C., and

$$\mathbf{J}(5, 1) = -F,$$

and all the other elements in $[\mathbf{M}]$ and $[\mathbf{J}]$ are equal to zero.

From the boundary conditions as shown in Eqs. (4.13): *i.e.*, (4.13)(a)–(j) interpreted as B.C. (1)–(10) here for the unbonded layered structure as shown in 4.3, $[\mathbf{X}]$ is a 10×1 vector of unknown amplitudes, and

$$[\mathbf{X}]^T = [C_1 \ C_2 \ C_3 \ C_4 \ C_5 \ C_6 \ W_t \ A_2 \ A_1 \ B_1]. \quad (\text{C.15})$$

$[\mathbf{M}]$ is a 10×10 coefficient matrix with the elements being

$$\begin{aligned}
\mathbf{M}(1, 7) &= Dk_x^4 - m_s \omega^2, \quad \mathbf{M}(1, 9) = i\omega \rho_0, \quad \mathbf{M}(1, 10) = i\omega \rho_0, \\
\mathbf{M}(2, 7) &= i\omega, \quad \mathbf{M}(2, 9) = -ik_z, \quad \mathbf{M}(2, 10) = ik_z, \\
\mathbf{M}(3, 1) &= Q + b_1 R, \quad \mathbf{M}(3, 2) = Q + b_1 R, \quad \mathbf{M}(3, 3) = Q + b_2 R, \\
\mathbf{M}(3, 4) &= Q + b_2 R, \quad \mathbf{M}(3, 9) = i\omega \rho_0 \phi, \quad \mathbf{M}(3, 10) = i\omega \rho_0 \phi, \\
\mathbf{M}(4, 1) &= 2Nk_{1z}^2/k_1^2 + A + b_1 Q, \quad \mathbf{M}(4, 2) = 2Nk_{1z}^2/k_1^2 + A + b_1 Q, \\
\mathbf{M}(4, 3) &= 2Nk_{2z}^2/k_2^2 + A + b_2 Q, \quad \mathbf{M}(4, 4) = 2Nk_{2z}^2/k_2^2 + A + b_2 Q, \\
\mathbf{M}(4, 5) &= 2Nk_x k_{3z}/k_3^2, \quad \mathbf{M}(4, 6) = -2Nk_x k_{3z}/k_3^2, \\
\mathbf{M}(4, 9) &= i\omega \rho_0 (1 - \phi), \quad \mathbf{M}(4, 10) = i\omega \rho_0 (1 - \phi), \\
\mathbf{M}(5, 1) &= -\omega(1 - \phi + \phi b_1) k_{1z}/k_1^2, \quad \mathbf{M}(5, 2) = \omega(1 - \phi + \phi b_1) k_{1z}/k_1^2, \\
\mathbf{M}(5, 3) &= -\omega(1 - \phi + \phi b_2) k_{2z}/k_2^2, \quad \mathbf{M}(5, 4) = \omega(1 - \phi + \phi b_2) k_{2z}/k_2^2, \\
\mathbf{M}(5, 5) &= -\omega(1 - \phi + \phi g) k_x/k_3^2, \quad \mathbf{M}(5, 6) = -\omega(1 - \phi + \phi g) k_x/k_3^2, \\
\mathbf{M}(5, 9) &= -ik_z, \quad \mathbf{M}(5, 10) = ik_z, \\
\mathbf{M}(6, 1) &= 2Nk_x k_{1z}/k_1^2, \quad \mathbf{M}(6, 2) = -2Nk_x k_{1z}/k_1^2, \\
\mathbf{M}(6, 3) &= 2Nk_x k_{2z}/k_2^2, \quad \mathbf{M}(6, 4) = -2Nk_x k_{2z}/k_2^2, \\
\mathbf{M}(6, 5) &= N(k_x^2 - k_{3z}^2)/k_3^2, \quad \mathbf{M}(6, 6) = N(k_x^2 - k_{3z}^2)/k_3^2, \\
\mathbf{M}(7, 1) &= (Q + b_1 R) e^{-ik_{1z}d}, \quad \mathbf{M}(7, 2) = (Q + b_1 R) e^{ik_{1z}d}, \\
\mathbf{M}(7, 3) &= (Q + b_2 R) e^{-ik_{2z}d}, \quad \mathbf{M}(7, 4) = (Q + b_2 R) e^{ik_{2z}d}, \\
\mathbf{M}(7, 8) &= i\omega \rho_0 \phi e^{-ik_zd}, \\
\mathbf{M}(8, 1) &= (2Nk_{1z}^2/k_1^2 + A + b_1 Q) e^{-ik_{1z}d}, \\
\mathbf{M}(8, 2) &= (2Nk_{1z}^2/k_1^2 + A + b_1 Q) e^{ik_{1z}d}, \\
\mathbf{M}(8, 3) &= (2Nk_{2z}^2/k_2^2 + A + b_2 Q) e^{-ik_{2z}d}, \\
\mathbf{M}(8, 4) &= (2Nk_{2z}^2/k_2^2 + A + b_2 Q) e^{ik_{2z}d}, \\
\mathbf{M}(8, 5) &= (2Nk_x k_{3z}/k_3^2) e^{-ik_{3z}d}, \\
\mathbf{M}(8, 6) &= (-2Nk_x k_{3z}/k_3^2) e^{ik_{3z}d}, \\
\mathbf{M}(8, 8) &= i\omega \rho_0 (1 - \phi) e^{-ik_zd},
\end{aligned}$$

$$\begin{aligned}
\mathbf{M}(9, 1) &= (-\omega(1 - \phi + \phi b_1)k_{1z}/k_1^2) e^{-ik_{1z}d}, \\
\mathbf{M}(9, 2) &= (\omega(1 - \phi + \phi b_1)k_{1z}/k_1^2) e^{ik_{1z}d}, \\
\mathbf{M}(9, 3) &= (-\omega(1 - \phi + \phi b_2)k_{2z}/k_2^2) e^{-ik_{2z}d}, \\
\mathbf{M}(9, 4) &= (\omega(1 - \phi + \phi b_2)k_{2z}/k_2^2) e^{ik_{2z}d}, \\
\mathbf{M}(9, 5) &= (-\omega(1 - \phi + \phi g)k_x/k_3^2) e^{-ik_{3z}d}, \\
\mathbf{M}(9, 6) &= (-\omega(1 - \phi + \phi g)k_x/k_3^2) e^{ik_{3z}d}, \quad \mathbf{M}(9, 8) = -ik_z e^{-ik_z d}, \\
\mathbf{M}(10, 1) &= (2Nk_x k_{1z}/k_1^2) e^{-ik_{1z}d}, \quad \mathbf{M}(10, 2) = (-2Nk_x k_{1z}/k_1^2) e^{ik_{1z}d}, \\
\mathbf{M}(10, 3) &= (2Nk_x k_{2z}/k_2^2) e^{-ik_{2z}d}, \quad \mathbf{M}(10, 4) = (-2Nk_x k_{2z}/k_2^2) e^{ik_{2z}d}, \\
\mathbf{M}(10, 5) &= [N(k_x^2 - k_{3z}^2)/k_3^2] e^{-ik_{3z}d}, \quad \mathbf{M}(10, 6) = [N(k_x^2 - k_{3z}^2)/k_3^2] e^{ik_{3z}d}.
\end{aligned}$$

$[\mathbf{J}]$ is a 10×1 forcing vector with the element

$$\mathbf{J}(1, 1) = F,$$

and all the other elements in $[\mathbf{M}]$ and $[\mathbf{J}]$ are equal to zero.

For both the bonded and the unbonded cases, $[\mathbf{M}]$ and $[\mathbf{J}]$ were conditioned by dividing each element, $\mathbf{M}(p, q)$, by the Euclidean norm of the p^{th} row of $[\mathbf{M}]$, which ensured a unity norm for each row of $[\mathbf{M}]$, and which helped avoid numerical errors during the matrix solution process due to the fact that some non-zero terms were much smaller than the other non-zero terms in the same row [93]. Note that alternative conditioning methods were studied in Refs. [94, 95], which can also be applied here. After the row-conditioning, the vector of unknowns was solved for in either the bonded or unbonded case by calculating

$$[\mathbf{X}] = [\mathbf{M}]^{-1} [\mathbf{J}], \quad (\text{C.16})$$

and for both the bonded and the unbonded cases, the wavenumber domain velocity response of the panel can be evaluated as

$$v_t(k_x, \omega) = i\omega W_t = i\omega \mathbf{X}(7, 1), \quad (\text{C.17})$$

and $v_{z2}(k_x, \omega)$ can be evaluated by

$$v_{z2}(k_x, \omega) = -ik_z A_2 e^{-ik_z d} = -ik_z \mathbf{X}(8, 1) e^{-ik_z d}. \quad (\text{C.18})$$

In addition, $Z_{a1}(k_x, \omega)$ can be calculated given $v_{z1}(k_x, \omega) = v_t(k_x, \omega)$ by using Eq. (4.7)

$$Z_{a1}(k_x, \omega) = \frac{F}{v_{z1}(k_x, \omega)} - Z_m(k_x, \omega). \quad (\text{C.19})$$

D. SPACE-HARMONIC ANALYSIS TO PREDICT THE RESPONSES OF PERIODICALLY-SUPPORTED BEAMS

The process for calculating the spatial response of a periodically-supported beam by using the space-harmonic theory described in Ref. [66] is summarized here, which was used in Section 4.7.3 to validate the NFD case having a two-dimensional stiff panel that is periodically-constrained by translational and rotational stiffnesses.

First, the time and space domain transverse displacement of a periodically-supported beam can be expressed as

$$w_t(x, t) = \sum_{n=-\infty}^{n=+\infty} A_n e^{-i(\mu_v + 2n\pi)x/l} e^{i\omega t}, \quad (\text{D.1})$$

and it can be transform to frequency and space domain as

$$w_t(x, \omega) = \sum_{n=-\infty}^{n=+\infty} A_n e^{-i(\mu_v + 2n\pi)x/l}, \quad (\text{D.2})$$

so the frequency and space domain transverse velocity of the beam can be expressed as

$$v_t(x, \omega) = i\omega \sum_{n=-\infty}^{n=+\infty} A_n e^{-i(\mu_v + 2n\pi)x/l}, \quad (\text{D.3})$$

where l is the separation between any two of the supports, $\mu_v = k_v l = \Omega/CV$ is the dimensionless excitation wavenumber parameter in terms of the excitation wavenumber (convective wavenumber in the NFD model), k_v , and the spacing, l ($= 1$ m), or in terms of the dimensionless frequency parameter, Ω , and the dimensionless convection velocity parameter, CV . The expressions for Ω and CV are

$$\Omega = (m_s \omega^2 l^4 / D)^{1/2}, \quad (\text{D.4})$$

and

$$CV = (m_s / D)^{1/2} \omega l / k_v, \quad (\text{D.5})$$

where m_s and D are mass per unit area and complex flexural stiffness of the panel defined in Section 4.2 of this thesis. And the amplitude coefficients, A_n 's, in Eq. (D.3) can then be solved by using a set of equations derived by the principle of virtual work.

For a rigid support case, the set of equations can be expressed as

$$\sum_{\substack{n=-\infty \\ n \neq 0}}^{n=+\infty} (\mu_v^4 - \Omega^2) A_n + \kappa_r \sum_{\substack{n=-\infty \\ n \neq 0}}^{n=+\infty} (2n\pi)(2m\pi)A_n + [(\mu_v + 2m\pi)^4 - \Omega^2] A_m = -P_v, \quad (\text{D.6})$$

where $\kappa_r = s_l l / D$ is the dimensionless rotational stiffness parameter, $P_v = Pl^4 / D$ is the dimensionless loading parameter, and by summing up the index n ranging from -20 to 20 except for 0 , 40 A_n 's (A_{-20} to A_{20} except for A_0) can be solved by using the 40 equations that result from assigning m from -20 to 20 , except for 0 in Eq. (D.6). Then A_0 can be calculated by

$$A_0 = - \sum_{\substack{n=-\infty \\ n \neq 0}}^{n=+\infty} A_n. \quad (\text{D.7})$$

For a flexible support case, the set of equations can be expressed as

$$\begin{aligned} \kappa_t \sum_{n=-\infty}^{n=+\infty} A_n + \kappa_r \sum_{n=-\infty}^{n=+\infty} (\mu_v + 2n\pi)(\mu_v + 2m\pi)A_n + [(\mu_v + 2m\pi)^4 - \Omega^2] A_m \\ = 0, \text{ when } m \neq 0 \\ = P_v, \text{ when } m = 0 \end{aligned} \quad (\text{D.8})$$

where $\kappa_t = k_l l / D$ is the dimensionless translational stiffness parameter, and by summing up the index n ranging from -20 to 20 , 41 A_n 's (A_{-20} to A_{20}) can be solved by using 41 equations resulted from assigning m from -20 to 20 in Eq. (D.8).

Finally, by submitting A_n 's, μ_v and l to Eq. (D.3), the frequency and space domain response of the periodically-supported beam can be calculated and used as a comparison to the periodically-constrained panel case of the NFD model.

E. SUMMARY OF THE FORMULAE FROM THE AFR-SCUR CLASSIC MODELS

All the formulae and some original applications related to the reviewed AFR-SCUR models including the ones mentioned in Ref. [19] are summarized here.

Carman's model from 1939 was developed for saturated sands or porous clay granules involved in petroleum engineering problems, and was expressed as

$$\sigma = \frac{4\eta k C^2}{r^2(1-C)^3}, \quad (\text{E.1})$$

where the factor k is the Kozeny constant.

Langmuir's model from 1942 was developed for bounded cylinders and was expressed as

$$\sigma = \frac{5.6\eta C}{r^2 \left(-\ln C + 2C - \frac{C^2}{2} - \frac{3}{2} \right)}. \quad (\text{E.2})$$

Davies' model from 1949 was developed for diffused particles in a wide vessel and was expressed as

$$\sigma = \frac{16\eta C^{1.5} (1 + 56C^3)}{r^2}. \quad (\text{E.3})$$

Happel's model from 1959 was developed for arrays of cylinders and was expressed as

$$\sigma = \frac{8\eta C}{r^2 \left[-\ln C - \frac{(1-C^2)}{(1+C^2)} \right]}. \quad (\text{E.4})$$

Kuwabara's model from 1959 was developed for distributed parallel cylinders and was expressed as

$$\sigma = \frac{8\eta C}{r^2 \left(-\ln C + 2C - \frac{C^2}{2} - \frac{3}{2} \right)}. \quad (\text{E.5})$$

Pich's model from 1966 was developed for dispersive aerosols passing a cylinder and was expressed as

$$\sigma = \frac{8\eta C(1 + 1.996\text{Kn})}{r^2 \left[-\ln C + 2C - \frac{C^2}{2} - \frac{3}{2} + 1.996\text{Kn} \left(-\ln C + \frac{C^2}{2} - \frac{1}{2} \right) \right]}. \quad (\text{E.6})$$

where Kn is the Knudsen number, which is the ratio of the mean free path of the air molecules to the fiber radius.

Tarnow's models from 1996 were developed for fibrous acoustical materials and they were expressed as

$$\sigma = \frac{4\eta C}{r^2 (-0.64 \ln C - 0.737 + C)}, \quad (\text{E.7a})$$

$$\sigma = \frac{4\eta C}{r^2 (-0.5 \ln C - 0.75 + C - 0.25C^2)}, \quad (\text{E.7b})$$

$$\sigma = \frac{4\eta C}{r^2 (-1.28 \ln C - 1.474 + 2C)}, \quad (\text{E.7c})$$

$$\sigma = \frac{4\eta C}{r^2 (-\ln C - 1.5 + 2C)}, \quad (\text{E.7d})$$

where Eq. (E.7a) was developed for random lattice fiber cylinders with perpendicular passing-by flow and it is the one same as Eq. (6.1), which was used for the modified AFR-TCVR model; Eq. (E.7b) was developed for square lattice fiber cylinders with perpendicular passing-by flow; Eq. (E.7c) was developed for random lattice fiber cylinders with parallel passing-by flow; Eq. (E.7d) was developed for square lattice fiber cylinders with parallel passing-by flow.

The BAL-semi-empirical AFR-TCUR model from 1997 developed by Lai *et al.* for fibrous acoustical materials was expressed as

$$\sigma = 10^{-5.7} \rho_b^{1.61} \left(\frac{X_1^{1.61}}{\rho_1^{1.61} r_1^{2.25}} + \frac{X_2^{1.61}}{\rho_2^{1.61} r_2^{2.25}} \right). \quad (\text{E.8})$$

Lind-Nordgren and Goransson's model from 2010 was developed for open porous foam and was expressed as

$$\sigma = \frac{32\eta\alpha_\infty C^2}{r^2 c_g^2 \phi}, \quad (\text{E.9})$$

where c_g is the pore shape dependent constant, which is equal to 1 when the pore is cylinder.

Doutres *et al.*'s model from 2011 was developed for polyurethane foam and was expressed as

$$\sigma = \frac{32\eta\alpha_\infty C^2}{r^2 c_g^2}. \quad (\text{E.10})$$

Pelegrinis *et al.*'s model from 2016 was developed for polyester fiber and was expressed as

$$\sigma = \frac{45\eta C^2}{r^2(1 - C)^3}. \quad (\text{E.11})$$

VITA

VITA

Yutong Xue was born on September 8th, 1991 in Shihezi, Xinjiang, China. He attended Urumqi No.1 Senior High School from 2007 to 2010, where he met his wife, April. He received his Bachelor of Science degree in Mechanical Engineering from Shanghai Jiao Tong University in 2014. He received his Master of Science degree in Mechanical Engineering from Columbia University in 2015. In 2016, He started his doctorate study at Purdue University focusing on acoustics and vibration with Professor J. Stuart Bolton, and he received his Ph.D. degree in Mechanical Engineering in December 2019. After graduation from Purdue, he started a job as Advanced Dynamics Senior Engineer in the Server Engineering and Research Group of Seagate Technology.